

University of Groningen

Coupled charge, spin and heat transport in metal-insulator hybrid systems

Shan, Juan

IMPORTANT NOTE: You are advised to consult the publisher's version (publisher's PDF) if you wish to cite from it. Please check the document version below.

Document Version

Publisher's PDF, also known as Version of record

Publication date:

2018

[Link to publication in University of Groningen/UMCG research database](#)

Citation for published version (APA):

Shan, J. (2018). *Coupled charge, spin and heat transport in metal-insulator hybrid systems*. Rijksuniversiteit Groningen.

Copyright

Other than for strictly personal use, it is not permitted to download or to forward/distribute the text or part of it without the consent of the author(s) and/or copyright holder(s), unless the work is under an open content license (like Creative Commons).

The publication may also be distributed here under the terms of Article 25fa of the Dutch Copyright Act, indicated by the "Taverne" license. More information can be found on the University of Groningen website: <https://www.rug.nl/library/open-access/self-archiving-pure/taverne-amendment>.

Take-down policy

If you believe that this document breaches copyright please contact us providing details, and we will remove access to the work immediately and investigate your claim.

Downloaded from the University of Groningen/UMCG research database (Pure): <http://www.rug.nl/research/portal>. For technical reasons the number of authors shown on this cover page is limited to 10 maximum.

Coupled charge, spin and heat transport in metal-insulator hybrid systems

Juan Shan



**university of
 groningen**

faculty of science
 and engineering

zernike institute for
 advanced materials

Zernike Institute PhD thesis series 2018-09

ISSN: 1570-1530

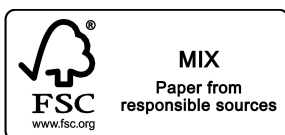
ISBN: 978-94-034-0599-5

ISBN: 978-94-034-0598-8 (electronic version)

The work described in this thesis was performed in the research group Physics of Nanodevices of the Zernike Institute for Advanced Materials at the University of Groningen, the Netherlands. This work was supported by NanoLab NL and the Zernike Institute for Advanced Materials.

Cover design: Juan Shan & Lei Liang

Printed by: Gildeprint, Enschede





rijksuniversiteit
 groningen

Coupled charge, spin and heat transport in metal-insulator hybrid systems

Proefschrift

ter verkrijging van de graad van doctor aan de
 Rijksuniversiteit Groningen
 op gezag van de
 rector magnificus prof. dr. E. Sterken,
 en volgens besluit van het College voor Promoties.

De openbare verdediging zal plaatsvinden op

maandag 16 april 2018 om 12:45 uur

door

Juan Shan

geboren op 2 juli 1990
 te Sichuan, China

Promotores

Prof. dr. ir. B. J. van Wees

Prof. dr. ir. C. H. van der Wal

Beoordelingscommissie

Prof. dr. J. P. Heremans

Prof. dr. M. Kläui

Prof. dr. R. C. Chiechi

*dedicated to my family,
friends and teachers*

Contents

1	Introduction	1
1.1	Spintronics	1
1.2	Magnon spintronics	2
1.3	Spin caloritronics	3
1.4	Motivation and outline	3
	References	6
2	Concepts	9
2.1	Charge and spin transport in metals	9
2.1.1	Electrical transport	9
2.1.2	Spin transport	11
2.1.3	Spin-charge conversion: spin Hall effect	18
2.2	Spin transport across a metal/ferromagnetic insulator interface	19
2.2.1	Spin-mixing conductance	20
2.2.2	Effective Spin-mixing conductance	21
2.2.3	Spin resistor model for interfacial spin transfer and backflow factor	21
2.2.4	Spin Hall magnetoresistance	25
2.3	Spin transport in magnetic insulators	27
2.3.1	Magnons	28
2.3.2	The chemical potential of magnons	29
2.3.3	The transport of exchange magnons	30
2.3.4	Yttrium iron garnet and nickel ferrite	33
2.4	Thermoelectrics and spin caloritronics in metallic systems	36
2.4.1	The Seebeck effect and the Peltier effect	37
2.4.2	Spin-dependent Seebeck effect and spin-dependent Peltier effect	39

2.4.3	Magneto-Seebeck effect and magneto-Peltier effect	40
2.5	Spin caloritronics in magnetic insulators	41
2.5.1	Spin Seebeck effect	42
2.5.2	Spin Peltier effect	46
References	47
3	Comparison of the magneto-Peltier and magneto-Seebeck effects in mag-	
	netic tunnel junctions	59
3.1	Introduction	59
3.2	Concept of the experiment	60
3.3	Experimental details	62
3.3.1	Device geometry	62
3.3.2	Measurement techniques	62
3.4	Results and discussion	63
3.5	Conclusions	67
3.6	Supplementary information	67
3.6.1	Results for two other samples	67
3.6.2	Extraction of the linear response from the lock-in measurements	67
3.6.3	Finite element thermoelectric model	69
3.6.4	Joule heating in higher-order responses	71
References	75
4	Influence of yttrium iron garnet thickness and heater opacity on the nonlo-	
	cal transport of electrically and thermally excited magnons	79
4.1	Introduction	79
4.2	Experimental details	81
4.3	Results and discussion	83
4.3.1	Nonlocal results for electrically injected magnons	83
4.3.2	Nonlocal results for thermally generated magnons	86
4.4	Finite element modeling results	91
4.4.1	Electrically injected magnons	93
4.4.2	Thermally generated magnons	95
4.4.3	Discussion	97
4.5	Conclusions	98
4.6	Supplementary information	98
4.6.1	Temperature profiles when Pt serves as a Joule heater	98
4.6.2	Local spin Seebeck effect as a function of YIG thickness	100
4.6.3	Vertical one-dimensional analytical model for the spin Seebeck effect	101
4.7	Linear-scale plots of V_{TG} for different YIG thickness	103

References	105
5 Criteria for accurate determination of the magnon relaxation length from the nonlocal spin Seebeck effect	109
5.1 Introduction	109
5.2 Experimental details	111
5.3 Results and discussion	113
5.3.1 Results on 2.7- μm -thick YIG	113
5.3.2 Results on 50- μm -thick YIG	118
5.3.3 Modeling results on bulk YIG	120
5.3.4 Summary	121
5.4 Conclusions	123
References	124
6 Nonlocal magnon spin transport in NiFe_2O_4 thin films	127
6.1 Introduction	127
6.2 Experimental details	128
6.3 Results and discussion	130
6.4 Conclusions	135
References	136
A Fabrication techniques	139
A.1 Overall procedure	139
A.2 Electron beam lithography	141
A.3 Electron beam evaporation	142
A.4 Sputter deposition	143
B Measurement techniques	145
B.1 Lock-in technique	145
C Finite element modeling method	149
C.1 Basic concepts	149
C.2 Nonlocal magnon spin transport	150
C.3 Anisotropic charge transport in a Hall bar geometry	153
References	156
Summary	157
Samenvatting	161
Acknowledgements	165

Contents

Publications	172
Curriculum Vitae	175

1.1 Spintronics

The utilization of electrons has led to giant leaps forward in the history of human technology. The Second Industrial Revolution, taking place around the end of the 19th century, is marked by the wide usage of electricity, giving birth to electric lights, electric telegraphs and phones, radios, electric railroads, etc. A few decades later came the Third Industrial Revolution, or the Digital Revolution, where the technology was transformed from analog electronic and mechanical devices to digital ones, thanks to the invention of semiconductor-based transistors. Digital devices like computers and smart phones were introduced to the society, and changed our way of life profoundly.

It is worth noting that these two technological revolutions involve mostly the exploration of only one side of electron's property—charge. Additionally, an electron also possesses a *spin angular momentum*, which is a pure quantum concept but can be classically imagined as the electron spinning around its own axis. This gives rise to an intrinsic magnetic moment of an electron. The alignment of electron spins is the underlying reason for various kinds of magnetism in solid state materials.

An interesting question is whether the electron spin can be also utilized to transport and store spin information, in combination with the electron charge, or even on its own. This question is answered by a burgeoning field of research—spintronics [1–3]. The generation, manipulation and detection of spin currents, the flow of the spin angular momentum, are of central focus in this field.

One of the most important breakthroughs in this field is the discovery of the giant magnetoresistance effect (GMR) by two independent research groups of Albert Fert and Peter Grünberg [4, 5], to which the Nobel Prize in Physics 2007 was awarded. In 1988, they found that a stack of alternating thin layers of iron (Fe) and chromium (Cr) experienced a large change of its resistance, when the relative magnetization configuration of the Fe layers was altered by the external magnetic field. Especially, the effect can be well described by a drift-diffusion model with the “two-current” conduction concept [6, 7], establishing the basis for spintronics.

The discovery of GMR is also a prime example of the rich and novel physics

phenomena at the nanoscale. Not only has it stimulated further research into nanotechnology, it also has had a significant practical impact on downscaling electronic devices, such as memory elements in hard disk drives. Later, a variation of GMR was discovered in magnetic tunnel junctions (MTJs), where the non-magnetic Cr layer was replaced by a thin insulating tunnel barrier. It exhibited an even larger magnetoresistance effect and was named as the tunneling magnetoresistance (TMR) [8, 9]. It is the central physical mechanism behind a novel non-volatile memory technology—magnetoresistive random-access memory.

After years of development, spintronics has grown into a large field and branched into many subfields, covering materials from traditional ones like metals, semiconductors [10] to novel two-dimensional systems such as graphene [11, 12]. Particularly, magnetic insulators were recently introduced to this field [13, 14]. Moreover, heat was lately added into the picture as a new ingredient and the coupling between heat and spin was studied in different material systems [15–22]. These two subfields are among the new frontiers of spintronics and is also where this thesis is focused. In the next two sections, we will give brief introductions to these two topics.

1.2 Magnon spintronics

Magnons are quanta of spin waves, which are collective excitations of the orderly aligned electron spins in magnetic materials. Early in 1930s, the concept of magnons was introduced by Felix Bloch to explain the decrease of spontaneous magnetization as the temperature increases [23, 24].

Since then, magnons have been intensively researched towards both fundamental and applicational directions for many decades, but the utilization of magnons as spin information carriers and, especially the combination of magnons with spintronics, is relatively new [25, 26]. This emerging field can be named as “magnon spintronics” [14], and is so far largely centered on magnetic insulators, such as the prototypical material yttrium iron garnet (YIG). In terms of magnon transport, two unique features can be expected in this material: First, YIG has a very low damping factor, which allows the magnon spin to propagate relatively far before it disappears. Second, the absence of conduction electrons assures that the magnon transport process is free from Joule heating produced by the moving and scattering electrons. This concept offers original methods for spin information transmission, and was successfully realized for magnons with frequencies of GHz [13] and THz [27], respectively.

Other important physical processes in this field include spin pumping [28], where coherent magnons generated from ferromagnetic resonance in the magnetic layer enter the adjacent nonmagnetic layer as spin currents and can even convert into a charge current [29]. Reciprocally, spin currents from the nonmagnetic layer can excite

magnons in the magnetic layer, as a result of the spin transfer torque [30, 31]. These two effects bridge magnon systems with conduction electrons systems, and are hence very important in the field of magnon spintronics.

1.3 Spin caloritronics

The well-established field “thermoelectrics” [32] focuses on the interaction between charge and heat transport. Two main effects in this field, the Seebeck effect and Peltier effect, both discovered more than a hundred years ago, describe the phenomena that an electric current can be induced by a heat current in conductive systems, and vice versa. These two effects are now widely used in temperature sensors, thermoelectric generators, Peltier coolers, etc.

Recently, in the growing subfield of spintronics, known as “spin caloritronics” [15, 16], the spin degree of freedom is brought to the playground and get coupled to charge and heat transport. This innovative idea soon triggered many new effects being discovered. For instance, it was found that in ferromagnetic metals [18] and semiconductors [19], temperature gradients can excite spin currents and therefore function as novel spin current sources.

Even more intriguing is the discovery of such an effect in magnetic insulators [17], named as the spin Seebeck effect, where no conduction electrons are present in the system. This effect shows that heat currents can directly interact with magnons, which unlike electrons, are bosonic in nature. The spin Seebeck effect not only advances new insights into the thermal magnon excitation mechanism, but also provides a new way to produce electricity from thermal energy [33].

A large part of this thesis falls into the intersection between the magnon spin caloritronics and magnon spintronics, where the propagation of thermally excited magnons is investigated.

1.4 Motivation and outline

The work presented in this thesis aims at demonstrating as well as a better understanding of the interaction between charge, spin and heat currents at micro- or nanoscale from the experimental point of view, particularly in magnetic tunnel junctions and magnetic insulator–heavy metal systems. In most of the work, a numerical model is also developed that incorporates the discussed physical picture. The experimental and modeling results are directly compared, from which we can extract certain parameter values that we are interested.

This thesis is structured as follows:

- *Chapter 2* introduces the main physical concepts in the fields of metallic spintronics, magnon spintronics and spin caloritronics, which are relevant to the work presented in the following chapters.

Starting from the diffusive spin transport based on a two-current model in metallic systems, we review important effects such as GMR, TMR and (inverse) spin Hall effect, which are caused by the coupling between charge and spin.

Next, spin transport across an interface between metals and magnetic insulators is treated, showing the interaction between independent conduction electron spins in conductors and collective magnonic spins in magnetic insulators. Effects like spin Hall magnetoresistance are introduced.

Furthermore, originating from the new understandings of recent experiments, the diffusive transport of magnonic spin currents in a magnetic insulator is introduced, where out-of-equilibrium magnons are parameterized by a nonzero magnon chemical potential, and magnons are driven by magnon chemical potential gradients.

Finally, heat transport is added into the picture. We first discuss the well-known thermoelectric effects that result from the interplay between charge and heat currents. Then we proceed further to introduce the novel concepts from the field of spin caloritronics, which come from the interaction of heat with independent conduction electron spins or collective magnonic spins.

- *Chapter 3* presents the first experimental study of the magneto-Peltier effect in MTJs. By fabricating a micro-scale thermocouple on top of an MTJ, we detect a temperature change upon changing the magnetic configuration. We further compare this effect with the reciprocal magneto-Seebeck effect in the same device, and identify that the asymmetry of the I - V characteristics of the MTJ also contributes to our detected signal. By harmonic analysis we can separate this contribution from the magneto-Peltier effect. These results open up the possibility of a magnetically controllable cooling mechanism in magnetic tunnel junctions.
- *Chapter 4* investigates the nonlocal spin Seebeck effect for YIG films with various thicknesses and different heater spin transparencies. We observe that the nonlocal spin Seebeck signals reverse sign at a certain distance away from the heater. We clearly demonstrate that this distance is directly influenced by both the YIG thickness and heater spin transparency, which further supports the bulk spin Seebeck effect picture.

- *Chapter 5* furthers the discussion in *Chapter 4*. In this work, we identify different regimes for nonlocal spin Seebeck signals, and stress that the magnon relaxation length of a magnetic insulator thin film can be and should only be extracted from the exponential relaxation regime. With this principle we extract the magnon relaxation length for a certain YIG film at various temperatures, from 3.5 to 300 K. We provide a general guideline for obtaining magnon relaxation length from the nonlocal spin Seebeck approach.
- *Chapter 6* extends the experimental study of both the magnon transport and nonlocal spin Seebeck effects in nickel ferrite at room temperature. We extracted the magnon relaxation length of the measured nickel ferrite sample and show the universal nature of magnons as spin information carriers.

Lastly, three appendices that describe the experimental methods used throughout this thesis are included: *Appendix A* introduces device fabrication details and *Appendix B* explains electrical measurement methods. Finally, a discussion of the finite element modeling method is given in *Appendix C*.

References

- [1] C. Chappert, A. Fert, and F. N. Van Dau, "The emergence of spin electronics in data storage," *Nature Materials* **6**, pp. 813–823, Nov. 2007.
- [2] S. A. Wolf, D. D. Awschalom, R. A. Buhrman, J. M. Daughton, S. v. Molnár, M. L. Roukes, A. Y. Chtchelkanova, and D. M. Treger, "Spintronics: A Spin-Based Electronics Vision for the Future," *Science* **294**, pp. 1488–1495, Nov. 2001.
- [3] I. Žutić, J. Fabian, and S. Das Sarma, "Spintronics: Fundamentals and applications," *Reviews of Modern Physics* **76**, pp. 323–410, Apr. 2004.
- [4] M. N. Baibich, J. M. Broto, A. Fert, F. N. Van Dau, F. Petroff, P. Etienne, G. Creuzet, A. Friederich, and J. Chazelas, "Giant Magnetoresistance of (001)Fe/(001)Cr Magnetic Superlattices," *Physical Review Letters* **61**, pp. 2472–2475, Nov. 1988.
- [5] G. Binash, P. Grünberg, F. Saurenbach, and W. Zinn, "Enhanced magnetoresistance in layered magnetic structures with antiferromagnetic interlayer exchange," *Physical Review B* **39**, pp. 4828–4830, Mar. 1989.
- [6] N. F. Mott, "The Electrical Conductivity of Transition Metals," *Proceedings of the Royal Society of London A: Mathematical, Physical and Engineering Sciences* **153**, pp. 699–717, Feb. 1936.
- [7] A. Fert and I. A. Campbell, "Two-Current Conduction in Nickel," *Physical Review Letters* **21**, pp. 1190–1192, Oct. 1968.
- [8] S. S. P. Parkin, C. Kaiser, A. Panchula, P. M. Rice, B. Hughes, M. Samant, and S.-H. Yang, "Giant tunnelling magnetoresistance at room temperature with MgO (100) tunnel barriers," *Nature Materials* **3**, pp. 862–867, Dec. 2004.
- [9] S. Yuasa, T. Nagahama, A. Fukushima, Y. Suzuki, and K. Ando, "Giant room-temperature magnetoresistance in single-crystal Fe/MgO/Fe magnetic tunnel junctions," *Nature Materials* **3**, pp. 868–871, Dec. 2004.
- [10] J. Fabian, A. Matos-Abiague, C. Ertler, P. Stano, and I. Zutic, "Semiconductor Spintronics," *Acta Physica Slovaca* **57**, p. 565, Jan. 2007.
- [11] N. Tombros, C. Jozsa, M. Popinciuc, H. T. Jonkman, and B. J. van Wees, "Electronic spin transport and spin precession in single graphene layers at room temperature," *Nature* **448**, pp. 571–574, Aug. 2007.
- [12] W. Han, R. K. Kawakami, M. Gmitra, and J. Fabian, "Graphene spintronics," *Nature Nanotechnology* **9**, pp. 794–807, Oct. 2014.
- [13] Y. Kajiwara, K. Harii, S. Takahashi, J. Ohe, K. Uchida, M. Mizuguchi, H. Umezawa, H. Kawai, K. Ando, K. Takanashi, S. Maekawa, and E. Saitoh, "Transmission of electrical signals by spin-wave interconversion in a magnetic insulator," *Nature* **464**, pp. 262–266, Mar. 2010.
- [14] A. V. Chumak, V. I. Vasyuchka, A. A. Serga, and B. Hillebrands, "Magnon spintronics," *Nature Physics* **11**, pp. 453–461, June 2015.
- [15] G. E. W. Bauer, A. H. MacDonald, and S. Maekawa, "'Spin Caloritronics'," *Solid State Communications* **150**, pp. 459–460, Mar. 2010.
- [16] G. E. W. Bauer, E. Saitoh, and B. J. van Wees, "Spin caloritronics," *Nature Materials* **11**, pp. 391–399, May 2012.
- [17] K.-i. Uchida, H. Adachi, T. Ota, H. Nakayama, S. Maekawa, and E. Saitoh, "Observation of longitudinal spin-Seebeck effect in magnetic insulators," *Applied Physics Letters* **97**, p. 172505, Oct. 2010.
- [18] A. Slachter, F. L. Bakker, J.-P. Adam, and B. J. van Wees, "Thermally driven spin injection from a ferromagnet into a non-magnetic metal," *Nature Physics* **6**, pp. 879–882, Nov. 2010.

- [19] C. M. Jaworski, J. Yang, S. Mack, D. D. Awschalom, J. P. Heremans, and R. C. Myers, "Observation of the spin-Seebeck effect in a ferromagnetic semiconductor," *Nature Materials* **9**, pp. 898–903, Nov. 2010.
- [20] M. Walter, J. Walowski, V. Zbarsky, M. Münzenberg, M. Schäfers, D. Ebke, G. Reiss, A. Thomas, P. Peretzki, M. Seibt, J. S. Moodera, M. Czerner, M. Bachmann, and C. Heiliger, "Seebeck effect in magnetic tunnel junctions," *Nature Materials* **10**, pp. 742–746, Oct. 2011.
- [21] J. Flipse, F. L. Bakker, A. Slachter, F. K. Dejene, and B. J. v. Wees, "Direct observation of the spin-dependent Peltier effect," *Nature Nanotechnology* **7**, pp. 166–168, Mar. 2012.
- [22] J. Flipse, F. K. Dejene, D. Wagenaar, G. E. W. Bauer, J. B. Youssef, and B. J. van Wees, "Observation of the Spin Peltier Effect for Magnetic Insulators," *Physical Review Letters* **113**, p. 027601, July 2014.
- [23] F. Bloch, "Zur Theorie des Ferromagnetismus," *Zeitschrift für Physik* **61**, pp. 206–219, Mar. 1930.
- [24] C. Kittel, *Introduction to Solid State Physics*, Wiley, Hoboken, NJ, 8th ed., Nov. 2004.
- [25] A. A. Serga, A. V. Chumak, and B. Hillebrands, "YIG magnonics," *Journal of Physics D: Applied Physics* **43**(26), p. 264002, 2010.
- [26] V. V. Kruglyak, S. O. Demokritov, and D. Grundler, "Magnonics," *Journal of Physics D: Applied Physics* **43**(26), p. 260301, 2010.
- [27] L. J. Cornelissen, J. Liu, R. A. Duine, J. B. Youssef, and B. J. van Wees, "Long-distance transport of magnon spin information in a magnetic insulator at room temperature," *Nature Physics* **11**, pp. 1022–1026, Dec. 2015.
- [28] Y. Tserkovnyak, A. Brataas, and G. E. W. Bauer, "Enhanced Gilbert Damping in Thin Ferromagnetic Films," *Physical Review Letters* **88**, p. 117601, Feb. 2002.
- [29] E. Saitoh, M. Ueda, H. Miyajima, and G. Tatara, "Conversion of spin current into charge current at room temperature: Inverse spin-Hall effect," *Applied Physics Letters* **88**, p. 182509, May 2006.
- [30] J. C. Slonczewski, "Current-driven excitation of magnetic multilayers," *Journal of Magnetism and Magnetic Materials* **159**, pp. L1–L7, June 1996.
- [31] L. Berger, "Emission of spin waves by a magnetic multilayer traversed by a current," *Physical Review B* **54**, pp. 9353–9358, Oct. 1996.
- [32] D. MacDonald, *Thermoelectricity: An Introduction to the Principles*, Dover Publications, Inc., Mineola, New York, 2006.
- [33] A. Kirihara, K.-i. Uchida, Y. Kajiwara, M. Ishida, Y. Nakamura, T. Manako, E. Saitoh, and S. Yorozu, "Spin-current-driven thermoelectric coating," *Nature Materials* **11**, pp. 686–689, Aug. 2012.

Abstract

In this chapter, we present a systematic overview of the basic concepts that are relevant for the work included in this thesis. First of all, we discuss the charge and spin transport in metallic systems, introducing the two-current model, which is central to understand the physics behind spin valves. Then we proceed to explain the interaction and communication between metallic and insulating systems at their interfaces, in respect of spin currents. Subsequently, the concept of magnons and the spin transport in magnetic insulators are introduced. Finally, we review the heat transport, thermoelectric effects and several novel spin caloritronic phenomena in both metallic and insulating systems.

2.1 Charge and spin transport in metals

Electrons intrinsically have an electric charge and an angular momentum, or spin. While the transport of electric charge has been widely exploited over the past centuries and gives rise to numerous applications that has reshaped our way of life, the study of the transport of electron spin, i.e., the field of spintronics [1, 2], is relatively new.

In 1988, the discovery of the giant magnetoresistance (GMR) effect initiated the manipulation of charge transport from the spin degree of freedom, igniting the research into spintronics. It turned out that the charge and spin transport are deeply intertwined, and many novel effects have been discovered based on this fact in the field of spintronics, in different material systems. In the section, we review the basics of charge and spin transport, as well as their interconnections, in metallic systems.

2.1.1 Electrical transport

Electric current is essentially the directional movement of electrons between atoms. In a metallic material, the electrons in outer shells are delocalized and can move easily through the entire sample. They are regarded as nearly free electrons moving in a periodic potential that has the same period as the crystal lattice [3].

If there is no external electric field (\vec{E}) or temperature gradient ($\vec{\nabla}T$) present, a system is in a thermal equilibrium state and electrons obey the standard Fermi-Dirac distribution. In this situation, the random movements of electrons cancel out, resulting in no macroscopic electric currents. When an \vec{E} is applied to the system, the system is brought out of equilibrium with all electrons gaining certain momentum. Free electrons can thus move directionally through the material, with the electric current described by the Ohm's law:

$$\vec{J}_c = \sigma \vec{E} = -\sigma \vec{\nabla}V = -\frac{\sigma}{e} \vec{\nabla}\mu, \quad (2.1)$$

where \vec{J}_c is the electric current density, σ the electrical conductivity, V the electric voltage, e the electron charge, and μ is the electrochemical potential.

In diffusive systems, the velocities of conduction electrons will not increase to infinity by the applied electric field, as electrons will encounter different scattering processes while they travel and consequently lose (part of) their momentum. These scattering processes include both elastic and inelastic collisions, such as interaction with lattice imperfections and impurities, electron-phonon and electron-electron interactions [3]. These collisions balance the accelerating force of the electric field, and a steady state can be reached for the conduction process.

One can thus define a time scale τ_e as the electron relaxation time, which can be thought as the average time interval between scattering events. The electrical conductivity σ is thus directly proportional to this relaxation time τ_e . Their relation is described by the Drude expression

$$\sigma = \frac{ne^2\tau_e}{m^*}, \quad (2.2)$$

where n and m^* is the density and effective mass of conduction electrons, respectively. In an isotropic system, τ_e is also the characteristic time for the electron system to relax to the equilibrium state after the removal of the applied electric field.

Since only the electrons that are close to the Fermi energy contribute to the electrical conductance, the average travel distance of electrons between scattering events, or the electron mean free path, can be expressed by $l_e = \tau_e v_F$ with v_F being the Fermi velocity. The system is said to be diffusive when l_e is much smaller than the system size, which is usually the case for metals at elevated temperatures. Throughout the works presented in this thesis, the electrical transport in metals is always in the diffusive regime.

The continuity equation for electric currents under an electrostatic field is

$$\vec{\nabla} \cdot \vec{J}_c = -\frac{\partial \rho}{\partial t} = 0, \quad (2.3)$$

which directly comes from the conservation law of electric charge.

2.1.2 Spin transport

In the absence of a magnetic field, ferromagnetic metals (FM) such as Fe, Co and Ni show spontaneous ferromagnetism below Curie temperature. These metals fulfill the Stoner criterion [4]: Due to strong Coulomb repulsions between itinerant electrons, it is energetically more favorable for the spin-up (\uparrow) and spin-down (\downarrow) 3d bands to shift in energy (see Fig. 2.1), as the gain in exchange energy is larger than the loss in kinetic energy. As a result, there are unequal numbers of spin-up and spin-down electrons per atom, and ferromagnetism occurs.

From the spin transport point of view, the most distinct feature of FM is the *spin-dependent conductivity*, that is, the electrical conductivity of spin-up electrons (σ_{\uparrow}) is not equal to that of spin-down electrons (σ_{\downarrow}), while for non-magnetic metals (NM) $\sigma_{\uparrow} = \sigma_{\downarrow}$. Two reasons can account for this fact [5]: First, the density of states (DOS) of spin-up and spin-down electrons are different around the Fermi level, due to the exchange splitting. As σ is directly related to the density of electrons n around the Fermi level, this leads to $\sigma_{\uparrow} \neq \sigma_{\downarrow}$. But this is generally a small effect, as the splitting occurs in the 3d band, while the electric current is primarily mediated by the 4s electrons due to their smaller effective electron mass. However, in tunneling effects the DOS asymmetry plays a significant role, such as in magnetic tunnel junctions. Second, which is a more dominant reason in fully metallic systems, is that the 4s spin-up and spin-down electrons will be scattered very differently with the 3d spin-up and spin-down electrons respectively, so their τ_e are different (see Eq. 2.1). These two mechanisms compete with each other [6] and both contribute to the spin-dependent conductivity.

Two-current model

A *two-current model* was proposed by Mott in the 1930s [7] and later applied by Fert and Campbell to describe conductivity behaviors of magnetic materials [8, 9]. In this model, the charge current \vec{J}_c is considered to be conveyed separately by spin-up and spin-down channels, driven by the gradients of their own quasi-electrochemical potentials:

$$\vec{J}_{\uparrow(\downarrow)} = -\frac{\sigma_{\uparrow(\downarrow)}}{e} \vec{\nabla} \mu_{\uparrow(\downarrow)}. \quad (2.4)$$

The total electric current density is $\vec{J}_c = \vec{J}_{\uparrow} + \vec{J}_{\downarrow}$, while the spin current (density) is defined as $\vec{J}_s = \vec{J}_{\uparrow} - \vec{J}_{\downarrow}$. Furthermore, the spin conductivity polarization P is introduced as $P = (\sigma_{\uparrow} - \sigma_{\downarrow})/\sigma$, where $\sigma = \sigma_{\uparrow} + \sigma_{\downarrow}$. One can then obtain $\sigma_{\uparrow(\downarrow)} = \sigma(1 \pm P)/2$.

In equilibrium situations, for both FM and NM the relation $\mu = \mu_{\uparrow} = \mu_{\downarrow}$ holds. Thus for an NM, $P = 0$ and $J_s = 0$, meaning that the charge current is evenly distributed to both the spin-up and spin-down channels. In contrast, an FM has a

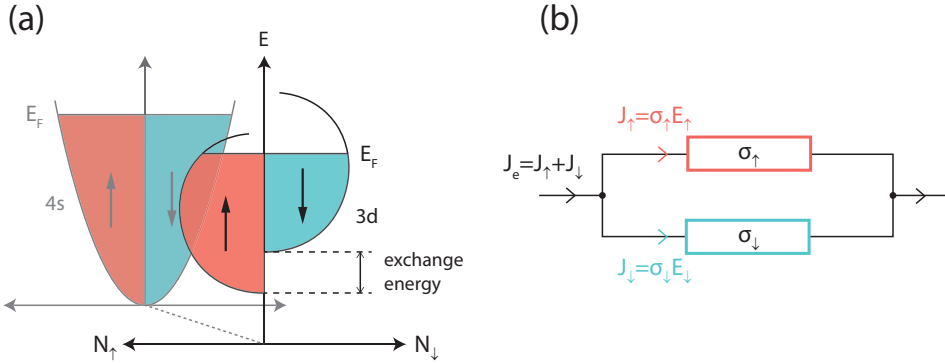


Figure 2.1: Schematic representations of (a) the spin-split bands in transition metal ferromagnets such as Fe, Co and Ni, where the 3d band is shifted by an exchange energy; (b) two-current model, where the electric current is distributed into spin-up and spin-down channels with different conductivities. $E_{\uparrow(\downarrow)} = -\nabla\mu_{\uparrow(\downarrow)}/e$ is the electric field of each channel.

nonzero P ($|P| \leq 1$). The charge current is said to be spin polarized with the higher-conductivity channel carrying more charge current, thus always accompanied by a spin current $J_s = PJ_c$.

Spin accumulation

Now let us turn to discuss the more interesting non-equilibrium situations, as spin transport phenomena essentially occur during the process when a system relaxes from a non-equilibrium to an equilibrium state. For spin transport, the non-equilibrium is marked by a nonzero *spin accumulation* ($\mu_s = \mu_{\uparrow} - \mu_{\downarrow}$)¹, which can be interpreted as a non-equilibrium magnetization [11], and can exist in both magnetic and non-magnetic materials.

In analogy to the excited electron system which relaxes to equilibrium by different electron scattering events, the spin system relaxes to equilibrium ($\mu_s = 0$) by various spin-flip scattering processes, mostly via spin-orbit interactions [2, 10, 12–14]. Similarly, we can define a time scale τ_s as the average time between two spin-flip scattering events. In diffusive systems, τ_s is often much longer than τ_e , indicating that an electron can experience several scattering events that change its momentum without flipping its spin direction [1, 15]. In fact, this is one of the prerequisites to be able to apply the two-current model in a system [6, 16, 17]: The condition $\tau_s \gg \tau_e$ guarantees that each spin channel first enters a quasi-equilibrium state that is characterized by its own quasi-electrochemical potential $\mu_{\uparrow(\downarrow)}$, and then the spin

¹Note that in some literature such as Ref. [10], μ_s is alternatively defined as $(\mu_{\uparrow} - \mu_{\downarrow})/2$.

system relaxes to equilibrium with μ_s gradually decaying to 0. We will see later in Sec. 2.3.2 that a diffusive magnon system shares certain analogies with a conduction electron system, in that a non-equilibrium magnetism can be also described by a quasi-magnon chemical potential, though a two-current model is not applicable for a magnon system. This is ensured by the much faster equilibration process of spin carriers than the disappearance of the spin imbalance, regardless the system being Fermionic or Bosonic.

Assuming the relaxation of μ_s is proportional to how much μ_s itself deviates from equilibrium, in a steady state the loss of the diffusive spin current at a certain location is equal to the relaxation:

$$\nabla \cdot J_s^{\text{diff}} = -D_s \nabla \cdot \nabla \mu_s = -\frac{\mu_s}{\tau_s}, \quad (2.5)$$

where D_s is the spin diffusive coefficient. One can define a length scale $\lambda_s = \sqrt{D_s \tau_s}$ as the *spin diffusion length* or *spin relaxation length*, which characterizes the typical distance over which a non-equilibrium spin accumulation loses its polarization in a particular material. Equation 2.5 can be then written as

$$\nabla^2 \mu_s = \frac{\mu_s}{\lambda_s^2}, \quad (2.6)$$

known as the Valet-Fert equation [16].

Spin injection from a FM to a NM material

There are various methods to create a spin accumulation in a material system, and here we discuss one of the most straightforward methods to realize it: By contacting an FM to an NM and driving a charge current through the junction, the spin polarized current is injected to the NM layer and this gives rise to a non-equilibrium in the vicinity of the FM/NM interface. At both sides of the interface, a nonzero μ_s arises and decreases exponentially on the scale of λ_s of each material, as shown in Fig 2.2. The buildup of μ_s at the interface is a consequence of the abrupt change of the spin conductivity polarization P from FM to NM. It prompts spin flips and helps adjust both J_\uparrow and J_\downarrow to the new ratio dictated by the P of the second material (here for an NM $P = 0$, so that $J_\uparrow/J_\downarrow = 1$). As a result, on the length scale of λ_{NM} near the interface, the NM is “magnetized” with a polarized J_s and a nonzero μ_s .

In the presence of a nonzero μ_s , the average chemical potential of the system can be calculated as

$$\mu = \frac{1}{\sigma} (\sigma_\uparrow \mu_\uparrow + \sigma_\downarrow \mu_\downarrow). \quad (2.7)$$

This is actually a measurable parameter from electrical experiments. While both μ_\uparrow and μ_\downarrow are continuous at the FM/NM interface, there is a jump of μ with the

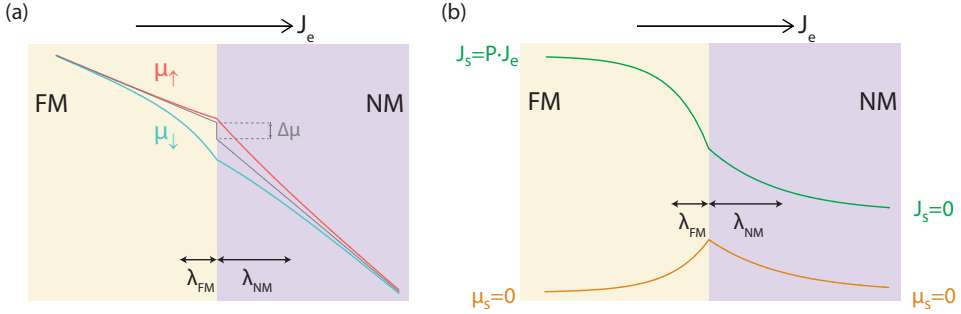


Figure 2.2: Illustration of relevant parameters near an FM/NM interface when an electric current flows from the FM to the NM. (a) Spatial variations of spin-dependent chemical potentials $\mu_{\uparrow(\downarrow)}$ and the average chemical potential μ . The splitting of μ_{\uparrow} and μ_{\downarrow} takes place in both FM and NM and the characteristic length it extends depends on the spin relaxation length of each material, λ_{FM} and λ_{NM} . The grey curve represents μ , with a discontinuity of $\Delta\mu$ at the interface. (b) Spatial variations of spin current J_s and spin accumulation μ_s , plotted by the green and orange curves, respectively. All results are calculated numerically with a finite element model using Eqs. 2.4 and 2.6, in the same way as described in Ref. [18].

amplitude of $\Delta\mu$ [19], as shown in Fig. 2.2. Although reversing the magnetization of the FM layer will not modulate $\Delta\mu$ in this bilayer system, we will see next that by introducing a second FM layer it is possible to achieve the modulation of the measurable electrical voltage, which is of great significance to both research and industrial applications.

Spin valves

An FM/NM/FM structure constitutes a *spin valve*: By aligning the relative magnetic orientation of the two FM layers in a parallel (P) or antiparallel (AP) configuration, one “opens” or “closes” the electron flow, corresponding to a low and a high electrical resistance of the stack, respectively.

The simplest method to control the magnetic arrangements of the two FM layers is by applying an external magnetic field. When one of the FM layers is pinned along one direction, or when the two FM layers have different coercive fields along the applied magnetic field direction, the stack will undergo the P and AP states at different magnetic field strengths and correspondingly change its resistance. This effect is referred to as the *giant magnetoresistance effect* (GMR) [20, 21], as the stack resistance is greatly dependent on the magnetization. In the initial discovery [20], the magnetoresistance ratio $\Delta R/R = (R_{AP} - R_P)/R_P$ reached already as high as 80% for Fe/Cr superlattices. The GMR effect has been applied in magnetic field sensors,

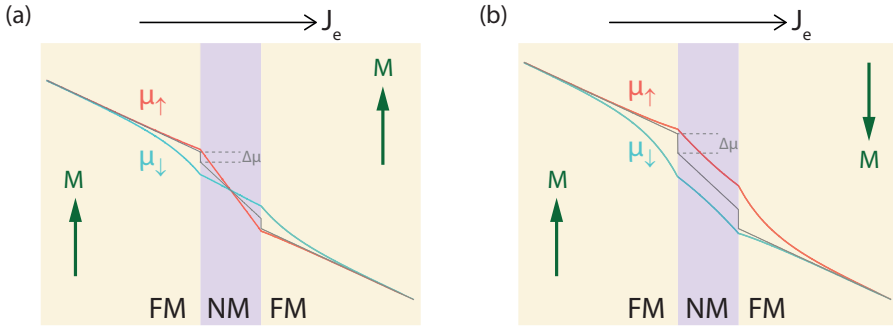


Figure 2.3: “Current perpendicular to plane” GMR structure that comprises a thin NM layer sandwiched between two FM layers. In this figure we plot the calculated spin chemical potential profiles when an electric current flows through the interfaces, for (a) parallel (P) and (b) antiparallel (AP) magnetization configurations of the two FM layers. The color indications are the same as Fig. 2.2(a). Compared to the P state, the discontinuities of the average chemical potential μ ($\Delta\mu$) are larger in the AP state. This results in a larger electrical resistance of the AP than the P state, which can be directly measured electrically.

hard disk drives and non-volatile memory devices, although it was later replaced by the even larger tunneling magnetoresistance (TMR) effect [22–26]. In 2007, Fert and Grünberg received the Nobel prize in physics for the discovery of the GMR effect.

The GMR effect can be understood in a simple way using the concepts of spin accumulation and spin injection [16], as we introduced previously. Figure 2.3 illustrates the calculated spatial distribution of μ_{\uparrow} , μ_{\downarrow} and μ for P and AP configurations. Just as shown in Fig. 2.2, when the electric current flows through the first FM/NM interface, a spin accumulation μ_s arises, accompanied by a jump of the average chemical potential $\Delta\mu$. Depending on the magnetic orientation of the second FM, μ_s at both interfaces have either different or the same sign, which affects the amplitudes of μ_s , as well as $\Delta\mu$. This leads to the different stack resistances between the two magnetic states.

Alternatively, the magnetic configurations of a spin valve can also be controlled by a large flow of spin angular momentum instead of external magnetic fields [27–30]. This type of current-induced magnetization dynamics [31] switches the magnetic orientation of one FM layer of the spin valve and is closely related to the spin transfer torque (STT) [32–35] effect that will be discussed in Sec. 2.2.1. The current-induced STT switching technique offers a better option than an Oersted-field-based control in manipulating magnetic devices, especially on nanoscale. This technique has been widely applied in hard-disk drives and MRAM (magnetoresistive random-access memory) technology [31].

Spin valves can also be realized into a lateral geometry that spatially separates the spin injection and detection circuits, known as the *nonlocal spin valves* [36–38]. The advantage of a nonlocal spin valve over a local one is that the detection circuit is not influenced by any charge currents that flow through the injection circuit, but is only sensitive to *pure spin currents* that diffuse from the spin injection site. This results in a much cleaner background for the detection signal and greatly enhances the signal-to-noise ratio. Furthermore, applying an out-of-plane magnetic field can induce the precession of the pure spin currents [37] while they travel through the NM material, leading to a detected spin signal modulated by the external magnetic field. This effect is referred to as the *Hanle effect* [2] and one can accurately obtain the spin-flip time τ_s and spin relaxation length λ_s of the NM material by fitting the experimental data to the Hanle curve. Nowadays, nonlocal spin valves have become standard tools for extracting τ_s and λ_s in novel materials, such as graphene [39].

Magnetic tunnel junctions

Replacing the NM layer of an all-metal spin valve by a thin insulating tunnel barrier can significantly enhance the magnetoresistance ratio of the spin valve. This FM/I/FM structure is termed as *magnetic tunnel junction* (MTJ) and the magnetoresistive effect is called *tunneling magnetoresistance* (TMR) [22–26, 40].

Although the magnetotransport behavior of an MTJ is similar to a GMR device, the underlying physics is quite different. The MTJ is based on the quantum-mechanical tunnel effect of electrons through an insulating barrier. According to a simple model by Jullière [22], the electron spin is assumed to be preserved during tunneling, and the tunnel current of each spin species is proportional to the product of the Fermi level DOS of the two electrodes. Hence when the two metals are ferromagnetic with different DOS at the Fermi level, the total tunnel current of spin-up and spin-down electrons will depend on the relative magnetic configuration of these two FM layers, as shown in Fig. 2.4. Therefore, the GMR effect relies on the conductivity difference while the TMR effect directly depends on the DOS asymmetry of the FM for the two spin channels.

The DOS polarization factor² of an FM can be defined as

$$p = \frac{N_{\uparrow}(E_F) - N_{\downarrow}(E_F)}{N_{\uparrow}(E_F) + N_{\downarrow}(E_F)}, \quad (2.8)$$

where $N_{\uparrow(\downarrow)}(E_F)$ is the effective tunneling DOS of the FM electrode at the Fermi level. Based on Jullière's physical picture, one can work out the TMR ratio to be

$$\frac{\Delta R}{R} = \frac{R_{AP} - R_P}{R_P} = \frac{G_P - G_{AP}}{G_{AP}} = \frac{2p_1 p_2}{1 - p_1 p_2}, \quad (2.9)$$

²To be distinguished from the conductivity polarization P defined earlier in this chapter.

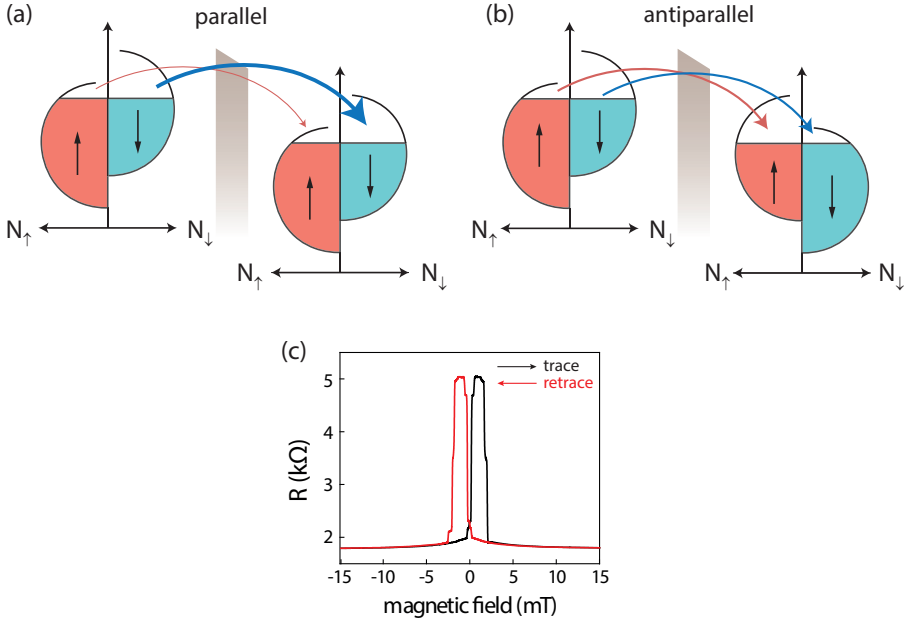


Figure 2.4: (a) (b) Schematic representation of the TMR effect for P and AP configurations, respectively. During the tunneling process, electron spin is conserved, meaning that an electron can only tunnel to the subband with the same spin orientation across the insulating barrier. The tunneling rate is proportional to the product of the DOS values of both sides of the barrier at the Fermi level, for that particular spin orientation. Hence, the total conductance of the MTJ is larger for the P state than the AP state. (c) A typical magnetoresistance curve of an MTJ junction with CoFeB/MgO/CoFeB structure. It shows a magnetoresistance ratio of more than 170% at room temperature. Data from: J. Shan et al., unpublished. Courtesy J. C. Leutenantsmeyer for device fabrication.

where $G_{P(AP)}$ is the conductance of the MTJ for P (AP) alignment, and $p_{1(2)}$ is the DOS polarization of the first (second) electrode.

Jullière's model has provided a basic and clear insight into the physical mechanism of the TMR effect, yet it cannot explain all experimental details, such as the influence of the morphology and material choice of the tunnel barrier. This requires more detailed theoretical considerations [41, 42] which prompted the development of the MTJ. For instance, by using an Al_2O_3 tunnel layer one can achieve a high TMR ratio at room temperature [23, 24]. Later it was theoretically predicted [43, 44] and experimentally demonstrated that with a crystalline MgO tunnel barrier, the TMR ratio was improved up to around 200% at room temperature [25, 26], and even reached 604% with further optimizations based on the structure of CoFeB (cobalt-iron-

boron compound)/MgO/CoFeB [45]. This large TMR effect is a result of the coherent tunneling of the half-metallic (fully spin-polarized), symmetric Δ_1 Bloch states (s , p_z and d_{z^2} hybridized states). More details can be found in Refs. [40, 46].

So far MTJ has been widely applied as read heads in hard disk drive [47] and memory elements in MRAM devices [48].

2.1.3 Spin-charge conversion: spin Hall effect

The *spin Hall effect* (SHE) is another prime example of how charge and spin currents couple to each other [49, 50]. Due to spin-orbit interactions, an electric flow can induce a transverse spin flow in the absence of external magnetic fields. In 1971, Dyakonov and Perel first predicted this effect in non-magnetic systems [51]. In Mott's two-current picture, The spin-asymmetric scattering of conduction electrons will lead to spatial separation of electrons with opposite spins. For a non-magnetic material with an unpolarized charge current, a pure spin current will be induced, known as the SHE (see Fig. 2.5(a)). For a magnetic material with a polarized charge current, the spatial separation of electrons is imbalanced, resulting in a measurable electric Hall voltage that depends on the magnetization of the material, known as the *anomalous Hall effect* (AHE) [52, 53].

Reciprocal to the SHE, a pure spin current can generate a transverse charge current, called the *inverse spin Hall effect* (ISHE) (see Fig. 2.5(b)). Macroscopically SHE and ISHE can be expressed as:

$$\vec{J}_s = \theta_{\text{SH}} \cdot \vec{s} \times \vec{J}_c, \quad (2.10a)$$

$$\text{and} \quad \vec{J}_c = \theta_{\text{SH}} \cdot \vec{s} \times \vec{J}_s, \quad (2.10b)$$

where \vec{s} is a unit vector that denotes the spin polarization direction, and θ_{SH} is the spin Hall angle of a particular material.

The experimental demonstration of the SHE took place more than 30 years after its first prediction. With several theoretical work that furthered the concepts of the SHE [54–57], it was eventually measured with optical detection techniques, by magneto-optical Kerr microscope [58] and circularly polarized electroluminescence detection based on p - n junctions [59] independently in semiconductor systems. Shortly after the optical detection, both SHE and ISHE were extended to metallic systems with electrical methods [60], and later even at room temperature [61, 62].

Both intrinsic and extrinsic mechanisms can contribute to the SHE [50, 52, 63]. The intrinsic mechanism [56, 57, 64–66] depends on the band structure of the perfect crystal. Due to the interband coherence, electrons gain an anomalous velocity that is related to the Berry phase curvature [52]. Extrinsic mechanisms occur during electron scattering processes, and include skew scattering [67] and side-jump [68] mechanisms.

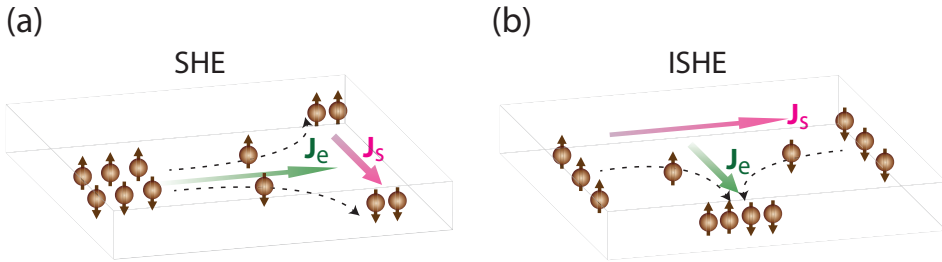


Figure 2.5: Schematic representations of (a) the spin Hall effect (SHE) and (b) the inverse spin Hall effect (ISHE). (a) In the SHE, a longitudinal charge flow induces a transverse spin flow, and creating spin accumulations at the edges of the sample. (b) Reciprocally, in the ISHE, a longitudinal spin flow produces a measurable transverse charge flow.

In platinum (Pt), one of the most popular materials to study SHE and ISHE, also what we employ in the work presented in this thesis, intrinsic mechanisms were argued to be dominant from literature [65, 66, 69–71].

Nowadays, the SHE and ISHE have become standard tools to electrically excite and detect spin currents in non-magnetic materials. For instance, the SHE in Pt or Ta films has been utilized to tune the magnetization dynamics [72, 73] or even switch the magnetization of the adjacent magnetic layer [30, 74]. The ISHE is commonly used to detect pure spin currents generated from, e.g., spin pumping [61] and spin Seebeck effect [75]. Particularly, in a pioneering work performed in our group [76], SHE and ISHE have been employed to electrically inject and detect magnonic spin currents in a magnetic insulator, which will be described in detail in Sec. 2.3.3.

2.2 Spin transport across a metal/ferromagnetic insulator interface

So far we have only discussed collinear situations where spin directions are either parallel or anti-parallel to the magnetization orientation. A non-collinear system [11], however, brings more interesting effects into play, in particular the spin transfer at an interface across two materials. It is therefore possible to communicate to the magnon system in magnetic insulators with the conduction electron spin system from metallic materials.

2.2.1 Spin-mixing conductance

According to the magnetism textbook by Blundell [4], *spin-mixing* means nothing different than spin-flip scattering: It refers to the blurring of the distinction between spin-up and spin-down electron channels by angular momentum transfer processes, such as the collisions of electrons with spin waves. Naturally this process can take place not only in the bulk of a material, but also at the interface between two different materials. The transfer of the spin angular momentum from one to another material results in the randomization of the spin state in the original one.

The term *spin-mixing conductance*, denoted as $G_{\uparrow\downarrow}$, is now widely applied in, for instance, a normal metal/ferromagnet system as an interfacial parameter, describing the amount of the angular momentum transfer per unit area from the spin accumulation in the normal metal to the ferromagnet magnetization, or vice versa [11, 77]. These two processes are at the heart of the well-known spin transfer torque [31–35] and spin pumping effects [78, 79], respectively.

The spin-mixing conductance describes only the non-collinear transfer of angular momentum, as it essentially comes from the non-diagonal terms of the 2×2 conductance matrix in Pauli spin space [77]. When the spin accumulation $\vec{\mu}_s$ in the normal metal is not collinear with the magnetization \vec{M} in the ferromagnet, the transverse part of $\vec{\mu}_s$ respective to \vec{M} is absorbed by the ferromagnetic order parameter and dissipated as a torque $\vec{\tau}$ on \vec{M} , given by [11, 31, 80]

$$\vec{\tau} = -\frac{\hbar}{2e} [2G_r \vec{m} \times (\vec{\mu}_s \times \vec{m}) + 2G_i (\vec{\mu}_s \times \vec{m})], \quad (2.11)$$

where \vec{m} is a unit vector along \vec{M} , and G_r (G_i) is the real (imaginary) part of $G_{\uparrow\downarrow}$ ($G_{\uparrow\downarrow} = G_r + iG_i$).

The first part of the torque related to G_r , is famously known as the “Slonczewski” torque. It is an “in-plane” torque, with the plane spanned by \vec{M} and $\vec{\mu}_s$. This torque destabilizes the \vec{M} in the magnetic layer and can ultimately leads to the reversal of \vec{M} when the torque is large enough [32, 33]. This spin-torque switching is the central physics of the MRAM technology [31]. The second part of the torque that contains G_i is commonly referred to as the “field-like” torque. It is perpendicular to the plane and can be regarded as an effective magnetic field along $\vec{\mu}_s$ that tries to make \vec{M} precess around it. While the $\vec{\mu}_s$ exerts an torque on \vec{M} , reciprocally the \vec{M} also exerts an opposite torque back on $\vec{\mu}_s$, modifying or re-orienting $\vec{\mu}_s$, such as in the spin Hall magnetoresistance picture [80–83] that will be described in Sec. 2.2.4 .

In the definition of Eq. 2.11, both G_r and G_i are in units of S/m^2 as in electrical units. It is also common in literature to express them in units of $1/m^2$ as in energy units (for example, in Ref. [84]), usually denoted as $g_{\uparrow\downarrow}$. It can be converted to $G_{\uparrow\downarrow}$ using the conductance quantum by $G_{\uparrow\downarrow} = \frac{2e^2}{h} g_{\uparrow\downarrow}$ [11, 80, 85]. In this thesis we use $G_{\uparrow\downarrow}$ in units of S/m^2 for the sake of consistency.

2.2.2 Effective Spin-mixing conductance

In the previous section, only the scenario when \vec{M} is non-collinear with $\vec{\mu}_s$ is discussed. It was only very recently unveiled that there is actually also spin transfer when $\vec{\mu}_s$ is collinear with \vec{M} at nonzero temperatures. The reason is closely linked to the Bloch $T^{3/2}$ law [3, 4], which states that at a certain temperature below the Curie temperature T_C , the spontaneous magnetization of a magnetic material is reduced compared with $T=0$ due to the excitation of magnons, with the relation given as

$$\frac{M(0) - M(T)}{M(0)} \propto T^{3/2}, \quad (2.12)$$

where $M(0)$ is the spontaneous magnetization at $T=0$. At $T > 0$, although the total magnetization \vec{M} of the magnetic material is collinear with $\vec{\mu}_s$, the individual spins are not fully aligned along \vec{M} as they are disturbed by magnons, making the spin transfer hence possible. Depending on the relative orientation between $\vec{\mu}_s$ and \vec{M} being parallel or antiparallel, out-of-equilibrium magnons are either created or annihilated as a result of spin transfer, which leads to a change of both the magnon temperature and the magnon chemical potential [85]. This process plays a crucial role in the spin Seebeck effect [75], spin Peltier effect [86] and the demonstration of the exchange magnon spin transport [76]. In the present SMR theory [80], however, this process is not considered due to the sharp contrast of spin transfer efficiency between the situations when $\vec{\mu}_s \parallel \vec{M}$ and $\vec{\mu}_s \perp \vec{M}$.

The spin-mixing conductance to describe the spin transfer when $\vec{\mu}_s$ and \vec{M} are collinear is therefore related to $G_{\uparrow\downarrow}$, but additionally being temperature dependent. It is referred to as the *effective spin-mixing conductance* and is expressed as [85]

$$G_s = \frac{3\zeta(3/2)}{2\pi s \Lambda^3} G_{\uparrow\downarrow}, \quad (2.13)$$

where ζ is the Riemann Zeta function [$\zeta(3/2) \approx 2.612$], s the spin density ($s = S/a^3$, where S is the total spin in a unit cell with volume a^3) and Λ the thermal de Broglie wavelength for magnons, equal to $\sqrt{4\pi J_s/k_B T}$, with J_{stiff} the spin-wave stiffness. The temperature dependence of G_s manifests itself in Λ , which leads to $G_s \propto T^{3/2}$, in the same way as the relation in Eq. 2.12. At lower T , the magnon number density reduces and spins are more orderly aligned, thus the spin transfer efficiency decreases.

2.2.3 Spin resistor model for interfacial spin transfer and backflow factor

When there is spin transfer from a normal metal to a magnetic material, or vice versa, the spin current flowing through the interface can now be expressed by the interfacial

mixing conductance. In most cases, a correction factor η needs to be included to account for spin backflow [79, 80, 84, 86–90]. In this section, we consider the typical YIG/Pt bilayer system for two scenarios where a spin imbalance is generated at either side. We use a simplified circuit model to illustrate what is going on at the interface, where we regard both the Pt and the interface as spin resistors. The interfacial mixing conductance is denoted as G_{int} , which can be G_r , G_i or G_s , depending on the specific process involved.

2

Spin current from YIG to Pt

This process is relevant in the detection of out-of-equilibrium magnons in general [76, 85], such as in the spin pumping effect [61, 91] and the spin Seebeck effect [75, 88, 92].

Consider a magnon imbalance present in YIG, denoted by a nonzero chemical potential μ_{YIG} in electrical units. In the extreme case where Pt is a perfect spin sink ($\lambda_{\text{Pt}} \rightarrow 0$), there is then no spin current backflow and the spin resistance of Pt is zero (see Fig. 2.6(a)). Thus the spin current flow is given by

$$J_s^0 = \frac{\mu_{\text{YIG}}}{e} \frac{1}{R_{\text{int}}} = \frac{\mu_{\text{YIG}}}{e} G_{\text{int}}, \quad (2.14)$$

where R_{int} is defined here as the interfacial resistance in units $\Omega \text{ m}^2$.

When the Pt is not a perfect spin sink which is often the reality (see Fig. 2.6(b)), the spin current is lower compared with J_s^0 owing to the finite Pt spin resistance. Now the spin current is given by

$$J_s^{\text{net}} = \frac{\mu_{\text{YIG}}}{e} \frac{1}{R_{\text{int}} + R_{\text{Pt}}} = J_s^0 \cdot \frac{R_{\text{int}}}{R_{\text{int}} + R_{\text{Pt}}} = J_s^0 \cdot \eta = \frac{\mu_{\text{YIG}}}{e} G_{\text{int}} \cdot \eta, \quad (2.15)$$

where η is the so-called *backflow factor*. The expression for the Pt spin conductance in this specific boundary condition is [91]

$$G_{\text{Pt}} = \frac{\sigma_{\text{Pt}}}{2\lambda_{\text{Pt}}} \tanh\left(\frac{t_{\text{Pt}}}{\lambda_{\text{Pt}}}\right), \quad (2.16)$$

where σ_{Pt} is the Pt electrical conductivity, and $\tanh(x) = \frac{1-e^{-2x}}{1+e^{-2x}}$. One can then rewrite η as

$$\begin{aligned} \eta &= \frac{R_{\text{int}}}{R_{\text{int}} + R_{\text{Pt}}} = \frac{G_{\text{Pt}}}{G_{\text{int}} + G_{\text{Pt}}} = \left(1 + \frac{G_{\text{int}}}{G_{\text{Pt}}}\right)^{-1} \\ &= \left[1 + 2\lambda_{\text{Pt}}\rho_{\text{Pt}}G_{\text{int}} \coth\left(\frac{t_{\text{Pt}}}{\lambda_{\text{Pt}}}\right)\right]^{-1}, \end{aligned} \quad (2.17)$$

where ρ_{Pt} is the Pt electrical resistivity. We see that η essentially reflects the ratio between the spin conductances of the Pt and the interface. If $G_{\text{Pt}} \gg G_{\text{int}}$, Pt can be

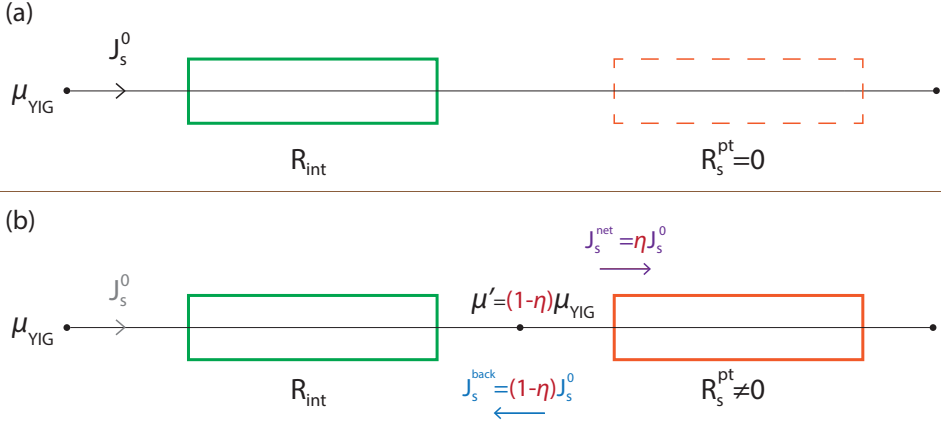


Figure 2.6: Spin resistor model of spin current flowing through the interface towards the Pt side. J_s is the spin current density, R is the spin resistance and μ represents the spin (magnon) accumulation. Two cases are plotted, where in (a) the Pt is an ideal spin sink with no spin resistance, and in (b) is a general situation where Pt has a certain spin resistance, and a backflow factor η needs to be therefore included.

considered as a good spin sink and $\eta \approx 1$. Otherwise, η lies somewhere between 0 and 1, which reduces the spin current across the interface because of the “backflow”. Note that in the latter case, there is a nonzero spin accumulation μ' at the bottom of the Pt layer, equals to $\mu_{\text{YIG}}(1 - \eta)$. The spin backflow can be understood as driven by μ' .

Spin current from Pt to YIG

This process is relevant in the excitation of the magnetic order parameter in general [76, 85], such as in the spin Hall magnetoresistance [80, 81], spin transfer torque [31, 71] and the spin Peltier effect [86].

A spin imbalance can be generated in Pt, most commonly by the SHE. In the extreme case where no spin current can leak out to adjacent materials, i.e., the open-circuit condition where the interfacial conductance is 0, then the spin current is fully reflected at the interface while a spin accumulation μ_{Pt} is induced, as shown in Fig. 2.7(a). The incoming and reflected spin current J_s^0 is

$$J_s^0 = \frac{\mu_{\text{Pt}}}{e} \frac{1}{R_{\text{Pt}}} = \frac{\mu_{\text{Pt}}}{e} G_{\text{Pt}}. \quad (2.18)$$

In the general case when the interface has a certain transparency (see Fig. 2.7(b)), part of the spin current can then flow through the interface, resulting in a smaller backflow spin current J_s^{back} into Pt and a reduced spin accumulation μ'' . The spin

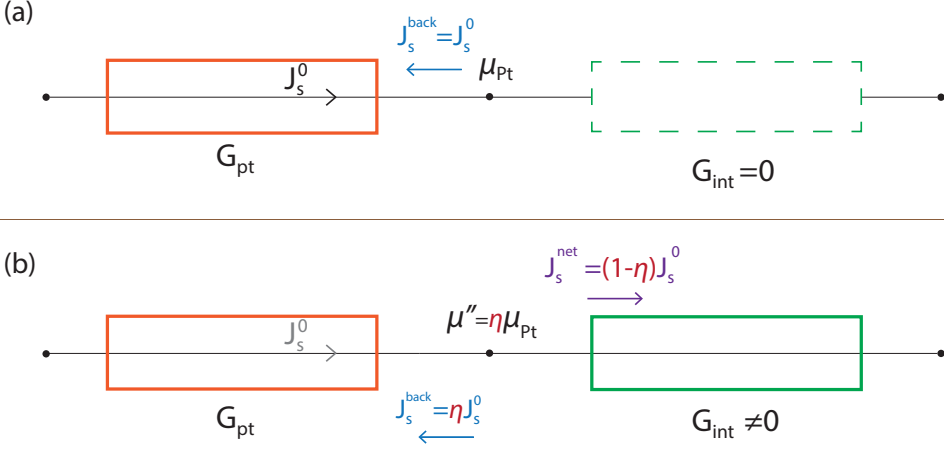


Figure 2.7: Spin resistor model of spin current flowing through the interface towards the YIG side. Two cases are plotted, where (a) is an open-circuit condition with the spin conductance of the interface being zero, and (b) is a general situation where the interface has a certain transparency, and a backflow factor η needs to be therefore included.

current that can flow away from Pt, denoted by J_s^{net} , is now

$$J_s^{\text{net}} = \frac{\mu_{\text{Pt}}}{e} \frac{1}{R_{\text{int}} + R_{\text{Pt}}} = J_s^0 \cdot \frac{R_{\text{Pt}}}{R_{\text{Pt}} + R_{\text{int}}} = J_s^0 \cdot (1 - \eta), \quad (2.19)$$

where η is defined in the same way as Eq. 2.17. The spin accumulation μ'' can be obtained as $\eta \mu_{\text{Pt}}$, which can be thought as a driving force for both J_s^{net} and J_s^{back} .

Although the spin resistances of Pt and the interface are acting in series, we see that η implies the competition of them. If $G_{\text{Pt}} \gg G_{\text{int}}$ and $\eta \approx 1$, the interface can be considered as fully opaque and no spin current can penetrate through the interface, accompanied by a total spin backflow and a maximum spin accumulation. Otherwise, η lies somewhere between 0 and 1, which allows a certain spin current through the interface, and the spin accumulation is reduced accordingly.

J_s^{net} can also be expressed as

$$J_s^{\text{net}} = \frac{\mu_{\text{Pt}}}{e} \frac{1}{R_{\text{int}}} \frac{R_{\text{int}}}{R_{\text{int}} + R_{\text{Pt}}} = \frac{\mu_{\text{Pt}}}{e} G_{\text{int}} \cdot \eta, \quad (2.20)$$

which is actually in the same form as Eq. 2.15 and is more convenient to get the net spin current through the interface [80, 84]. According to Refs. [80, 86], if the spin accumulation is induced by the SHE in Pt, $\mu_{\text{Pt}} = 2e\lambda_{\text{Pt}}\rho_{\text{Pt}}J_c\theta_{\text{SH}}\tanh(t_{\text{Pt}}/2\lambda_{\text{Pt}})$, where J_c is the excited charge current sending through Pt and θ_{SH} is the spin Hall angle.

Sometimes $G_{\text{int}} \cdot \eta$ is referred to as the effective interfacial conductance G_{eff} (different from what we defined in Sec. 2.2.2 as G_s) [79], so that

$$\frac{1}{G_{\text{eff}}} = \frac{1}{G_{\text{int}}} + \frac{1}{G_{\text{Pt}}}. \quad (2.21)$$

Summary

From the spin resistor model, we present a simplified physics picture of the spin transfer across the interface, and the role of the backflow correction factor η . One can see that η contains the relative magnitude between the spin conductivities of Pt and the interface, and therefore it accounts for how much the reality deviates from the simple case where the Pt spin conductance can be disregarded. The simple resistor model is fully consistent with the expression from the results by solving the spin-diffusion equation [80, 91]. This model is not restricted for Pt/YIG systems. For instance, the non-magnetic layer can be also two-dimensional material such as graphene, and the generation (detection) mechanism does not have to be (inverse) spin Hall effect, but can be other mechanisms like spin valve detection.

Note that in reality the spin transport across an interface is often more complicated than described by this model. For instance, the model does not capture possible interfacial “spin memory loss” effects [93–95], which suggest additional spin relaxation at the interface. Besides, the spin conductance of YIG is not taken into account in the discussion above; including it certainly further modifies the real spin current flowing through the interface. A finite element model, such as employed in Chapt. 4, solves the spin-diffusion equation by considering the magnon spin conductivity in YIG.

2.2.4 Spin Hall magnetoresistance

Magnetoresistance (MR) refers to the change of the electrical resistance of a material by an external magnetic field. Some well-known MR effects, such as GMR [20, 21], TMR [22–26] and anisotropic magnetoresistance (AMR) [96], usually involve the transport of conduction electrons in magnetic materials. A recently discovered phenomenon called *spin Hall magnetoresistance* (SMR) [80, 81, 83, 97] showed that it is not necessarily so. A paramagnetic heavy metal, such as Pt, exhibits an MR effect when closely attached to a magnetic insulator, such as YIG. The Pt electrical resistance (R_{Pt}) is tuned by the direction of YIG magnetization \vec{M} , which can be controlled by the external magnetic field. SMR is a typical interfacial effect where the spin currents across the Pt/YIG interface play a crucial role.

When a charge current \vec{J}_c is passed through the Pt layer, spin currents are generated by the SHE, resulting a spin accumulation $\vec{\mu}_{\text{Pt}}$ with its direction normal to \vec{J}_c , as shown in Fig. 2.8. Changing the direction of the YIG magnetization \vec{M} essentially

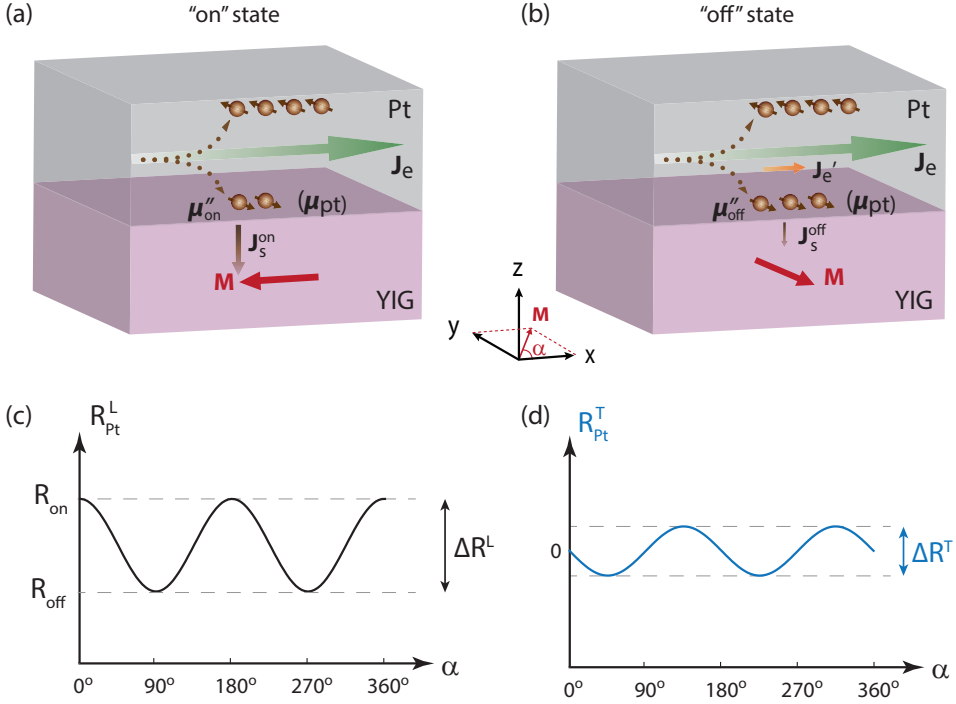


Figure 2.8: Schematic illustrations of the SMR concept. A charge flow \vec{J}_c in the Pt layer induces spin accumulations at boundaries of Pt due to the SHE. At the YIG/Pt interface, a spin accumulation $\vec{\mu}_{Pt}$ is built up. (a) The YIG magnetization \vec{M} is perpendicular to $\vec{\mu}_{Pt}$, corresponding to maximal spin current absorption into YIG and a high Pt electrical resistance. (b) \vec{M} is parallel to $\vec{\mu}_{Pt}$, corresponding to minimal spin current absorption into YIG and a low Pt electrical resistance. (c),(d) Conceptual illustrations of typical in-plane SMR measurement curves obtained with sweeping the angle of the external field, for (c) longitudinal and (d) transverse configurations, respectively. There is a phase shift of 45 degrees between them.

alters the boundary condition for the spin accumulation profile in Pt by tuning the spin transparency of the interface. In other words, \vec{M} behaves like a “spin valve”, and it can be switched relatively “on” and “off” depending on its direction in respect to $\vec{\mu}_{Pt}$:

- ★ When $\vec{M} \perp \vec{\mu}_{Pt}$, as shown in Fig. 2.8(a), this is an “on” state where maximum spin currents can enter the YIG layer and act as an STT on \vec{M} . The amount of the spin currents flowing through the interface is related to G_r .
- ★ When $\vec{M} \parallel \vec{\mu}_{Pt}$, as shown in Fig. 2.8(b), this is an “off” state where minimum

spin currents can flow from Pt to YIG to create or annihilate magnons. The amount of the interfacial spin currents is related to G_s .

Because $G_s < G_r$, the interface in the “off” state is less transparent compared with the “on” state. This results in a larger spin accumulation μ (see Fig. 2.7) in the “off” state, and hence a larger spin current back into Pt. The ISHE now comes to play and converts this spin backflow again into a charge flow. The difference of the converted charge flow between the two situations is denoted as \vec{J}_c' in Fig. 2.8(b). The “off” state thus has a larger charge flow, and thus a higher Pt conductance and a lower R_{Pt} .

In most of the SMR pictures so far, when $\vec{M} \parallel \vec{\mu}_{Pt}$, the Pt/YIG interface is treated as fully opaque without any spin transfer. This approximation should be valid as G_s is usually a small fraction of G_r . Hence, the resistivity difference $\Delta\rho$ between the “on” and “off” state is only expressed with G_r [80]. However, the fact that there is indeed spin transfer when $\vec{M} \parallel \vec{\mu}_{Pt}$ is crucial for the experiment that will be discussed in Sec. 2.3.3, which can be thought of as the “nonlocal” version of the SMR effect.

When \vec{M} lies in between these two extreme states, R_{Pt} falls somewhere in the middle. Sweeping the angle of \vec{M} in respect to \vec{J}_c would yield a sinusoidal curve of R_{Pt} with a period of 180° , as shown in Fig. 2.8(c). When the Pt is made into a Hall bar which enables the transverse measurement, i.e., probing the electric voltage drop (or current flow) perpendicular to \vec{J}_c , one would get the transverse resistance R^T like Fig. 2.8(d). Note that ΔR^T is independent from the Hall bar geometry, but is only related to the SMR ratio and the Pt film thickness ($\Delta R^T = \Delta\rho/t_{Pt}$). In contrast, in the longitudinal configuration ΔR^L depends additionally on the Hall bar geometry, and the ratio between ΔR^L and ΔR^T can be derived simply from geometrical factors [98].

It is worth noting that G_i can be identified in transverse SMR measurements when \vec{M} is tilted out of plane [82, 99]. In this case, the out-of-plane component of \vec{M} causes $\vec{\mu}_{Pt}$ to precess around it and thus rotate in the plane, which can be detected in the transverse configuration. Due to the symmetry in Eq. 2.11, this effect reverses sign upon reversing the magnetic field, and is analogous to the anomalous Hall effect [80, 82, 99]. Experimental SMR results show that G_i is one order of magnitude smaller than G_r [82], consistent with theoretical estimations [100].

2.3 Spin transport in magnetic insulators

Effects such as SMR only look at the interface between a metal and a magnetic insulator. But what happens to the injected spin angular momentum in the bulk of the magnetic insulator? In this section, we discuss this issue on the basis of magnons.

In solid materials and at nonzero temperature, the atomic lattice in real space is disturbed by the thermally excited lattice waves, which can be quantized as *phonons*.

In close analogy, in magnetically ordered materials the electron spin lattice is disrupted by spin waves, quantized as *magnons* [3, 4]. Phonons and magnons are hence quasiparticles that represent the collective excitations of the crystal and spin lattice, respectively.

Due to their wave-like nature which allows them to propagate in a material, both of them are carriers of heat [101], and magnons additionally carry spin angular momentum. This is a very important property, especially in magnetic insulators where the electrons cannot move freely, the spin information can still be delivered by magnons.

2

2.3.1 Magnons

In (anti)ferromagnetic materials, the key to long-range magnetic order is the exchange interaction, described by the Heisenberg Hamiltonian [3, 4]

$$\hat{H} = -J \sum_{\langle ij \rangle} \mathbf{S}_i \cdot \mathbf{S}_j, \quad (2.22)$$

where the sum is over all neighboring spins, \mathbf{S}_i is the electron spin at the i th site and J is the exchange constant which is assumed here to be the same for all pairs. J is closely related to the spin-wave stiffness J_{stiff} that is introduced in Sec. 2.2.2 [102]. At the ground state ($T=0$ K), the spins will align in such a way that the system energy is minimized. For ferromagnets $J > 0$, and from Eq. 2.22 one can see that all spins favor to align in the same direction, while for antiferromagnets and ferrimagnets $J < 0$, where all neighboring spins prefer to align in opposite directions. Here we use only the simple, ferromagnetic case as an example to describe magnons.

At an elevated temperature, the system enters an excited state with magnons created by thermal fluctuations. One magnon is an elementary excitation of the spin lattice, and is equivalent to one spin reversal. However, this spin flip will not locate only at one spin site: the neighboring spins tend to align parallel to it and thus tilt a certain angle from the magnetization direction, and through exchange interactions this tendency to tilt is passed on to other spin sites one by one, leading to this spin reversal distributed evenly over many spin sites, as shown in Fig. 2.9. They all precess around the quantization axis at the same frequency ω , with a phase difference ka between neighboring spin, where $k = |\mathbf{k}|$ is the wave number and a is the lattice constant. The dispersion relation $\omega(\mathbf{k})$ describes the relation between ω and \mathbf{k} , or in other words, between the magnon energy and momentum.

These magnons governed by exchange interactions are commonly referred to as exchange magnons, or sometimes as thermal magnons, since they possess energy around $k_B T$ [103, 104]. There is also another type of magnons that are dominated by the magnetic dipolar interaction which is much weaker than the exchange interaction,

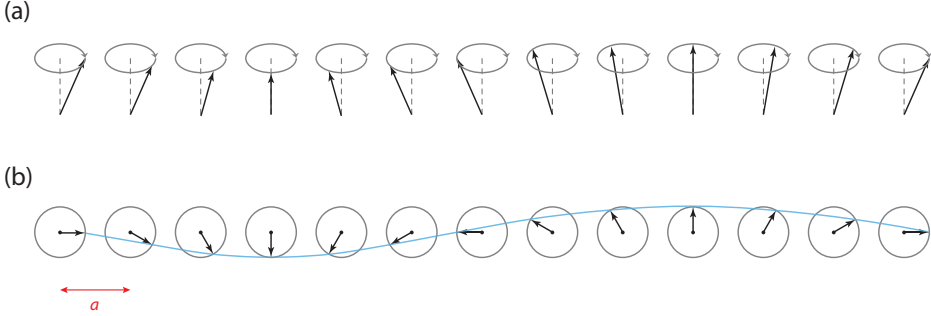


Figure 2.9: Schematic representation of a magnon in a one-dimensional chain across one wavelength, from (a) perspective view and (b) top view. Replotted from Ref. [3].

called dipolar or magnetostatic magnons [105]. Dipolar magnons are mostly excited coherently by inductive microwave technique while exchange magnons can be both coherently [106] and incoherently excited [75, 76, 85, 107]. Another different property between them is that the propagation of dipolar magnons is generally anisotropic due to the inherent anisotropy of the dipolar interaction [105], while for exchange magnons the transport is mostly isotropic, unless there are Dzyaloshinskii-Moriya interaction [108–111] or other asymmetries present [112]. Very recently, the interplay between these two groups of magnons gains plenty of interest [107, 113–115], opening up new possibilities in the field of magnon spintronics. In this thesis we focus only on the incoherent, exchange magnons which are what we encounter in our experiments.

2.3.2 The chemical potential of magnons

Magnons have integer spin and are therefore bosons. At thermal equilibrium, magnons are created and annihilated at the same rate, so that the magnon number density of a system is unchanged over time. They follow the Bose-Einstein distribution with zero chemical potential when the temperature is far below T_C :

$$f(\epsilon) = \frac{1}{\exp(\frac{\epsilon}{k_B T}) - 1}, \quad (2.23)$$

where $\epsilon = \hbar\omega$ is the magnon energy, k_B is the Boltzmann's constant and T is the system temperature, or the lattice temperature. The reason why the magnon chemical potential $\mu_m = 0$ at equilibrium is that the magnon number does not have to follow the conservation law, so that the magnon number can be easily altered to minimize the system free energy [116]. This in general holds for bosonic particles that do not obey the conservation law for the particle number, such as photons in the black body radiation. Equation 2.23 is essentially Planck's law.

When the system is driven out of equilibrium, for instance, when there are extra magnons introduced to the system compared with the equilibrium state, the system will gradually relax back to equilibrium by destroying these out-of-equilibrium magnons over a certain time scale. This process is mainly realized through the inelastic magnon-phonon interaction [85], where the angular momentum is dissipated into the lattice. However, it has been reckoned that another process, which is the magnon thermalization through elastic magnon-magnon scattering, takes place orders of magnitude faster than the magnon relaxation process [85, 116–120]. The magnon thermalization, which preserves the total number of the magnons, distributes energy over all magnons and brings the system into a *quasi-equilibrium* state. Thus in the time window after the magnon thermalization and before the magnon decay, the system can still be described by a Bose-Einstein distribution, with a nonzero chemical potential and an effective magnon temperature T_m :

$$f(\epsilon) = \frac{1}{\exp\left(\frac{\epsilon - \mu_m}{k_B T_m}\right) - 1}. \quad (2.24)$$

During the magnon decay process, T_m gradually goes back to the lattice (phonon) temperature T_{ph} , and μ_m goes back to 0, as they are in thermal equilibrium.

There are again differences in the time and length scales for the decay of T_m and μ_m . From both experimental results [76, 86, 92, 121] and theoretical considerations [85], one can say that the length scale (λ_{m-ph}) governing the relaxation of T_m is orders of magnitude shorter than the one (λ_m) for the relaxation of μ_m , at least for YIG at room temperature. It is therefore reasonable to simplify the picture by assuming $T_m = T_{ph}$ everywhere and consider only the relaxation of μ_m when the system decays back to equilibrium. μ_m is also referred to as the “magnon accumulation”, in close analogy to the spin accumulation $\mu_\uparrow - \mu_\downarrow$, where both of them represent non-equilibrium magnetization, one for magnon systems and another for conductive electron spin systems.

The thermal magnon relaxation rate through the magnon-phonon inelastic scattering is proportional to $\alpha_G k_B T / \hbar$ [85, 122], where α_G is a phenomenological, dimensionless parameter called Gilbert damping coefficient [31, 123].

2.3.3 The transport of exchange magnons

Given the fact that out-of-equilibrium magnons can survive for a certain time and their ability to propagate in the magnetic material, one can hence excite them at a certain position and detect them at a distance away, which enables the nonlocal magnonic spin transport. The transport property of coherent, low-energy magnons [124–126] are substantially different from the one of incoherent, thermal magnons [76, 85]. Here we discuss only the transport of thermal magnons, which is assume to

be diffusive at elevated temperatures [85, 127] due to relatively short magnon mean free paths [103].

With μ_m being the single parameter to characterize how the magnon system deviates from equilibrium, it follows the diffusion equation [16, 128]

$$\nabla^2 \mu_m = \frac{\mu_m}{\lambda_m^2}. \quad (2.25)$$

The diffusive magnon spin current is then

$$\vec{J}_m = -\sigma_m \vec{\nabla} \mu_m, \quad (2.26)$$

where σ_m is the magnon spin conductivity. It is closely related to the spin-wave stiffness J_{stiff} and the magnon relaxation rate, and has been both theoretically estimated and experimentally determined to be around 10^5 - 10^6 S/m [85, 105].

The first experimental demonstration of exchange magnon transport was performed by Cornelissen *et al.* [76], where they employ a nonlocal geometry with two Pt contacts as spin current injector and detector, respectively, and a YIG thin film as the magnon transport channel, as schematically shown in Fig. 2.10. Two parallel Pt strips are grown in close contact with a YIG thin film grown typically on a GGG (gadolinium gallium garnet) substrate. As discussed in Sec. 2.2.2, a spin accumulation in Pt that is generated by the SHE can excite out-of-equilibrium magnons in YIG through interfacial exchange coupling, raising or lowering the local μ_m depending on the spin accumulation direction relative to the YIG magnetization \vec{M} . These injected magnons undergo diffusion process and part of them reach the Pt detector. A nonzero μ_m would pump a spin current into the Pt detector and subsequently converted to a measurable charge current by the ISHE. The energy flow is thus charge current \rightarrow electron spin current \rightarrow magnon spin current and the same way back to charge current, which is a reciprocal process.

Since this effect remains unchanged upon reversing the magnetic field—just like SMR, an angular sweep measurement would give a more straightforward and complete picture than a magnetic field sweep measurement. Figures 2.10(b) and (c) show the experimental configuration with the definition of the angle α and an expected measurement curves with sweeping α , respectively. The effect is usually measured in the nonlocal resistance R^{NL} , defined as the voltage drop across the detector over the current sent through the injector. The effect R^{NL} reaches its maximum when $\vec{M} \parallel \vec{\mu}_{\text{Pt}}$ whereby the out-of-equilibrium magnons that are both injected and detected are maximized. When $\vec{M} \perp \vec{\mu}_{\text{Pt}}$, no magnons are injected or detected, and R^{NL} drops to 0 as shown in Fig. 2.10(c). Due to the similarity in shape to the SMR curve (Fig. 2.8), this effect can be regarded as a nonlocal version of the SMR [129]. While in the SMR picture both the SHE and ISHE occur at the same Pt strip, here they separately take

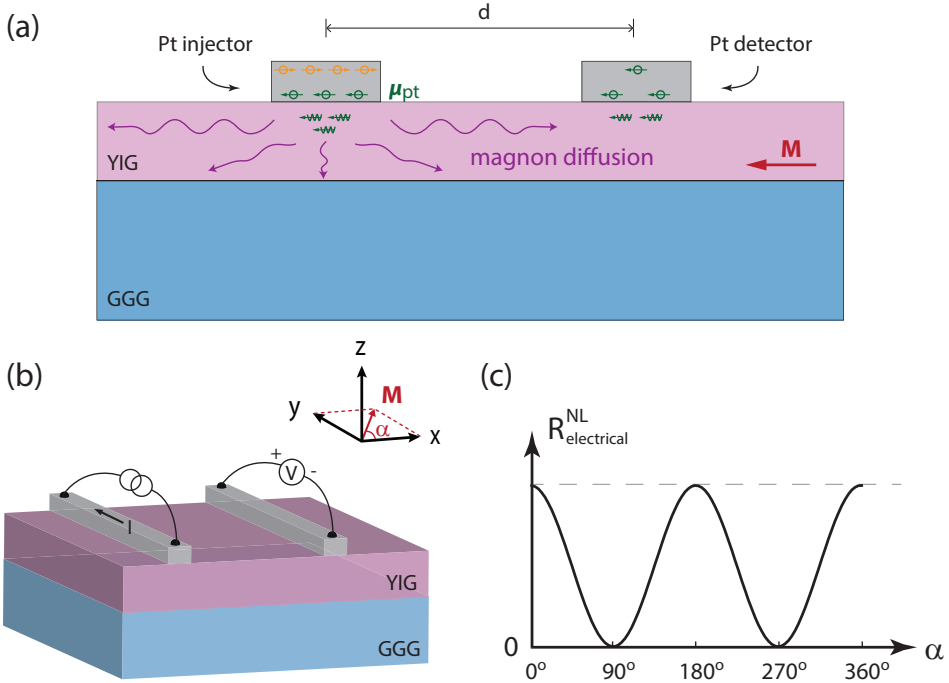


Figure 2.10: (a) Cross-section view of the nonlocal geometry used by Ref. [76] to study the diffusive magnon spin transport. A charge current through the Pt injector can induce an electric voltage at the Pt detector nonlocally, achieved by the magnon transport in YIG. (b) Schematic illustration of the typical measurement configuration for magnon spin transport. (c) Conceptual illustration of a typical measurement curve under angle sweep of the external field.

place in two strips, mediated by the magnon spin transport in the adjacent magnetic material.

Studying how signals decay as a function of d , the spacing between the Pt injector and detector, allows one to determine λ_m . It was reported in Ref. [76] that λ_m in the studied YIG sample was around $10 \mu\text{m}$ at room temperature, in the same order of magnitude as one of the best spin transport materials based on conduction electrons—graphene [39, 130–132]. This observation opens up the possibility for magnons as efficient spin information carriers.

The nonlocal magnon spin transport was later also demonstrated by using a vertical Pt/YIG/Pt sandwich structure [133, 134]. It was further studied at lower temperatures to explore how λ_m and σ_m depend on T [135]. Other follow-up experiments include magnetic field and YIG thickness dependent studies [136, 137], and

even the extension of this effect to other magnetic materials [138, 139].

It is worth mentioning that exchange magnons out of thermal equilibrium can not only be excited by the spin voltage bias adjacent to the magnetic insulator, but can also be generated by temperature gradients, known as the spin Seebeck effect [75, 140, 141]. In fact, the experiment in Ref. [76] also excited magnons thermally parallel to electrical injection, by the Joule heating in the Pt injector. These heat-induced magnons exhibit very similar relaxation length as the electrically injected ones, suggesting that in both methods the same kind of magnons are excited. The excitation and transport of thermally excited magnons will be discussed in detail in Sec. 2.5.1.

2.3.4 Yttrium iron garnet and nickel ferrite

Most ferrimagnets are electrical insulators [4], which serve ideal platforms for studying pure magnonic spin currents in the absence of charge currents. In this section two ferrimagnetic materials that are employed in the our experiments are introduced, one of them being yttrium iron garnet ($\text{Y}_3\text{Fe}_5\text{O}_{12}$, YIG) and the other being nickel ferrite (NiFe_2O_4 , NFO). The detailed material parameters are listed in Table 2.1.

YIG

YIG is a type of ferrimagnetic garnet, which has the general chemical formula as $\text{R}_3\text{Fe}_2(\text{FeO}_4)_3$, where R is a trivalent rare earth atom or Y^{3+} as in YIG. The Y^{3+} ions are on dodecahedral sites, and do not contribute to the magnetism since they have no magnetic moments and are diamagnetic. All Fe cations are trivalent, i.e., Fe^{3+} , with three of them occupying tetrahedral sites and the other two on octahedral sites in one formula unit, as shown in Fig. 2.11. Through superexchange interactions the differently located Fe^{3+} align antiparallel to each other (the exchange constant $J < 0$), resulting in net magnetic moments for one Fe^{3+} , equal to 5 Bohr magneton (μ_B) in a formula unit [3, 4, 142].

Table 2.1: The material properties for YIG and NFO.

	YIG	NFO
Curie Temperature T_C	560 K [4]	858 K [4]
electric bandgap	2.7 eV	1.5 eV
Gilbert damping factor α_G	$2 \cdot 10^{-4}$ [97]	$3.5 \cdot 10^{-3}$ [143]
lattice parameter	12.376 Å	8.33 Å

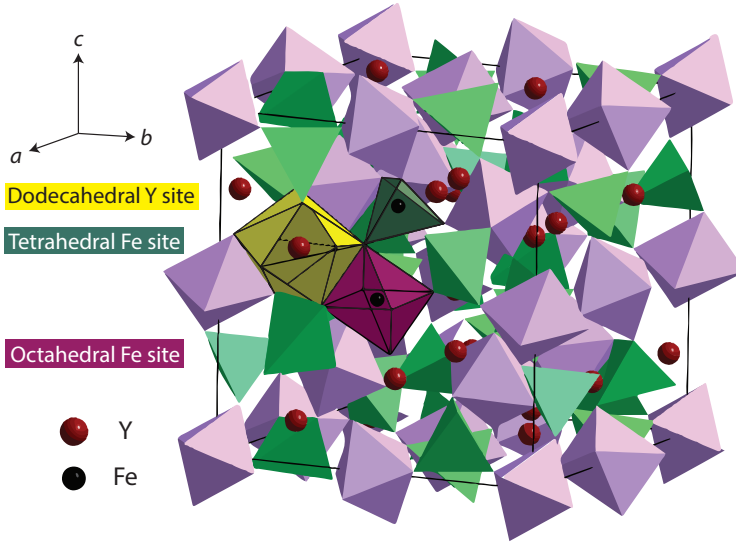


Figure 2.11: The crystal structure of YIG, which belongs to the cubic crystal system. The non-magnetic Y^{3+} cations locate at dodecahedral sites (yellow), each with 20 neighboring oxygen atoms. Three out of five Fe^{3+} occupy the tetrahedral sites (green) with 4 oxygen neighbors and the other two Fe^{3+} occupy the octahedral sites (purple) with 6 oxygen neighbors. The antiparallel alignment between the tetrahedral and octahedral sublattices of Fe^{3+} results in a net magnetization.

This artificially synthesized material owns superb magnetic properties: It has a high T_C and the lowest known spin-wave damping factor α_G [144], corresponding to relatively long magnon lifetimes. Traditionally it was widely used in high frequency applications such as microwave filters, oscillators and resonators owing to its high quality factor [145, 146]. Recently, it enters the field of spintronics and triggered the discovery of many important physical phenomena [75, 76, 81, 83, 124]. Now it becomes the standard material for studying magnonic spintronics [105] based on magnetic insulators.

The YIG materials employed in this thesis are all (thin) films grown by liquid phase epitaxy (LPE) [147] on top of gadolinium gallium garnet ($Gd_3Ga_5O_{12}$, GGG) substrates. GGG is a paramagnetic insulator [148] that has a very small lattice mismatch to YIG, thereby reducing strain and dislocation during the growth of YIG. The employed YIG films exhibit a shape anisotropy that prefers in-plane magnetization. The coercive field in the plane is as small as 0.1 mT [83]. Other common growth techniques for YIG films are pulsed laser deposition (PLD) [149] and sputtering [150], which can also yield high-quality YIG films [151] and can even produce

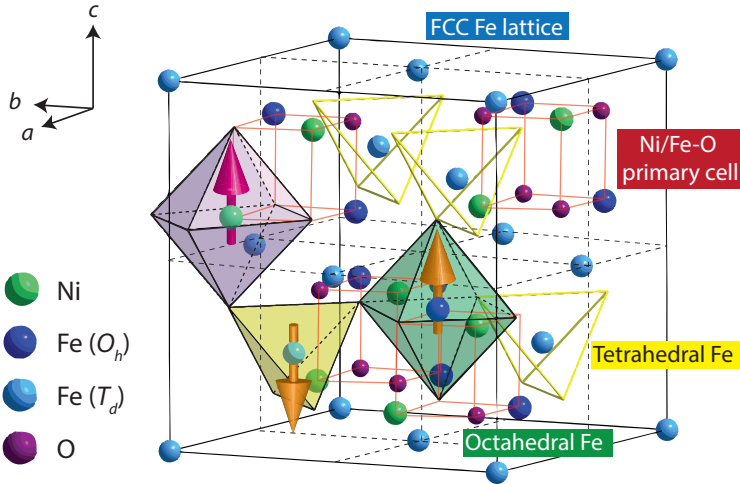


Figure 2.12: The crystal structure of NFO which is also in the cubic crystal system. Ni^{2+} ions (green) and half of the Fe^{3+} (dark blue) occupy octahedral sites, while the other half of the Fe^{3+} (light blue) on tetrahedral sites. All magnetic moments of Fe^{3+} are compensated from the two sublattices and only Ni^{2+} contribute to the total magnetization.

nanometer-thick YIG thin films [152, 153].

NFO

NFO belongs to another important family of ferrimagnets—ferrites. The general chemical formula for ferrites is $\text{MO}\cdot\text{Fe}_2\text{O}_3$, where M is a divalent cation such as Ni^{2+} in NFO, and all Fe cations are trivalent, i.e., Fe^{3+} . Ferrites have the spinel crystal structure, as shown in Fig. 2.12.

In spinels there are also tetrahedral and octahedral sites for metallic atoms, commonly known as A and B sites, respectively. The number of B sites are twice that of A sites. By how A and B sites are occupied, spinels can be categorized into two groups: normal spinels and inverse spinels. In normal spinels all M^{2+} ions occupy A sites and all Fe^{3+} ions (or other trivalent ions) occupy B sites. In inverse spinels [154] such as NFO, however, half of the Fe^{3+} ions occupy A sites and the other half, together with all M^{2+} , occupy B sites (see Fig. 2.12). Because of the strong exchange interaction between the A and B sublattices ($J_{AB} < 0$), Spins on A and B sites align antiparallel to each other. Thus in NFO the magnetic moments of Fe^{3+} cancel out, with the net magnetization coming solely from Ni^{2+} [3, 4].

The NFO films used in chapter 6 were grown by reactive co-sputtering on magnesium aluminate spinel (MgAl_2O_4 , MAO) substrates [155]. MAO is the most commonly known spinel. It is diamagnetic [156] and has a relatively small lattice mismatch to NFO [155]. But it was shown very recently that two other substrates which also belong to the spinel group, magnesium gallate spinel (MgGa_2O_4 , MGO) and cobalt gallium oxide spinel (CoGa_2O_4 , CGO) have even smaller lattice mismatches to NFO and can serve as better substrates for NFO thin films. As a result, the NFO thin films grown on these substrates have less antiphase boundary defects and show an enhancement of the spin Seebeck effect due to the decrease of the Gilbert damping coefficient α_G compared with the ones grown on MAO [157].

2.4 Thermoelectrics and spin caloritronics in metallic systems

A heat flow can be induced in a material when a temperature gradient ($\vec{\nabla}T$) is present. The heat transport can be expressed in a similar fashion as Ohm's law (Eq. 2.1):

$$\vec{J}_q = -\kappa \vec{\nabla}T, \quad (2.27)$$

where \vec{J}_q is the heat current density and κ is the thermal conductivity of a material. In solid materials, a heat current can be carried by phonons, and by conduction electrons in metallic materials and (or) by magnons in magnetic materials as well.

In pure metals, the thermal conductivity is dominated by the contribution from electrons at all temperatures [3], i.e., $\kappa \approx \kappa_e$. For free electrons, κ_e can be further expressed as [3]

$$\kappa_e = \frac{1}{3} C v_F l_e = \frac{\pi^2 n k_B^2 T \tau_e}{3 m^*}, \quad (2.28)$$

where C is the electron heat capacity per unit volume. There is then a direct scaling between the electrical and thermal conductivity in metals

$$\frac{\kappa_e}{\sigma} = \frac{\pi^2}{3} \left(\frac{k_B}{e} \right)^2 T = L_0 T, \quad (2.29)$$

known as the *Wiedemann-Franz law* [158]. L_0 is a material-independent constant called Lorenz number. Note that at a certain temperature range this law can break down, as inelastic scattering becomes dominant with electrons being transported without the transport of heat. In this case the scattering time in Eq. 2.28 is not equal to τ_e but smaller, resulting in a smaller ratio of κ_e/σ than predicted by Eq. 2.29.

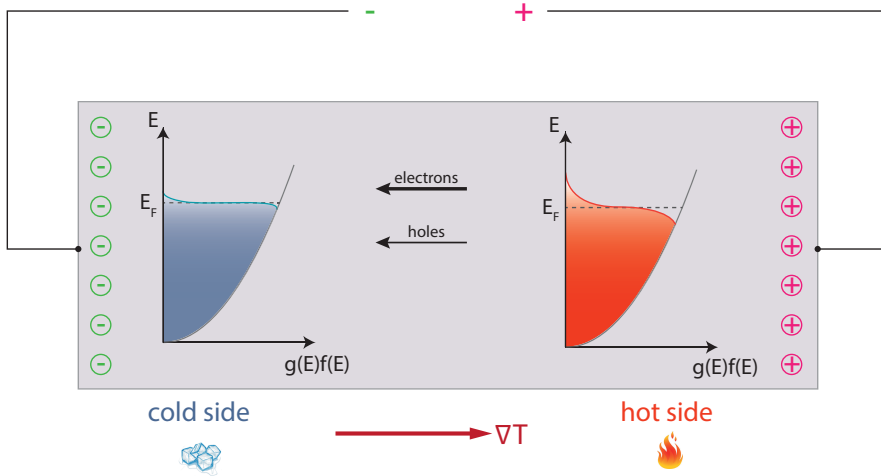


Figure 2.13: Sketch of the Seebeck effect mechanism. A temperature gradient is applied to a material with Seebeck coefficient $S < 0$. $f(E)$ is the Fermi-Dirac distribution function and $g(E)$ is the density of states. The shaded blue and red colors represent the product of $g(E)$ and $f(E)$ and shows the electron number density as a function of energy. Due to the thermal broadening, at the hot end $f(E)$ has a smoother transition around the Fermi energy E_F compared with the cold end, implying more hot electrons and hot holes around E_F . Both of them diffuse from the hot to the cold part, and a net charge flow appears if there is electron-hole asymmetry regarding to electrical conductance. Figure inspired by Ref. [141] and [17].

2.4.1 The Seebeck effect and the Peltier effect

Temperature plays a crucial role in the Fermi-Dirac distribution of electrons. Thus, when a temperature gradient is applied to a conducting material, not only does it drive a heat flow, but it may also induce a charge flow, for instance, if electron-hole asymmetry exists at the Fermi energy. This gives rise to the interplay between charge and heat currents, as described in the well-known Seebeck and Peltier effects.

The Seebeck effect

The Seebeck effect, discovered almost two hundred years ago, refers to the generation of an electric current as a result of a temperature gradient in a conductor. The physical mechanism of this effect is illustrated in Fig. 2.13.

At absolute zero temperature, The Fermi-Dirac distribution function is a step function that sharply transits from 0 to 1 at the Fermi level E_F , meaning that electrons in the system fully occupy all the states below E_F , whereas above E_F the states are empty. At elevated temperatures, however, the distribution function gets smeared

out, as some electrons are thermally excited to energy levels above E_F . Hence, in a material under a temperature gradient, the hot side has more electrons above E_F as well as more holes below E_F compared with the cold side. Both these hot electrons and hot holes will diffuse from the hot to the cold side. However, if the conductivities of these electrons and holes (essentially σ of the electrons above and below E_F) are not equal, the two charge flows will not cancel each other, and a net charge flow will arise in the material. Under an open-circuit condition, as shown in Fig. 2.13, opposite charges will accumulate at the sample edges. An electric field is therefore built up that counteracts the thermally-induced charge flow, and at the steady state there is no charge flow in the sample.

The Seebeck effect can be expressed as

$$\vec{J}_S = -S\vec{\nabla}T, \quad (2.30)$$

where \vec{J}_S is the thermally induced charge flow and S is the Seebeck coefficient or thermopower. In simple metals, S can be determined by [141, 159, 160]

$$S = -eL_0T \left. \frac{\partial[\ln \sigma(E)]}{\partial E} \right|_{E_F}, \quad (2.31)$$

where L_0 is the Lorenz number defined in Eq. 2.29.

Although the Seebeck effect can occur in a single material, the measurement of the Seebeck voltage often requires two materials with different S [160]. A thermocouple is such a device that consists of two dissimilar materials and can convert a temperature difference into an electric voltage, as shown in Fig. 2.14(a). It is widely applied as a temperature sensor, and was recently employed in micro-scale and nano-scale devices as a temperature indicator to study spin-related thermoelectrics effects [86, 161–164], as also employed in Chapt. 3.

The Peltier effect

The *Peltier effect* is a reciprocal process of the Seebeck effect. It tells that when a charge current passes through a conductive material, it is accompanied by a heat current. The Peltier effect can be expressed as

$$\vec{Q} = \Pi\vec{J}_c, \quad (2.32)$$

where Q is the induced Peltier heat flux and Π is the Peltier coefficient. Π and S are related to each other by the Onsager reciprocity relation [165]: $\Pi = ST$.

Similar to the Seebeck effect, the detection of the Peltier effect also often needs two dissimilar materials, typically at the junction when two materials are connected to each other, as shown in Fig. 2.14(b). When a charge current flows from one material

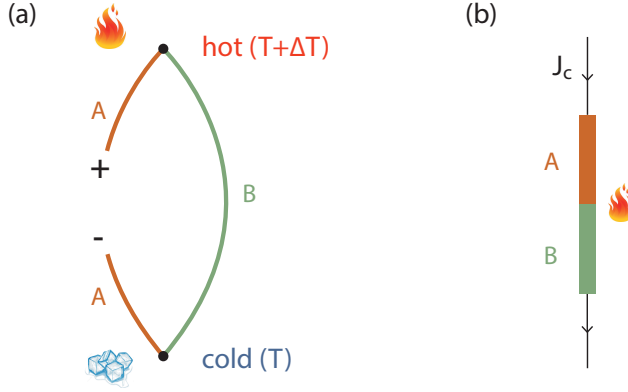


Figure 2.14: Illustrations of basic Seebeck and Peltier devices. (a) A temperature difference ΔT is imposed on a thermocouple that comprises two materials A and B, with $S_A > S_B$. The generated Seebeck voltage is $(S_A - S_B)\Delta T$ with the polarity defined in the figure. (b) A charge current flows from material A to B. If $S_A > S_B$, certain amount of heat will develop at the junction. Reverse the current direction leads to the absorption of the heat, thus cooling at the junction. Figures adapted from Ref. [160].

to the other, the induced Peltier heat currents are not equal in these two materials. If $S_A > S_B$, heat will accumulate and result in a raise of temperature at the junction. Reversing the current direction changes the Peltier heating into cooling.

The Peltier effect should be distinguished from Joule heating. First of all, the Peltier effect is a reversible process ($\propto J_c$) while Joule heating is irreversible ($\propto J_c^2$). Furthermore, whereas Joule heating actually creates heat everywhere as the charge flows in a material with certain resistivity, the Peltier effect only transports heat along the charge current, without producing additional heat.

The charge and heat transports, as well as their coupling, can be summarized into

$$\begin{pmatrix} \vec{J}_c \\ \vec{Q} \end{pmatrix} = - \begin{pmatrix} \sigma & \sigma S \\ \sigma \Pi & \kappa \end{pmatrix} \begin{pmatrix} -\vec{\nabla} V \\ \vec{\nabla} T \end{pmatrix}, \quad (2.33)$$

where the Seebeck and Peltier coefficients enter as off-diagonal terms and represent the interaction between the charge and heat currents.

2.4.2 Spin-dependent Seebeck effect and spin-dependent Peltier effect

In magnetic materials, not only is σ spin dependent, but also the electron-hole asymmetry at E_F may not be the same for spin-up and spin-down electron bands. This

leads to the spin-dependent Seebeck coefficients S_\uparrow and S_\downarrow , as well as the spin-dependent Peltier coefficients Π_\uparrow and Π_\downarrow , straight from the Onsager relation [166].

The condition that $S_\uparrow \neq S_\downarrow$ provides another method to create a spin current in an FM. Instead of imposing an electrical voltage bias, one can apply simply a temperature gradient on an FM which produces a spin current that is proportional to $S_\uparrow - S_\downarrow$. This spin current can be injected into an NM and detected electrically with another FM, similar as the picture discussed in Sec. 2.1.2. This *spin-dependent Seebeck effect* was first observed laterally using a nonlocal spin valve [167], and later in vertical pillar spin valve (essentially GMR) structures with greatly improved signal-to-noise ratio [168].

Reciprocally, the *spin-dependent Peltier effect* should also exist, and can actually be detected with same devices as for the spin-dependent Seebeck effect with the input and output reversed. The first direct observation of this effect was reported in Ref. [162] using a GMR pillar structure. By employing a nanoscale thermocouple, the authors demonstrate that when changing from P to AP configurations, the temperature drop across the pillar is altered, as a result of the change of the ratio J_\uparrow/J_\downarrow close to the FM/NM interfaces.

Taking into account the spin-dependent Seebeck and Peltier coefficients in magnetic materials, a more general transport equation can be formulated as [141]:

$$\begin{pmatrix} \vec{J}_\uparrow \\ \vec{J}_\downarrow \\ \vec{Q} \end{pmatrix} = - \begin{pmatrix} \sigma_\uparrow & 0 & \sigma_\uparrow S_\uparrow \\ 0 & \sigma_\downarrow & \sigma_\downarrow S_\downarrow \\ \sigma_\uparrow \Pi_\uparrow & \sigma_\downarrow \Pi_\downarrow & \kappa \end{pmatrix} \begin{pmatrix} \vec{\nabla} V_\uparrow \\ \vec{\nabla} V_\downarrow \\ \vec{\nabla} T \end{pmatrix}. \quad (2.34)$$

A more careful treatment further distinguishes the thermal conductivity κ for spin-up and spin down electrons in magnetic materials, i.e., $\kappa_\uparrow \neq \kappa_\downarrow$ [163, 169], which directly comes from the Wiedemann-Franz law with $\sigma_\uparrow \neq \sigma_\downarrow$. In this case a “two-current model” is also applicable for the heat current Q , which can be considered as carried unevenly by spin-up and spin-down electrons ($Q_\uparrow \neq Q_\downarrow$).

2.4.3 Magneto-Seebeck effect and magneto-Peltier effect

Not surprisingly, similar to all-metal spin valves, magnetic tunnel junctions also exhibit spin-dependent thermoelectric phenomena. Between P and AP magnetic configurations, the Seebeck coefficient of an MTJ was found to be different. This effect was termed as the *magneto-Seebeck effect*, and was first observed in CoFeB/MgO MTJs [170, 171] and later in Al_2O_3 -based MTJs [172]. Very recently, a large enhancement of the magneto-Seebeck effect was achieved by using half-metallic Heusler compounds as electrodes [173].

The magneto-Seebeck effect can be also understood from the electron-hole asymmetry for the tunneling DOS [170, 174]. While the conductance of an MTJ is governed

by the transmission probability $T(E)$ around E_F , the Seebeck coefficient is determined by the asymmetry of $T(E)$ around E_F . If this asymmetry for $T_{\uparrow}(E)$ and $T_{\downarrow}(E)$ is different, a magneto-Seebeck effect can be expected ($S_P \neq S_{AP}$).

For a certain configuration, the conductance of the junction can be expressed as [170, 174]

$$G = \frac{e^2}{h} \int T(E)(-\partial_E f_{F-D}(E, \mu, T))dE, \quad (2.35)$$

where $f_{F-D}(E, \mu, T)$ is the Fermi-Dirac distribution. The derivative of f_{F-D} with respect to energy gives a δ function centered at E_F for $T = 0$ and a broadened one for an elevated temperature. The Seebeck coefficient of the junction, on the other hand, can be calculated as [170, 174]

$$S = -\frac{1}{eT} \frac{\int (E - \mu)T(E)(-\partial_E f_{F-D}(E, \mu, T))dE}{\int T(E)(-\partial_E f_{F-D}(E, \mu, T))dE}. \quad (2.36)$$

S can thus be regarded as the deviation of the geometric center of $T(E)f_{F-D}(E, \mu, T)$ with respect to μ . Although both G and S can be calculated from the transmission probability function, they are not directly related to each other. Hence, a large TMR effect ($(R_{AP} - R_P)/R_P$) does not guarantee a large magneto-Seebeck effect ($(S_{AP} - S_P)/\min(S_P, S_{AP})$).

An alternative approach to theoretically interpret the magneto-Seebeck effect was reported recently, where the magnonic contribution to the thermopower of an MTJ was considered [175]. Together with the single-electron approach described above, it could bring a more complete picture to understand and estimate the magneto-Seebeck effect.

A reciprocal effect, which can be named as the ‘‘magneto-Peltier effect’’ is expected from the Onsager relation, where the heat flow carried by the tunneling electrons can be altered by switching between P and AP configurations ($\Pi_P \neq \Pi_{AP}$). Consequently, the temperature buildup over the junction depends on the magnetic configuration, which can be detected by a sensitive microscale thermocouple. Our work described in Chapt. 3 is the first experimental study of this effect. We will further discuss this topic closely in that chapter.

2.5 Spin caloritronics in magnetic insulators

So far, we have discussed how charge, spin and heat interact with each other in conduction electron systems which are Fermionic. Similarly, temperature also plays a pivotal role in the Bose-Einstein distribution function, so heat currents are also expected to couple to the transport mediated by Bosonic carriers. In this section,

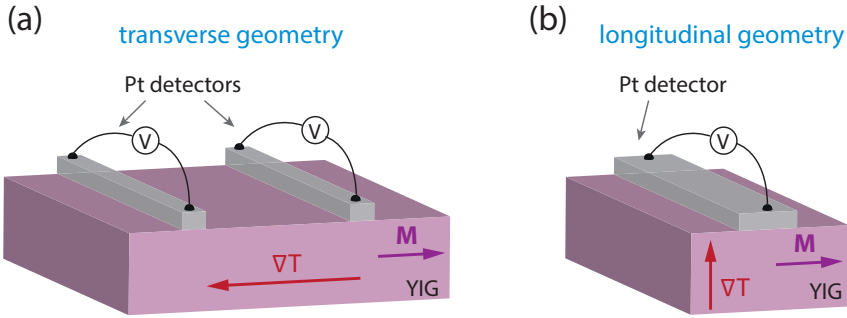


Figure 2.15: Two basic device configurations for observing the spin Seebeck effect (SSE) in, for instance, the prototypical YIG/Pt systems. (a) The transverse geometry where the temperature gradient (∇T) is applied laterally and perpendicular to the spin current detection direction. (b) The longitudinal geometry where ∇T is applied vertically and parallel to the spin current detection direction. In both cases, part of the thermally excited spin currents flow into Pt detectors and convert into electric voltages by ISHE.

we will discuss the influence of heat on magnon transport. In contrast to electrons, magnons are quasiparticles that do not obey the particle conservation law. This makes the discussion even more interesting, as the temperature can directly control the number of magnons. Particularly, we look at magnetic insulators where the charge transport can be excluded, which allows us to focus only on the coupling between spin and heat currents.

2.5.1 Spin Seebeck effect

Longitudinal and transverse spin Seebeck effects

The generation of a magnonic spin current by a temperature gradient in magnetic materials is called the *spin Seebeck effect* (SSE). When this effect was first observed a few years back [75, 140], a “transverse geometry” was utilized, as shown in Fig. 2.15(a). The ∇T is applied in the horizontal direction along the YIG material, with Pt detectors placed on top at different locations, separated by distances on a millimeter scale. The detected ISHE signals show opposite signs between hot and cold ends and vary linearly as a function of position. However, it was argued later on that the transverse SSE was not fully reproducible and was related to unwanted ∇T in the vertical direction [176]. The other “longitudinal geometry” [177, 178] is nowadays more widely employed, where the ∇T is applied perpendicular to the film and along the spin detection path (see Fig. 2.15(b)). Our discussion in this section is mainly based on the longitudinal SSE mechanism.

Interpretation of the spin Seebeck effect

Generally speaking, the SSE is an out-of-equilibrium phenomenon of the magnon system driven by ∇T , but this non-equilibrium can be specified in different perspectives. The first theoretical description of the SSE was given by Xiao *et al.* [179], on the basis of the earlier work by Sanders and Walton [180]. In this approach, the non-equilibrium is interpreted as an individual temperature T_m for magnons (see Eq. 2.24) that deviates from the phonon temperature T_{ph} . On the other hand, the electrons and phonons are assumed to strongly interact with each other, so that the electrons and phonons share the same temperature ($T_{ph} = T_e$). The spin current that pumps from the FM to the NM layer (J_{SSE}) depends on how much T_m on the FM side deviates from T_e on the NM side at the FM/NM interface, i.e., $J_{SSE} \propto T_m - T_e$. The SSE is thus thought as an *interfacial* effect. The spatial profile of T_m depends on the magnon-phonon relaxation time and specific boundary conditions [92].

The experimental observations of a much longer length scale (typically a few micrometers) associated with the SSE [76, 181, 182], however, challenged the completeness of the magnon temperature approach, as the magnon-phonon relaxation length (λ_{m-ph}) is expected to be very short [85] (see also Sec. 2.3.2) and cannot be linked to the observed length scale. Because of the longer length scale involved, the SSE is instead considered as a *bulk* effect. In the longitudinal SSE configuration, increasing the thickness of the FM on the order of this length scale resulted in an increase of the SSE signal until it saturated at a certain point [181, 183]. Besides, the nonlocal detection of the SSE also showed an exponential decay as a function of the heater-detector distance [76, 137, 182, 184], which will be further discussed in the next subsection.

These experimental results necessitate the inclusion of another parameter to describe the non-equilibrium of the magnon systems excited thermally. As already discussed in Sec. 2.3.2, a nonzero magnon chemical potential (μ_m) can parametrize a relatively long-lived non-equilibrium magnon state. In a simplified theory, the magnon and phonon temperature can be approximated to be equal ($T_m = T_{ph}$) and the non-equilibrium magnon state is described exclusively by μ_m [85, 185]. Thus, in a magnon drift-diffusion picture (see Sec. 2.3.3), the magnon relaxation length (λ_m) should correspond to the length scale found experimentally.

In this theory, a thermally excited magnon current is driven everywhere in the FM as

$$\vec{J}_{m,q} = -\sigma_m S_S \vec{\nabla} T, \quad (2.37)$$

where S_S is the bulk magnon Seebeck coefficient. The total magnon current includes also the diffusive magnon current, and is thus

$$\vec{J}_{m,total} = -\sigma_m (\vec{\nabla} \mu_m + S_S \vec{\nabla} T). \quad (2.38)$$

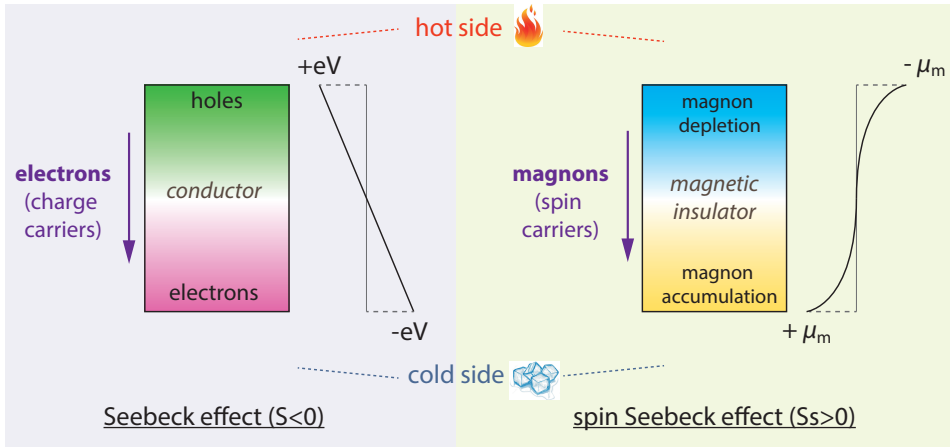


Figure 2.16: The analogy between the Seebeck effect (left) and the SSE (right). A temperature gradient is applied either on a conductor (Seebeck effect) or a magnetic insulator (SSE) under open-circuit conditions. This causes redistribution of carriers to balance the thermally excited charge/spin currents, resulting in an extra and less amount of particles on two ends, which can be described by positive and negative electro-/magnon chemical potentials. One difference between the two effects is that magnons are not conserved and relax on a length scale of λ_m . Therefore, in SSE the nonzero μ_m can only extend up to a few λ_m away from the boundaries, while in the Seebeck effect, a linear variation of eV is expected.

This expression shares a high similarity with the thermoelectric equation in metallic systems (Eq. 2.33). The Seebeck effect and SSE can therefore be understood in a similar way, as plotted in Fig. 2.16. Given proper boundary conditions, one can determine the magnon current flowing into the NM detector and calculate the corresponding SSE voltage.

The microscopic origin of the SSE is not (solely) the energy-dependent conductivity, as is the case for the Seebeck effect. In a conduction electron system, a higher temperature translates into a larger thermal broadening of the Fermi-Dirac distribution without changing the total number of the electrons, whereas in a magnon system, a higher temperature indicates a higher magnon number density, as already revealed in the Bloch $T^{3/2}$ law (Eq. 2.12). As a result, magnons will diffuse from the hot to the cold part, and this process will be balanced by the buildup of nonzero chemical potentials under an open-circuit condition, as illustrated in Fig. 2.16. An expression of S_S is given in Ref. [85] theoretically. Our work presented in Chapt. 4 is the first experimental endeavor to estimate S_S .

Nonlocal spin Seebeck effect

Besides the basic longitudinal and transverse configurations, a nonlocal geometry can be used to study the SSE, where the detection location is separated from the heat source by a certain distance d (see Fig. 2.17(a) as an example). The nonlocal SSE signals are often studied as a function of d , which can yield additional information compared with the local study with the longitudinal SSE configuration, although they share the same physical mechanism as described in Eq. 2.38.

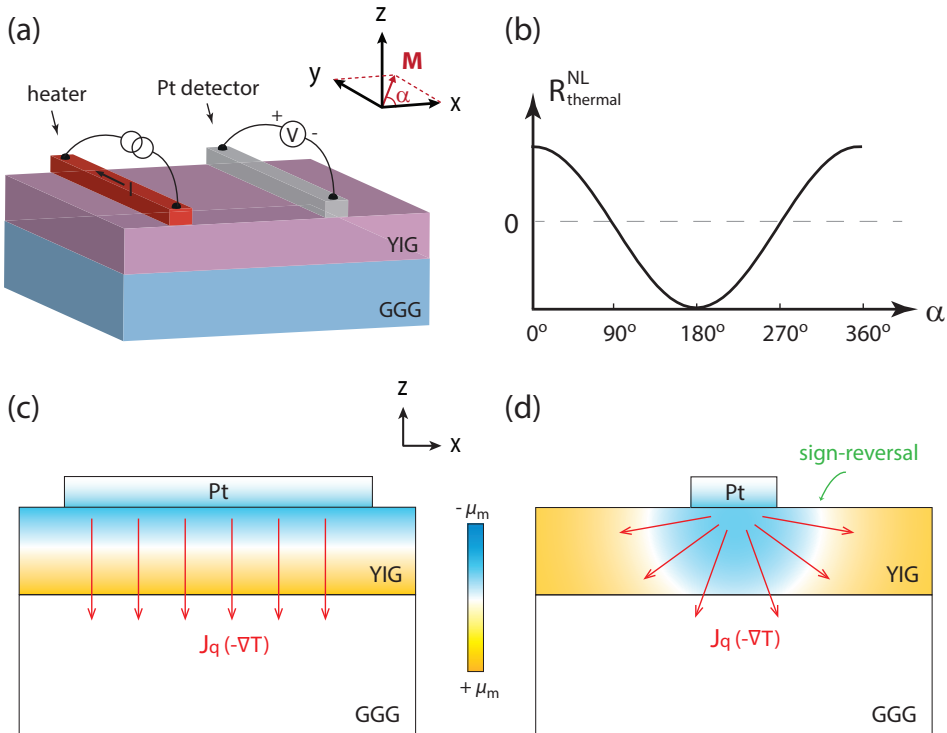


Figure 2.17: The nonlocal SSE detection. (a) A possible nonlocal SSE measurement configuration, where the ∇T in YIG is generated by the Joule heating of the heater strip. Part of the thermally excited spin current flows into the Pt detector positioned at a distance away from the heater. In this way, the nonlocal SSE can be studied fully electrically. (b) Illustration of a typical measurement curve under angle sweep of the external magnetic field. (c) (d) Schematic illustration of the cross-section view of μ_m profile for a vertical and a radial ∇T , respectively. A longitudinal (local) SSE configuration largely corresponds to (c) and a nonlocal SSE configuration with a narrow heater corresponds to (d). A calculated illustration of (d) from a finite element model is shown in Fig. C.3(b).

2

Firstly, it provides a direct examination of the bulk SSE picture. It is already possible to confirm it with a longitudinal SSE geometry by varying the YIG thickness [181, 183]. The profile of μ_m is schematically shown in Fig. 2.17(c), and an analytical study can be found in Sec. 4.6.3. However, this study involves the comparison of data among different YIG samples and may contain some uncertainty. The nonlocal geometry yields more direct results thanks to its unique radial temperature profile (see Fig. 2.17(d)). The corresponding μ_m is also radial around the heater with μ_m along the x direction at the YIG surface mimicking μ_m along the z direction. Thus for Pt detector close to and far away from the heater, the sign of the nonlocal SSE signals should be opposite, as measured indeed experimentally [76, 137, 186]. The work in Chapt. 4 discusses this topic extensively, studying the dependence of nonlocal SSE signals by changing the YIG thickness and heater spin transparency to further confirm the bulk SSE picture.

Secondly, the nonlocal method is a powerful tool to extract λ_m of a magnetic insulator. As can be seen from Ref. [76], in very thin YIG films, after the sign-reversal the SSE signals start to exhibit an exponential decay as a function of d . As already mentioned in Sec. 2.3.3, from the exponential regime, the decay length scale of the thermally excited magnons is almost the same as electrically injected magnons, further proving the consistency of the exchange magnon picture. However, one needs to be very careful in identifying the exponential decay distance range, as including data outside this range would lead to a misjudgment of the λ_m . This issue is discussed in greater detail in Chapt. 5, where we identify different decay regimes for nonlocal SSE signals and provide a general guideline to correctly determine λ_m .

2.5.2 Spin Peltier effect

The reciprocal of the SSE is called the *spin Peltier effect* (SPE), describing that a magnonic spin current is accompanied by a heat current in magnetic materials. This effect was first observed a few years ago in a YIG/Pt system, where the spin current was injected by the Pt contact via the SHE, and a temperature modulation was detected nonlocally by a micro-structured thermocouple when switching the YIG magnetization direction by a magnetic field [86]. Because of the spin Peltier effect, reversing the YIG magnetization alters the system from being heated to being cooled. Later, SPE was further demonstrated by a direct thermal imaging method [187]. Although the magnon temperature model was employed to describe the observed SPE [86], it can be expected that the bulk SPE mechanism also plays a role [85]. Further investigations are thus needed to better understand the SPE.

References

- [1] C. Chappert, A. Fert, and F. N. Van Dau, "The emergence of spin electronics in data storage," *Nature Materials* **6**, pp. 813–823, Nov. 2007.
- [2] I. Žutić, J. Fabian, and S. Das Sarma, "Spintronics: Fundamentals and applications," *Reviews of Modern Physics* **76**, pp. 323–410, Apr. 2004.
- [3] C. Kittel, *Introduction to Solid State Physics*, Wiley, Hoboken, NJ, 8th ed., Nov. 2004.
- [4] S. Blundell, *Magnetism in Condensed Matter*, Oxford University Press, Oxford, 2001.
- [5] P. M. Levy, "Current understanding and open questions on giant magnetoresistance," *Journal of Magnetism and Magnetic Materials* **140-144**, pp. 485–487, Feb. 1995.
- [6] J. F. Gregg, I. Petej, E. Jouguelet, and C. Dennis, "Spin electronics—a review," *Journal of Physics D: Applied Physics* **35**(18), p. R121, 2002.
- [7] N. F. Mott, "The Electrical Conductivity of Transition Metals," *Proceedings of the Royal Society of London A: Mathematical, Physical and Engineering Sciences* **153**, pp. 699–717, Feb. 1936.
- [8] A. Fert and I. A. Campbell, "Two-Current Conduction in Nickel," *Physical Review Letters* **21**, pp. 1190–1192, Oct. 1968.
- [9] A. Fert and I. A. Campbell, "Electrical resistivity of ferromagnetic nickel and iron based alloys," *Journal of Physics F: Metal Physics* **6**, p. 849, May 1976. 00305.
- [10] J. Fabian, A. Matos-Abiague, C. Ertler, P. Stano, and I. Zutic, "Semiconductor Spintronics," *Acta Physica Slovaca* **57**, p. 565, Jan. 2007.
- [11] A. Brataas, G. E. W. Bauer, and P. J. Kelly, "Non-collinear magnetoelectronics," *Physics Reports* **427**, pp. 157–255, Apr. 2006.
- [12] R. J. Elliott, "Theory of the Effect of Spin-Orbit Coupling on Magnetic Resonance in Some Semiconductors," *Physical Review* **96**, pp. 266–279, Oct. 1954.
- [13] Y. Yafet, "g Factors and Spin-Lattice Relaxation of Conduction Electrons," in *Solid State Physics*, F. Seitz and D. Turnbull, eds., **14**, pp. 1–98, Academic Press, Jan. 1963.
- [14] M. I. D'Yakonov and V. I. Perel', "Spin Orientation of Electrons Associated with the Interband Absorption of Light in Semiconductors," *Soviet Journal of Experimental and Theoretical Physics* **33**, p. 1053, 1971.
- [15] A. Fert, J.-L. Duvail, and T. Valet, "Spin relaxation effects in the perpendicular magnetoresistance of magnetic multilayers," *Physical Review B* **52**, pp. 6513–6521, Sept. 1995.
- [16] T. Valet and A. Fert, "Theory of the perpendicular magnetoresistance in magnetic multilayers," *Physical Review B* **48**, pp. 7099–7113, Sept. 1993.
- [17] F. Bakker, *Thermoelectric Effects in Magnetic Nanostructures*, PhD thesis, University of Groningen, 2012.
- [18] A. Slachter, F. L. Bakker, and B. J. van Wees, "Modeling of thermal spin transport and spin-orbit effects in ferromagnetic/nonmagnetic mesoscopic devices," *Physical Review B* **84**, p. 174408, Nov. 2011.
- [19] P. C. van Son, H. van Kempen, and P. Wyder, "Boundary Resistance of the Ferromagnetic-Nonferromagnetic Metal Interface," *Physical Review Letters* **58**, pp. 2271–2273, May 1987.
- [20] M. N. Baibich, J. M. Broto, A. Fert, F. N. Van Dau, F. Petroff, P. Etienne, G. Creuzet, A. Friederich, and J. Chazelas, "Giant Magnetoresistance of (001)Fe/(001)Cr Magnetic Superlattices," *Physical Review Letters* **61**, pp. 2472–2475, Nov. 1988.

- [21] G. Binasch, P. Grünberg, F. Saurenbach, and W. Zinn, "Enhanced magnetoresistance in layered magnetic structures with antiferromagnetic interlayer exchange," *Physical Review B* **39**, pp. 4828–4830, Mar. 1989.
- [22] M. Julliere, "Tunneling between ferromagnetic films," *Physics Letters A* **54**, pp. 225–226, Sept. 1975.
- [23] T. Miyazaki and N. Tezuka, "Giant magnetic tunneling effect in Fe/Al₂O₃/Fe junction," *Journal of Magnetism and Magnetic Materials* **139**, pp. L231–L234, Jan. 1995.
- [24] J. S. Moodera, L. R. Kinder, T. M. Wong, and R. Meservey, "Large Magnetoresistance at Room Temperature in Ferromagnetic Thin Film Tunnel Junctions," *Physical Review Letters* **74**, pp. 3273–3276, Apr. 1995.
- [25] S. Yuasa, T. Nagahama, A. Fukushima, Y. Suzuki, and K. Ando, "Giant room-temperature magnetoresistance in single-crystal Fe/MgO/Fe magnetic tunnel junctions," *Nature Materials* **3**, pp. 868–871, Dec. 2004.
- [26] S. S. P. Parkin, C. Kaiser, A. Panchula, P. M. Rice, B. Hughes, M. Samant, and S.-H. Yang, "Giant tunneling magnetoresistance at room temperature with MgO (100) tunnel barriers," *Nature Materials* **3**, pp. 862–867, Dec. 2004.
- [27] M. Tsoi, A. G. M. Jansen, J. Bass, W.-C. Chiang, M. Seck, V. Tsoi, and P. Wyder, "Excitation of a Magnetic Multilayer by an Electric Current," *Physical Review Letters* **80**, pp. 4281–4284, May 1998.
- [28] E. B. Myers, D. C. Ralph, J. A. Katine, R. N. Louie, and R. A. Buhrman, "Current-Induced Switching of Domains in Magnetic Multilayer Devices," *Science* **285**, pp. 867–870, Aug. 1999.
- [29] J. A. Katine, F. J. Albert, R. A. Buhrman, E. B. Myers, and D. C. Ralph, "Current-Driven Magnetization Reversal and Spin-Wave Excitations in Co/Cu/Co Pillars," *Physical Review Letters* **84**, pp. 3149–3152, Apr. 2000.
- [30] L. Liu, C.-F. Pai, Y. Li, H. W. Tseng, D. C. Ralph, and R. A. Buhrman, "Spin-Torque Switching with the Giant Spin Hall Effect of Tantalum," *Science* **336**, pp. 555–558, May 2012.
- [31] A. Brataas, A. D. Kent, and H. Ohno, "Current-induced torques in magnetic materials," *Nature Materials* **11**, pp. 372–381, Apr. 2012.
- [32] J. C. Slonczewski, "Current-driven excitation of magnetic multilayers," *Journal of Magnetism and Magnetic Materials* **159**, pp. L1–L7, June 1996.
- [33] L. Berger, "Emission of spin waves by a magnetic multilayer traversed by a current," *Physical Review B* **54**, pp. 9353–9358, Oct. 1996.
- [34] D. C. Ralph and M. D. Stiles, "Spin transfer torques," *Journal of Magnetism and Magnetic Materials* **320**, pp. 1190–1216, Apr. 2008.
- [35] M. D. Stiles and A. Zangwill, "Anatomy of spin-transfer torque," *Physical Review B* **66**, p. 014407, June 2002.
- [36] F. J. Jedema, A. T. Filip, and B. J. van Wees, "Electrical spin injection and accumulation at room temperature in an all-metal mesoscopic spin valve," *Nature* **410**, pp. 345–348, Mar. 2001.
- [37] F. J. Jedema, H. B. Heersche, A. T. Filip, J. J. A. Baselmans, and B. J. v. Wees, "Electrical detection of spin precession in a metallic mesoscopic spin valve," *Nature* **416**, p. 416713a, Apr. 2002.
- [38] M. Johnson and R. H. Silsbee, "Interfacial charge-spin coupling: Injection and detection of spin magnetization in metals," *Physical Review Letters* **55**, pp. 1790–1793, Oct. 1985.
- [39] N. Tombros, C. Jozsa, M. Popinciuc, H. T. Jonkman, and B. J. van Wees, "Electronic spin transport and spin precession in single graphene layers at room temperature," *Nature* **448**, pp. 571–574, Aug. 2007.

- [40] J.-G. J. Zhu and C. Park, "Magnetic tunnel junctions," *Materials Today* **9**, pp. 36–45, Nov. 2006.
- [41] J. C. Slonczewski, "Conductance and exchange coupling of two ferromagnets separated by a tunneling barrier," *Physical Review B* **39**, pp. 6995–7002, Apr. 1989.
- [42] J. Mathon, "Tight-binding theory of tunneling giant magnetoresistance," *Physical Review B* **56**, pp. 11810–11819, Nov. 1997.
- [43] W. H. Butler, X.-G. Zhang, T. C. Schulthess, and J. M. MacLaren, "Spin-dependent tunneling conductance of Fe|MgO|Fe sandwiches," *Physical Review B* **63**, p. 054416, Jan. 2001.
- [44] J. Mathon and A. Umerski, "Theory of tunneling magnetoresistance of an epitaxial Fe/MgO/Fe(001) junction," *Physical Review B* **63**, p. 220403, May 2001.
- [45] S. Ikeda, J. Hayakawa, Y. Ashizawa, Y. M. Lee, K. Miura, H. Hasegawa, M. Tsunoda, F. Matsukura, and H. Ohno, "Tunnel magnetoresistance of 604% at 300k by suppression of Ta diffusion in CoFeB/MgO/CoFeB pseudo-spin-valves annealed at high temperature," *Applied Physics Letters* **93**, p. 082508, Aug. 2008.
- [46] S. Yuasa, "Giant Tunneling Magnetoresistance in MgO-Based Magnetic Tunnel Junctions," *Journal of the Physical Society of Japan* **77**, p. 031001, Mar. 2008.
- [47] K. Tsunekawa, D. D. Djayaprawira, M. Nagai, H. Maehara, S. Yamagata, N. Watanabe, S. Yuasa, Y. Suzuki, and K. Ando, "Giant tunneling magnetoresistance effect in low-resistance CoFeB/MgO(001)/CoFeB magnetic tunnel junctions for read-head applications," *Applied Physics Letters* **87**, p. 072503, Aug. 2005.
- [48] W. J. Gallagher and S. S. P. Parkin, "Development of the magnetic tunnel junction MRAM at IBM: From first junctions to a 16-Mb MRAM demonstrator chip," *IBM Journal of Research and Development* **50**, pp. 5–23, Jan. 2006.
- [49] T. Jungwirth, J. Wunderlich, and K. Olejník, "Spin Hall effect devices," *Nature Materials* **11**, p. nmat3279, Apr. 2012.
- [50] J. Sinova, S. O. Valenzuela, J. Wunderlich, C. H. Back, and T. Jungwirth, "Spin Hall effects," *Reviews of Modern Physics* **87**, pp. 1213–1260, Oct. 2015.
- [51] M. I. Dyakonov and V. I. Perel, "Current-induced spin orientation of electrons in semiconductors," *Physics Letters A* **35**, pp. 459–460, July 1971.
- [52] N. Nagaosa, J. Sinova, S. Onoda, A. H. MacDonald, and N. P. Ong, "Anomalous Hall effect," *Reviews of Modern Physics* **82**, pp. 1539–1592, May 2010.
- [53] J. Inoue and H. Ohno, "Taking the Hall Effect for a Spin," *Science* **309**, p. 2004, Sept. 2005.
- [54] J. E. Hirsch, "Spin Hall Effect," *Physical Review Letters* **83**, pp. 1834–1837, Aug. 1999.
- [55] S. Zhang, "Spin Hall Effect in the Presence of Spin Diffusion," *Physical Review Letters* **85**, pp. 393–396, July 2000.
- [56] S. Murakami, N. Nagaosa, and S.-C. Zhang, "Dissipationless Quantum Spin Current at Room Temperature," *Science* **301**, pp. 1348–1351, Sept. 2003.
- [57] J. Sinova, D. Culcer, Q. Niu, N. A. Sinitsyn, T. Jungwirth, and A. H. MacDonald, "Universal Intrinsic Spin Hall Effect," *Physical Review Letters* **92**, p. 126603, Mar. 2004.
- [58] Y. K. Kato, R. C. Myers, A. C. Gossard, and D. D. Awschalom, "Observation of the Spin Hall Effect in Semiconductors," *Science* **306**, pp. 1910–1913, Dec. 2004.
- [59] J. Wunderlich, B. Kaestner, J. Sinova, and T. Jungwirth, "Experimental Observation of the Spin-Hall Effect in a Two-Dimensional Spin-Orbit Coupled Semiconductor System," *Physical Review Letters* **94**, p. 047204, Feb. 2005.

- [60] S. O. Valenzuela and M. Tinkham, "Direct electronic measurement of the spin Hall effect," *Nature* **442**, pp. 176–179, July 2006.
- [61] E. Saitoh, M. Ueda, H. Miyajima, and G. Tatara, "Conversion of spin current into charge current at room temperature: Inverse spin-Hall effect," *Applied Physics Letters* **88**, p. 182509, May 2006.
- [62] T. Kimura, Y. Otani, T. Sato, S. Takahashi, and S. Maekawa, "Room-Temperature Reversible Spin Hall Effect," *Physical Review Letters* **98**, p. 156601, Apr. 2007.
- [63] A. Hoffmann, "Spin Hall Effects in Metals," *IEEE Transactions on Magnetics* **49**, pp. 5172–5193, Oct. 2013.
- [64] R. Karplus and J. M. Luttinger, "Hall Effect in Ferromagnetics," *Physical Review* **95**, pp. 1154–1160, Sept. 1954.
- [65] G. Y. Guo, S. Murakami, T.-W. Chen, and N. Nagaosa, "Intrinsic Spin Hall Effect in Platinum: First-Principles Calculations," *Physical Review Letters* **100**, p. 096401, Mar. 2008.
- [66] T. Tanaka, H. Kontani, M. Naito, T. Naito, D. S. Hirashima, K. Yamada, and J. Inoue, "Intrinsic spin Hall effect and orbital Hall effect in 4d and 5d transition metals," *Physical Review B* **77**, p. 165117, Apr. 2008.
- [67] J. Smit, "The spontaneous hall effect in ferromagnetics II," *Physica* **24**, pp. 39–51, Jan. 1958.
- [68] L. Berger, "Side-Jump Mechanism for the Hall Effect of Ferromagnets," *Physical Review B* **2**, pp. 4559–4566, Dec. 1970.
- [69] M. Morota, Y. Niimi, K. Ohnishi, D. H. Wei, T. Tanaka, H. Kontani, T. Kimura, and Y. Otani, "Indication of intrinsic spin Hall effect in 4d and 5d transition metals," *Physical Review B* **83**, p. 174405, May 2011.
- [70] M. Isasa, E. Villamor, L. E. Hueso, M. Gradhand, and F. Casanova, "Temperature dependence of spin diffusion length and spin Hall angle in Au and Pt," *Physical Review B* **91**, p. 024402, Jan. 2015.
- [71] M.-H. Nguyen, D. C. Ralph, and R. A. Buhrman, "Spin Torque Study of the Spin Hall Conductivity and Spin Diffusion Length in Platinum Thin Films with Varying Resistivity," *Physical Review Letters* **116**, p. 126601, Mar. 2016.
- [72] K. Ando, S. Takahashi, K. Harii, K. Sasage, J. Ieda, S. Maekawa, and E. Saitoh, "Electric Manipulation of Spin Relaxation Using the Spin Hall Effect," *Physical Review Letters* **101**, p. 036601, July 2008.
- [73] L. Liu, T. Moriyama, D. C. Ralph, and R. A. Buhrman, "Spin-Torque Ferromagnetic Resonance Induced by the Spin Hall Effect," *Physical Review Letters* **106**, p. 036601, Jan. 2011.
- [74] L. Liu, O. J. Lee, T. J. Gudmundsen, D. C. Ralph, and R. A. Buhrman, "Current-Induced Switching of Perpendicularly Magnetized Magnetic Layers Using Spin Torque from the Spin Hall Effect," *Physical Review Letters* **109**, p. 096602, Aug. 2012.
- [75] K. Uchida, J. Xiao, H. Adachi, J. Ohe, S. Takahashi, J. Ieda, T. Ota, Y. Kajiwara, H. Umezawa, H. Kawai, G. E. W. Bauer, S. Maekawa, and E. Saitoh, "Spin Seebeck insulator," *Nature Materials* **9**, pp. 894–897, Nov. 2010.
- [76] L. J. Cornelissen, J. Liu, R. A. Duine, J. B. Youssef, and B. J. van Wees, "Long-distance transport of magnon spin information in a magnetic insulator at room temperature," *Nature Physics* **11**, pp. 1022–1026, Dec. 2015.
- [77] A. Brataas, Y. V. Nazarov, and G. E. W. Bauer, "Finite-Element Theory of Transport in Ferromagnet-Normal Metal Systems," *Physical Review Letters* **84**, pp. 2481–2484, Mar. 2000.
- [78] Y. Tserkovnyak, A. Brataas, and G. E. W. Bauer, "Enhanced Gilbert Damping in Thin Ferromagnetic Films," *Physical Review Letters* **88**, p. 117601, Feb. 2002.

- [79] Y. Tserkovnyak, A. Brataas, and G. E. W. Bauer, "Spin pumping and magnetization dynamics in metallic multilayers," *Physical Review B* **66**, p. 224403, Dec. 2002.
- [80] Y.-T. Chen, S. Takahashi, H. Nakayama, M. Althammer, S. T. B. Goennenwein, E. Saitoh, and G. E. W. Bauer, "Theory of spin Hall magnetoresistance," *Physical Review B* **87**, p. 144411, Apr. 2013.
- [81] H. Nakayama, M. Althammer, Y.-T. Chen, K. Uchida, Y. Kajiwara, D. Kikuchi, T. Ohtani, S. Geprägs, M. Opel, S. Takahashi, R. Gross, G. E. W. Bauer, S. T. B. Goennenwein, and E. Saitoh, "Spin Hall Magnetoresistance Induced by a Nonequilibrium Proximity Effect," *Physical Review Letters* **110**, p. 206601, May 2013.
- [82] N. Vlietstra, J. Shan, V. Castel, J. Ben Youssef, G. E. W. Bauer, and B. J. van Wees, "Exchange magnetic field torques in YIG/Pt bilayers observed by the spin-Hall magnetoresistance," *Applied Physics Letters* **103**, p. 032401, July 2013.
- [83] N. Vlietstra, J. Shan, V. Castel, B. J. van Wees, and J. Ben Youssef, "Spin-Hall magnetoresistance in platinum on yttrium iron garnet: Dependence on platinum thickness and in-plane/out-of-plane magnetization," *Physical Review B* **87**, p. 184421, May 2013.
- [84] M. Weiler, M. Althammer, M. Schreier, J. Lotze, M. Pernpeintner, S. Meyer, H. Huebl, R. Gross, A. Kamra, J. Xiao, Y.-T. Chen, H. Jiao, G. E. W. Bauer, and S. T. B. Goennenwein, "Experimental Test of the Spin Mixing Interface Conductivity Concept," *Physical Review Letters* **111**, p. 176601, Oct. 2013.
- [85] L. J. Cornelissen, K. J. H. Peters, G. E. W. Bauer, R. A. Duine, and B. J. van Wees, "Magnon spin transport driven by the magnon chemical potential in a magnetic insulator," *Physical Review B* **94**, p. 014412, July 2016.
- [86] J. Flipse, F. K. Dejene, D. Wagenaar, G. E. W. Bauer, J. B. Youssef, and B. J. van Wees, "Observation of the Spin Peltier Effect for Magnetic Insulators," *Physical Review Letters* **113**, p. 027601, July 2014.
- [87] H. Jiao and G. E. W. Bauer, "Spin Backflow and ac Voltage Generation by Spin Pumping and the Inverse Spin Hall Effect," *Physical Review Letters* **110**, p. 217602, May 2013.
- [88] N. Vlietstra, J. Shan, B. J. van Wees, M. Isasa, F. Casanova, and J. Ben Youssef, "Simultaneous detection of the spin-Hall magnetoresistance and the spin-Seebeck effect in platinum and tantalum on yttrium iron garnet," *Physical Review B* **90**, p. 174436, Nov. 2014.
- [89] C. Du, H. Wang, F. Yang, and P. C. Hammel, "Enhancement of Pure Spin Currents in Spin Pumping Y₃Fe₅O₁₂/Cu/Metal Trilayers through Spin Conductance Matching," *Physical Review Applied* **1**, p. 044004, May 2014.
- [90] W. Zhang, W. Han, X. Jiang, S.-H. Yang, and S. S. P. Parkin, "Role of transparency of platinum-ferromagnet interfaces in determining the intrinsic magnitude of the spin Hall effect," *Nature Physics* **11**, pp. 496–502, June 2015.
- [91] V. Castel, N. Vlietstra, J. B. Youssef, and B. J. v. Wees, "Platinum thickness dependence of the inverse spin-Hall voltage from spin pumping in a hybrid yttrium iron garnet/platinum system," *Applied Physics Letters* **101**, p. 132414, Sept. 2012.
- [92] M. Schreier, A. Kamra, M. Weiler, J. Xiao, G. E. W. Bauer, R. Gross, and S. T. B. Goennenwein, "Magnon, phonon, and electron temperature profiles and the spin Seebeck effect in magnetic insulator/normal metal hybrid structures," *Physical Review B* **88**, p. 094410, Sept. 2013.
- [93] W. Park, D. V. Baxter, S. Steenwyk, I. Moraru, W. P. Pratt, and J. Bass, "Measurement of resistance and spin-memory loss (spin relaxation) at interfaces using sputtered current perpendicular-to-plane exchange-biased spin valves," *Physical Review B* **62**, pp. 1178–1185, July 2000.
- [94] J.-C. Rojas-Sánchez, N. Reyren, P. Laczkowski, W. Savero, J.-P. Attané, C. Deranlot, M. Jamet, J.-M. George, L. Vila, and H. Jaffrès, "Spin Pumping and Inverse Spin Hall Effect in Platinum: The

- Essential Role of Spin-Memory Loss at Metallic Interfaces," *Physical Review Letters* **112**, p. 106602, Mar. 2014.
- [95] Y. Liu, Z. Yuan, R. J. H. Wesselink, A. A. Starikov, and P. J. Kelly, "Interface Enhancement of Gilbert Damping from First Principles," *Physical Review Letters* **113**, p. 207202, Nov. 2014.
- [96] T. McGuire and R. Potter, "Anisotropic magnetoresistance in ferromagnetic 3d alloys," *IEEE Transactions on Magnetics* **11**, pp. 1018–1038, July 1975.
- [97] C. Hahn, G. de Loubens, O. Klein, M. Viret, V. V. Naletov, and J. Ben Youssef, "Comparative measurements of inverse spin Hall effects and magnetoresistance in YIG/Pt and YIG/Ta," *Physical Review B* **87**, p. 174417, May 2013.
- [98] L. Liang, J. Shan, Q. Chen, J. Lu, G. R. Blake, T. T. M. Palstra, G. E. W. Bauer, B. J. Van Wees, and J. Ye, "Gate-controlled spin-dependent magnetoresistance of a platinum/paramagnetic insulator interface," *submitted*.
- [99] S. Meyer, R. Schlitz, S. Geprägs, M. Opel, H. Huebl, R. Gross, and S. T. B. Goennenwein, "Anomalous Hall effect in YIG|Pt bilayers," *Applied Physics Letters* **106**, p. 132402, Mar. 2015.
- [100] K. Xia, P. J. Kelly, G. E. W. Bauer, A. Brataas, and I. Turek, "Spin torques in ferromagnetic/normal-metal structures," *Physical Review B* **65**, p. 220401, May 2002.
- [101] R. L. Douglass, "Heat Transport by Spin Waves in Yttrium Iron Garnet," *Physical Review* **129**, pp. 1132–1135, Feb. 1963.
- [102] A. I. Liechtenstein, M. I. Katsnelson, and V. A. Gubanov, "Exchange interactions and spin-wave stiffness in ferromagnetic metals," *Journal of Physics F: Metal Physics* **14**(7), p. L125, 1984.
- [103] S. R. Boona and J. P. Heremans, "Magnon thermal mean free path in yttrium iron garnet," *Physical Review B* **90**, p. 064421, Aug. 2014.
- [104] H. Jin, S. R. Boona, Z. Yang, R. C. Myers, and J. P. Heremans, "Effect of the magnon dispersion on the longitudinal spin Seebeck effect in yttrium iron garnets," *Physical Review B* **92**, p. 054436, Aug. 2015.
- [105] A. V. Chumak, V. I. Vasyuchka, A. A. Serga, and B. Hillebrands, "Magnon spintronics," *Nature Physics* **11**, pp. 453–461, June 2015.
- [106] C. W. Sandweg, Y. Kajiwara, A. V. Chumak, A. A. Serga, V. I. Vasyuchka, M. B. Jungfleisch, E. Saitoh, and B. Hillebrands, "Spin Pumping by Parametrically Excited Exchange Magnons," *Physical Review Letters* **106**, p. 216601, May 2011.
- [107] C. Du, T. v. d. Sar, T. X. Zhou, P. Upadhyaya, F. Casola, H. Zhang, M. C. Onbasli, C. A. Ross, R. L. Walsworth, Y. Tserkovnyak, and A. Yacoby, "Control and local measurement of the spin chemical potential in a magnetic insulator," *Science* **357**, pp. 195–198, July 2017.
- [108] I. Dzyaloshinsky, "A thermodynamic theory of "weak" ferromagnetism of antiferromagnetics," *Journal of Physics and Chemistry of Solids* **4**, pp. 241–255, Jan. 1958.
- [109] T. Moriya, "Anisotropic Superexchange Interaction and Weak Ferromagnetism," *Physical Review* **120**, pp. 91–98, Oct. 1960.
- [110] Y. Onose, T. Ideue, H. Katsura, Y. Shiomi, N. Nagaosa, and Y. Tokura, "Observation of the Magnon Hall Effect," *Science* **329**, pp. 297–299, July 2010.
- [111] A. Manchon, P. B. Ndiaye, J.-H. Moon, H.-W. Lee, and K.-J. Lee, "Magnon-mediated Dzyaloshinskii-Moriya torque in homogeneous ferromagnets," *Physical Review B* **90**, p. 224403, Dec. 2014.
- [112] J. Liu, L. J. Cornelissen, J. Shan, T. Kuschel, and B. J. van Wees, "Magnon planar Hall effect and anisotropic magnetoresistance in a magnetic insulator," *Physical Review B* **95**, p. 140402, Apr. 2017.
- [113] B. Flebus, S. A. Bender, Y. Tserkovnyak, and R. A. Duine, "Two-Fluid Theory for Spin Superfluidity

- in Magnetic Insulators," *Physical Review Letters* **116**(11), p. 117201, 2016.
- [114] B. Flebus, P. Upadhyaya, R. A. Duine, and Y. Tserkovnyak, "Local thermomagnonic torques in two-fluid spin dynamics," *Physical Review B* **94**, p. 214428, Dec. 2016.
- [115] S. A. Bender and Y. Tserkovnyak, "Thermally driven spin torques in layered magnetic insulators," *Physical Review B* **93**, p. 064418, Feb. 2016.
- [116] L. H. Bennett and E. D. Torre, "The chemical potential of magnons in quasi-equilibrium," *Physica B: Condensed Matter* **403**, pp. 324–329, Feb. 2008.
- [117] S. O. Demokritov, V. E. Demidov, O. Dzyapko, G. A. Melkov, A. A. Serga, B. Hillebrands, and A. N. Slavin, "Bose–Einstein condensation of quasi-equilibrium magnons at room temperature under pumping," *Nature* **443**, pp. 430–433, Sept. 2006.
- [118] O. Dzyapko, V. E. Demidov, G. A. Melkov, and S. O. Demokritov, "Bose–Einstein condensation of spin wave quanta at room temperature," *Philosophical Transactions of the Royal Society of London A: Mathematical, Physical and Engineering Sciences* **369**, pp. 3575–3587, Sept. 2011.
- [119] D. Snoke, "Condensed-matter physics: Coherent questions," *Nature* **443**, pp. 403–404, Sept. 2006.
- [120] S. A. Bender and Y. Tserkovnyak, "Interfacial spin and heat transfer between metals and magnetic insulators," *Physical Review B* **91**, p. 140402, Apr. 2015.
- [121] M. Agrawal, V. I. Vasyuchka, A. A. Serga, A. D. Karenowska, G. A. Melkov, and B. Hillebrands, "Direct Measurement of Magnon Temperature: New Insight into Magnon-Phonon Coupling in Magnetic Insulators," *Physical Review Letters* **111**, p. 107204, Sept. 2013.
- [122] S. A. Bender, R. A. Duine, and Y. Tserkovnyak, "Electronic Pumping of Quasiequilibrium Bose-Einstein-Condensed Magnons," *Physical Review Letters* **108**, p. 246601, June 2012.
- [123] T. L. Gilbert, "A phenomenological theory of damping in ferromagnetic materials," *IEEE Transactions on Magnetics* **40**, pp. 3443–3449, Nov. 2004.
- [124] Y. Kajiwara, K. Harii, S. Takahashi, J. Ohe, K. Uchida, M. Mizuguchi, H. Umezawa, H. Kawai, K. Ando, K. Takanashi, S. Maekawa, and E. Saitoh, "Transmission of electrical signals by spin-wave interconversion in a magnetic insulator," *Nature* **464**, pp. 262–266, Mar. 2010.
- [125] A. V. Chumak, A. A. Serga, M. B. Jungfleisch, R. Neb, D. A. Bozhko, V. S. Tiberkevich, and B. Hillebrands, "Direct detection of magnon spin transport by the inverse spin Hall effect," *Applied Physics Letters* **100**, p. 082405, Feb. 2012.
- [126] A. V. Chumak, P. Pirro, A. A. Serga, M. P. Kostylev, R. L. Stamps, H. Schultheiss, K. Vogt, S. J. Hermsdoerfer, B. Laegel, P. A. Beck, and B. Hillebrands, "Spin-wave propagation in a microstructured magnonic crystal," *Applied Physics Letters* **95**, p. 262508, Dec. 2009.
- [127] S. S.-L. Zhang and S. Zhang, "Magnon Mediated Electric Current Drag Across a Ferromagnetic Insulator Layer," *Physical Review Letters* **109**, p. 096603, Aug. 2012.
- [128] P. Atkins and J. de Paula, *Atkins' Physical Chemistry*, Oxford University Press, Oxford, 2010.
- [129] S. T. B. Goennenwein, R. Schlitz, M. Pernpeintner, K. Ganzhorn, M. Althammer, R. Gross, and H. Huebl, "Non-local magnetoresistance in YIG/Pt nanostructures," *Applied Physics Letters* **107**, p. 172405, Oct. 2015.
- [130] M. H. D. Guimarães, A. Veligura, P. J. Zomer, T. Maassen, I. J. Vera-Marun, N. Tombros, and B. J. van Wees, "Spin Transport in High-Quality Suspended Graphene Devices," *Nano Letters* **12**, pp. 3512–3517, July 2012.
- [131] J. Ingla-Aynés, M. H. D. Guimarães, R. J. Meijerink, P. J. Zomer, and B. J. van Wees, "24- μm spin relaxation length in boron nitride encapsulated bilayer graphene," *Physical Review B* **92**, p. 201410,

- Nov. 2015.
- [132] W. Han, R. K. Kawakami, M. Gmitra, and J. Fabian, "Graphene spintronics," *Nature Nanotechnology* **9**, pp. 794–807, Oct. 2014.
- [133] H. Wu, C. H. Wan, X. Zhang, Z. H. Yuan, Q. T. Zhang, J. Y. Qin, H. X. Wei, X. F. Han, and S. Zhang, "Observation of magnon-mediated electric current drag at room temperature," *Physical Review B* **93**, p. 060403, Feb. 2016.
- [134] J. Li, Y. Xu, M. Aldosary, C. Tang, Z. Lin, S. Zhang, R. Lake, and J. Shi, "Observation of magnon-mediated current drag in Pt/yttrium iron garnet/Pt(Ta) trilayers," *Nature Communications* **7**, p. 10858, Mar. 2016.
- [135] L. J. Cornelissen, J. Shan, and B. J. van Wees, "Temperature dependence of the magnon spin diffusion length and magnon spin conductivity in the magnetic insulator yttrium iron garnet," *Physical Review B* **94**, p. 180402, Nov. 2016.
- [136] L. J. Cornelissen and B. J. van Wees, "Magnetic field dependence of the magnon spin diffusion length in the magnetic insulator yttrium iron garnet," *Physical Review B* **93**, p. 020403, Jan. 2016.
- [137] J. Shan, L. J. Cornelissen, N. Vlietstra, J. Ben Youssef, T. Kuschel, R. A. Duine, and B. J. van Wees, "Influence of yttrium iron garnet thickness and heater opacity on the nonlocal transport of electrically and thermally excited magnons," *Physical Review B* **94**, p. 174437, Nov. 2016.
- [138] J. Shan, P. Bougiatioti, L. Liang, G. Reiss, T. Kuschel, and B. J. van Wees, "Nonlocal magnon spin transport in NiFe₂O₄ thin films," *Applied Physics Letters* **110**, p. 132406, Mar. 2017.
- [139] K. Ganzhorn, T. Wimmer, J. Barker, G. E. W. Bauer, Z. Qiu, E. Saitoh, N. Vlietstra, S. Geprägs, R. Gross, H. Huebl, and S. T. B. Goennenwein, "Non-local magnon transport in the compensated ferrimagnet GdIG," *arXiv:1705.02871 [cond-mat]*, May 2017. arXiv: 1705.02871.
- [140] K. Uchida, S. Takahashi, K. Harii, J. Ieda, W. Koshibae, K. Ando, S. Maekawa, and E. Saitoh, "Observation of the spin Seebeck effect," *Nature* **455**, p. 778, Oct. 2008.
- [141] G. E. W. Bauer, E. Saitoh, and B. J. van Wees, "Spin caloritronics," *Nature Materials* **11**, pp. 391–399, May 2012.
- [142] S. Geller and M. A. Gilleo, "The crystal structure and ferrimagnetism of yttrium-iron garnet, Y₃Fe₂(FeO₄)₃," *Journal of Physics and Chemistry of Solids* **3**, pp. 30–36, Jan. 1957.
- [143] C. Vittoria, S. D. Yoon, and A. Widom, "Relaxation mechanism for ordered magnetic materials," *Physical Review B* **81**, p. 014412, Jan. 2010.
- [144] V. Cherepanov, I. Kolokolov, and V. L'vov, "The saga of YIG: Spectra, thermodynamics, interaction and relaxation of magnons in a complex magnet," *Physics Reports* **229**, pp. 81–144, July 1993.
- [145] W. S. Ishak, "Magnetostatic wave technology: a review," *Proceedings of the IEEE* **76**, pp. 171–187, Feb. 1988.
- [146] J. Krupka, B. Salski, P. Kopyt, and W. Gwarek, "Electrodynamic study of YIG filters and resonators," *Scientific Reports* **6**, p. srep34739, Oct. 2016.
- [147] H. J. Levinstein, S. Licht, R. W. Landorf, and S. L. Blank, "Growth of High-Quality Garnet Thin Films from Supercooled Melts," *Applied Physics Letters* **19**, pp. 486–488, Dec. 1971.
- [148] S. M. Wu, J. E. Pearson, and A. Bhattacharya, "Paramagnetic Spin Seebeck Effect," *Physical Review Letters* **114**, p. 186602, May 2015.
- [149] P. C. Dorsey, S. E. Bushnell, R. G. Seed, and C. Vittoria, "Epitaxial yttrium iron garnet films grown by pulsed laser deposition," *Journal of Applied Physics* **74**, pp. 1242–1246, July 1993.
- [150] B. W. Delf, A. Green, and R. J. Stevens, "Sputtering of yttrium iron garnet (YIG) thin films from a

- powder mixture of Fe₂O₃ and Y₂O₃," *physica status solidi (a)* **13**, pp. 493–498, Oct. 1972.
- [151] M. C. Onbasli, A. Kehlberger, D. H. Kim, G. Jakob, M. Kläui, A. V. Chumak, B. Hillebrands, and C. A. Ross, "Pulsed laser deposition of epitaxial yttrium iron garnet films with low Gilbert damping and bulk-like magnetization," *APL Materials* **2**, p. 106102, Oct. 2014.
- [152] Y. Sun, Y.-Y. Song, H. Chang, M. Kabatek, M. Jantz, W. Schneider, M. Wu, H. Schultheiss, and A. Hoffmann, "Growth and ferromagnetic resonance properties of nanometer-thick yttrium iron garnet films," *Applied Physics Letters* **101**, p. 152405, Oct. 2012.
- [153] T. Liu, H. Chang, V. Vlaminck, Y. Sun, M. Kabatek, A. Hoffmann, L. Deng, and M. Wu, "Ferromagnetic resonance of sputtered yttrium iron garnet nanometer films," *Journal of Applied Physics* **115**, p. 17A501, Jan. 2014.
- [154] E. J. W. Verwey and E. L. Heilmann, "Physical Properties and Cation Arrangement of Oxides with Spinel Structures I. Cation Arrangement in Spinels," *The Journal of Chemical Physics* **15**, pp. 174–180, Apr. 1947.
- [155] C. Klewe, M. Meinert, A. Boehnke, K. Kuepper, E. Arenholz, A. Gupta, J.-M. Schmalhorst, T. Kuschel, and G. Reiss, "Physical characteristics and cation distribution of NiFe₂O₄ thin films with high resistivity prepared by reactive co-sputtering," *Journal of Applied Physics* **115**, p. 123903, Mar. 2014.
- [156] M. Khalid, A. Setzer, M. Ziese, P. Esquinazi, D. Spemann, A. Pöppl, and E. Goering, "Ubiquity of ferromagnetic signals in common diamagnetic oxide crystals," *Physical Review B* **81**, p. 214414, June 2010.
- [157] A. Rastogi, A. V. Singh, Z. Li, D. Meier, J. B. Mohammadi, B. Khodadadi, T. Mewes, R. Mishra, J. Gazquez, A. Y. Borisevich, Z. Galazka, R. Uecker, G. Reiss, T. Kuschel, and A. Gupta, "Enhancement in Thermally Generated Spin Voltage at Nickel Ferrite/Pt Interface," *submitted* .
- [158] R. Franz and G. Wiedemann, "Ueber die Wärme-Leitungsfähigkeit der Metalle," *Annalen der Physik* **165**(8), pp. 497–531, 1853.
- [159] S. N. F. Mott and H. Jones, *The Theory of the Properties of Metals and Alloys*, Courier Dover Publications, 1958.
- [160] D. MacDonald, *Thermoelectricity: An Introduction to the Principles*, Dover Publications, Inc., Mineola, New York, 2006.
- [161] F. L. Bakker, A. Slachter, J.-P. Adam, and B. J. van Wees, "Interplay of Peltier and Seebeck Effects in Nanoscale Nonlocal Spin Valves," *Phys. Rev. Lett.* **105**, p. 136601, Sept. 2010.
- [162] J. Flipse, F. L. Bakker, A. Slachter, F. K. Dejene, and B. J. v. Wees, "Direct observation of the spin-dependent Peltier effect," *Nature Nanotechnology* **7**, pp. 166–168, Mar. 2012.
- [163] F. K. Dejene, J. Flipse, G. E. W. Bauer, and B. J. van Wees, "Spin heat accumulation and spin-dependent temperatures in nanopillar spin valves," *Nature Physics* **9**, pp. 636–639, Oct. 2013.
- [164] J. Shan, F. K. Dejene, J. C. Leutenantsmeyer, J. Flipse, M. Münzenberg, and B. J. van Wees, "Comparison of the magneto-Peltier and magneto-Seebeck effects in magnetic tunnel junctions," *Physical Review B* **92**, p. 020414, July 2015.
- [165] L. Onsager, "Reciprocal Relations in Irreversible Processes. I.," *Physical Review* **37**, pp. 405–426, Feb. 1931.
- [166] F. K. Dejene, J. Flipse, and B. J. van Wees, "Verification of the Thomson-Onsager reciprocity relation for spin caloritronics," *Physical Review B* **90**, p. 180402, Nov. 2014.
- [167] A. Slachter, F. L. Bakker, J.-P. Adam, and B. J. van Wees, "Thermally driven spin injection from a ferromagnet into a non-magnetic metal," *Nature Physics* **6**, pp. 879–882, Nov. 2010.

- [168] F. K. Dejene, J. Flipse, and B. J. van Wees, "Spin-dependent Seebeck coefficients of Ni80Fe20 and Co in nanopillar spin valves," *Physical Review B* **86**, p. 024436, July 2012. 00006.
- [169] T. T. Heikkilä, M. Hatami, and G. E. W. Bauer, "Spin heat accumulation and its relaxation in spin valves," *Physical Review B* **81**, p. 100408, Mar. 2010.
- [170] M. Walter, J. Walowski, V. Zbarsky, M. Münzenberg, M. Schäfers, D. Ebke, G. Reiss, A. Thomas, P. Peretzki, M. Seibt, J. S. Moodera, M. Czerner, M. Bachmann, and C. Heiliger, "Seebeck effect in magnetic tunnel junctions," *Nature Materials* **10**, pp. 742–746, Oct. 2011.
- [171] N. Liebing, S. Serrano-Guisan, K. Rott, G. Reiss, J. Langer, B. Ocker, and H. W. Schumacher, "Tunneling Magnetothermopower in Magnetic Tunnel Junction Nanopillars," *Physical Review Letters* **107**, p. 177201, Oct. 2011.
- [172] W. Lin, M. Hehn, L. Chaput, B. Negulescu, S. Andrieu, F. Montaigne, and S. Mangin, "Giant spin-dependent thermoelectric effect in magnetic tunnel junctions," *Nature Communications* **3**, p. 744, Mar. 2012.
- [173] A. Boehnke, U. Martens, C. Sterwerf, A. Niesen, T. Huebner, M. von der Ehe, M. Meinert, T. Kuschel, A. Thomas, C. Heiliger, M. Münzenberg, and G. Reiss, "Large magneto-Seebeck effect in magnetic tunnel junctions with half-metallic Heusler electrodes," *Nature Communications* **8**, p. 1626, Dec. 2017.
- [174] M. Czerner, M. Bachmann, and C. Heiliger, "Spin caloritronics in magnetic tunnel junctions: Ab initio studies," *Physical Review B* **83**, p. 132405, Apr. 2011.
- [175] B. Flebus, G. E. W. Bauer, R. A. Duine, and Y. Tserkovnyak, "Theory of the magnon-mediated tunnel magneto-Seebeck effect," *Physical Review B* **96**, p. 094429, Sept. 2017.
- [176] D. Meier, D. Reinhardt, M. van Straaten, C. Klewe, M. Althammer, M. Schreier, S. T. B. Goennenwein, A. Gupta, M. Schmid, C. H. Back, J.-M. Schmalhorst, T. Kuschel, and G. Reiss, "Longitudinal spin Seebeck effect contribution in transverse spin Seebeck effect experiments in Pt/YIG and Pt/NFO," *Nature Communications* **6**, p. 8211, Sept. 2015.
- [177] K.-i. Uchida, H. Adachi, T. Ota, H. Nakayama, S. Maekawa, and E. Saitoh, "Observation of longitudinal spin-Seebeck effect in magnetic insulators," *Applied Physics Letters* **97**, p. 172505, Oct. 2010.
- [178] K. Uchida, M. Ishida, T. Kikkawa, A. Kirihara, T. Murakami, and E. Saitoh, "Longitudinal spin Seebeck effect: from fundamentals to applications," *Journal of Physics: Condensed Matter* **26**, p. 343202, Aug. 2014.
- [179] J. Xiao, G. E. W. Bauer, K.-c. Uchida, E. Saitoh, and S. Maekawa, "Theory of magnon-driven spin Seebeck effect," *Physical Review B* **81**, p. 214418, June 2010.
- [180] D. J. Sanders and D. Walton, "Effect of magnon-phonon thermal relaxation on heat transport by magnons," *Physical Review B* **15**, pp. 1489–1494, Feb. 1977.
- [181] A. Kehlberger, U. Ritzmann, D. Hinzke, E.-J. Guo, J. Cramer, G. Jakob, M. C. Onbasli, D. H. Kim, C. A. Ross, M. B. Jungfleisch, B. Hillebrands, U. Nowak, and M. Kläui, "Length Scale of the Spin Seebeck Effect," *Physical Review Letters* **115**, p. 096602, Aug. 2015.
- [182] B. L. Giles, Z. Yang, J. S. Jamison, and R. C. Myers, "Long-range pure magnon spin diffusion observed in a nonlocal spin-Seebeck geometry," *Physical Review B* **92**, p. 224415, Dec. 2015.
- [183] E.-J. Guo, J. Cramer, A. Kehlberger, C. A. Ferguson, D. A. MacLaren, G. Jakob, and M. Kläui, "Influence of Thickness and Interface on the Low-Temperature Enhancement of the Spin Seebeck Effect in YIG Films," *Physical Review X* **6**, p. 031012, July 2016.
- [184] J. Shan, L. J. Cornelissen, J. Liu, J. B. Youssef, L. Liang, and B. J. van Wees, "Criteria for accurate determination of the magnon relaxation length from the nonlocal spin Seebeck effect," *Physical*

- Review B* **96**, p. 184427, Nov. 2017.
- [185] R. A. Duine, A. Brataas, S. A. Bender, and Y. Tserkovnyak, *Universal themes of Bose-Einstein condensation, chapter 26*, Cambridge University Press, Cambridge, United Kingdom, Apr. 2017. Edited by David Snoke, Nikolaos Proukakis and Peter Littlewood.
- [186] K. Ganzhorn, T. Wimmer, J. Cramer, R. Schlitz, S. Geprägs, G. Jakob, R. Gross, H. Huebl, M. Kläui, and S. T. B. Goennenwein, "Temperature dependence of the non-local spin Seebeck effect in YIG/Pt nanostructures," *AIP Advances* **7**, p. 085102, Aug. 2017.
- [187] S. Daimon, R. Iguchi, T. Hioki, E. Saitoh, and K.-i. Uchida, "Thermal imaging of spin Peltier effect," *Nature Communications* **7**, p. 13754, Dec. 2016.

Chapter 3

Comparison of the magneto-Peltier and magneto-Seebeck effects in magnetic tunnel junctions

Abstract

Understanding heat generation and transport processes in a magnetic tunnel junction (MTJ) is a significant step towards improving its application in current memory devices. Recent work has experimentally demonstrated the magneto-Seebeck effect in MTJs, where the Seebeck coefficient of the junction varies as the magnetic configuration changes from a parallel (P) to an anti-parallel (AP) configuration. Here we report a study on its reciprocal effect, the magneto-Peltier effect, where the heat flow carried by the tunneling electrons is altered by changing the magnetic configuration of the MTJ. The magneto-Peltier signal that reflects the change in the temperature difference across the junction between the P and AP configurations scales linearly with the applied current in the small bias but is greatly enhanced in the large bias regime, due to higher-order Joule heating mechanisms. By carefully extracting the linear response which reflects the magneto-Peltier effect, and comparing it with the magneto-Seebeck measurements performed on the same device, we observe results consistent with Onsager reciprocity. We estimate a magneto-Peltier coefficient of 13.4 mV in the linear regime using a three-dimensional thermoelectric model. Our result opens up the possibility of programmable thermoelectric devices based on the Peltier effect in MTJs.

3.1 Introduction

The electrical resistance of a magnetic tunnel junction (MTJ), a stack of two ferromagnetic layers separated by an insulating tunnel barrier, depends on the relative magnetic orientation of the two magnetic layers [1–3]. This tunnel magnetoresistance (TMR) effect puts MTJs at the forefront of the applications in the field of spintronics [4]. Spin caloritronics [5–7] is an emerging field that couples thermoelectric effects with spintronics. Many interesting physical phenomena were discovered such as the spin(-dependent) Seebeck effect in magnetic metal [8], magnetic semiconductor [9] and magnetic insulator [10]. Particularly, in spin tunneling devices,

the magneto-Seebeck effect was theoretically studied [11–14] and experimentally observed [15–20] in MTJs, where the Seebeck coefficient of the junction can be varied by changing the magnetic configuration. More recently, the spin(-dependent) Peltier effect that is driven by spin(-polarized) currents has been experimentally observed in metallic [21, 22] and insulating ferromagnets [23], which are shown to obey the Thomson-Onsager reciprocity relation [24–26] to the spin(-dependent) Seebeck effect. From this relation, the reciprocal effect of the magneto-Seebeck effect, which can be called the magneto-Peltier effect, is also expected in MTJs [see Figs. 3.1(a) and 3.1(b)].

However, experimental studies of the magneto-Peltier effect are lacking. Its small effect compared to the often-dominant Joule heating effects has left the experimental observation elusive. In this chapter, we report the first experimental study of the magneto-Peltier effect as well as higher-order heating effects, and compare the Peltier measurements to the Seebeck measurements on the same junction. Via sensitive thermometry architecture and measurement techniques, we are able to measure small temperature changes as well as distinguish between the linear (due to Peltier effect) and nonlinear effects (due to Joule heating).

3.2 Concept of the experiment

Although both the electric conductance and Seebeck coefficient depend on the relative magnetic configuration in an MTJ, the mechanisms behind them are not the same. While the electric conductance is determined by the transmission probability $T_{P,AP}(E)$ of electrons across the insulating barrier around the Fermi energy E_F , the Seebeck coefficient $S_{P,AP}$ solely depends on the electron-hole asymmetry of $T_{P,AP}(E)$ around E_F . By Onsager reciprocity, the Peltier coefficient Π is closely related to S by $\Pi = ST_0$, where T_0 denotes certain temperature. Using the expression for S [11, 15] we can express Π as

$$\Pi_{P,AP} = -\frac{\int T_{P,AP}(E)(E - E_F)(-\partial_E f_0)dE}{e \int T_{P,AP}(E)(-\partial_E f_0)dE}, \quad (3.1)$$

where e is the elementary charge and f_0 is the Fermi-Dirac distribution function at temperature T_0 . For a constant tunneling current I through the MTJ, the Peltier heat Q_{Π} carried by this current is different for the P and AP configurations, leading to different temperature biases across the junction between the two configurations. Disregarding Joule heating, the temperature difference between the parallel and antiparallel configuration $\Delta T = \Delta T_{AP} - \Delta T_P$ can be estimated by balancing the Peltier heat Q_{Π} with the backflow of the heat current through the junction as

$$\Delta T = \frac{tI}{\kappa_{MgO}A}(\Pi_{AP} - \Pi_P), \quad (3.2)$$

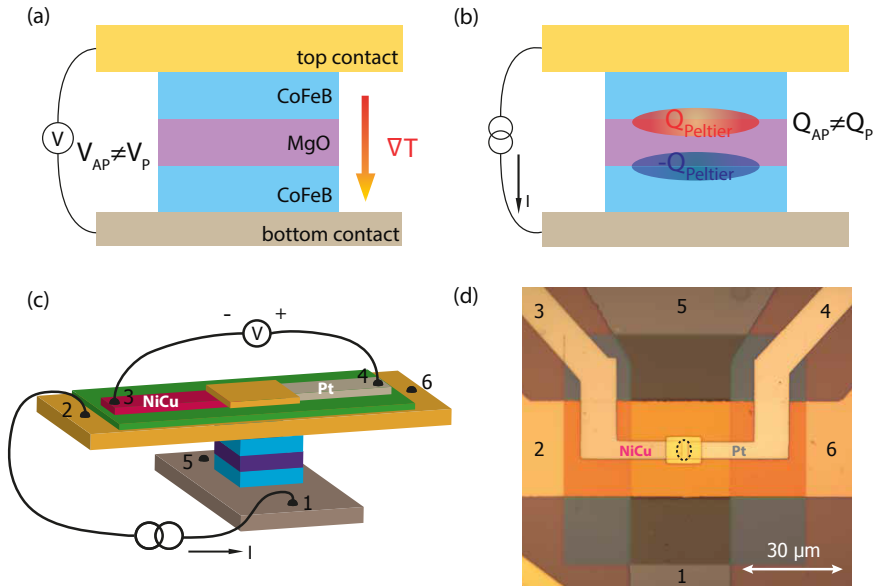


Figure 3.1: Concept and device geometry. (a) Concept of the magneto-Seebeck effect. A temperature gradient is applied across an MTJ, resulting in a Seebeck voltage that is dependent on the magnetic configuration. (b) Concept of the magneto-Peltier effect. A charge current is sent through an MTJ, resulting in a Peltier heating/cooling at the interfaces that also depends on the magnetic configuration. Joule heating is not shown for simplicity. (c) Schematic representation of the measured device. A Pt-NiCu (constantan) thermocouple that is electrically isolated from the top contact by an Al_2O_3 layer (green color) is used to detect temperature changes. In the Peltier measurement, charge current is sent through the pillar (from contact 1 to 2), while recording the voltage over the thermocouple (contacts 3 and 4), as plotted here. Contacts 5 and 6 are used for four-probe TMR measurements. For the reciprocal Seebeck measurement, current is sent through the thermocouple while recording the voltage over the pillar using contacts 1 and 2. (d) Optical microscope image of the measured device. The dotted circle indicates the location of the MTJ. The size of the junction measured in the main text is $2.7 \times 5 \mu\text{m}^2$ by size.

where t is the thickness of the tunnel barrier, κ_{MgO} is the thermal conductivity of the MgO layer¹, and A is the area of the junction. Using the parameters given in Ref. [15], it can be estimated that for an electric current density of $5 \times 10^3 \text{ A/cm}^2$ through the junction, the change in temperature due to the magneto-Peltier effect can reach ~ 100

¹The κ_{MgO} can be assumed to be independent of the magnetic configuration, since the thermal transport through MgO is dominated by phonons (κ_{ph}) instead of electrons (κ_e), given the thickness of the MgO we used (10 monolayers) [27]. In contrast to κ_e , κ_{ph} is not sensitive to magnetic configuration.

μK at room temperature, which requires a sensitive thermometry technique, as we use here.

3.3 Experimental details

3.3.1 Device geometry

Figures 3.1(c) and 3.1(d) show the device geometry and measurement configuration as employed in our experiment. We study the CoFeB/MgO/CoFeB MTJs, the same as in Ref. [15] that are reported to have a large magneto-Seebeck effect [11, 15, 16] due to their half-metallic transmission property [3]. The layer structure of the patterned MTJ sample stack (from bottom to top) is: Si (100)/SiO₂ 500 nm/Ta 15 nm/CoFeB 2.5 nm/MgO 2.1 nm/CoFeB 5.4 nm/Ta 5 nm/Ru 3 nm/Cr 5 nm/Au 25 nm. Detailed fabrication processes can be found in Ref. [15]. To sense the temperature change locally at the top of the junction, a thermocouple consisting of constantan (Ni₄₅Cu₅₅) and Pt is fabricated over the top contact of the MTJ [22, 25, 28]. Constantan is dc sputtered and Pt is *e*-beam evaporated, both 90 nm in thickness. A 50-nm-thick Al₂O₃ layer is *e*-beam evaporated over the top contact to electrically isolate MTJ and thermocouple from the top contact, so that no charge-related effects are picked up by the thermocouple. Finally, an 130 nm layer of Au is deposited to connect the two arms of thermocouple, creating a uniform temperature distribution over the junction. In the Peltier measurement configuration, we send a charge current through the pillar (contact 1 to 2) while recording the thermovoltage using the thermocouple (contact 3 to 4). Note that in this configuration the temperature changes resulting from both the Peltier and Joule heating effects are measured. Meanwhile we also record the tunnel magnetoresistance (TMR) by a four-probe method using contacts 5 and 6. All measurements shown in the main text are performed on a single device at room temperature. Measurements on two other samples can be found in section 3.6.1.

3.3.2 Measurement techniques

A standard lock-in technique is used for our measurements, where an ac current (with an rms value of I_0) is sent through the system at a low excitation frequency (~ 17 Hz), so that a steady-state temperature condition is reached and at the same time capacitive coupling is suppressed. The voltage output from the sample is separated into different harmonic signals (V^{1f}, \dots, V^{nf}) in terms of the input frequency. With this technique it is possible to isolate the Peltier effect that is linear with current from the Joule heating effect that is of second or even higher responses. In a simple case where only V^{1f} and V^{2f} are present, the first-order response ($R_1 I_0$, such as the Peltier effect) is linked to V^{1f} while the second-order response ($R_2 I_0^2$, such as the Joule

heating effect) is linked to V^{2f} . But in a more complex case where higher-order effects are also present [25, 29], the n th-order response ($R_n I_0^n$) is not directly equal to the n th-harmonic signal (V^{nf}); instead, all higher-harmonic signals (with the same parity as n) that are nonzero need to be included by a straightforward algebraic operation, for instance,

$$R_1 I_0 = \sum_{\text{odd } n} n V^{nf}. \quad (3.3)$$

So we can calculate the linear response from different harmonic signals (see section 3.6.2 for details).

3.4 Results and discussion

Figure 3.2 shows the experimental results of the magneto-Peltier measurements. We apply an ac current of $150 \mu\text{A}$ (rms) through the MTJ while sweeping the magnetic field. Both the first and second-harmonic voltages recorded at the thermocouple (V^{1f} and V^{2f}), shown in Figs. 3.2(a) and 3.2(b), exhibit four abrupt changes corresponding to the switching from P to AP configuration and back, implying a change in the temperature at the top contact. V^{1f} of TMR is shown in Fig. 3.2(c). We measure the current dependence of these signals correspondingly, for both the P and AP configurations, as shown in Figs. 3.2(d)-3.2(f). We did not apply ac currents higher than $150 \mu\text{A}$ to avoid a dielectric breakdown of the MTJ ($\sim 2 \text{ V}$ across the junction for 2.1 nm MgO) [30]. In the P configuration we have a simple case where no higher-harmonic signals can be detected, and the V^{1f} (V^{2f}) signal detected at the thermocouple is linear (quadratic) with the current, which can be considered as the Peltier signal (Joule heating signal). However, for the AP configuration, we have a more complex case where higher-order effects are present. The I - V characteristic of the MTJ (see section 3.6.4) is nonlinear with the current in contrast to the linear behavior in the P configuration [31]; in other words, the resistance of the junction R is bias dependent for AP [32–34]. Therefore, the Joule heating effect ($I \cdot V$) is not only present in the second order, but also brings on higher-order responses. The consequence of this nonlinearity is twofold: First, R decreases with both larger positive and negative biases. This leads to even higher-order responses at the thermocouple which deviate the V^{2f} from a quadratic behavior, as shown in Fig. 3.2(e). Second, R also shows an asymmetric dependence for $+I$ and $-I$, i.e., $V(+I) \neq -V(-I)$, indicating that the dissipation at the junction is different when the bias is reversed. The reason for this asymmetry can be attributed to the inevitable difference between the two interfaces across the MgO [34, 35]. Although this effect is only present in higher odd-order heating signals on thermocouple, it mimics a Peltier-like effect and strongly deviates V^{1f} from a linear behavior [see Fig. 3.2(d)]. A more extensive quantitative analysis

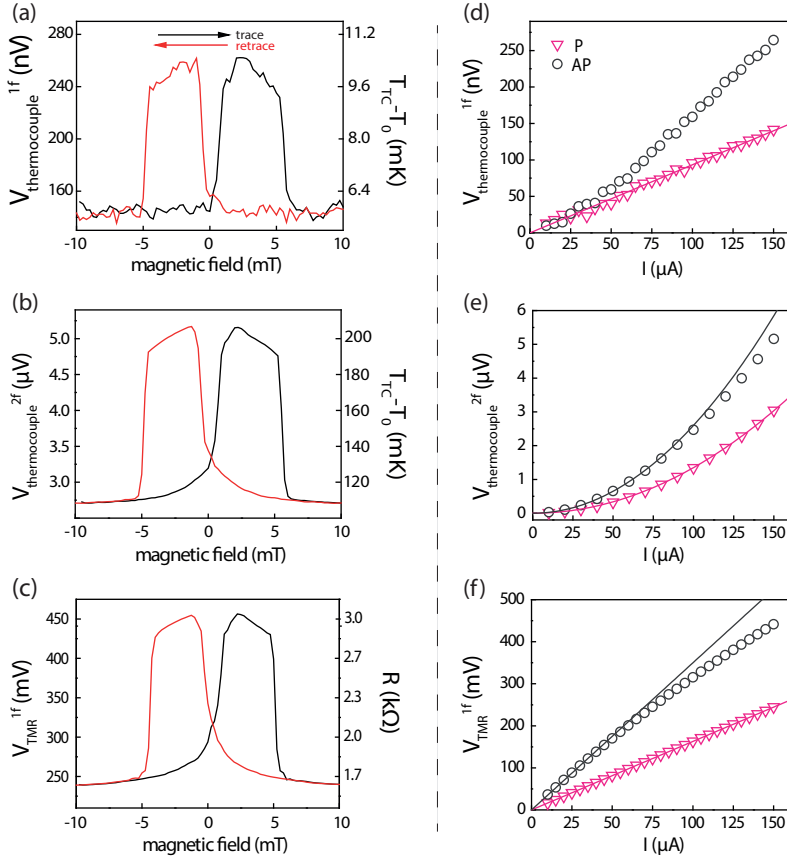


Figure 3.2: Lock-in signals from magneto-Peltier and TMR measurement configurations. (a), (b) First (V^{1f}) and second (V^{2f})-harmonic signal measured at the thermocouple for an rms current of $150 \mu\text{A}$. (c) First (V^{1f})-harmonic signal of TMR measured at the same current. On the right axes the temperature differences detected by the thermocouple relative to the room temperature T_0 are given as $T_{TC} - T_0 = V^{1f(2f)} / (S_{\text{Pt}} - S_{\text{NiCu}})$, where T_0 is 290 K. (d)-(f) Current dependence of the corresponding measurements, for P (open triangles) and AP (open circles) configurations, where P (AP) is obtained when setting the magnetic field at 10 (2) mT. Solid lines are linear [in (d) and (f)] or quadratic fits [in (e)], as references.

can be found in section 3.6.4.

It is therefore important to determine the pure linear signal ($R_1 I_0$) of the AP case in order to discuss the magneto-Peltier effect. Taking advantage of the lock-in detection technique, we can measure the higher-harmonic signals (V^{3f}, V^{5f}, \dots) by tuning the lock-in detection frequency to the corresponding harmonics frequency. The first-order

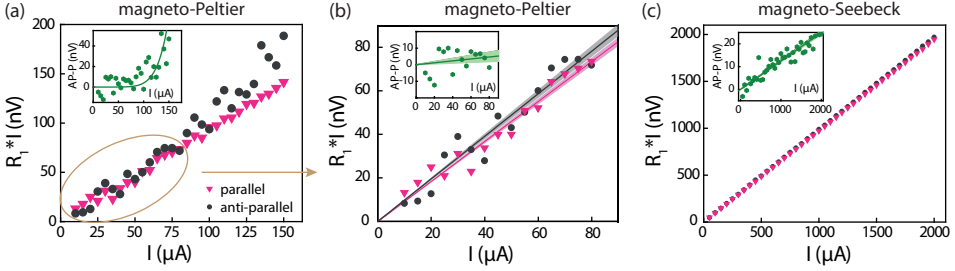


Figure 3.3: Comparison of the magneto-Peltier and magneto-Seebeck linear responses. (a) The extracted linear response calculated up to including the V^{5f} , as a function of applied current. The circled part is where the V^{7f} is close to 0 and is therefore represents pure linear signals. The inset shows the difference between the P and AP configurations which is fitted to a seventh-order behavior. (b) Linear fitting of the circled part in (a). The shaded zones indicate the standard deviations of the fitted slopes. The inset shows the difference between the P and AP configurations which is linearly fitted, with the shaded area indicating one standard deviation. (c) Current dependence of the Seebeck measurements, without any compensations from higher-harmonic signals. The inset shows the difference between the AP and P configurations which is fitted to a linear behavior.

(linear) response can be obtained using Eq. 3.3. Here we only include higher-harmonic signals up to V^{5f} , as V^{7f} cannot be determined accurately within our noise level ($\leq |5 \text{ nV}|$). The results are shown in Fig. 3.3(a). However, the difference between P and AP still shows a seventh-order behavior as a function of the current. This means that, especially at larger currents (above $80 \mu\text{A}$), the seventh-order response is still present; however, the V^{7f} signal that can be measured is only $1/8$ of the seventh-order response, which made it difficult to be included to extract $R_1 I_0$. Nevertheless, we can still rely on the lower-current regime before the onset of the seventh-order response [below $80 \mu\text{A}$, the circled part in Fig. 3.3(a)], which can be regarded as a purely linear regime. We fit the curves for P and AP individually for this regime and especially focus on their difference, which can be considered as the magneto-Peltier effect. Although the difference is small compared to the noise, we fit it linearly and estimate a slope range bounded by one standard deviation, $58 \pm 35 \mu\Omega$, as shown in the inset of Fig. 3.3(b).

To support our estimation of the magneto-Peltier signal, we perform magneto-Seebeck measurements on the same device by effectively reversing the role of the current and voltage contacts as used in the Peltier measurement. Here we send an ac current through the thermocouple (contact 3 to 4) thereby creating a vertical temperature gradient over the MTJ via the Peltier heating/cooling ($\propto I$) at the NiCu-Au and Au-Pt interfaces. The Seebeck voltage (open-circuit thermovoltage) due to this vertical

temperature gradient is measured using contacts 1 to 2. In Seebeck measurements, it is possible to send larger currents up to 2 mA through the thermocouple with a resistance of 190 Ω . Unlike the Peltier measurement, in the Seebeck measurement no higher, odd-harmonic features are observed for either P or AP configuration, implying a linear behavior for the Seebeck signal in the measured current range. This is because the thermocouple is purely ohmic, in contrast to the nonlinear MTJ. The current dependence of the magneto-Seebeck measurements are shown in Fig. 3.3(c). According to the Thomson-Onsager reciprocity relation, the linear response signals for the Peltier and Seebeck effect should be the same, as well as the difference between P and AP configurations [25]. From Fig. 3.3(c), the difference between the two configurations is $12.5 \pm 0.4 \mu\Omega$, which falls into the estimated range of the magneto-Peltier effect within two standard deviations (corresponding to a confidence level of 95%), therefore showing no statistically significant difference. This is consistent with the reciprocity between the magneto-Seebeck and magneto-Peltier measurements. In our opinion, there is no fundamental reason for the rather large difference in the average values for magneto-Peltier and Seebeck coefficients, except for the experimental difficulties in obtaining the magneto-Peltier coefficient. Note that the background signals for Seebeck and Peltier configurations correspond closely, indicating the validity of our approach. However, the backgrounds contain Seebeck or Peltier effects from all metal interfaces, and therefore are not directly linked to the Seebeck or Peltier coefficient of the MTJ.

By using a three-dimensional finite element model (3D-FEM) [36] we can quantify our results. We focus on the estimation of the relative change of the Peltier coefficient from the P to AP configuration of the MTJ. We do not model the electron tunneling process, but regard MgO as a conductor whose electrical conductivity and Peltier coefficient vary between P and AP states, while keeping other properties of the MTJ constant. The details can be found in section 3.6.3. We find that the modeled magneto-Peltier signal is very sensitive to the choice of κ_{MgO} , and the difficulty of measuring this quantity directly can create a big uncertainty in our estimation. Here we adopt the same value from Ref. [15], where $\kappa_{\text{MgO}} = 4 \text{ W}/(\text{m}\cdot\text{K})$ was used for the 2.1-nm MgO layer, taking into account both the crystalline quality of MgO and its thermal interfaces with CoFeB. By fitting to our experimental result $12.5 \pm 0.4 \mu\Omega$ from the Seebeck measurements (which has less statistical uncertainty), we obtain the change of the Peltier coefficient of MgO to be $\Delta\Pi = \Pi_{\text{AP}} - \Pi_{\text{P}} = \Delta S \cdot T = 13.4 \text{ mV}$ from P to AP, which by Onsager relation corresponds to $\Delta S = S_{\text{AP}} - S_{\text{P}} = 46.2 \mu\text{V}/\text{K}$. This is close to the Seebeck coefficient change of MgO reported in Ref. [15]. Note that κ_{MgO} could actually be smaller, as recently suggested by Zhang *et al.* from *ab initio* calculations [27]. In that case, $\Delta\Pi$ would be proportionally lower.

3.5 Conclusions

In conclusion, we have observed the magneto-Peltier effect in magnetic tunnel junctions and confirmed its reciprocity to the magneto-Seebeck effect by measuring both effects in a single device. We also observed higher-order heating effects which greatly enhance the magneto-Peltier signal in the large-bias regime. We attribute this effect to the asymmetric resistance of MTJ for the opposite bias. In addition to providing additional insight in the nature of heat dissipation in MTJs, our results open up the possibility of a magnetically controllable cooling mechanism in MTJs, which can be potentially applied in novel magnetic logic devices. We anticipate that the magneto-Peltier effect could be further increased in lower resistance junctions with a larger contrast of the electron-hole asymmetry of $T(E)$ between the P and AP configurations, perhaps in optimized material systems.

3.6 Supplementary information

3.6.1 Results for two other samples

In the main text, all the measurements shown were performed on a single device, which we here denote as sample A. In this section we show additional measurements performed on two other samples, sample B (Figs. 3.4(a)-3.4(c)) and sample C (Figs. 3.4(d)-3.4(f)). From left to right, V^{1f} and V^{2f} of magneto-Peltier measurements and V^{1f} of TMR measurement are plotted. Similar features are observed compared to Fig. 3.2 in the main text.

3.6.2 Extraction of the linear response from the lock-in measurements

The measurements shown in this paper are all performed using a lock-in detection technique. In this technique, an ac current $I(t) = \sqrt{2}I_0 \sin(\omega t)$ with an angular frequency ω , generated by one of the lock-in amplifiers, is sent to the studied system as an input current. In general, the system output in terms of voltage can be written as:

$$V(t) = R_1 I(t) + R_2 I^2(t) + R_3 I^3(t) + R_4 I^4(t) + R_5 I^5(t) + \dots \quad (3.4)$$

where $R_n I^n(t)$ is the n th-order response and R_n is the n th-order coefficient, which we want to determine. The lock-in technique can separate different harmonic contributions of $V(t)$ according to the orthogonality of sinusoidal functions: it multiplies $V(t)$ by a reference sine-wave signal, with an angular frequency that is an integral

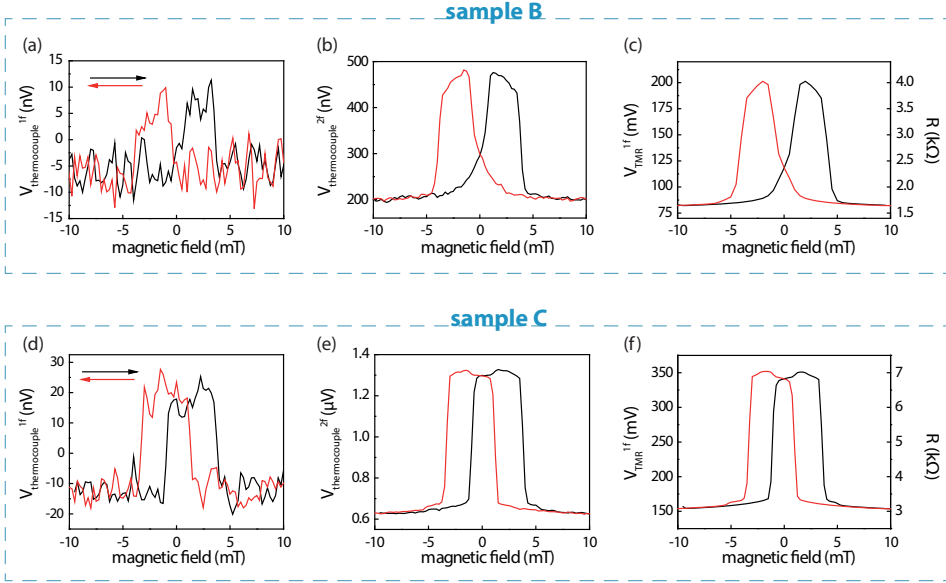


Figure 3.4: Magneto-Peltier and TMR measurements for two other samples. (a)-(c) Measurements on a sample where the junction size is $2.1 \times 3.2 \mu\text{m}^2$. (d)-(f) Measurements on a sample where the junction size is $1.8 \times 3.1 \mu\text{m}^2$. Here the rms current for both measurements is $50 \mu\text{A}$.

(denoted by n) multiple of ω , and then averages this product over time as:

$$V^{nf} = \frac{\sqrt{2}}{T} \int_0^T \sin(n\omega t + \phi) V(t) dt, \quad (3.5)$$

where we can obtain a signal V^{nf} as the n th-harmonic signal directly from the output of the n th lock-in amplifiers. In this way, different harmonic components of $V(t)$ are separated. However, the n th-harmonic signal V^{nf} is often not equal to the n th-order response $R_n I^n(t)$, especially at large current biases where higher-order responses are non-negligible, although it is possible to express one from the other. Assuming we have a voltage response only up to the fifth order, different harmonic signals can

be expressed as:

$$V^{1f} = R_1 I_0 + \frac{3}{2} R_3 I_0^3 + \frac{5}{2} R_5 I_0^5 \quad (\phi = 0^\circ), \quad (3.6a)$$

$$V^{2f} = \frac{1}{\sqrt{2}} (R_2 I_0^2 + 2R_4 I_0^4) \quad (\phi = -90^\circ), \quad (3.6b)$$

$$V^{3f} = -\frac{1}{4} (2R_3 I_0^3 + 5R_5 I_0^5) \quad (\phi = 0^\circ), \quad (3.6c)$$

$$V^{4f} = -\frac{\sqrt{2}}{4} R_4 I_0^4 \quad (\phi = -90^\circ), \quad (3.6d)$$

$$V^{5f} = \frac{1}{4} R_5 I_0^5 \quad (\phi = 0^\circ). \quad (3.6e)$$

It is then possible to find the n th-order response as a linear combination of V^{nf} , for example, for linear response, we have

$$R_1 I_0 = V^{1f} + 3V^{3f} + 5V^{5f}. \quad (3.7)$$

In the magneto-Peltier measurement, we are interested in $R_1 I_0$, which reflects the (magneto-)Peltier effect. By using three lock-in amplifiers to record V^{1f} , V^{3f} and V^{5f} simultaneously, it is possible to determine $R_1 I_0$ using Eq. (3.7). Such calculation has been performed to obtain Fig. 3.3(a) of the main text.

Fig. 3.5 shows different higher-harmonic signals V^{3f} , V^{4f} , V^{5f} and V^{7f} , measured with an rms current of 150 μA on the same sample as the main text, where the higher-harmonic signals are the most prominent in our measured current range. For the odd-harmonic signals, switches from P to AP are visible in V^{3f} and V^{5f} , but not in V^{7f} , as the signal amplitude is already within the noise level. Therefore, it is reasonable to perform Eq. (3.7) to obtain linear response in our results.

For the even-harmonic signals, they are only relevant if we want to obtain even-order responses. Here we present the magnetic field dependence of V^{4f} as shown in Fig. 3.5(b). Taking the contribution of V^{4f} into consideration by using Eq. (3.6b), we can get the second-order response $R_2 I_0^2$ whose dependence on the applied current is close to a quadratic behavior.

3.6.3 Finite element thermoelectric model

To understand the thermoelectric transport properties and extract the Peltier coefficient of the MTJ, we make use of a finite element model [36] that solves the steady-state three-dimensional current and heat equation. In this model the charge current density \mathbf{J} , driven by the applied voltage, and the heat current \mathbf{Q} , driven by the thermal gradient, are related to each other as

$$\begin{pmatrix} \mathbf{J} \\ \mathbf{Q} \end{pmatrix} = - \begin{pmatrix} \sigma & \sigma S \\ \sigma \Pi & \kappa \end{pmatrix} \begin{pmatrix} \nabla V \\ \nabla T \end{pmatrix} \quad (3.8)$$

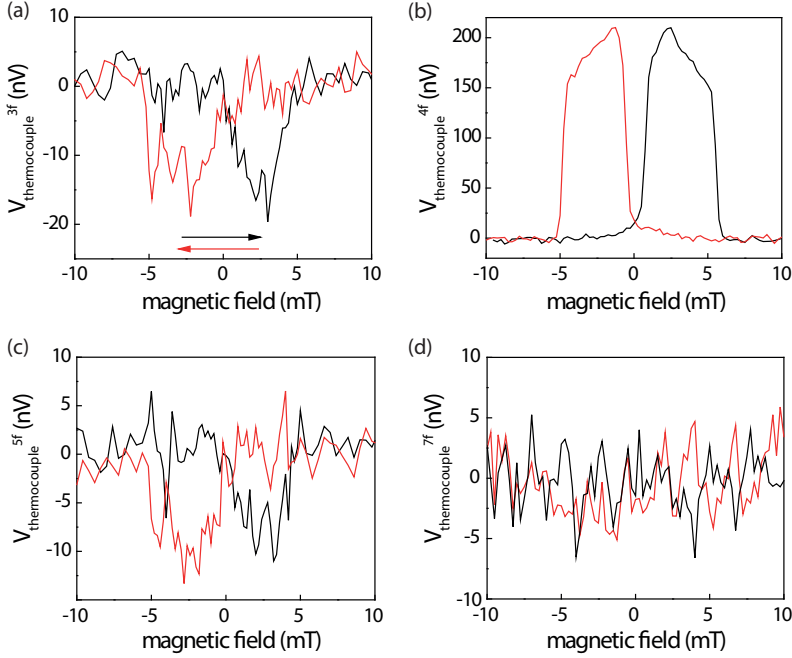


Figure 3.5: Higher-harmonic signals for magneto-Peltier measurement. Magnetic field sweep with Peltier measurement configuration for an r.m.s current of $150 \mu\text{A}$, where (a) V^{3f} , (b) V^{4f} , (c) V^{5f} and (d) V^{7f} are shown.

where σ is the electrical conductivity, S is the Seebeck coefficient, $\Pi = ST_0$ is the Peltier coefficient at any temperature T_0 . Conservation of charge and Joule heating are included as

$$\nabla \cdot \begin{pmatrix} \mathbf{J} \\ \mathbf{Q} \end{pmatrix} = \begin{pmatrix} 0 \\ \mathbf{J}^2/\sigma \end{pmatrix} = \begin{pmatrix} 0 \\ \sigma(\nabla^2 V + S^2 \nabla^2 T + 2S \nabla V \cdot \nabla T) \end{pmatrix} \quad (3.9)$$

The material parameters used in the FEM are shown in Table 3.1. We do not model the tunneling process directly but consider the MgO as a material whose electrical or thermal parameters, such as the conductivity and Peltier coefficient, depend on the magnetic configuration of the MTJ, a similar approach as employed in Ref. [15, 18, 37]. From the four-probe resistance of the MTJ (TMR measurement), we obtain the conductivity for the parallel σ_P and antiparallel configurations σ_{AP} and assign these conductivity values to the MgO barrier. The thermal conductivity of the insulating MgO barrier is estimated to be $4 \text{ W}/(\text{m}\cdot\text{K})$, according to Walter *et al.* [15]. The Peltier coefficient of MgO is then varied to fit our experimental results.

In the following, we describe our approach for extracting the Seebeck (Peltier)

Table 3.1: For Au, Pt and NiCu, σ was measured in dedicated devices [38] and for Ta, σ is obtained from Ref. [39]. The thermal conductivities κ were obtained using the Wiedemann-Franz relation valid at the temperature of our experiment. The rest of the material parameters were taken from Walter *et al.* [15]. For MgO, σ is determined from TMR measurement and S is varied as a fitting parameter.

Material (thickness)	σ (10^6 S/m)	S (μ V/K)	κ (W/(m·K))
Au (130 nm)	27	1.7	180
Pt (90 nm)	4.8	-5	37
Ni ₄₅ Cu ₅₅ (90 nm)	2	-30	20
Al ₂ O ₃ (50 nm)	0	-	0.15
Au top contact (25 nm)	18	1.7	120
CoFeB (5.4 nm, 2.5 nm)	12	-10	87
MgO (2.1 nm)	*	**	4
Ta (1.5 nm)	0.75	-5	5.3
SiO ₂ (500 nm)	0	-	1

coefficient of the MTJ. We first start by obtaining the electrical conductivity of the MgO from the tunnel magnetoresistance measurements. In device A where we observed a TMR of 87.5% (with parallel resistance $R_P=1.6$ k Ω and antiparallel resistance $R_{AP}=3.0$ k Ω) when $I = 150$ μ A, we obtain the corresponding conductivities $\sigma_P=0.093$ S/m and $\sigma_{AP}=0.05$ S/m, respectively. Although the thermal conductance of MgO is expected to depend on the magnetic configuration of the MTJ [13], for simplicity, we do not take this scenario into account. In the estimation of the magneto-Peltier coefficient, we match the measured Peltier signals by varying the magneto-Seebeck coefficient $\Delta S = \Delta S_{AP} - \Delta S_P$. Using the results from earlier studies of Walter *et al.* [15] in similar MTJs (Seebeck coefficient values $S_P = -108$ μ V/K and $S_{AP} = -99$ μ V/K), we obtain a Peltier signal $\Delta V = \Delta V_{AP} - \Delta V_P$ of 0.37 nV for $I = 150$ μ A, which is 5 times smaller than our experimental result (1.9 nV, corresponding to 12.5 $\mu\Omega$). Increasing ΔS by 5 times to 46.2 μ V/K fits our result and gives a $\Delta\Pi$ of 13.4 mV for the magneto-Peltier coefficient of the MTJ.

3.6.4 Joule heating in higher-order responses

In the magneto-Peltier measurements as shown above, non-negligible higher, odd-harmonic signals have been observed, as plotted in Fig. 3.5. In this section, we show that these signals can be ascribed to Joule heating-related mechanisms.

The resistance of an MTJ is in general bias-dependent, i.e., the I - V curve is non-

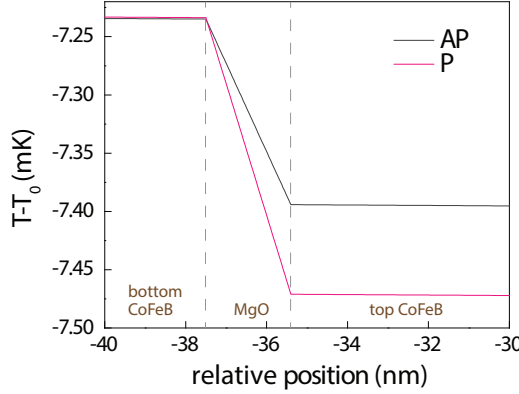


Figure 3.6: A finite element simulation result showing the temperature profiles due to the Peltier effect without including the dissipation. Charge current of $150 \mu\text{A}$ is sent through the MTJ resulting in a Peltier heating/cooling. If the temperature of one side of the junction is anchored, the temperature change due to Peltier effect would be most prominent on the other side. Due to magneto-Peltier effect a different temperature at the top contact will be observed between P and AP configurations. In this figure, $S_{AP} = -99 \mu\text{V/K}$ and $S_P = -145.2 \mu\text{V/K}$ are used. T_0 is taken as 290 K .

linear. The I - V curves we obtain for device A in both the P and AP configurations are shown in Fig. 3.7. They are obtained by integrating the differential resistance dV/dI over current, which is acquired using a modulation technique, where a small ac current ($1 \mu\text{A}$ in rms) is superimposed on a dc bias in the lock-in measurements. For the P case, as can be seen from Fig. 3.7(a) (pink curve), the I - V characteristic is very close to a linear behavior, which is known as a special property for MgO-based MTJs [31]. In this case the MTJ can be regarded as a normal resistor, where the Joule heating (power dissipation) at the junction ($I \cdot V$) is quadratically dependent on the current. For the AP case, however, the I - V curve is nonlinear especially at higher bias (grey curve), and the Joule heating effects would therefore deviate from a quadratic behavior, showing additional higher-order dependences on the current. These additional heating effects thus yield higher-order thermoelectric effects at the thermocouple in the magneto-Peltier measurement.

Suppose the I - V dependence can be expressed as:

$$V(I) = a \cdot I + b \cdot I^2 + c \cdot I^3 + d \cdot I^4 + \dots \quad (3.10)$$

where a , b , c and d are different-order response coefficients. The signal at the thermocouple due to Joule heating can then be written as:

$$V_{\text{thermocouple}}(I) = C \cdot (a \cdot I^2 + b \cdot I^3 + c \cdot I^4 + d \cdot I^5 + \dots) \quad (3.11)$$

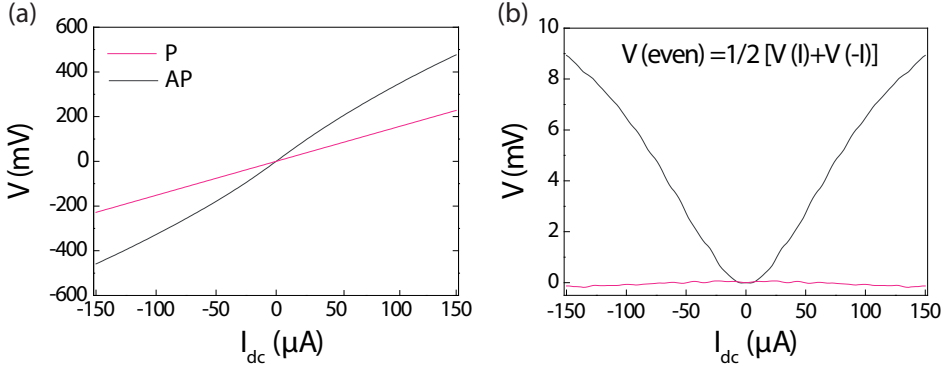


Figure 3.7: (a) I - V characteristics of TMR for P (pink) and AP (grey) configurations, respectively. (b) The even parts of the I - V characteristics extracted for these two configurations.

where C is a coefficient describing the efficiency of the conversion of heat generated in the MTJ to the voltage at the thermocouple, which is in a unit of A^{-1} . Specifically, we are interested in the higher, odd-order responses shown up in the magneto-Peltier measurement, which come from the even parts of the I - V characteristics (related to coefficients b, d, \dots), as can be directly seen from Eq. (3.10) and Eq. (3.11). To discuss them separately, we extract the even parts of the I - V curves, by performing

$$V(\text{even}) = \frac{1}{2}[V(+I) + V(-I)] \quad (3.12)$$

on the I - V curves, with the results shown in Fig. 3.7(b). Note that in Ref. [18], this part of signal is regarded as the magneto-Seebeck signal from the asymmetric temperature profile across the MTJ. Here, however, using our finite element model we find this signal to be too large if explained in that way. We thus interpret the even parts as the intrinsic I - V characteristic of the MTJ, due to the inevitable difference between the two interfaces across MgO.

For P configuration, the I - V curve follows an almost-linear behavior, and the even part is almost negligible compared to the AP configuration. The higher-harmonic signals generated from the P configuration are all around 0 nV. From here, we only discuss the AP case.

Now we calculate the odd Joule heating signal expected at thermocouple that is caused by this even part, by multiplying the coefficient C defined in Eq. (3.11). C can be determined in the much simpler parallel case, by comparing the overall signal on thermocouple which is dominated by Joule heating with the I - V curve. Multiplying C and I with the grey curve in Fig. 3.7(b), we obtain an expected signal as the red solid line shown in Fig. 3.8. This is the expected signal on thermocouple that originates from the even I - V characteristic for the AP configuration due to dissipation.

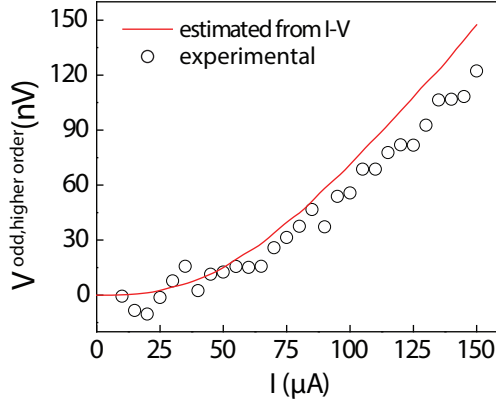


Figure 3.8: Odd Joule heating signal that is expected to show on thermocouple in magneto-Peltier measurement configuration (red curve) and odd responses from magneto-Peltier measurement configuration that are calculated from lock-in measurements (black circles). Only the positive bias is shown.

On the other hand, the odd-order responses can be obtained by performing

$$\begin{aligned} V^{\text{odd-order responses}} &= R_1 I_0 + R_3 I_0^3 + R_5 I_0^5 (+R_7 I_0^7) \\ &= V^{1f} + V^{3f} - V^{5f} (-V^{7f}) \end{aligned} \quad (3.13)$$

on the signals we obtained from lock-in measurements. The V^{7f} is ignored here, as it is too small compared to other signals therefore omitting it does not change the overall analysis. Subtracting the linear response which we already know that originates from Peltier effect, we can get the odd non-linear signals, as plotted in Fig. 3.8 as black circles. It can be seen that the measured signals are very close to the expected values. It suggests that the nonlinear thermoelectric signals are indeed from Joule heating.

In summary, the even component of the TMR I - V curve, that we clearly observe in our measurements, can produce Joule heating that shows higher, odd-order dependence with the current which mimics the magneto-Peltier effect. Note that this implies that Joule heating is different with opposite tunneling current direction, a similar observation as in Ref. [40], though the interpretation we have (based on careful harmonics analysis) is different from theirs (dissipation occurs at different contacts for opposite current direction). By comparing with our lock-in measurement signals detected on thermocouple we conclude that the higher, odd-harmonic signals that we observed are generated by this higher-order Joule heating effect.

References

- [1] T. Miyazaki and N. Tezuka, "Giant magnetic tunneling effect in Fe/Al₂O₃/Fe junction," *Journal of Magnetism and Magnetic Materials* **139**, pp. L231–L234, Jan. 1995.
- [2] S. S. P. Parkin, C. Kaiser, A. Panchula, P. M. Rice, B. Hughes, M. Samant, and S.-H. Yang, "Giant tunnelling magnetoresistance at room temperature with MgO (100) tunnel barriers," *Nature Materials* **3**, pp. 862–867, Dec. 2004.
- [3] S. Yuasa, T. Nagahama, A. Fukushima, Y. Suzuki, and K. Ando, "Giant room-temperature magnetoresistance in single-crystal Fe/MgO/Fe magnetic tunnel junctions," *Nature Materials* **3**, pp. 868–871, Dec. 2004.
- [4] I. Žutić, J. Fabian, and S. Das Sarma, "Spintronics: Fundamentals and applications," *Reviews of Modern Physics* **76**, pp. 323–410, Apr. 2004.
- [5] G. E. W. Bauer, A. H. MacDonald, and S. Maekawa, "Spin Caloritronics," *Solid State Communications* **150**, pp. 459–460, Mar. 2010.
- [6] G. E. W. Bauer, E. Saitoh, and B. J. van Wees, "Spin caloritronics," *Nature Materials* **11**, pp. 391–399, May 2012.
- [7] S. R. Boona, R. C. Myers, and J. P. Heremans, "Spin caloritronics," *Energy & Environmental Science* **7**, pp. 885–910, Feb. 2014.
- [8] A. Slachter, F. L. Bakker, J.-P. Adam, and B. J. van Wees, "Thermally driven spin injection from a ferromagnet into a non-magnetic metal," *Nature Physics* **6**, pp. 879–882, Nov. 2010.
- [9] C. M. Jaworski, J. Yang, S. Mack, D. D. Awschalom, J. P. Heremans, and R. C. Myers, "Observation of the spin-Seebeck effect in a ferromagnetic semiconductor," *Nature Materials* **9**, pp. 898–903, Nov. 2010.
- [10] K. Uchida, J. Xiao, H. Adachi, J. Ohe, S. Takahashi, J. Ieda, T. Ota, Y. Kajiwara, H. Umezawa, H. Kawai, G. E. W. Bauer, S. Maekawa, and E. Saitoh, "Spin Seebeck insulator," *Nature Materials* **9**, pp. 894–897, Nov. 2010.
- [11] M. Czerner, M. Bachmann, and C. Heiliger, "Spin caloritronics in magnetic tunnel junctions: Ab initio studies," *Physical Review B* **83**, p. 132405, Apr. 2011.
- [12] C. Heiliger, C. Franz, and M. Czerner, "Ab initio studies of the tunneling magnetoresistance effect: Influence of magnetic material," *Physical Review B* **87**, p. 224412, June 2013.
- [13] S.-Z. Wang, K. Xia, and G. E. W. Bauer, "Thermoelectricity and disorder of FeCo/MgO/FeCo magnetic tunnel junctions," *Physical Review B* **90**, p. 224406, Dec. 2014.
- [14] C. López-Monís, A. Matos-Abiague, and J. Fabian, "Tunneling magnetothermopower in magnetic tunnel junctions," *Physical Review B* **89**, p. 054419, Feb. 2014.
- [15] M. Walter, J. Walowski, V. Zbarsky, M. Münzenberg, M. Schäfers, D. Ebke, G. Reiss, A. Thomas, P. Peretzki, M. Seibt, J. S. Moodera, M. Czerner, M. Bachmann, and C. Heiliger, "Seebeck effect in magnetic tunnel junctions," *Nature Materials* **10**, pp. 742–746, Oct. 2011.
- [16] N. Liebing, S. Serrano-Guisan, K. Rott, G. Reiss, J. Langer, B. Ocker, and H. W. Schumacher, "Tunneling Magnetothermopower in Magnetic Tunnel Junction Nanopillars," *Physical Review Letters* **107**, p. 177201, Oct. 2011.
- [17] W. Lin, M. Hehn, L. Chaput, B. Negulescu, S. Andrieu, F. Montaigne, and S. Mangin, "Giant spin-dependent thermoelectric effect in magnetic tunnel junctions," *Nature Communications* **3**, p. 744, Mar. 2012.
- [18] Z. H. Zhang, Y. S. Gui, L. Fu, X. L. Fan, J. W. Cao, D. S. Xue, P. P. Freitas, D. Houssameddine, S. Hemour, K. Wu, and C.-M. Hu, "Seebeck Rectification Enabled by Intrinsic Thermoelectrical

- Coupling in Magnetic Tunneling Junctions," *Physical Review Letters* **109**, p. 037206, July 2012.
- [19] J. M. Teixeira, J. D. Costa, J. Ventura, M. P. Fernandez-Garcia, J. Azevedo, J. P. Araujo, J. B. Sousa, P. Wisniewski, S. Cardoso, and P. P. Freitas, "Giant intrinsic thermomagnetic effects in thin MgO magnetic tunnel junctions," *Applied Physics Letters* **102**, p. 212413, May 2013.
- [20] A. Boehnke, M. Milnikel, M. von der Ehe, C. Franz, V. Zbarsky, M. Czerner, K. Rott, A. Thomas, C. Heiliger, G. Reiss, and M. Münzenberg, "On/off switching of bit readout in bias-enhanced tunnel magneto-Seebeck effect," *Scientific Reports* **5**, Mar. 2015.
- [21] L. Gravier, S. Serrano-Guisan, F. Reuse, and J.-P. Ansermet, "Spin-dependent Peltier effect of perpendicular currents in multilayered nanowires," *Physical Review B* **73**, p. 052410, Feb. 2006.
- [22] J. Flipse, F. L. Bakker, A. Slachter, F. K. Dejene, and B. J. v. Wees, "Direct observation of the spin-dependent Peltier effect," *Nature Nanotechnology* **7**, pp. 166–168, Mar. 2012.
- [23] J. Flipse, F. K. Dejene, D. Wagenaar, G. E. W. Bauer, J. B. Youssef, and B. J. van Wees, "Observation of the Spin Peltier Effect for Magnetic Insulators," *Physical Review Letters* **113**, p. 027601, July 2014.
- [24] L. Onsager, "Reciprocal Relations in Irreversible Processes. I.," *Physical Review* **37**, pp. 405–426, Feb. 1931.
- [25] F. K. Dejene, J. Flipse, and B. J. van Wees, "Verification of the Thomson-Onsager reciprocity relation for spin caloritronics," *Physical Review B* **90**, p. 180402, Nov. 2014.
- [26] A. D. Avery and B. L. Zink, "Peltier Cooling and Onsager Reciprocity in Ferromagnetic Thin Films," *Physical Review Letters* **111**, p. 126602, Sept. 2013.
- [27] J. Zhang, M. Bachman, M. Czerner, and C. Heiliger, "Thermal Transport and Nonequilibrium Temperature Drop Across a Magnetic Tunnel Junction," *Physical Review Letters* **115**, p. 037203, July 2015.
- [28] F. K. Dejene, J. Flipse, G. E. W. Bauer, and B. J. van Wees, "Spin heat accumulation and spin-dependent temperatures in nanopillar spin valves," *Nature Physics* **9**, pp. 636–639, Oct. 2013.
- [29] N. Vlietstra, J. Shan, B. J. van Wees, M. Isasa, F. Casanova, and J. Ben Youssef, "Simultaneous detection of the spin-Hall magnetoresistance and the spin-Seebeck effect in platinum and tantalum on yttrium iron garnet," *Physical Review B* **90**, p. 174436, Nov. 2014.
- [30] A. A. Khan, J. Schmalhorst, A. Thomas, O. Schebaum, and G. Reiss, "Dielectric breakdown in Co-Fe-B/MgO/Co-Fe-B magnetic tunnel junction," *Journal of Applied Physics* **103**, p. 123705, June 2008.
- [31] G. X. Miao, Y. J. Park, J. S. Moodera, M. Seibt, G. Eilers, and M. Münzenberg, "Disturbance of Tunneling Coherence by Oxygen Vacancy in Epitaxial Fe/MgO/Fe Magnetic Tunnel Junctions," *Physical Review Letters* **100**, p. 246803, June 2008.
- [32] J. S. Moodera, L. R. Kinder, T. M. Wong, and R. Meservey, "Large Magnetoresistance at Room Temperature in Ferromagnetic Thin Film Tunnel Junctions," *Physical Review Letters* **74**, pp. 3273–3276, Apr. 1995.
- [33] S. Zhang, P. M. Levy, A. C. Marley, and S. S. P. Parkin, "Quenching of Magnetoresistance by Hot Electrons in Magnetic Tunnel Junctions," *Physical Review Letters* **79**, pp. 3744–3747, Nov. 1997.
- [34] S. O. Valenzuela, D. J. Monsma, C. M. Marcus, V. Narayanamurti, and M. Tinkham, "Spin Polarized Tunneling at Finite Bias," *Physical Review Letters* **94**, p. 196601, May 2005.
- [35] C. Heiliger, P. Zahn, B. Y. Yavorsky, and I. Mertig, "Interface structure and bias dependence of Fe/MgO/Fe tunnel junctions: Ab initio calculations," *Physical Review B* **73**, p. 214441, June 2006.
- [36] A. Slachter, F. L. Bakker, and B. J. van Wees, "Modeling of thermal spin transport and spin-orbit effects in ferromagnetic/nonmagnetic mesoscopic devices," *Physical Review B* **84**, p. 174408, Nov. 2011.

- [37] N. Liebing, S. Serrano-Guisan, K. Rott, G. Reiss, J. Langer, B. Ocker, and H. W. Schumacher, "Determination of spin-dependent Seebeck coefficients of CoFeB/MgO/CoFeB magnetic tunnel junction nanopillars," *Journal of Applied Physics* **111**, p. 07C520, Apr. 2012.
- [38] F. L. Bakker, J. Flipse, and B. J. v. Wees, "Nanoscale temperature sensing using the Seebeck effect," *Journal of Applied Physics* **111**, p. 084306, Apr. 2012.
- [39] C. Hahn, G. de Loubens, O. Klein, M. Viret, V. V. Naletov, and J. Ben Youssef, "Comparative measurements of inverse spin Hall effects and magnetoresistance in YIG/Pt and YIG/Ta," *Physical Review B* **87**, May 2013.
- [40] E. Gapihan, J. Hérault, R. C. Sousa, Y. Dahmane, B. Dieny, L. Vila, I. L. Prejbeanu, C. Ducruet, C. Portemont, K. Mackay, and J. P. Nozières, "Heating asymmetry induced by tunneling current flow in magnetic tunnel junctions," *Applied Physics Letters* **100**, p. 202410, May 2012.

Chapter 4

Influence of yttrium iron garnet thickness and heater opacity on the nonlocal transport of electrically and thermally excited magnons

Abstract

We studied the nonlocal transport behavior of both electrically and thermally excited magnons in yttrium iron garnet (YIG) as a function of its thickness. For electrically injected magnons, the nonlocal signals decrease monotonically as the YIG thickness increases. For the nonlocal behavior of the thermally generated magnons, or the nonlocal spin Seebeck effect (SSE), we observed a sign reversal which occurs at a certain heater-detector distance, and it is influenced by both the spin opacity of the YIG/heater interface and the YIG thickness. Our nonlocal SSE results can be qualitatively explained by the bulk-driven SSE mechanism together with the magnon diffusion model. Using a two-dimensional finite element model (2D-FEM), we estimated the bulk spin Seebeck coefficient of YIG at room temperature. The quantitative disagreement between the experimental and modeled results indicates more complex processes going on in addition to magnon diffusion and relaxation, especially close to the contacts.

4.1 Introduction

Magnons, the quanta of spin waves, are collective excitations of electron spin angular momentum in magnetically ordered materials. Recently, magnons entered the field of spintronics [1] as novel spin information carriers, opening the field of magnon spintronics [2]. Just as the study of spin-polarized electric currents, the excitation, transmission, and detection of magnons are of central interest to this field.

Though magnons exist in magnetic materials at any finite temperature below the Curie temperature T_c , following the Bose-Einstein distribution with a zero chemical potential, only the magnons in excess of equilibrium, i.e., the nonequilibrium magnons, can be manipulated and are relevant for spin information encoding and transmission. Nonequilibrium magnons can be excited either coherently or incoherently. Coherent precession of the magnetic moments can be generated by, for

instance, ferromagnetic resonance (FMR) [3] or spin transfer torque (STT) [4–7]. In the frequency spectrum, these excited magnons form a narrow peak, typically in the GHz range.

The alternative incoherent generation of magnons is attractive in that it does not require an external microwave field or a large threshold electric current density, though the frequencies of the excited magnons cannot be well controlled and are spread out in a broad spectrum. One prominent example is the spin Seebeck effect (SSE) [8, 9], the excitation of magnons by a thermal gradient applied to the magnetic material. When the magnon current flows into a neighboring metal with strong spin-orbit coupling, such as platinum (Pt), a charge current is induced as a result of the inverse spin Hall effect (ISHE). Different theories [10–16] were proposed to explain the mechanism of the thermal excitation of the magnons; meanwhile, experimental results [17–24] have revealed its complex nature. In particular, the yttrium iron garnet (YIG) thickness-dependent study [22] indicates the bulk nature of the SSE and shows a finite magnon diffusion length λ_m with an upper limit of $1 \mu\text{m}$ for the YIG grown by liquid phase epitaxy (LPE) at room temperature. The lateral transport of the thermally excited magnons, however, was recently investigated at both room and low temperatures using a nonlocal geometry [25–27]. In both studies relatively long magnon diffusion lengths have been found, one order of magnitude longer than reported in Ref. [22]. A YIG thickness-dependent study of the nonlocal thermal magnon transport is thus necessary to further clarify these issues.

Another way to generate incoherent magnons is spin-flip scattering with a nonequilibrium spin accumulation adjacent to the magnetic material [28–30], for instance, in a spin Hall metal like Pt. A charge current through Pt creates a transverse spin current by the spin Hall effect (SHE), resulting in a spin accumulation at the YIG/Pt interface. Through interfacial exchange interaction, the angular momentum of the conduction electrons is transferred to the magnon system in YIG and thus creating or annihilating magnons, when the orientation of the spin accumulation is parallel or antiparallel to the YIG order parameter. This electrical magnon injection method was first experimentally demonstrated to heat or cool the YIG lattice by magnon-phonon interaction, known as the spin Peltier effect [31]. Recently, Cornelissen *et al.* [25] investigated the transport properties of such magnons using a lateral nonlocal geometry, with another Pt strip serving as a detector. This work demonstrates that incoherent magnons created electrically can also be used as an information carrier on a relatively long length scale, typically about $10 \mu\text{m}$. Later this effect was compared with the spin Hall magnetoresistance (SMR) [32] and also observed in a vertical geometry [33, 34]. In contrast to the auto-oscillation driven by the STT, this method was demonstrated to be a linear process [25, 31, 33, 34] with respect to the injected current. Furthermore, this work is interpreted in terms of nonequilibrium magnons, described by the magnon chemical potential [35]. For the results obtained on a $0.21\text{-}\mu\text{m}$ -thick YIG sample, the

magnon propagation was well described in a diffusive model, driven by the magnon accumulation gradient. To further examine the magnon diffusive picture, the study for different YIG thicknesses is necessary.

In the device structure employed by Cornelissen *et al.* [25], magnons are simultaneously excited both electrically and thermally, and the detection of these two types of magnons can be separated by the linear or quadratic dependence on the injection current. The magnons generated in these two methods exhibited very similar diffusion lengths, showing the same behavior in the long-distance regime. However, their short-distance behaviors are different, owing to the different magnon generation mechanisms. In this chapter, by tuning the spin transparency of the YIG/heater interface from transparent to fully opaque for the spin currents, we associate the behavior of the magnons excited in these two ways also in the short distance regime, further proving their same nature. We also systematically investigate the effect of YIG thickness on the transport of electrically and thermally injected magnons, which allows us to examine the magnon diffusive transport model [35] and the bulk spin Seebeck model [16, 36].

4.2 Experimental details

In our experiment, we used YIG (111) films with different thicknesses grown by LPE on single-crystal $\text{Gd}_3\text{Ga}_5\text{O}_{12}$ (GGG) (111) substrates. The $0.21\ \mu\text{m}$, $1.5\ \mu\text{m}$, $12\ \mu\text{m}$, and $50\text{-}\mu\text{m}$ -thick YIG samples were purchased from Matesy GmbH, and the $2.7\text{-}\mu\text{m}$ -thick YIG sample was provided by the Université de Bretagne in Brest, France. The FMR linewidths are similar among all the YIG samples ($< 2\ \text{Oe}$, measured at $3.1\ \text{GHz}$).

For each set of devices, three Pt strips that are $7\ \text{nm}$ in thickness, typically with size $10\ \mu\text{m}$ (length) \times $100\ \text{nm}$ (width), were sputtered at equal distance d relative to each other. The device geometry is schematically shown in Fig. 4.1(a). For the left strip, we deposited a thin Al_2O_3 layer ($5\ \text{nm}$) by e -beam evaporation before depositing Pt, in order to suppress the spin exchange interaction between Pt and YIG while preserving good thermal conduction. This provides a direct comparison to the right strip, where Pt is directly in contact with YIG. Equally large currents sent through both strips will generate the same Joule heating effects and the same temperature gradients in the YIG, and the only difference is the heater interface opacity for spin currents. Finally, the Pt strips were connected to Ti ($5\ \text{nm}$)/Au ($75\ \text{nm}$) contacts. The devices were not capped by any protection layers, given the good chemical stability of Pt and Au in air. We fabricated multiple sets of devices, with various heater-detector separation distances, ranging from 0.2 to $18\ \mu\text{m}$, on all our YIG samples. All structures were patterned using e -beam lithography. For the long-distance device sets (where $d \geq 2\ \mu\text{m}$), we doubled the lengths of the Pt strips, in order to reduce the geometric effects

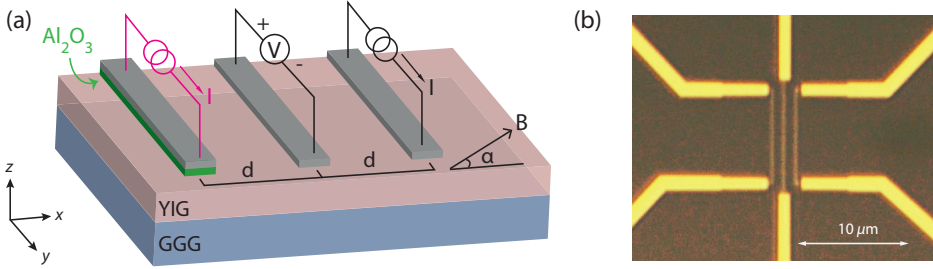


Figure 4.1: (a) Schematic representation of the device structure, where two Pt strips, with and without a thin (5 nm) Al_2O_3 layer underneath, are placed on the sides as injectors, and they share a Pt detector positioned in the middle. The center-to-center distance of the injector and detector is d , and α denotes the angle by which the in-plane magnetic field is applied. The Pt strips are all 7 nm in thickness. (b) The optical microscope image of one device, where the Pt strips are connected to Ti/Au contacts.

4

so that the system can still be approximated to be a 2D problem in the xz plane. The Pt widths were also increased accordingly, to allow for larger currents sent through and therefore boost the signal-to-noise ratio. The nonlocal results for these larger Pt strips were normalized carefully to the aforementioned typical size ¹.

For the measurements, we used a standard lock-in detection technique to separate the linear and quadratic effects, as described in our previous papers [21, 25, 37]. A low-frequency (~ 13 Hz) ac current, typically with an rms value $I_0 = 100 \mu\text{A}$, was sent through either the left or right strip, and the output voltage was nonlocally detected along the middle strip. The sample was rotated in a constant in-plane (xy plane) magnetic field ($B = 10$ mT), large enough to saturate the YIG magnetization [38], and the signal was recorded as a function of the angle α , as shown in Fig. 4.1(a). The output voltage V has both linear and quadratic contributions as $V = I_0 \cdot R_1 + I_0^2 \cdot R_2$, where R_1 and R_2 is the first and second order response coefficient, respectively, and is separated into the first (V^{1f}) and second (V^{2f}) harmonic signals by the lock-in measurement. When the third or even higher harmonic signals are negligible, as we checked is the case for our devices, the first and second harmonic signals are

¹For the electrically injected magnon detection, the V^{1f} signals were first normalized by current, divided by the factor (I/I_0) , where I is the used current and I_0 is the standard current $100 \mu\text{A}$; and then normalized by Pt strip length, divided by the factor (l/l_0) , where l is the used Pt strip and l_0 is standard length $10 \mu\text{m}$. For the thermally excited magnon detection, the V^{2f} signals were first normalized by current, divided by the factor $(I/I_0)^2$, and then normalized to the Pt strip size, divided by the factor $(l/l_0 * w_0/w)$, where w is the used Pt strip width and w_0 is the standard width 100 nm.

proportional to I_0 and I_0^2 , respectively [21, 37, 39]:

$$\begin{aligned} V^{1f} &= I_0 \cdot R_1 \quad \text{for } \phi = 0^\circ \\ \text{and } V^{2f} &= \frac{1}{\sqrt{2}} I_0^2 \cdot R_2 \quad \text{for } \phi = -90^\circ, \end{aligned} \quad (4.1)$$

where ϕ is the phase shift of the signal. V^{1f} thus represents the linear signal where the nonequilibrium magnons are electrically injected via the SHE at the Pt injector and detected nonlocally at the Pt detector via the ISHE, while V^{2f} represents the quadratic spin Seebeck signal from Joule heating, where nonequilibrium magnons are thermally excited, and detected in the same fashion [25].

We also measured the locally generated voltage on the left (Pt/Al₂O₃) and right (Pt-only) strips. The local V^{1f} is in this case the spin Hall magnetoresistance (SMR) signal [38, 40, 41] and V^{2f} the local spin Seebeck signal induced by current heating [21, 42]. For the Pt/Al₂O₃ strips, the local V^{1f} and V^{2f} signals do not show any observable angular variations, indicating the effective suppression of the spin transport through the Al₂O₃ layer. For the Pt-only strips, the magnitudes of the SMR ratio ($\Delta R/R$) collected from different samples all fall in between 2×10^{-4} and 3×10^{-4} . We can thus assume that the interface quality among our YIG samples is comparable. The local SSE results on Pt-only strips are shown in section 4.6.1. All measurements shown in this chapter were performed at room temperature, in ambient atmosphere, unless stated otherwise. As a comparison, one sample was also measured in vacuum. Very similar results were obtained as measured in air, with signal magnitude variations below 15% in the full range of Pt spacing. This indicates that possible heat flow carried away by air is negligible in this experiment.

4.3 Results and discussion

4.3.1 Nonlocal results for electrically injected magnons

We start by presenting the V^{1f} results for various YIG thicknesses. Figure 4.2(a) shows the angular dependent results when using the right-side Pt-only strip as injector, with $d=1 \mu\text{m}$ on different YIG samples. When sending a charge current through the injector, via the SHE a spin accumulation builds up at the bottom of the Pt strip, and its projection on the YIG magnetization will induce nonequilibrium magnons through the interfacial spin mixing conductance. The magnon injection efficiency is therefore proportional to $\cos(\alpha)$, where α is the angle between the spin accumulation direction and the YIG magnetization. The injected magnons diffuse and at the same time relax in the YIG. When part of them successfully reaches the detector, the reciprocal magnon detection process depends on $\cos(\alpha)$ as well, and this

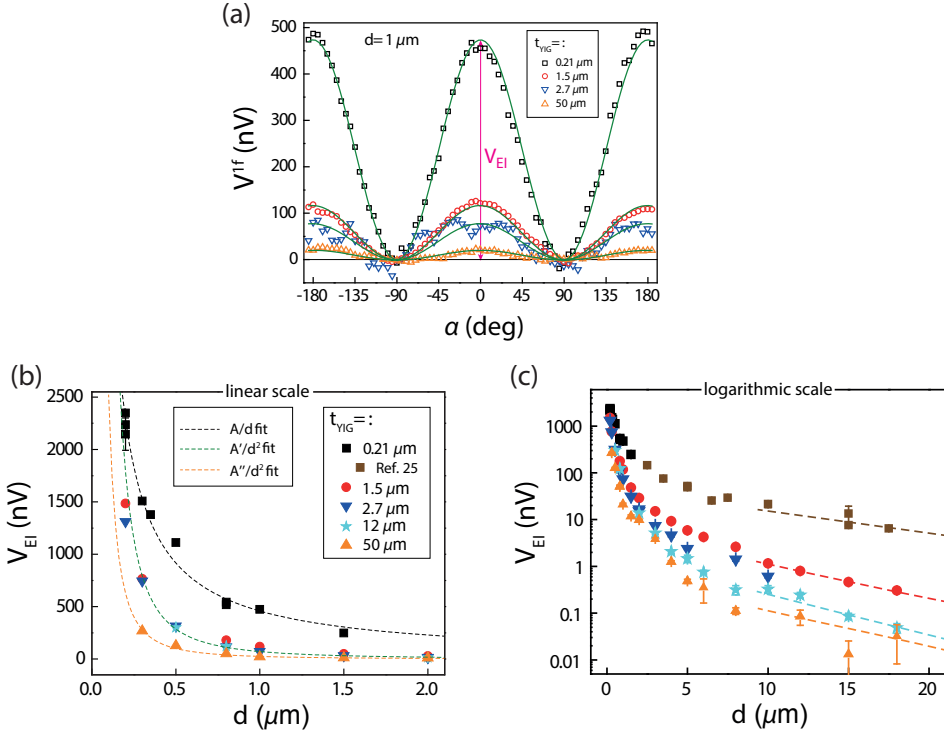


Figure 4.2: The first harmonic signal (V^{1f}) as a function of YIG thickness. (a) V^{1f} as a function of α , at the injector-detector spacing distance $d=1 \mu\text{m}$. The injected current I has an rms value of $100 \mu\text{A}$. The green solid curves are $\cos^2(\alpha)$ fits to the data. V_{EI} is defined as the amplitude of the electrically injected magnon signal. (b),(c) V_{EI} plotted as a function of d for different YIG thicknesses, in linear ($d \leq 2 \mu\text{m}$) and logarithmic scale, respectively. Dashed lines in (b) show the A/d fit and $A'(A'')/d^2$ fits to the data. The data in brown squares in (c) are adapted from Ref. [25] for the sake of completeness. Dashed lines in (c) are the exponential fits using the parameters listed in Table 4.1.

in total gives a $\cos^2(\alpha)$ dependence. The signal thus reaches its maximum when the spin accumulation in Pt is fully (anti)parallel with the external magnetic field ($\alpha = -180^\circ, 0^\circ$, and 180°). We denote V_{EI} , the maximal signal due to electrical injection, as the V^{1f} signal amplitude.

It can be seen from Fig. 4.2(a) that V_{EI} decreases as YIG becomes thicker, at the spacing distance $d = 1 \mu\text{m}$. As we further plot V_{EI} as a function of d for all YIG samples, as shown in Figs. 4.2(b) and (c), we find that V_{EI} decreases monotonically as the YIG thickness increases, for nearly all spacings d . Particularly, for YIG thicker than

Table 4.1: The estimated magnon diffusion length λ_m for different YIG samples. Only the data points where $d > 8 \mu\text{m}$ were used for exponential fits, with the equation $V_{\text{EI}} = A \cdot \exp(-d/\lambda)$, where A is a coefficient that depends on YIG thickness. Given the large uncertainties in the datapoints on $50 \mu\text{m}$ YIG sample, the fitting weights were set to be larger for datapoints with smaller error bars.

YIG thickness (μm)	λ_m (μm)
0.21	9.2 ± 1.0
1.5	6.0 ± 0.3
2.7	-
12	5.0 ± 0.8
50	5.7 ± 3.4

$0.21 \mu\text{m}$, V_{EI} decays faster as a function of d in the short-distance regime. For a clear visualization we only plotted up to $2 \mu\text{m}$ in the linear scale in Fig. 4.2(b). While for $0.21 \mu\text{m}$ V_{EI} exhibits a $1/d$ behavior, as we reported previously [25], for thicker YIG, V_{EI} no longer follows the $1/d$ behavior and can be better fitted with $1/d^2$ functions.

As d becomes larger, the V_{EI} signals can be better described by exponential decays, as can be seen in Fig. 4.2(c). Similar slopes of V_{EI} as a function of d can be observed, which indicates comparable λ_m for all our YIG samples. We take the data points where $d > 8 \mu\text{m}$ for exponential decay fits and extract the λ_m for different YIG samples, listed in Table 4.1. Given that $d = 8 \mu\text{m}$ may not yet be the onset for pure exponential decay, and that the V_{EI} signals for large d gives larger uncertainties, the estimate of λ_m from this method can be inaccurate. Nevertheless, the estimates in Table 4.1 can be regarded as the lower limits of λ_m , as the pure exponential decays may start at a distance even further, which we could not probe due to reaching the noise limit of our detection method. We can conclude that the variance of λ_m is not more than 50% among our samples; in fact, the variance could be actually smaller given the uncertainty from our estimation method. The reduction of the V_{EI} signals for thicker YIG samples, hence, cannot be attributed to the different magnon spin relaxation lengths among our YIG samples.

These observations cannot be fully explained by the magnon diffusive model [35]. From the diffusive picture, if the YIG thickness is increased, but is still much thinner than the magnon diffusion length λ_m , an increase of the V_{EI} would be expected, since from the injector to the detector the magnon channel is widened and hence the magnon conductance is increased. Magnon relaxation in the vertical z direction enters when the YIG thickness becomes comparable to λ_m , in this case of the order of $9 \mu\text{m}$. Increasing the YIG thickness even further would lead to a decrease of the signal, as the relaxation starts to play a more dominant role. This dependence has

been calculated using the 2D-FEM with a magnon diffusion-relaxation model, as shown in Section 4.4.1. In contrast, in our experiment V_{EI} reduces monotonically as the YIG thickness increases from 0.21 μm to 50 μm . Also, the stronger-decay behavior in the short-distance regime for thicker YIG samples cannot be fully explained.

When using the left-side Pt/ Al_2O_3 strip as injector, the V^{1f} signals do not show any observable angular dependences, as expected. This further confirms that the spin current through the YIG/Pt interface indeed plays a crucial role in this linear effect and that the interface becomes fully opaque with a thin Al_2O_3 layer inserted in between.

4.3.2 Nonlocal results for thermally generated magnons

The effect of the heater interface transparency

Now we move to the V^{2f} results, which represent the nonlocal signals of the thermally generated magnons, or the nonlocal SSE. The Joule heating effect of the injected current through the injector creates a radial temperature gradient in the YIG and GGG substrates, as shown in Figs. 4.3(a) and 4.3(b). Firstly, in this subsection, we show the strong influence of the heater interface transparency on nonlocal SSE signals by comparing the results between sending currents through the Pt-only strip and the Pt/ Al_2O_3 strip. We consider the heater interface in Fig. 4.3(a) to be transparent, though not fully, due to the finite effective spin mixing conductance between Pt and YIG [38, 40, 41, 43, 44]. On the other hand, the heater interface with the insertion of the Al_2O_3 layer is regarded to be fully opaque without any spin current flowing between Pt and YIG through the Al_2O_3 layer (Fig. 4.3(b)). The temperature profiles with and without the Al_2O_3 layer are very comparable, given that the Pt strips are identical and that the Al_2O_3 layer is thin (5 nm). It has been checked in the 2D-FEM that the temperature profile ($T - T_0$, where T is the lattice temperature and T_0 is the room temperature) varies not more than 3% locally and 0.02% nonlocally with the insertion of the Al_2O_3 layer (see section 4.6.1).

The results for the device sets on the 0.21 μm YIG sample are presented in Fig. 4.3. Figure 4.3(c) shows the angular dependence for the measured V^{2f} when d is 200 nm, for both the two heating configurations where the current is sent through the Pt/ Al_2O_3 or Pt strip. Both curves show a $\cos(\alpha)$ behavior, which is governed by the ISHE at the detector. Strikingly, for the same distance, same heating power, the V^{2f} signals for the two heating configurations differ by a factor of three. Even more interestingly, when d is 300 nm, the V^{2f} signals of the two heating configurations are opposite in sign, as shown in Fig. 4.3(d). Given that the only difference between the two configurations is the heater transparency, it can be inferred that the thermally generated magnon flow does not only rely on the temperature profile, but is also

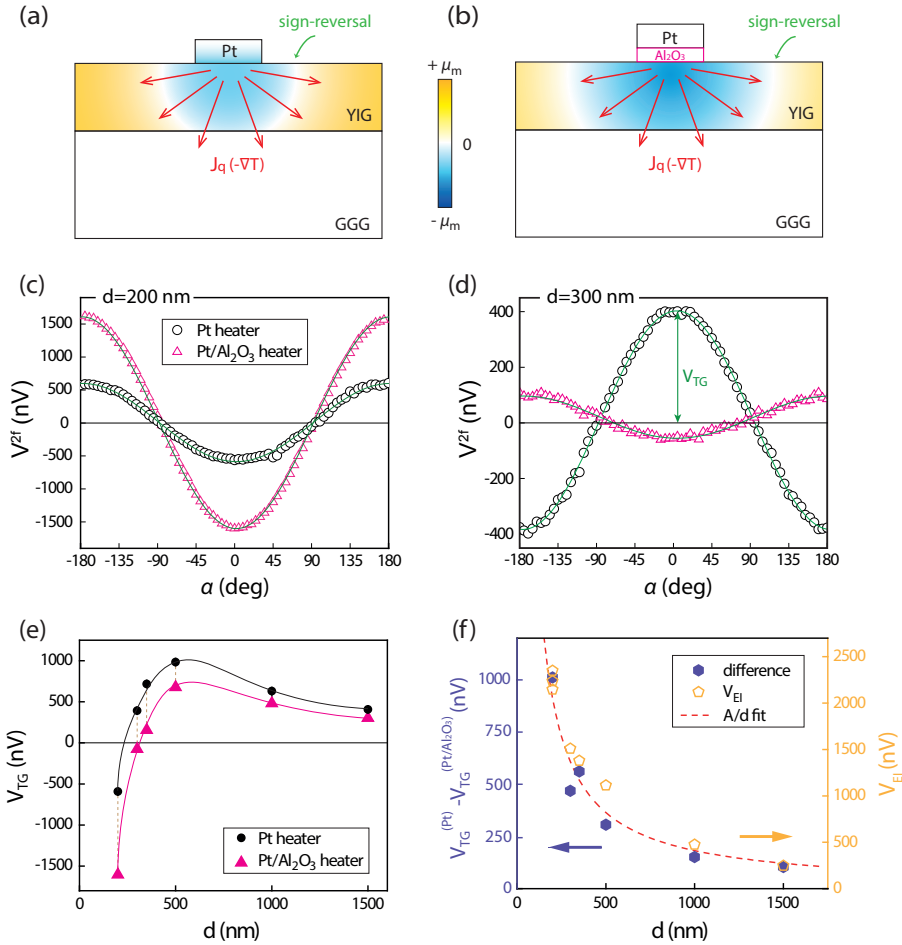


Figure 4.3: The nonlocal detection of the thermally generated magnons for the $0.21 \mu\text{m}$ YIG sample. (a),(b) Schematic cross-section view of the magnon accumulation μ_m profile under a radial temperature gradient, when current is sent through (a) the Pt heater or (b) Pt/Al₂O₃ heater, respectively. Red arrows represent heat flows J_q , and $+$ ($-$) μ_m denotes magnon accumulation (magnon depletion) in yellow (blue). (c),(d) Second harmonic signal V^{2f} as a function of α , with an rms injection current of $100 \mu\text{A}$. In these plots the heater-detector distance is 200 nm and 300 nm, respectively. The black circles and pink triangles show results when the current is sent through either the Pt-only or the Pt/Al₂O₃ strip. Solid green curves are the $\cos(\alpha)$ fits. V_{TG} are defined as the amplitude of the thermally excited, nonlocal SSE signal. (e) V_{TG} as a function of the heater-detector distance for both heating configurations. Solid curves are guidelines for the eyes. (f) The difference of the V_{TG} between the two heating configurations (solid purple polygons) compared with the electrically injected signal V_{EI} (open yellow polygons). Both of them follow the $1/d$ behavior.

sensitive to the heater opacity at some distance away.

The difference between the two heating configurations can be seen more clearly in the distance dependence data. We define V_{TG} , the maximal signal due to thermal generation, as the magnitude of V^{2f} , and plot it for both heating configurations as a function of d in Fig. 4.3(e). Note that the negative sign of V_{TG} corresponds to the same sign as the SSE signal measured locally. For the Pt heater series, a sign reversal of the V_{TG} occurs when d is in between 200 and 300 nm, consistent with the results we reported in Ref. [25], though in this study the YIG sample is from a different provider. For the other Pt/Al₂O₃ heater series, the sign reversal of V_{TG} occurs at a slightly further distance, between 300 and 350 nm. In fact, for each d , the signals obtained from heating the Pt/Al₂O₃ strip are always more negative than for heating the Pt-only strip. These results strongly indicate that the thermally generated magnon current is not only determined by the temperature profile, but also sensitive to the boundary conditions that modify the magnon currents.

These observations can be described by the concept of a bulk SSE theory [15, 16, 35]. An analytical description can be found in section 4.6.3. According to this theory, a heat flow J_q in YIG will excite a thermal magnon flow $J_{m,q}$ along with it, related by the bulk spin Seebeck coefficient S_S :

$$J_{m,q} = -\sigma_m S_S \nabla T \propto J_q = -\kappa \nabla T, \quad (4.2)$$

where σ_m is the magnon conductivity and κ is the thermal conductivity of YIG. While the heat flow is continuous through the boundaries, the magnon flow stops, resulting in the buildup of magnon accumulations μ_m , opposite in sign for the YIG/heater and YIG/GGG boundaries. The positive μ_m corresponds to more magnons in excess of equilibrium, hence magnon *accumulation*, and the negative μ_m corresponds to fewer magnons as compared to equilibrium, hence magnon *depletion*. This picture is analogous to the traditional Seebeck effect in conductive systems, where positive and negative charge voltages are built up as a result of a temperature gradient.

A diffusive magnon flow $J_{m,diff}$ is induced to balance the thermal magnon flow, until the system reaches a steady state:

$$J_{m,diff} = -\sigma_m \nabla \mu_m. \quad (4.3)$$

The total magnon current ($J_m = J_{m,diff} + J_{m,q}$) hence includes both the thermal and diffusive parts, and relaxes on the length scale of λ_m :

$$\nabla \cdot \mathbf{J}_m = -\sigma_m \frac{\mu_m}{\lambda_m^2}. \quad (4.4)$$

In our device geometry, owing to the radial temperature gradient, an intensive negative μ_m builds up beneath the heater, surrounded by the sparsely distributed

positive μ_m (supposing a positive S_S), as shown in Figs. 4.3(a) and 4.3(b). When placing a Pt detector nonlocally at the YIG surface, the Pt detector then serves as a spin sink, extracting or injecting a certain magnon flow, depending on the sign of the μ_m at that position. The nonlocal signal would hence first probe the negative μ_m for shorter d and then the positive μ_m for longer d , reversing sign in between.

Changing the transparency of the YIG/heater interface will influence the amount of negative μ_m below the heater and thus tune the sign-reversal distance. Compared to the fully opaque YIG/heater interface for the Pt/Al₂O₃ heater series, the transparent YIG/Pt interface allows for certain magnon flow into the heater via the spin mixing conductance, hence a less negative μ_m will be preserved beneath the heater. Consequently, the sign-reversal occurs at a shorter d , closer to the heater [see Fig. 4.3(a)]. The fully opaque interface thus corresponds to the furthest sign-reversal distance, as shown in Fig. 4.3(b). Our results confirm the fact that, in addition to the temperature profile, the magnon accumulation and the magnon current are essential in the spin Seebeck picture.

Remarkably, the difference of the signals from the two heating configurations exhibits a $1/d$ behavior, similar to the electrical injection induced signal (V_{EI}) shown in the previous section, as plotted in Fig. 4.3(f). This can also be explained by the bulk SSE picture: In comparison with the Pt heating series, the Pt/Al₂O₃ heating series has an extra negative μ_m beneath the heater. It can be compared with the nonequilibrium magnons created by electrical injection at the injector. The fact that both of them can be fitted to a $1/d$ behavior suggests that magnons generated thermally and electrically are very similar in nature.

At first sight, our results could be reminiscent of the transverse SSE experiments performed by Uchida *et al.* [9] with the sign-reversal feature. It is important to point out a fundamental difference between the two experiments: In our experiment the spatial variation of μ_m can only be observed a few times of λ_m away from the heater, whereas in Ref. [9] the SSE signal is varying throughout the whole YIG in the range of a few millimeters, which cannot be explained in the magnon diffusive framework with the so-far reported λ_m in YIG [22, 25, 26, 45]. Our results hence do not share the same origin as the transverse SSE.

The effect of the YIG thickness

Apart from the transparency of the YIG/heater interface, varying the YIG thickness is also expected to influence the nonlocal spin Seebeck signals, due to the bulk nature of the SSE [15, 16, 22]. Figure 4.4 shows the measured V_{TG} results on a 2.7- μm -thick YIG sample. As can be immediately seen, the sign-reversal distances of V_{TG} [Fig. 4.4(b)] for both heating configurations are much further away from the heater, around 5 μm as shown in the inset, compared with the 0.21 μm YIG sample [Fig. 4.3(e)]. In addition,

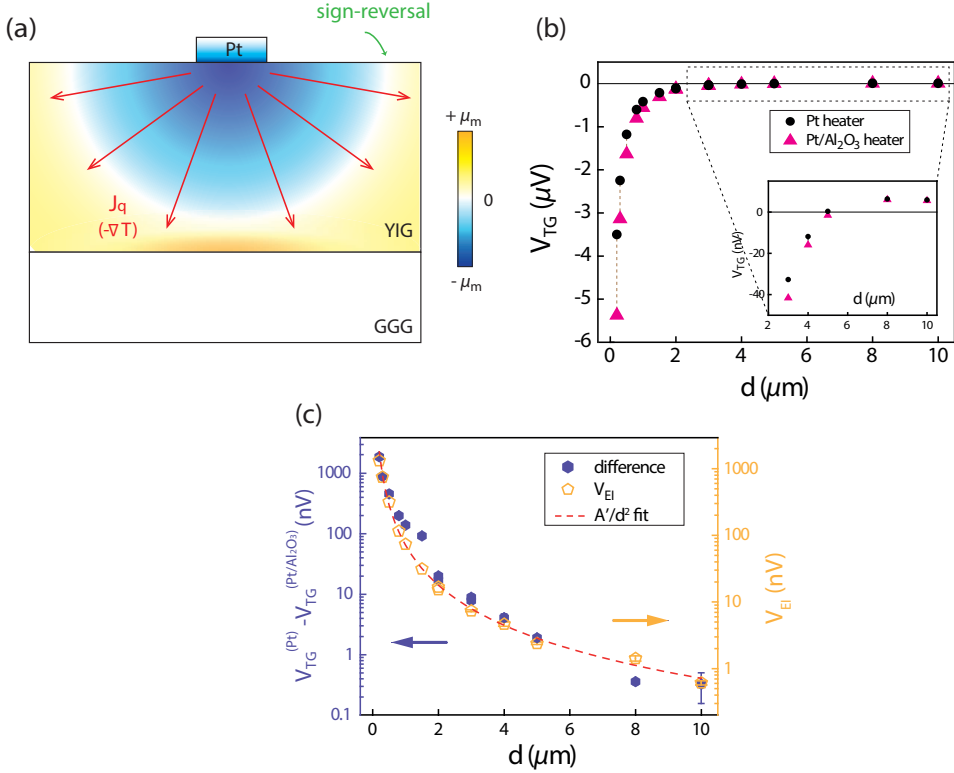


Figure 4.4: The nonlocal detection of the thermally generated magnons for the $2.7 \mu m$ YIG sample. (a) Schematic cross-section view of the magnon accumulation μ_m profile under a radial temperature gradient, when the YIG thickness is increased. Larger magnon accumulations are present at both the YIG/heater and YIG/GGG boundaries, compared to the situation for thinner YIG. (b) V_{TG} as a function of the heater-detector distance for both heating configurations. Inset zooms in for longer-distance data and shows the sign-reversal behavior. (c) The difference of V_{TG} between the two heating configurations compared with the electrically injected signal V_{EI} , plotted in logarithmic scale.

for the very short distances, as when $d = 200$ nm, the SSE signals of the thicker YIG are a few times larger compared with the thinner YIG, for both heating configurations. It is interesting to point out that the local SSE signals we measured on the Pt-only strips do not show such a big difference between the $0.21 \mu m$ YIG and $2.7 \mu m$ YIG (see section 4.6.2 for more discussion).

The different behavior of V_{TG} with varying YIG thickness can be understood as follows: When YIG becomes thicker, the positive and negative μ_m will be separated

further and have a smaller counter effect to each other. As a result, both the positive and negative μ_m will increase, and the positive μ_m will be pushed further away from the heater, more sparsely distributed at a larger YIG volume, as shown in Fig. 4.4(a). Therefore, the sign-reversal distance becomes larger as the YIG thickness increases.

One common feature is observed for both 0.21 and 2.7 μm YIG samples: For all distances, the signals from the Pt/Al₂O₃ heater series are more negative than the Pt-only heater series. For the 2.7 μm YIG sample, we can also plot the difference between the two heater series as a function of d , shown in Fig. 4.4(c). Its shape matches with the V_{EI} signal; both can also be described by a $1/d^2$ behavior. This observation proves again the similar nature for the electrically and thermally excited magnons.

More results from other YIG samples with different thicknesses are shown in Fig. 4.5, in logarithmic scale (plots in linear scale can be found in section 4.7). In this plot we include the results for a third measurement configuration: sending current through the Pt/Al₂O₃ heater, and measuring voltage at the right Pt strip, which in this case serves as the detector. This measurement configuration enables us to probe twice as far distance data for our present devices, and investigate the effect of a Pt absorber (the middle Pt strip) in between the heater and detector for nonlocal SSE. Comparing the results from this configuration (star-shaped symbols) and the Pt/Al₂O₃ heater series in Fig. 4.5, we can conclude that there is only a small reduction, mostly within 10%, when there is a Pt absorber present in between. It is therefore reliable to include this series to look at how the V_{TC} decay as a function of d for the long-distance regime. It can be seen from Fig. 4.5 that for all YIG samples the exponential decay rates are comparable. Using the data points where $d > 8 \mu\text{m}$ in the exponential fits, we obtain λ_m of $7.5 \pm 0.5 \mu\text{m}$ for the 1.5 μm YIG sample and $11.1 \pm 0.3 \mu\text{m}$ for the 50 μm YIG sample. Comparing with the 0.21 μm sample which gives a λ_m of $9.6 \pm 1.0 \mu\text{m}$, this further proves the fact that for a long- d regime, λ_m is not varying by more than 22% among different thick YIG samples.

We can also plot the sign-reversal distance as a function of YIG thickness, as shown in the inset of Fig. 4.5. As expected, the sign reversal takes place at a further distance for thicker YIG. The trend can be fitted to a linear dependence, and the sign-reversal distance is around 1.6 times the YIG thickness. Additionally, for the 50 μm YIG sample, we observed a sign reversal between $d = 60 \mu\text{m}$ and $d = 80 \mu\text{m}$. Due to the relatively large uncertainty for the sign-reversal distance we did not include it for the linear fitting, but it agrees with this dependence as well.

4.4 Finite element modeling results

Using a 2D steady-state FEM allows us to quantitatively compare our results with the theory. In this section, we present the 2D-FEM results for the nonlocal behavior of

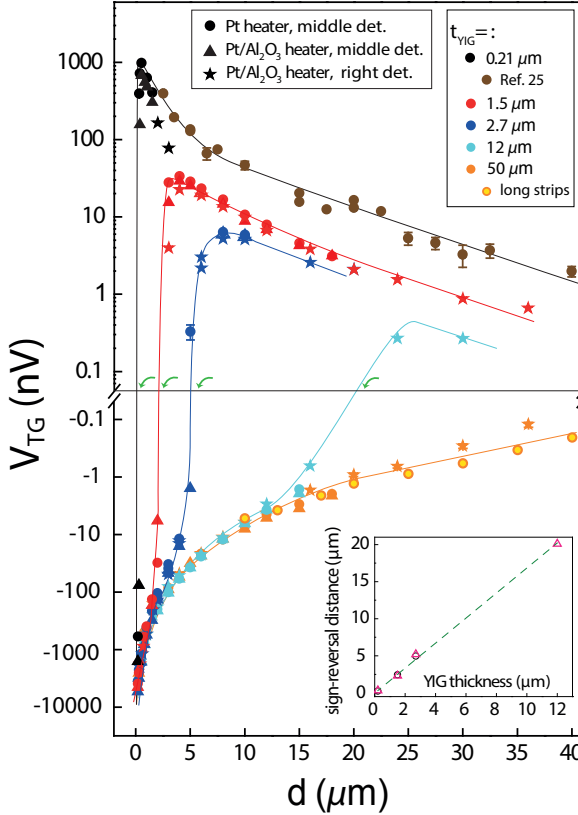


Figure 4.5: Nonlocal V_{TG} results as a function of d for different YIG thicknesses (indicated by symbol colors) and heating configurations (indicated by symbol shapes), plotted in a logarithmic scale. The data from the third heating configuration, where current is sent through the left Pt/Al₂O₃ strip and voltage is measured at the right Pt strip, are shown in this figure with star shaped symbols for all YIG samples. The orange circles with yellow color filling stand for a data series that was obtained on a 50 μm YIG sample with 8 ± 1 nm-thick Pt strips, and measured in vacuum. For this series, the length of the Pt strips (100 μm) is much longer than for the other samples on the 50 μm YIG sample, so that the edge effects of the Pt injectors and absorbers can be reduced. The brown circles are adapted from Ref. [25] for the sake of completeness. Solid curves are guidelines for the eyes, and green arrows indicate sign reversals. Inset plots the sign-reversal distance as a function of the YIG thickness.

the electrically and thermally injected magnons in the framework of a pure magnon diffusive model [35], where the magnon current is driven by the nonequilibrium magnon accumulation μ_m .

4.4.1 Electrically injected magnons

First we discuss the transport of the electrically injected magnons. The model solves in the whole geometry the magnon (spin) transport equation

$$\mathbf{J}_m = -\sigma_m \cdot \nabla \mu_m, \quad (4.5)$$

where \mathbf{J}_m is the magnon current density, σ_m is the magnon spin conductivity, and μ_m is the magnon (spin) accumulation. The relaxation of the magnons is described by the Valet-Fert equation [46, 47]

$$\nabla \cdot \mathbf{J}_m = -\sigma_m \frac{\mu_m}{\lambda_m^2}. \quad (4.6)$$

This equation is applied to the whole geometry shown in Fig. 4.6. The interface is modeled as a layer with thickness $t_{\text{interface}}$ equal to 1 nm [35]. The spin conductivity of the interface is then $g_S \cdot t_{\text{interface}}$, where g_S is the effective spin mixing conductivity [28, 31, 35].

The SHE and ISHE processes in the Pt are not included in the model but calculated analytically. The spin accumulation at the bottom of Pt created by the SHE is denoted by $\mu_{s,\text{inj}}$, and is calculated as [31, 41]

$$\mu_{s,\text{inj}} = \frac{2e}{\sigma_{\text{pt}}} \cdot \lambda_{\text{pt}} \cdot \theta_{\text{SH}} \cdot J_c \cdot \tanh\left(\frac{t_{\text{pt}}}{2\lambda_{\text{pt}}}\right), \quad (4.7)$$

where e is the electron charge, and t_{pt} , λ_{pt} , and σ_{pt} are the thickness, spin diffusion length, and electrical conductivity of Pt, respectively; θ_{SH} is the spin Hall angle of the

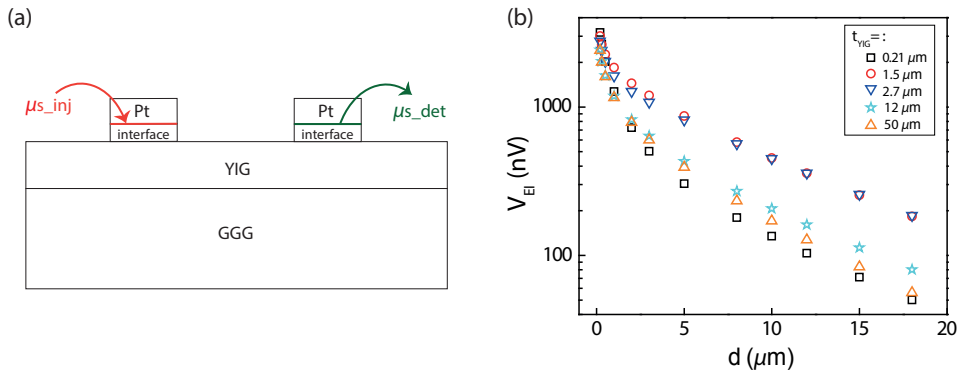


Figure 4.6: The calculated V_{EI} results as a function of d for different YIG thicknesses. (a) Schematic illustration of geometry that was employed in the model. The injected spin voltage $\mu_{s,\text{inj}}$ is set as a Dirichlet boundary condition, and the spin voltage at the detector $\mu_{s,\text{det}}$ is extracted from the calculation. (b) The modeled V_{EI} results plotted on a logarithmic scale.

Table 4.2: Material parameters that were used in the model. σ_e and σ_s (σ_m) is the electron and spin (magnon) conductivity, respectively. For the YIG/Pt interface, the spin conductivity σ_m is calculated by $\sigma_m = g_S \cdot t_{\text{interface}}$, where g_S is the effective spin mixing conductance [31] and was estimated in our recent work [35]. The other parameters of the YIG/Pt interface are assigned to be the same as YIG. Note that the spin conductivity of a paramagnetic metal, such as Pt, is half of its electrical conductivity [41]. The spin Hall angle of Pt θ_{SH} is taken as 0.11 [14, 31, 35].

Material (thickness)	σ_e (S/m)	σ_s (σ_m) (S/m)	κ (W/(m·K))	λ (m)
Pt (7 nm)	$2.5 \cdot 10^6$	$1.25 \cdot 10^6$	26	$1.5 \cdot 10^{-9}$
YIG/Pt interface (1 nm)	-	$0.96 \cdot 10^4$	6	$9.4 \cdot 10^{-6}$
Al ₂ O ₃ (5 nm)	-	-	0.15	-
YIG (various thickness)	-	$5 \cdot 10^5$	6	$9.4 \cdot 10^{-6}$
GGG (500 μm)	-	-	8	-

Pt, and J_c is the injected electric charge current density, equal to 1.43×10^{11} A/m². $\mu_{s,\text{inj}}$ serves as the input of the model.

The output of the model is extracted from the spin accumulation $\mu_{s,\text{det}}$ at the detector. Following the derivation from Ref. [44], The induced ISHE electrical voltage, which equals V_{EI} here, is expressed as

$$V_{\text{ISHE}} = \frac{1}{2e} \cdot \frac{L_{\text{Pt}}}{t_{\text{Pt}}} \cdot \theta_{\text{SH}} \cdot \frac{(1 - e^{-\frac{t_{\text{Pt}}}{\lambda_{\text{Pt}}}})^2}{1 + e^{-\frac{2t_{\text{Pt}}}{\lambda_{\text{Pt}}}}} \cdot \mu_{s,\text{det}}, \quad (4.8)$$

where L_{Pt} is the length of the Pt strip. To be consistent with our previous calculations, for all parameters, we take the same values as used in Ref. [35], except for the σ_{Pt} which is 2.5×10^6 S/m extracted from the average Pt resistance from the measured Pt strips. The used material parameters are listed in Table 4.2.

The calculated results for different YIG thicknesses are shown in Fig. 4.6(b). The modeled results do not show the same trend as the experimental results: Except for the datapoints at very short d , the modeled signals increase first with increasing the YIG thickness, when the YIG thickness is still much smaller compared to λ_m . Further increase of the YIG thickness leads to the reduction of V_{EI} , as the magnon relaxation in the vertical direction starts to play a role. This trend is different from the monotonic decrease of the V_{EI} with the increase of YIG thickness, as observed experimentally. Moreover, in the short- d regime, the modeling results cannot capture the sharp decrease of the signals as observed experimentally for thicker YIG samples.

These discrepancies between the modeling and experiments indicate the limits of a model based on magnon spin accumulation only, and may call for additional

shorter length scales in the short-distance regime, such as the magnon-phonon and other relaxation lengths introduced in Ref. [35]. Close to the injector the magnon diffusion may be characterized by a shorter length scale². This scenario can explain the significant drop of the V_{EI} from 0.2 μm to 1.5 μm YIG samples, as 0.2 μm is still within or comparable to this shorter length scale but 1.5 μm far exceeds it, resulting in more magnon relaxation. The vertical relaxation thus begins at much thinner YIG than modeled. The faster decay of the V_{EI} in thicker YIG samples could also be understood when taking into account another shorter length scale. More discussions can be found in Section 4.4.3.

4.4.2 Thermally generated magnons

We can also use the 2D-FEM to obtain a quantitative picture of the nonlocal behavior for the thermally generated magnons.

We consider the magnon spin current flow and the heat flow, related to their driving forces as [35]:

$$\begin{pmatrix} \mathbf{J}_m \\ \mathbf{Q} \end{pmatrix} = - \begin{pmatrix} \sigma_m & \sigma_m S_S \\ \sigma_m S_S T & \kappa \end{pmatrix} \begin{pmatrix} \nabla \mu_m \\ \nabla T \end{pmatrix} \quad (4.9)$$

where S_S is the bulk magnon Seebeck coefficient that is only nonzero for YIG, and we assume it to be the same for different YIG thicknesses, as an intrinsic material parameter. The source terms of the two current flows are

$$\nabla \cdot \mathbf{J}_m = -\sigma_m \frac{\mu_m}{\lambda_m^2} \quad \text{and} \quad \nabla \cdot \mathbf{Q} = \frac{J_c^2}{\sigma_{\text{pt}}}, \quad (4.10)$$

where the first equation stands for the magnon relaxation, and the second equation represents the Joule heating effect. The Joule heating only takes place in the heater and serves as the input in the spin Seebeck scenario. The output of the signal is also extracted from the $\mu_{\text{s,det}}$ at the detector, from which the ISHE voltage is calculated using Eq. 4.8.

The modeled results are shown in Fig. 4.7, with S_S taken as 4.5 $\mu\text{V}/\text{K}$ for all YIG samples. The fitting for the long- d range is satisfactory, where only the magnon diffusion and relaxation take place, and the V_{TG} exhibits pure exponential decay. From the Pt heater series on 0.21 μm YIG (Fig. 4.7(c)), we can determine the value of S_S to be 4.5 $\mu\text{V}/\text{K}$.

The short- d data, however, only shows qualitative agreement with the experimental data. The signals from the Pt/ Al_2O_3 heater series are more negative than from

²After this work was published, a recent study by Prakash *et. al.* [48] experimentally demonstrated two length scales involved in the spin Seebeck effect, and associated the shorter one to magnon-phonon energy relaxation.

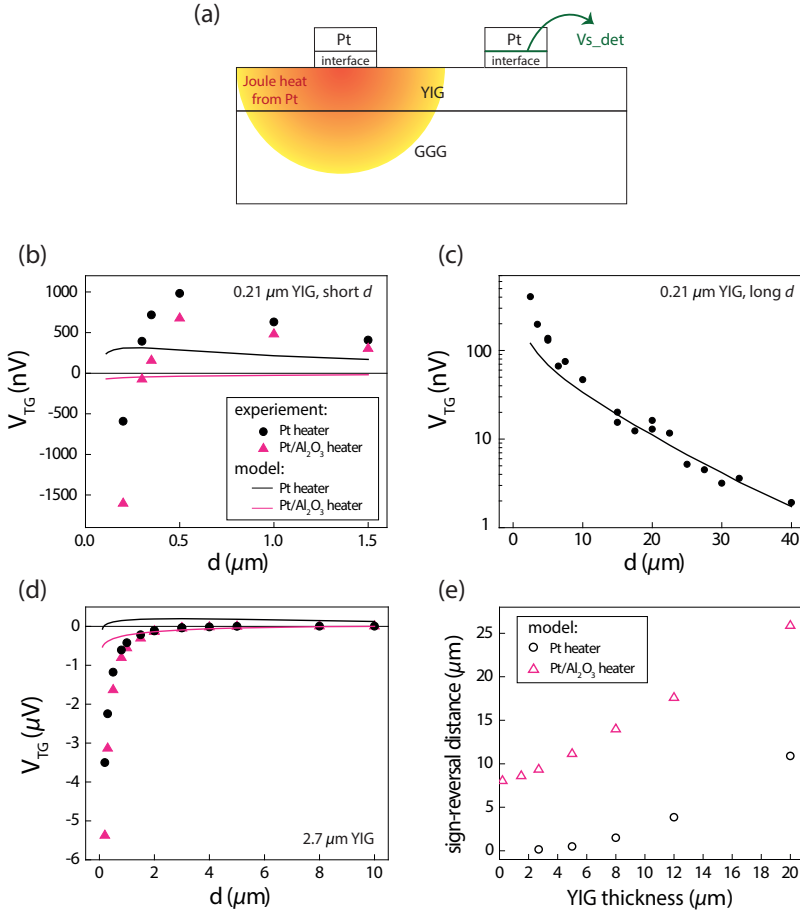


Figure 4.7: The modeling of nonlocal SSE signals with parameters in Table 4.2 and $S_S=4.5 \mu\text{V}/\text{K}$. (a) The 2D geometry that was studied in the model. (b)(c), Modeled results (solid lines) compared with experimental (solid symbols) nonlocal SSE signals for the two heating series on 0.21 μm YIG for (b) short and (c) long distances. The experimental data (black dots) in (c) are from Ref. [25]. (d), The comparison between experimental and modeled results for 2.7 μm YIG. (e) The calculated sign-reversal distances as a function of the YIG thickness for the two heating configurations.

the Pt heater series, and the sign-reversal distance takes place at a further d than the Pt heater series, consistent with the observation from the experiments. As the YIG thickness increases, the sign-reversal distances also shift to further distance. But in the model, for the parameters we used from Table 4.2, the difference for the two heating

configurations is larger than in the experiment [as is shown in Fig. 4.7(e)]. Compared to the experiment, the sign reversal for the Pt series is much closer to the heater, and for the Pt/Al₂O₃ heater series is much further away. Also, from Fig. 4.7(d) one can see that the fast decay of the V_{TG} signals in the short- d regime cannot be captured by the model; same as the electrical injection, a short length scale may be needed to be introduced in the short- d regime.

4.4.3 Discussion

So far the model works in showing that there are indeed sign reversals when probing the thermally generated magnon signals nonlocally and that this sign reversal is indeed influenced by both the YIG thickness and the heater opacity. Moreover, the signals from the Pt/Al₂O₃ heater series are more negative than from the Pt heater series, which is qualitatively consistent with the experimental results. However, full quantitative agreement cannot be reached.

Here we provide some tentative explanations of the quantitative deviation between the model and experiments. First of all, in our model we only consider μ_m to describe the nonequilibrium magnons and assume the magnon temperature T_m to be the same as the phonon temperature T_{ph} , based on the very short magnon-phonon relaxation length [31, 35, 49]. It could be possible that the difference between T_{ph} and T_m cannot be fully ignored, and thus the magnon-phonon interaction affects the magnon diffusion process, which would introduce another length scale shorter than λ_m .

Secondly, the magnons may not follow a purely diffusive motion when they are excited. As magnons are quasiparticles, it is possible that they gain certain momentum when they are excited, for instance from the electrons in Pt. The mass of magnons at energies around $k_B T$ is roughly 1 to 2 orders of magnitude larger than the mass of electrons. In the electrical injection case, as the electrons reflect from the YIG/Pt interface, they need to transfer a vertical momentum to the magnons. This will deviate the magnon transport from a fully diffusive picture, as the magnons prefer to go vertically into the YIG film, though this picture requires a relatively large magnon mean free path at room temperature.

Finally, heat-related processes can also affect our observed signals. In fact, at very long distances, the contributions of the nonlocal signals from heat diffusion were identified and analyzed [50, 51]. More details can be found in Chapt. 5.

4.5 Conclusions

We have studied the YIG thickness dependence of the nonlocal transport behavior for both electrically and thermally excited magnons. We investigated YIG thicknesses from $0.21\ \mu\text{m}$ up to $50\ \mu\text{m}$ and found that the nonlocal signals of the electrically injected magnons reduce monotonically as the YIG thickness increases. Furthermore, we observed sign reversals of the nonlocal signals for the thermally injected magnons, the distance of which depends on both the heater/YIG interface transparency and the YIG thickness. The qualitative agreement between our results and the bulk spin Seebeck model indicates the necessity to include the magnon current and magnon accumulation in the SSE picture. Using a 2D model we estimate the bulk spin Seebeck coefficient to be $4.5\ \mu\text{V}/\text{K}$. Our results also suggest that more complex physics processes are involved, which cannot be captured by the employed magnon diffusion-relaxation model. For instance, additional length scales may need to be introduced to describe the short-distance regime, or possibly the excitation process of magnons cannot be described in a fully diffusive picture.

4.6 Supplementary information

4.6.1 Temperature profiles when Pt serves as a Joule heater

In Fig. 4.8, we calculated the temperature profiles of the device induced by Joule heating, to compare the temperature profiles between different heater interfaces and YIG thicknesses. For the Pt/ Al_2O_3 heater scenario, an additional Al_2O_3 layer is included beneath the Pt layer in the model, with a thermal conductivity of $0.15\ \text{W}/(\text{m}\cdot\text{K})$. The calculated results from the model show that the temperature profiles with and without the Al_2O_3 layer have very little difference. We also calculated the temperature profiles for thicker YIG films, as plotted when the YIG thickness is $2.7\ \mu\text{m}$ in Figs. 4.8(b) and 4.8(c). The temperature profile is not varied more than 10% with increasing YIG thickness. Clearly, the different behaviors of the nonlocal thermal signals V_{TG} between different heater opacity or different YIG thickness cannot be attributed to the temperature profiles, but to the bulk property of the magnon flow, which is sensitive to the boundary conditions.

At further distance, the elevated temperature $(T - T_0)$ by Joule heating decreases on a natural logarithmic scale as a function of d . Notably, compared with the exponential decay of the V_{TG} in the long- d regime (see Fig. 4.5), the temperature decay is much slower than the V_{TG} signal decay with increasing d . For instance, with $10\ \mu\text{m}$ further away, the temperature drops by 6% and V_{TG} drops by 66%. This again strongly proves that it is the magnon accumulation instead of the temperature profile that determines the V_{TG} we measured.

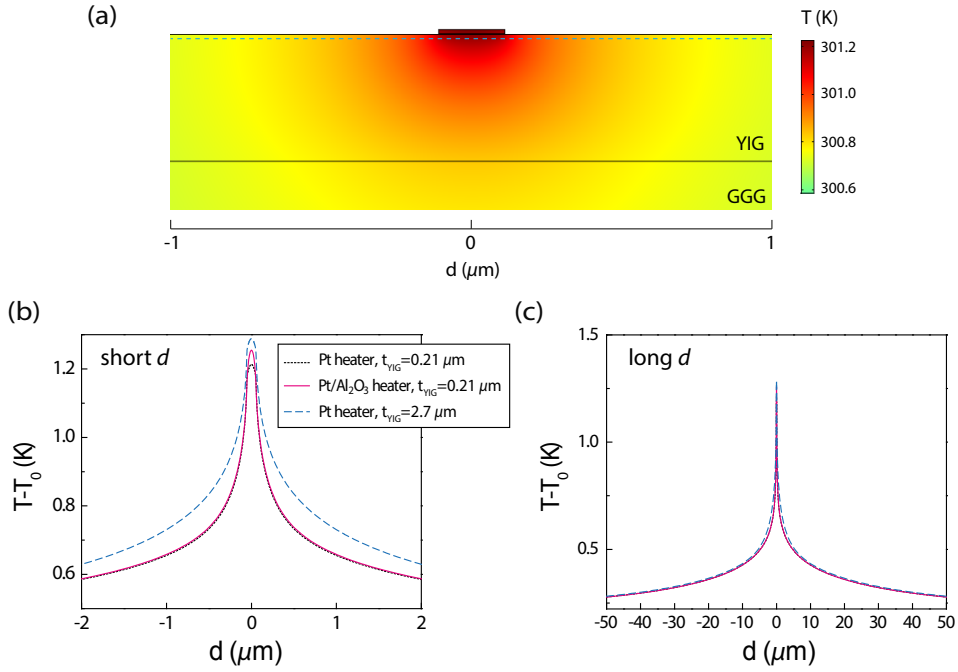


Figure 4.8: Temperature profile of the device induced by Joule heating. (a) Two-dimensional temperature profile close to the heat source, for Pt heater and 0.21- μm -thick YIG. The room temperature $T_0 = 300 \text{ K}$ is set as a boundary condition at the bottom of GGG. (b),(c) Temperature profiles for different heating configuration and YIG thickness along the cut line in the YIG, which is 1 nm beneath the YIG surface, as indicated by the dashed line in (a). (b) shows the short-distance range and (c) shows the long-distance range.

Given that the present data in this chapter was obtained in air, one may argue that there could be some heat carried away by air, cooling the Pt detector and giving rise to an interfacial SSE driven by the temperature difference between the Pt detector and YIG. To prove that this effect is negligible, we measured the 2.7 μm YIG sample also in vacuum, and obtained almost the same results as we measured in air. The sign reversal distance is reproducible under vacuum conditions, and the signal magnitudes were not varied by more than 15%. One may also argue that heat could be carried away by the Ti/Au leads, and this amount of heat is proportional to $T - T_0$ at the specific distance. If the Pt detector temperature is lowered by this effect, this could generate an additional spin Seebeck voltage which is opposite in sign compared with the local SSE signal. However, the results we obtained experimentally decrease much faster than the reduction of $T - T_0$ as a function of d [see Figs. 4.5 and 4.8(c)]. Based on

this fact, we conclude that these effects have no significant influence on the measured signals.

4.6.2 Local spin Seebeck effect as a function of YIG thickness

When sending an electrical current to the Pt-only strip, the local SSE can be measured as the V^{2f} signal generated at the Pt strip itself [21, 42]. Note that for the Pt/ Al_2O_3 heater, the local SSE signal vanishes, as the Al_2O_3 layer fully blocks the interaction between Pt and YIG. As shown in section 4.6.3 and also in Ref. [22], from the dependence of the local SSE on YIG thickness we can obtain an estimation of λ_m .

Figure 4.9 shows the local V_{TG} results as a function of YIG thickness. It can be seen that the local V_{TG} for the different thick YIG samples are comparable. No clear trend for V_{TG} can be observed as a function of YIG thickness. This behavior clearly contradicts with the modeled results (red curve in Fig. 4.9), using the λ_m we extracted from the long d regime from the nonlocal SSE measurements. Furthermore, the local SSE is roughly one order of magnitude larger than the largest nonlocal SSE signal we obtained, which requires a much larger S_S in order to obtain the red curve as shown in Fig. 4.9. We further modeled the situation where the YIG surface is fully covered by Pt, with the same charge current density sent in the Pt layer, creating the same

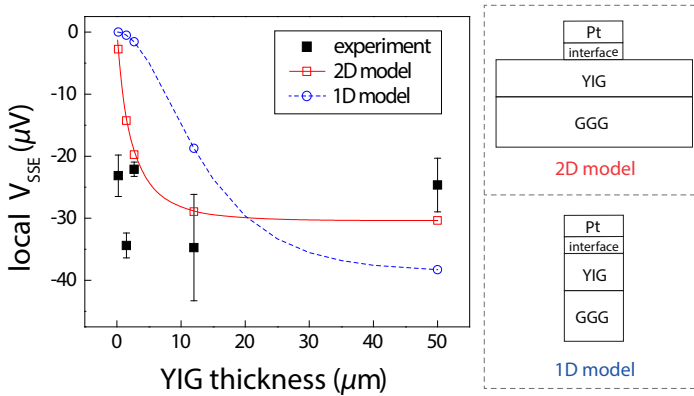


Figure 4.9: Local spin Seebeck voltages measured at the Pt heater strips as a function of YIG thickness. The injection current I_{ac} is $100 \mu\text{A}$. The width and length of the Pt strips is 100 nm and $10 \mu\text{m}$, respectively. Each point is an average from measurements over a few Pt strips and the error bars represent the standard deviations. The red curve shows the modeling results when taking $\lambda_m = 9.4 \mu\text{m}$ and $S_S = 125 \mu\text{V/K}$. The blue curve shows the modeling results when the YIG and GGG substrates are as wide as the Pt strip, with the same λ_m and S_S .

amount of Joule heat as the 2D situation. Now the heat flow is not radial but vertical, normal to the plane, as shown in the blue dashed curve in Fig. 4.9. In this case the SSE signal would saturate at a larger YIG thickness, compared to the 2D model.

Our results suggest that the length scale that governs the local SSE can be different from the λ_m that we extracted from the nonlocal SSE signals. As the local detection corresponds to the limit where $d \rightarrow 0$, this further confirms that for local or very short distances, more complex physics is involved.

4.6.3 Vertical one-dimensional analytical model for the spin Seebeck effect

In this section, we analytically solve a simple one-dimensional model from the bulk SSE theory [15, 16] to give a clear qualitative picture and relate it to our experimental results.

Consider a standard triple structure where YIG is sandwiched by Pt and GGG, as shown in Fig. 4.10(a). The heat flow J_q , generated by the Joule heating in Pt, flows through the YIG uniformly towards the GGG side. From the bulk magnonic Seebeck model, a thermal magnon flow is induced in the YIG, directly proportional to J_q :

$$J_{m,q} = -\sigma_m S_S \frac{d}{dx} T(x) \propto J_q = -\kappa \frac{d}{dx} T(x), \quad (4.11)$$

where σ_m is the magnon conductivity, S_S the bulk spin Seebeck coefficient, and κ the thermal conductivity of YIG, as defined in the main text. Here the temperatures of the magnon and phonon systems are assumed to be equal. On the other hand, the gradient of the magnon accumulation μ_m drives a diffusive magnon current

$$J_{m,diff} = -\sigma_m \frac{d}{dx} \mu_m(x), \quad (4.12)$$

where σ_m is the magnon conductivity in YIG. From the drift-diffusion model we also have [47]:

$$\frac{d^2}{dx^2} \mu_m(x) = \frac{1}{\lambda_m^2} \mu_m(x), \quad (4.13)$$

where λ_m is the magnon diffusion length of YIG. The general solution to Eq. 4.13 is

$$\mu_m(x) = A \exp\left(-\frac{x}{\lambda_m}\right) + B \exp\left(\frac{x}{\lambda_m}\right) \quad (4.14)$$

with coefficients A and B that are determined by the boundary conditions. At $x = w$ (the YIG/GGG interface), we assume no magnon current can flow through, and therefore the total magnon current $J_m = J_{m,q} + J_{m,diff}$ should vanish to 0. At $x = 0$ (the YIG/Pt interface), J_m is equal to the net pumping current $J_{pump} = g_S \cdot \mu_m(0)$,

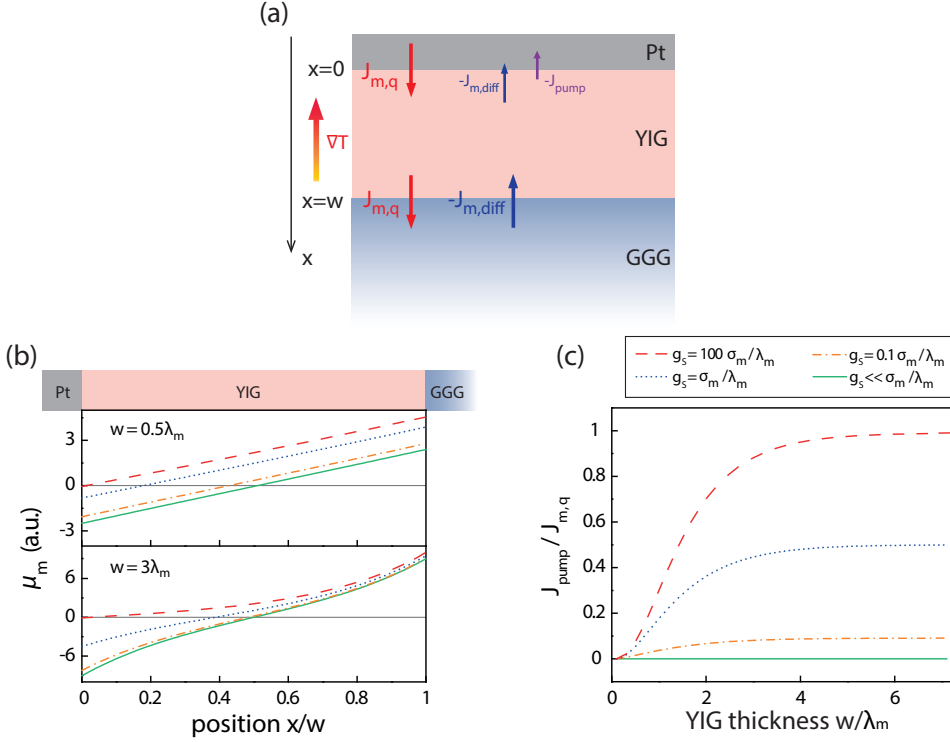


Figure 4.10: The application of the bulk magnonic Seebeck model to a one-dimensional vertical geometry. (a) Schematic of the Pt/YIG/GGG trilayer structure, with magnon currents only shown at the interfaces. Pt is the hotter side. (b) The calculated spatial distribution of the magnon accumulation in the YIG for different g_s compared with σ_m/λ_m . We take $w = 0.5\lambda_m$ in the top figure and $w = 3\lambda_m$ in the bottom. (c) The calculated pumping current as a function of YIG thickness for different g_s .

where g_s is the effective spin mixing conductance between YIG and Pt [28, 31]. These constraints set the Neumann boundary conditions for Eq. 4.13, and we can then solve A and B as

$$A = J_{m,q} \cdot \frac{1 - (1 - \frac{\lambda_m}{\sigma_m} g_s) \exp(-\frac{w}{\lambda_m})}{\frac{\sigma_m}{\lambda_m} [\exp(-\frac{2w}{\lambda_m}) - 1] - g_s [\exp(-\frac{2w}{\lambda_m}) + 1]}$$

and

$$B = J_{m,q} \cdot \frac{\lambda_m}{\sigma_m} \exp(-\frac{w}{\lambda_m}) + A \cdot \exp(-\frac{2w}{\lambda_m}), \quad (4.15)$$

from which we can determine μ_m and J_{pump} , as shown in Figs. 4.10(b) and 4.10(c).

In Fig. 4.10(b) we plot μ_m as a function of the spatial coordinate x . In the top

figure where $w = 0.5\lambda_m$, the magnon relaxation effect is small. When the YIG/Pt interface is opaque ($g_S \ll \sigma_m/\lambda_m$), the two interfaces are symmetric for YIG. An equal amount of positive and negative μ_m builds up at the two ends of YIG, and μ_m changes sign exactly at the YIG center. As the top interface becomes more transparent, the whole μ_m shifts gradually up, as the J_{pump} at the YIG/Pt interface takes away some negative magnon accumulation. The sign-reversal of the μ_m takes place closer and closer to the Pt side. In the limit where $g_S \gg \sigma_m/\lambda_m$, there will only be a very tiny negative μ_m at $x = 0$.

When w is larger than λ_m , as shown in the bottom figure, relaxation starts to enter the picture. The distribution of μ_m becomes curved, and the difference of the slope between $x = 0$ and $x = w$ becomes more significant (except for the case when $g_S \ll \sigma_m/\lambda_m$), indicating a larger J_{pump} compared to a smaller w . In Fig. 4.10(c) we plot the J_{pump} as a function of the YIG thickness for different g_S . It increases almost linearly for small g_S and nearly quadratically for large g_S , and saturates when w is comparable to a few times of λ_m . This result is similar to Fig. 5 in Ref. [15], which can be used to explain the thickness dependent SSE data from Ref. [22], although in Ref. [22] they adopted a magnon temperature model to explain their data.

To test the bulk-generated SSE model, the most straightforward check is to directly probe μ_m along the YIG as a function of x in a 1D-like structure. However, experimentally this is not easy to realize. It either requires a vertical ∇T , and probe μ_m as a function of depth, or a fully in-plane ∇T , and probe μ_m within a few λ_m from the sample edges. Alternatively, in this experiment we adopt a nonlocal geometry where a charge current through a Pt strip (Joule heater) creates a radial thermal gradient (Fig. 4.3(a)). Similar to the 1D situation, the temperature gradient induces a negative μ_m close to the heater and a positive μ_m far away. Due to the radial ∇T shape, the μ_m distribution now “goes around” and becomes detectable at the YIG surface. If we place a detector next to the heater that can sense the μ_m at the surface, it should detect negative μ_m for short distances and positive μ_m for long distances. If the YIG/heater interface is more opaque, this sign reversal should take place at a longer distance as a larger negative μ_m is preserved, as that we observed in the experiments.

4.7 Linear-scale plots of V_{TG} for different YIG thickness

In this section we replot the thermally generated nonlocal signals V_{TG} for different YIG thicknesses and heating configurations, shown in Fig. 4.5, all in linear scale. Note that for the longer distance plots (Figs. 4.11(b) and 4.11(c)) the y -axes are significantly zoomed in comparison with the full scale (Fig. 4.11(a)), so that the sign reversals for thicker YIG samples can be resolved. In the short- d regime, except for the thin 0.21- μm -thick YIG, all the YIG samples show similar behavior. At further distance, the

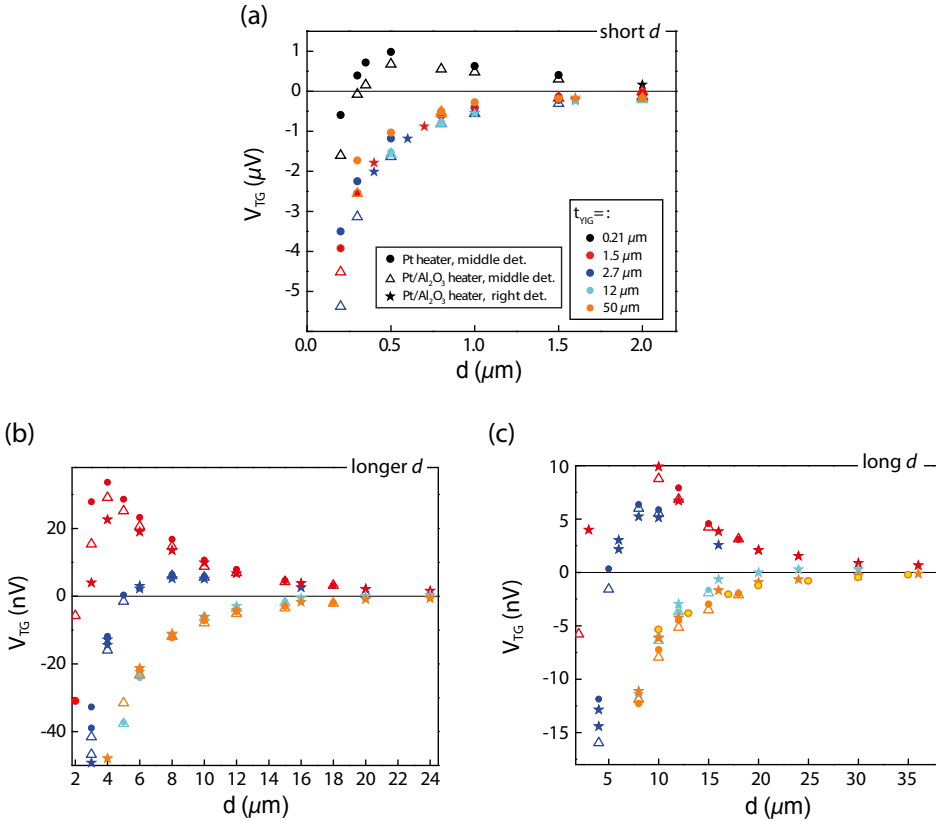


Figure 4.11: The linear-scale plots of the data in Fig. 4.5. Color indicates YIG thickness and symbol shape distinguishes different heating configurations, as defined in Fig. 4.5.

sign reversals gradually take place and move towards a further distance for thicker YIG film.

References

- [1] I. Žutić, J. Fabian, and S. Das Sarma, “Spintronics: Fundamentals and applications,” *Reviews of Modern Physics* **76**, pp. 323–410, Apr. 2004.
- [2] A. V. Chumak, V. I. Vasyuchka, A. A. Serga, and B. Hillebrands, “Magnon spintronics,” *Nature Physics* **11**, pp. 453–461, June 2015.
- [3] C. Kittel, *Introduction to Solid State Physics*, Wiley, Hoboken, NJ, 8th ed., Nov. 2004.
- [4] Y. Kajiwara, K. Harii, S. Takahashi, J. Ohe, K. Uchida, M. Mizuguchi, H. Umezawa, H. Kawai, K. Ando, K. Takanashi, S. Maekawa, and E. Saitoh, “Transmission of electrical signals by spin-wave interconversion in a magnetic insulator,” *Nature* **464**, pp. 262–266, Mar. 2010.
- [5] M. Madami, S. Bonetti, G. Consolo, S. Tacchi, G. Carlotti, G. Gubbiotti, F. B. Mancoff, M. A. Yar, and J. Åkerman, “Direct observation of a propagating spin wave induced by spin-transfer torque,” *Nature Nanotechnology* **6**, pp. 635–638, Oct. 2011.
- [6] V. E. Demidov, S. Urazhdin, H. Ulrichs, V. Tiberkevich, A. Slavin, D. Baither, G. Schmitz, and S. O. Demokritov, “Magnetic nano-oscillator driven by pure spin current,” *Nature Materials* **11**, pp. 1028–1031, Dec. 2012.
- [7] M. Collet, X. de Milly, O. d. Kelly, V. V. Naletov, R. Bernard, P. Bortolotti, J. Ben Youssef, V. E. Demidov, S. O. Demokritov, J. L. Prieto, M. Muñoz, V. Cros, A. Anane, G. de Loubens, and O. Klein, “Generation of coherent spin-wave modes in yttrium iron garnet microdiscs by spin-orbit torque,” *Nature Communications* **7**, p. 10377, Jan. 2016.
- [8] K. Uchida, S. Takahashi, K. Harii, J. Ieda, W. Koshibae, K. Ando, S. Maekawa, and E. Saitoh, “Observation of the spin Seebeck effect,” *Nature* **455**, p. 778, Oct. 2008.
- [9] K. Uchida, J. Xiao, H. Adachi, J. Ohe, S. Takahashi, J. Ieda, T. Ota, Y. Kajiwara, H. Umezawa, H. Kawai, G. E. W. Bauer, S. Maekawa, and E. Saitoh, “Spin Seebeck insulator,” *Nature Materials* **9**, pp. 894–897, Nov. 2010.
- [10] J. Xiao, G. E. W. Bauer, K.-c. Uchida, E. Saitoh, and S. Maekawa, “Theory of magnon-driven spin Seebeck effect,” *Physical Review B* **81**, p. 214418, June 2010.
- [11] H. Adachi, J.-i. Ohe, S. Takahashi, and S. Maekawa, “Linear-response theory of spin Seebeck effect in ferromagnetic insulators,” *Physical Review B* **83**, p. 094410, Mar. 2011.
- [12] H. Adachi, K.-i. Uchida, E. Saitoh, and S. Maekawa, “Theory of the spin Seebeck effect,” *Reports on Progress in Physics* **76**, p. 036501, Mar. 2013.
- [13] S. Hoffman, K. Sato, and Y. Tserkovnyak, “Landau-Lifshitz theory of the longitudinal spin Seebeck effect,” *Physical Review B* **88**, p. 064408, Aug. 2013.
- [14] M. Schreier, A. Kamra, M. Weiler, J. Xiao, G. E. W. Bauer, R. Gross, and S. T. B. Goennenwein, “Magnon, phonon, and electron temperature profiles and the spin Seebeck effect in magnetic insulator/normal metal hybrid structures,” *Physical Review B* **88**, p. 094410, Sept. 2013.
- [15] S. M. Rezende, R. L. Rodríguez-Suárez, R. O. Cunha, A. R. Rodrigues, F. L. A. Machado, G. A. Fonseca Guerra, J. C. Lopez Ortiz, and A. Azevedo, “Magnon spin-current theory for the longitudinal spin-Seebeck effect,” *Physical Review B* **89**, p. 014416, Jan. 2014.
- [16] R. A. Duine, A. Brataas, S. A. Bender, and Y. Tserkovnyak, *Universal themes of Bose-Einstein condensation, chapter 26*, Cambridge University Press, Cambridge, United Kingdom, Apr. 2017. Edited by David Snoke, Nikolaos Proukakis and Peter Littlewood.
- [17] C. M. Jaworski, J. Yang, S. Mack, D. D. Awschalom, R. C. Myers, and J. P. Heremans, “Spin-Seebeck Effect: A Phonon Driven Spin Distribution,” *Physical Review Letters* **106**, p. 186601, May 2011.

- [18] K.-i. Uchida, T. Kikkawa, A. Miura, J. Shiomi, and E. Saitoh, "Quantitative Temperature Dependence of Longitudinal Spin Seebeck Effect at High Temperatures," *Physical Review X* **4**, p. 041023, Nov. 2014.
- [19] T. Kikkawa, K.-i. Uchida, S. Daimon, Z. Qiu, Y. Shiomi, and E. Saitoh, "Critical suppression of spin Seebeck effect by magnetic fields," *Physical Review B* **92**, p. 064413, Aug. 2015.
- [20] H. Jin, S. R. Boona, Z. Yang, R. C. Myers, and J. P. Heremans, "Effect of the magnon dispersion on the longitudinal spin Seebeck effect in yttrium iron garnets," *Physical Review B* **92**, p. 054436, Aug. 2015.
- [21] N. Vlietstra, J. Shan, B. J. van Wees, M. Isasa, F. Casanova, and J. Ben Youssef, "Simultaneous detection of the spin-Hall magnetoresistance and the spin-Seebeck effect in platinum and tantalum on yttrium iron garnet," *Physical Review B* **90**, p. 174436, Nov. 2014.
- [22] A. Kehlberger, U. Ritzmann, D. Hinzke, E.-J. Guo, J. Cramer, G. Jakob, M. C. Onbasli, D. H. Kim, C. A. Ross, M. B. Jungfleisch, B. Hillebrands, U. Nowak, and M. Kläui, "Length Scale of the Spin Seebeck Effect," *Physical Review Letters* **115**, p. 096602, Aug. 2015.
- [23] E.-J. Guo, J. Cramer, A. Kehlberger, C. A. Ferguson, D. A. MacLaren, G. Jakob, and M. Kläui, "Influence of Thickness and Interface on the Low-Temperature Enhancement of the Spin Seebeck Effect in YIG Films," *Physical Review X* **6**, p. 031012, July 2016.
- [24] D. Meier, D. Reinhardt, M. van Straaten, C. Klewe, M. Althammer, M. Schreier, S. T. B. Goennenwein, A. Gupta, M. Schmid, C. H. Back, J.-M. Schmalhorst, T. Kuschel, and G. Reiss, "Longitudinal spin Seebeck effect contribution in transverse spin Seebeck effect experiments in Pt/YIG and Pt/NFO," *Nature Communications* **6**, p. 8211, Sept. 2015.
- [25] L. J. Cornelissen, J. Liu, R. A. Duine, J. B. Youssef, and B. J. van Wees, "Long-distance transport of magnon spin information in a magnetic insulator at room temperature," *Nature Physics* **11**, pp. 1022–1026, Dec. 2015.
- [26] B. L. Giles, Z. Yang, J. S. Jamison, and R. C. Myers, "Long-range pure magnon spin diffusion observed in a nonlocal spin-Seebeck geometry," *Physical Review B* **92**, p. 224415, Dec. 2015.
- [27] L. J. Cornelissen, J. Shan, and B. J. van Wees, "Temperature dependence of the magnon spin diffusion length and magnon spin conductivity in the magnetic insulator yttrium iron garnet," *Physical Review B* **94**, p. 180402, Nov. 2016.
- [28] J. Xiao and G. E. W. Bauer, "Transport between metals and magnetic insulators," *arXiv:1508.02486 [cond-mat]*, Aug. 2015. arXiv: 1508.02486.
- [29] S. A. Bender, R. A. Duine, and Y. Tserkovnyak, "Electronic Pumping of Quasiequilibrium Bose-Einstein-Condensed Magnons," *Physical Review Letters* **108**, p. 246601, June 2012.
- [30] S. Takahashi, E. Saitoh, and S. Maekawa, "Spin current through a normal-metal/insulating-ferromagnet junction," *Journal of Physics: Conference Series* **200**(6), p. 062030, 2010.
- [31] J. Flipse, F. K. Dejene, D. Wagenaar, G. E. W. Bauer, J. B. Youssef, and B. J. van Wees, "Observation of the Spin Peltier Effect for Magnetic Insulators," *Physical Review Letters* **113**, p. 027601, July 2014.
- [32] S. T. B. Goennenwein, R. Schlitz, M. Pernpeintner, K. Ganzhorn, M. Althammer, R. Gross, and H. Huebl, "Non-local magnetoresistance in YIG/Pt nanostructures," *Applied Physics Letters* **107**, p. 172405, Oct. 2015.
- [33] J. Li, Y. Xu, M. Aldosary, C. Tang, Z. Lin, S. Zhang, R. Lake, and J. Shi, "Observation of magnon-mediated current drag in Pt/yttrium iron garnet/Pt(Ta) trilayers," *Nature Communications* **7**, p. 10858, Mar. 2016.
- [34] H. Wu, C. H. Wan, X. Zhang, Z. H. Yuan, Q. T. Zhang, J. Y. Qin, H. X. Wei, X. F. Han, and S. Zhang, "Observation of magnon-mediated electric current drag at room temperature," *Physical Review B* **93**, p. 060403, Feb. 2016.

- [35] L. J. Cornelissen, K. J. H. Peters, G. E. W. Bauer, R. A. Duine, and B. J. van Wees, "Magnon spin transport driven by the magnon chemical potential in a magnetic insulator," *Physical Review B* **94**, p. 014412, July 2016.
- [36] S. M. Rezende, R. L. Rodríguez-Suárez, J. C. Lopez Ortiz, and A. Azevedo, "Thermal properties of magnons and the spin Seebeck effect in yttrium iron garnet/normal metal hybrid structures," *Physical Review B* **89**, p. 134406, Apr. 2014.
- [37] J. Shan, F. K. Dejene, J. C. Leutenantsmeyer, J. Flipse, M. Münzenberg, and B. J. van Wees, "Comparison of the magneto-Peltier and magneto-Seebeck effects in magnetic tunnel junctions," *Physical Review B* **92**, p. 020414, July 2015.
- [38] N. Vlietstra, J. Shan, V. Castel, B. J. van Wees, and J. Ben Youssef, "Spin-Hall magnetoresistance in platinum on yttrium iron garnet: Dependence on platinum thickness and in-plane/out-of-plane magnetization," *Physical Review B* **87**, p. 184421, May 2013.
- [39] F. K. Dejene, J. Flipse, and B. J. van Wees, "Verification of the Thomson-Onsager reciprocity relation for spin caloritronics," *Physical Review B* **90**, p. 180402, Nov. 2014.
- [40] H. Nakayama, M. Althammer, Y.-T. Chen, K. Uchida, Y. Kajiwara, D. Kikuchi, T. Ohtani, S. Geprägs, M. Opel, S. Takahashi, R. Gross, G. E. W. Bauer, S. T. B. Goennenwein, and E. Saitoh, "Spin Hall Magnetoresistance Induced by a Nonequilibrium Proximity Effect," *Physical Review Letters* **110**, p. 206601, May 2013.
- [41] Y.-T. Chen, S. Takahashi, H. Nakayama, M. Althammer, S. T. B. Goennenwein, E. Saitoh, and G. E. W. Bauer, "Theory of spin Hall magnetoresistance," *Physical Review B* **87**, p. 144411, Apr. 2013.
- [42] M. Schreier, N. Roschewsky, E. Dobler, S. Meyer, H. Huebl, R. Gross, and S. T. B. Goennenwein, "Current heating induced spin Seebeck effect," *Applied Physics Letters* **103**, p. 242404, Dec. 2013.
- [43] M. Weiler, M. Althammer, M. Schreier, J. Lotze, M. Pernpeintner, S. Meyer, H. Huebl, R. Gross, A. Kamra, J. Xiao, Y.-T. Chen, H. Jiao, G. E. W. Bauer, and S. T. B. Goennenwein, "Experimental Test of the Spin Mixing Interface Conductivity Concept," *Physical Review Letters* **111**, p. 176601, Oct. 2013.
- [44] V. Castel, N. Vlietstra, J. B. Youssef, and B. J. v. Wees, "Platinum thickness dependence of the inverse spin-Hall voltage from spin pumping in a hybrid yttrium iron garnet/platinum system," *Applied Physics Letters* **101**, p. 132414, Sept. 2012.
- [45] S. R. Boona and J. P. Heremans, "Magnon thermal mean free path in yttrium iron garnet," *Physical Review B* **90**, p. 064421, Aug. 2014.
- [46] T. Valet and A. Fert, "Theory of the perpendicular magnetoresistance in magnetic multilayers," *Physical Review B* **48**, pp. 7099–7113, Sept. 1993.
- [47] S. S.-L. Zhang and S. Zhang, "Magnon Mediated Electric Current Drag Across a Ferromagnetic Insulator Layer," *Physical Review Letters* **109**, p. 096603, Aug. 2012.
- [48] A. Prakash, B. Flebus, J. Brangham, F. Yang, Y. Tserkovnyak, and J. P. Heremans, "Evidence for the role of the magnon energy relaxation length in the spin Seebeck effect," *Physical Review B* **97**, p. 020408, Jan. 2018.
- [49] M. Agrawal, V. I. Vasyuchka, A. A. Serga, A. D. Karenowska, G. A. Melkov, and B. Hillebrands, "Direct Measurement of Magnon Temperature: New Insight into Magnon-Phonon Coupling in Magnetic Insulators," *Physical Review Letters* **111**, p. 107204, Sept. 2013.
- [50] J. Shan, L. J. Cornelissen, J. Liu, J. B. Youssef, L. Liang, and B. J. van Wees, "Criteria for accurate determination of the magnon relaxation length from the nonlocal spin Seebeck effect," *Physical Review B* **96**, p. 184427, Nov. 2017.
- [51] B. L. Giles, Z. Yang, J. S. Jamison, J. M. Gomez-Perez, S. Vélez, L. E. Hueso, F. Casanova, and R. C.

Myers, "Thermally driven long-range magnon spin currents in yttrium iron garnet due to intrinsic spin Seebeck effect," *Physical Review B* **96**, p. 180412, Nov. 2017.

Chapter 5

Criteria for accurate determination of the magnon relaxation length from the nonlocal spin Seebeck effect

Abstract

The nonlocal transport of thermally generated magnons not only unveils the underlying mechanism of the spin Seebeck effect, but also allows for the extraction of the magnon relaxation length (λ_m) in a magnetic material, the average distance over which thermal magnons can propagate. In this study, we experimentally explore in yttrium iron garnet (YIG)/platinum systems much further ranges compared with previous investigations. We observe that the nonlocal SSE signals at long distances (d) clearly deviate from a typical exponential decay. Instead, they can be dominated by the nonlocal generation of magnon accumulation as a result of the temperature gradient present away from the heater, and decay geometrically as $1/d^2$. We emphasize the importance of looking only into the exponential regime (i.e., the intermediate distance regime) to extract λ_m . With this principle, we study λ_m as a function of temperature in two YIG films which are 2.7 and 50 μm in thickness, respectively. We find λ_m to be around 15 μm at room temperature and it increases to 40 μm at $T = 3.5$ K. Finite element modeling results agree with experimental studies qualitatively, showing also a geometrical decay beyond the exponential regime. Based on both experimental and modeling results we put forward a general guideline for extracting λ_m from the nonlocal spin Seebeck effect.

5.1 Introduction

Since its discovery [1, 2], the spin Seebeck effect (SSE) has been a central topic in the burgeoning field of spin caloritronics [3–5], not only due to its promising application in utilizing thermal energy on a large scale [6], but also because of its rich and interesting physics [7–16]. When a heat current flows through magnetic insulators such as yttrium iron garnet (YIG), a pure magnonic spin current is excited without any charge currents flowing. A magnon spin accumulation is thereby built up at the boundaries of YIG [17–19], which can induce a spin angular momentum flow into an adjacent platinum (Pt) layer through interfacial exchange coupling [20–22].

It can then convert into a measurable electric voltage by the inverse spin Hall effect (ISHE) [23].

Due to various scattering processes, the magnon spin accumulation relaxes at a certain length scale with the system going back to equilibrium. In the diffusive magnon transport picture, the magnon relaxation length λ_m , the average distance over which magnons can propagate, can be expressed with the phenomenological Gilbert damping coefficient α [18]. Owing to the diffusive nature of thermally excited magnons, λ_m is thus important for the understanding of the SSE.

So far, λ_m has been obtained experimentally based on longitudinal SSE in various approaches, such as the time-resolved method [24, 25], the study of SSE signals as a function of the YIG thickness t_{YIG} [12, 13], and the nonlocal method that employs a lateral nonlocal geometry to study SSE signals at a distance d away from the heating source and investigate how they decay as a function of d [15, 19, 26–30]. Particularly, λ_m 's that are acquired from the latter two methods exhibit roughly one order of magnitude difference at room temperature, which has been ascribed to different energy spectrum of magnons probed locally and nonlocally [13].

Compared to the local study that requires YIG films in different thicknesses, the lateral approach is experimentally more favorable in the sense that it allows the experiments to be conducted on the same YIG surface, which circumvents the possible differences among different YIG surfaces and YIG/Pt interfaces. Nevertheless, the λ_m 's reported from the lateral geometry still seem to differ by one order of magnitude in both room and lower temperatures among different groups [15, 27, 28, 31]. These discrepancies should be clearly addressed despite the material quality variations.

In the lateral approach, the electrical injection of magnons through spin voltage bias [18, 26, 32] takes place only at the injector, but the thermal generation of magnons is much more nonlocal. According to the bulk SSE picture [12, 17–19, 33], a thermal magnon current is excited wherever a temperature gradient (∇T) is present, which exists not only close to the heating source, but also much further away. Therefore, the decay of nonlocal SSE signals as a function of d is not solely due to magnon relaxation, but also related to ∇T . This behavior complicates the extraction of λ_m . Very recently, an additional decay on top of the exponential relaxation has been observed in bulk YIG films of 500 μm in thickness, and a longer decay length scale was associated with it [34].

Despite that the electrical approach gives well-defined magnon excitation location, the nonlocal signals obtained with this approach diminish as the sample temperature is reduced [31, 32], making it very difficult to study λ_m at low temperatures. In contrast, the nonlocal signals from thermal generation often remain sufficiently large or even increase substantially at lower temperatures [28, 31]. It is hence more practical to study λ_m with a Joule heating approach.

In this study, we investigate the nonlocal SSE signals carefully by exploring

the ultra-long heater-detector distance regime, i.e., around one order larger than the typical λ_m we found in our previous studies [19, 26, 31]. We can then clearly distinguish two decay regimes, which are governed by two different processes: One is dominated by the relaxation of the magnon chemical potential buildup around the local heating source, where the signals exhibit an exponential decay on the length scale of λ_m ; the other regime is located at a much longer distance, dominated by the magnon accumulation generated nonlocally as a result of the nonzero ∇T in the vicinity of the detector, with the signals clearly deviating from an exponential decay. We found and established that they exhibited a $1/d^2$ decay manner instead. We demonstrate the complexity to study λ_m from a thermal method, and highlight the importance to only evaluate the proper regime to obtain λ_m .

Furthermore, we carry out a systematic study at a wide range of temperatures, and find that the magnon exponential regime extends to a further distance as λ_m becomes larger at lower temperatures ($T < 20$ K). By exponential fitting only the magnon exponential regime we reliably extract λ_m ranging from 3.5 K to 300 K. Finally, we perform finite element modeling with various λ_m , which yields consistent results that support our understanding by showing also different decay regimes, with the same decay manners as observed experimentally. We conclude with a general rule for extracting λ_m in nonlocal SSE studies.

5.2 Experimental details

In the present study, we use YIG (111) films with two different thicknesses, 2.7 and 50 μm , both grown by liquid phase epitaxy on single-crystal $\text{Gd}_3\text{Ga}_5\text{O}_{12}$ (GGG) (111) substrates. The 50- μm -thick YIG sample was purchased from Matesy GmbH, and the 2.7- μm -thick YIG sample was provided by the Université de Bretagne in Brest, France. Pt strips (6.5 ± 0.5 nm in thickness, 100 μm and 1 μm in length and width, respectively) aligned in parallel directions with distance d relative to each other were patterned by electron beam lithography and sputtered onto a YIG substrate, as schematically shown in Fig. 5.1(a). Multiple devices were fabricated with various d on a single substrate. Contacts consisting of Ti (5 nm)/Au (75 nm) were subsequently patterned and evaporated to connect the Pt strips.

Compared to our previous experiments on this YIG substrate [19], the Pt strips were designed to be wider and longer in this study for two main reasons. First, with wider strips one can send larger currents through, which significantly improves the signal-to-noise ratio, making it possible to probe the small signals in the long- d regime. Second, longer strips reduce the effects of magnon currents that leak away in the y -axis direction, allowing for a 2D analysis in the x - z plane.

The samples were measured by sweeping the magnetic field along the x -axis. A

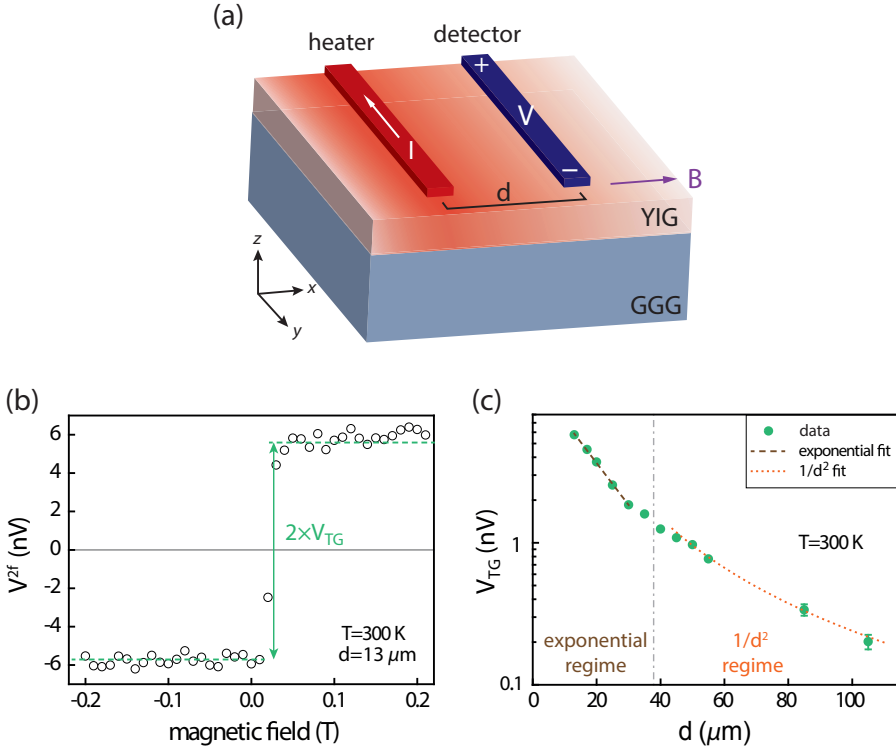


Figure 5.1: (a) Schematic illustration of the device structure. An ac current is sent to the heater (left Pt strip) and the voltage is detected nonlocally at the detector (right Pt strip), which is separated by a center-to-center distance d from the heater. An in-plane magnetic field B is applied along the x -axis to achieve maximal detection efficiency. (b) One typical field-sweep measurement of V^{2f} performed for $d=13$ μ m at $T=300$ K on a 2.7 - μ m-thick YIG film, normalized to $I=100$ μ A, from which the amplitude of the thermally generated nonlocal signal V_{TG} can be extracted. (c) V_{TG} as a function of d at $T=300$ K for the same YIG film, plotted in a logarithmic scale. The datapoints in this plot are after the sign-reversal and are opposite in sign with the local SSE signal, and are defined as positive throughout the paper. For the datapoints in the range of 10 μ m $\leq d \leq 30$ μ m, they are fitted exponentially with the equation $V_{TG} = C \exp(-d/\lambda_m)$ as shown by the brown dashed line, where $\lambda_m = 14.7 \pm 0.4$ μ m. In the range of 45 μ m $\leq d \leq 105$ μ m, the datapoints are fitted with $V_{TG} = C'/d^2$, shown by the orange dotted line. C and C' are coefficients that incorporate the system material properties, such as the bulk spin Seebeck coefficient S_S , the magnon spin conductivity σ_m , and the YIG film thickness.

lock-in detection technique is used, where an ac current I , typically with a frequency of 13 Hz and an rms value of $100 \mu\text{A}$, was sent through one of the Pt strips (the heater), and the voltage output was monitored nonlocally at the other Pt strip (the detector). In this study, we focus on the behavior of the thermally excited magnons, which results from Joule heating at the heater and is hence a second-order effect with respect to I . This is captured in the second harmonic signals V^{2f} in the lock-in measurement, as $V^{2f} = \frac{1}{\sqrt{2}} I_0^2 \cdot R_2$ with a phase shift of -90° provided no higher even harmonic signals are present. The data plotted in this paper were all normalized to $I=100 \mu\text{A}$. The samples were placed in a superconducting magnet cryostat with a variable temperature insert to enable temperature-dependent measurements, ranging from 3.5 to 300 K in this study. The sample temperature is always checked to be fully stabilized before performing measurements on all devices at that specific temperature. Furthermore, the applied charge current I is ensured to be in the linear regime, such that the Joule heating does not increase the average device temperature significantly.

5.3 Results and discussion

5.3.1 Results on 2.7- μm -thick YIG

Room temperature results

A typical field-sweep measurement curve is shown in Fig. 5.1(b). From the ISHE, one gets a maximum signal when the YIG magnetization is perpendicular to the Pt detector strip. Reversing the YIG magnetization results in an opposite polarization of the magnon spin current and consequently a reverse sign of the signal. As the employed YIG films have very small coercive fields [35], the signal jump around zero field allows us to extract the amplitude of the thermally generated nonlocal signal V_{TG} . We focus on the low-field regime where the magnetic-field-induced SSE suppression [9, 36] can be excluded in our analysis.

To study how the signals decay laterally, we further measured V_{TG} for all devices and plot them as a function of d , as shown in Fig. 5.1(c). Note that the shortest distance we probed here ($d = 10 \mu\text{m}$) is already further than the sign-reversal distance d_{rev} for the 2.7- μm -thick-YIG, around $5 \mu\text{m}$ at room temperature [19], so that the sign of V_{TG} in this study is opposite to the sign of the local spin Seebeck signal, which is obtained with the heater itself as the detector. In the beginning, the signals follow an exponential decay, where $\lambda_m = 14.7 \pm 0.4 \mu\text{m}$ can be extracted by fitting the first few datapoints with the exponential decay equation $V_{\text{TG}} = C \exp(-d/\lambda_m)$. This is the “relaxation regime” described in Ref. [26]. Here we name it “exponential regime.” The signals at further distances, however, clearly deviate from this exponential fit. They exhibit a slower decay, which can be well fitted with a $1/d^2$ function. Here we name

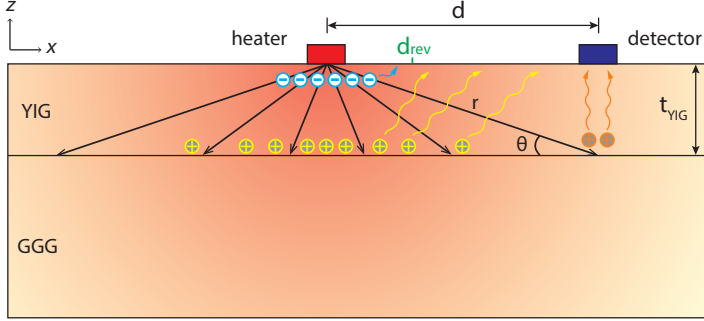


Figure 5.2: Schematic cross-section view of the device in the xz -plane. A charge current flows through the heater and generates a radial temperature gradient profile in both YIG and GGG layers, centered around the heater, as illustrated with the background color. A thermal magnon flow (represented by black arrows) is induced along the same direction as the heat flow in the YIG layer, as a result of the SSE. Unlike the heat flow, the magnon flow cannot enter the GGG layer, and a magnon accumulation (indicated by grey circles with “+” sign) is therefore built up at the YIG/GGG interface. Likewise, at the YIG/heater interface, a magnon depletion (indicated by white circles with the “-” sign) is formed. For the magnon accumulation, the yellow circles indicate the generation below the heater, and the orange circles indicate the nonlocal generation near the detector.

it “ $1/d^2$ regime.”

According to our previously proposed SSE picture [15, 18, 19], the heat flow J_q sourced from the heater induces a thermal magnon flow $J_{m,q}$ along with it inside the YIG layer. When $J_{m,q}$ reaches the YIG/GGG interface, it cannot enter further into the GGG layer. Because of this abrupt change in magnon spin conductivity, a magnon accumulation (corresponding to a positive magnon chemical potential, μ_m^+) is formed at the bottom of the YIG layer, as shown in Fig. 5.2. Similarly, a magnon depletion (corresponding to a negative magnon chemical potential, μ_m^-) is formed at around the heater. As a consequence, the gradient of μ_m drives a diffusive magnon flow $J_{m,diff}$ to counteract $J_{m,q}$, such that the boundary conditions are satisfied (in this case an open-circuit condition for spin currents at the bottom interface of YIG, and at the top of YIG the boundary condition depends on the spin opacity of the YIG/heater interface [19]).

Because of the radial shape of the temperature profile, μ_m^- is present close to the heater, surrounded by μ_m^+ that extends further away. The relative position of the two, or essentially the zero-crossing line of μ_m , is influenced by t_{YIG} and heater spin opacity among others [19]. After the sign reversal, μ_m^+ first grows to its maximum, and then diffuses in the lateral direction, relaxing exponentially on the length scale

of λ_m . This can be mapped by the ISHE signal produced by the Pt detector, which reflects the μ_m along the YIG surface. λ_m can be extracted by fitting the obtained signals in the exponential regime by an exponential decay [15, 19, 26].

The determination of λ_m from data before the sign-reversal [19, 27, 34], i.e., checking the relaxation of the μ_m^- , is also possible, but only valid when $t_{\text{YIG}} \gg \lambda_m$. This issue will be further discussed in Sec. 5.3.2.

This is however not the end of the story. At very long distances where μ_m^+ from the local region (yellow circles in Fig. 5.2) reduces almost to zero due to magnon spin relaxation, there can still be a small ∇T present at the YIG/GGG interface below the detector. Within the same framework of the bulk SSE picture, this will induce a thermal magnon flow $J_{m,q}$ proportional to it, building μ_m^+ nonlocally (orange circles in Fig. 5.2) due to the open-circuit condition. A $J_{m,\text{diff}}$ driven by it can therefore diffuse into the detector and convert into a signal, as shown in Fig. 5.2. Note that we do not assume the Pt detector to be a heat sink so that there is no heat current flowing into the Pt detector, but the detected magnon current is diffused from the YIG/GGG interface beneath it.

The signals at long distances hence decay independent of λ_m . To derive how they decay as a function of d , for simplicity we first assume that the thermal conductivities of YIG and GGG, κ_{YIG} and κ_{GGG} , are similar in value such that the heat flows radially even when $d > t_{\text{YIG}}$. At a certain d , the magnitude of the J_q that crosses the YIG/GGG interface is then proportional to $1/\pi r$, with $r = \sqrt{d^2 + t_{\text{YIG}}^2}$. $J_{m,q}$ reaches the bottom of the YIG layer at an angle θ , where $\theta = \arctan(t_{\text{YIG}}/d)$, as shown in Fig. 5.2. Yet only the part of $J_{m,q}$ that is normal to the YIG/GGG interface would encounter the GGG barrier and generates a μ_m^+ :

$$J_{m,q}^z \propto \frac{1}{\pi r} \cdot \sin \theta = \frac{t_{\text{YIG}}}{\pi(d^2 + t_{\text{YIG}}^2)} \stackrel{t_{\text{YIG}} \ll d}{\approx} \frac{t_{\text{YIG}}}{\pi d^2}. \quad (5.1)$$

The resulting μ_m^+ would then induce a diffusive magnon flow proportional to $J_{m,q}^z$, which can enter the detector at d . This explains the $1/d^2$ dependence of V_{TG} . Note that the signal at the detector V_{TG} is not necessarily proportional to t_{YIG} , as the relaxation from the bottom to the top side of YIG needs to be taken into account, unless t_{YIG} is much smaller than λ_m .

For the relation in Eq. 5.1 to hold, κ_{YIG} does not have to be strictly equal to κ_{GGG} . When $\kappa_{\text{YIG}} \neq \kappa_{\text{GGG}}$, the temperature profile is not radial any more, as the heat current J_q either prefers to flow laterally along the YIG layer ($\kappa_{\text{YIG}} \gg \kappa_{\text{GGG}}$) or tends to flow towards the bottom of the GGG layer ($\kappa_{\text{YIG}} \ll \kappa_{\text{GGG}}$). This complicates the math to derive the spatial dependence of $J_{m,q}^z$. However, from the numerical model discussed later we found that the $1/d^2$ dependence is in general valid as long as $\kappa_{\text{YIG}} \leq \kappa_{\text{GGG}}$ or $\kappa_{\text{YIG}} \approx \kappa_{\text{GGG}}$. Conversely, when $\kappa_{\text{YIG}} \gg \kappa_{\text{GGG}}$, the $1/d^2$ dependence no longer holds.

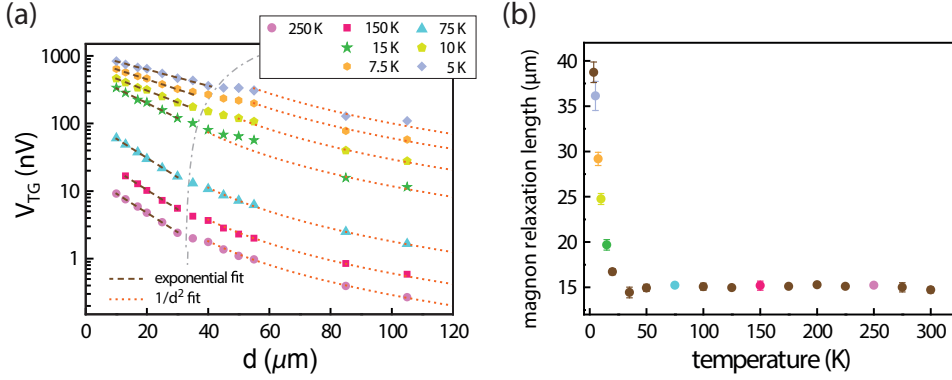


Figure 5.3: (a) Measured V_{TG} as a function of d for various temperatures on a 2.7- μm -thick YIG film. The exponential and quadratic decay fits are performed in a similar fashion as in Fig. 5.1. For $T < 20$ K, due to the increased λ_m , the exponential regimes extend to longer d , and consequently quadratic decay regimes start at further distances. But for the sake of consistency, the λ_m 's are all determined from exponential fits performed on the datapoints within $10 \mu\text{m} \leq d \leq 30 \mu\text{m}$. (b) λ_m 's extracted from exponential fits at temperatures from $T = 3.5$ to 300 K.

Results at low temperatures

We further performed the same measurements at various temperatures on 2.7- μm -thick YIG, in order to study λ_m carefully as a function of temperature, as well as to confirm the above picture.

The main results are shown in Fig. 5.3. As shown in Fig. 5.3(a), the V_{TG} for all distances is enhanced when decreasing the temperature, consistent with the general trend in our previous results on 0.21- μm -thick YIG film [31]. However, in this study, we do not observe reductions of V_{TG} below 7 K as in Ref. [31], which could be due to the subtle differences between the employed YIG films in both studies and still requires further investigation.

For almost all temperatures at which measurements are carried out, V_{TG} apparently cannot be fitted by a single exponential decay, similar to the observation at room temperature. Following the same procedure, we separate the data into two regimes and fit them into exponential and quadratic decay, respectively.

The extracted λ_m 's from the exponential fits across the whole temperature range are shown in Fig. 5.3(b). One can see that down to $T = 35$ K, λ_m remains more or less unchanged as a function of temperature. This is also in line with our previous study on 0.21- μm -thick YIG film [31]. At $T < 20$ K, however, we observe a sharp and monotonic increase of λ_m when reducing temperature. Consequently, the transition between the two decay regimes extend to a longer d , as the diffused magnon accumulation can be

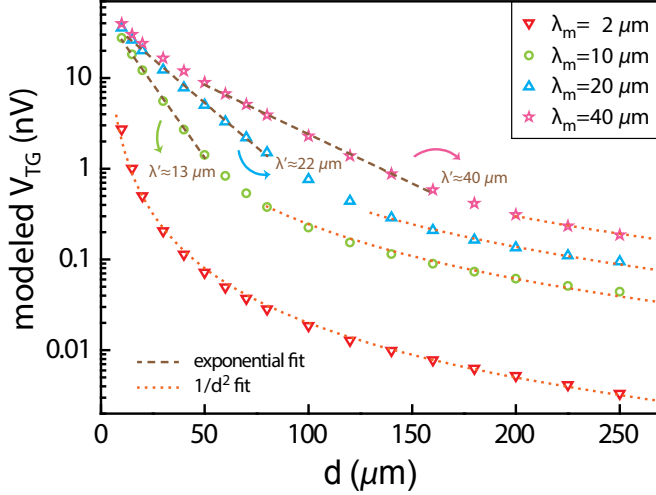


Figure 5.4: Modeling results of the nonlocal SSE signals on a 2.7- μm -thick YIG film in the range of $10 \mu\text{m} \leq d \leq 250 \mu\text{m}$, with different λ_m as modeling input, while all the other parameters are kept unvaried. The extracted length scales λ' by exponential fittings are indicated nearby. All the modeled signals presented here are after the sign-reversal distance.

further preserved.

The $1/d^2$ decay can be fitted satisfactorily at long distances even down to very low temperatures. From literature, both κ_{YIG} and κ_{GGG} of bulk materials vary by more than one order of magnitude from room temperature to their peak values, which take place roughly between 20 and 30 K [37–39]. Yet the general shapes of κ_{YIG} and κ_{GGG} as a function of temperature are very similar. Additionally, for YIG thin films, the thermal conductivities are found to be smaller than their bulk values [40]. Therefore, we can say that in the measured temperature range, $\kappa_{\text{YIG}} \leq \kappa_{\text{GGG}}$ should hold according to literature values.

2D Comsol modeling results

We perform next numerical modeling that solves profiles of the temperature and μ_m in our studied system using a Comsol model. From the model we can calculate V_{TG} for even further d than studied experimentally, which allows us to identify and study the different decay regimes more clearly.

We use a two-dimensional finite element model as already described in detail in Chap. 4. Except for a few geometrical parameters, such as Pt strip widths, Pt and YIG film thicknesses, the physics and the rest of the material parameters are kept to be the same as in Chap. 4 for the sake of consistency. In particular, the YIG magnon spin

conductivity σ_m and the effective spin mixing conductance G_s are $\sigma_m=5\times 10^5$ S/m and $G_s=9.6\times 10^{12}$ S/m², respectively. The focus of the numerical study in this section, however, is the modeled signals in the $1/d^2$ regime, which has not been investigated so far.

We do not aim for quantitative agreement between the experimental and modeled results, as in the model we only vary the input λ_m , while in reality, the change of temperature does not only evoke the variation of λ_m , but also other crucial parameters such as κ_{YIG} and κ_{GGG} , the magnon spin conductivity of YIG [31], the effective spin mixing conductance at the YIG/Pt interface and the spin Seebeck coefficient of YIG [18], etc. The absolute magnitudes of V_{TG} and the exact starting and ending distances of the exponential regimes, cannot be directly compared between the experimental and modeled results without several assumptions. Nevertheless, the model works qualitatively, so that the decay manner of V_{TG} can be studied and compared with experimental results.

Figure 5.4 shows the modeled V_{TG} as a function of distance up to $d = 250 \mu\text{m}$. We calculated the signals for different magnon relaxation length input λ_m to check the dependence of the two decay regimes on λ_m . The datapoints at very short distances before the sign reversal are not plotted here, as they are not of central interest in this study.

The modeled results reproduce the shapes of the experimental data quite well. The signals first exhibit an exponential decay, where the starting and ending distances depend on λ_m , and then followed by a $1/d^2$ decay. For $\lambda_m = 2 \mu\text{m}$, the exponential regime is too short and takes place before $d = 10 \mu\text{m}$, and therefore not captured in this plot. Instead, $1/d^2$ decay dominates the full investigated distance range.

One can also obtain the extracted magnon relaxation length λ' by fitting the exponential regimes. λ' is very close to the input λ_m , which justifies the way we extracted λ_m in Fig. 5.3.

5.3.2 Results on 50- μm -thick YIG

We now show a set of measurements on a 50- μm -thick YIG film. Similar devices as on 2.7- μm -thick YIG film were fabricated with d ranging from 10 μm to 80 μm .

In Ref. [19] we have already investigated d_{rev} of this YIG film at room temperature, which takes place between $d = 60 \mu\text{m}$ and $d = 80 \mu\text{m}$. In this study, we look at how the nonlocal SSE signals evolve at lower temperatures.

Figure 5.5(a) shows the V_{TG} as a function of d before the sign-reversal for various temperatures on a logarithmic scale. Except for the datapoints that are still close to the heater or close to the sign-reversals, the rest of the datapoints decay exponentially. The d_{rev} for each measured temperature is obtained by either interpolation or extrapolation, as shown in Fig. 5.5(b). The general trend of d_{rev} is similar as reported in

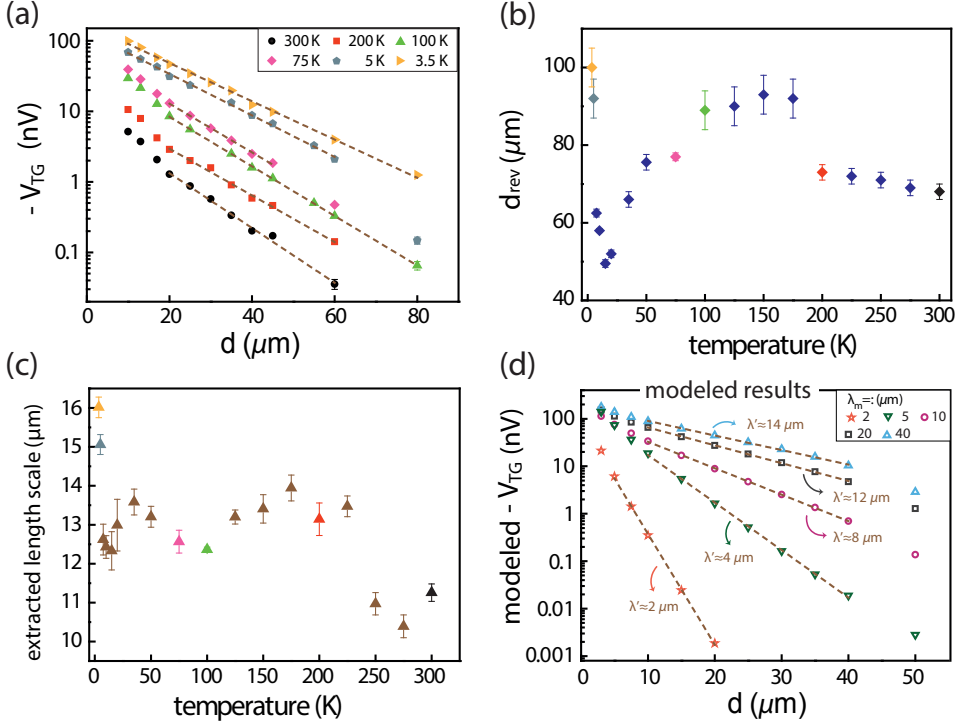


Figure 5.5: Experimental and modeling results on a 50- μm -thick YIG film. (a) $-V_{TG}$ as a function of d for various temperatures. Note that the sign of all datapoints plotted here are the same as the local SSE signal, which we define as negative. Only the datapoints before the sign-reversal are shown in this plot. Brown dashed lines are exponential fittings similar as described in Fig. 5.1, with the pre-exponential coefficients C being opposite in sign. (b) The sign-reversal distances obtained by interpolation ($d_{rev} < 80$ μm) and extrapolation ($d_{rev} > 80$ μm) for different temperatures. (c) The extracted length scales (not necessarily equal to λ_m) from exponential fits from $T = 3.5$ K to 300 K. (d) The modeled V_{TG} for different input λ_m , with extracted length scales λ' indicated nearby.

Ref. [30] down to $T=15$ K, where much thinner YIG films were investigated. However, we observed a clear upturn below $T=15$ K, which seems to correspond to the upturn of the increased λ_m as discussed below.

The length scales that are extracted from exponential fittings are shown in Fig. 5.5(c). However, the length scales extracted before the sign-reversal can underestimate the real λ_m if d_{rev} falls in the exponential regime, which can happen when t_{YIG} is comparable to λ_m . This can be true for low temperatures where λ_m greatly increases.

To see how much we could possibly undervalue λ_m , we perform finite element

modeling similar as above in Fig. 5.4, and check the results for different λ_m . For the modeling here, we adjusted two parameters to better fit the sign-reversal: σ_m was increased to 5×10^6 S/m and G_s was decreased to 1×10^{12} S/m². Note that the adjustment of these parameters is not related to the material property change between YIG films of different thicknesses, but is due to the model not being able to quantitatively fit the experimental data, especially between data series from different YIG thicknesses [15, 19]. This modification does not influence the qualitative behavior of the nonlocal SSE signals.

We fit the modeled V_{TG} exponentially and obtain the corresponding length scales λ' , as indicated in the figure. One can see that for $\lambda_m=2 \mu\text{m}$, we could extract a λ' which equals to λ_m . As λ_m is longer, the condition $t_{YIG} \gg \lambda_m$ gradually becomes invalid, and the deviation of λ' from λ_m gets larger.

It is therefore reasonable to assume that the extracted length scales in Fig. 5.5(b) are only valid at higher temperatures, while at lower temperatures the real λ_m 's can be longer than the extracted ones. Considering the model shows more than a factor of 2 difference between λ_m and λ' when $\lambda_m = 40 \mu\text{m}$, it is highly possible that, for instance, the real λ_m reaches around 30 to 40 μm at $T = 3.5$ K, which is consistent with the results obtained from the 2.7- μm -thick YIG film as shown in Fig. 5.3(b). However, experimentally it is very difficult to obtain the real λ_m for this thickness with the SSE method at very low temperatures.

5.3.3 Modeling results on bulk YIG

For the sake of completeness, we further model the nonlocal SSE signals for a bulk YIG sample, as employed in a recent experiment [34]. For such a thick YIG material, the sign reversal takes place much further than the normal studied distances, and the extraction of λ_m becomes again possible in the exponential regime. We do not expect the $1/d^2$ decay to play a significant role, as it should only show up after the sign-reversal. Yet it was shown both in the model and experiment that a deviation from the exponential decay can be observed at longer distances, caused by the presence of a ∇T close to the detector [34].

In the simulation, when we thermally detach the detector by setting the thermal conductivity of the detector/YIG interface to zero, the modeling results show a single exponential decay based on λ_m , as shown by the black circles. This suggests that the deviation is indeed caused by the unwanted heat current flowing into or out of the detector. To show to which extent the detector signals can be influenced, we intentionally introduce a Joule heating into the detector which amounts to 10^{-6} of the power in the injection heater, with the detector thermally coupled with YIG. The results are shown by the green triangles in Fig. 5.6, indicating that even very small heat flows would strong affect the signals at long distances.

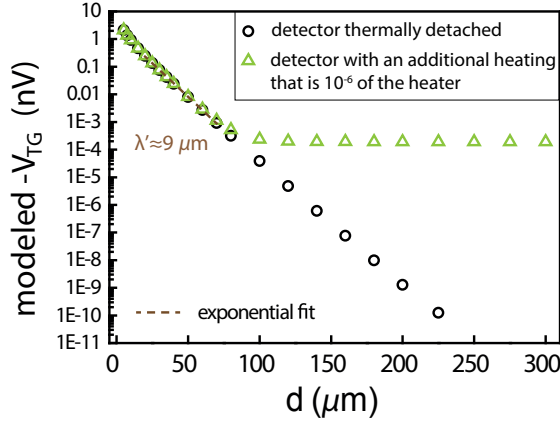


Figure 5.6: Modeling results of the nonlocal SSE signals on a bulk YIG material ($450 \mu\text{m}$ in thickness) in the range of $5 \mu\text{m} \leq d \leq 300 \mu\text{m}$. Black circles show a single exponential decay, with the detector thermally uncoupled from YIG. Green triangles show the situation when additional Joule heating (one millionth of the amount of the heating power in the heater) is added to the detector, deviating the signals significantly in the long-distance regime. All the modeled signals presented here are before the sign reversal.

These results show that in bulk YIG materials, one should extract λ_m by only investigating the exponential regime, whereas the datapoints beyond this regime should also be excluded. However, another length scale is not necessary to be included to describe the long- d behavior of the signals.

5.3.4 Summary

Based on the results from both YIG samples as well as previous results [19, 26] and modeling results, we map out a general diagram for different regimes in nonlocal SSE signals, as shown in Fig. 5.7. We consider three lengths, with d and t_{YIG} being geometrical lengths and λ_m being the system parameter.

In very short distances ($d < \lambda_m$), the system is in the diffusive regime, where the signals drop typically faster than the exponential decay [19, 26]. In the subsequent intermediate distances, the signals decay exponentially if the sign reversal is outside this regime. If there is no overlap between the relaxations of μ_m^+ and μ_m^- , then one can extract λ_m accurately from the decay of one of them, as indicated by the red zones in Fig. 5.7. Lastly, in very long distances ($d \gg \lambda_m$) the system enters the $1/d^2$ regime, where the signal reduction no longer depends on λ_m . But for bulk YIG materials, the long-distance range deviates from the exponential regime because of the heat flow into the detector, which is distinct from the $1/d^2$ regime.

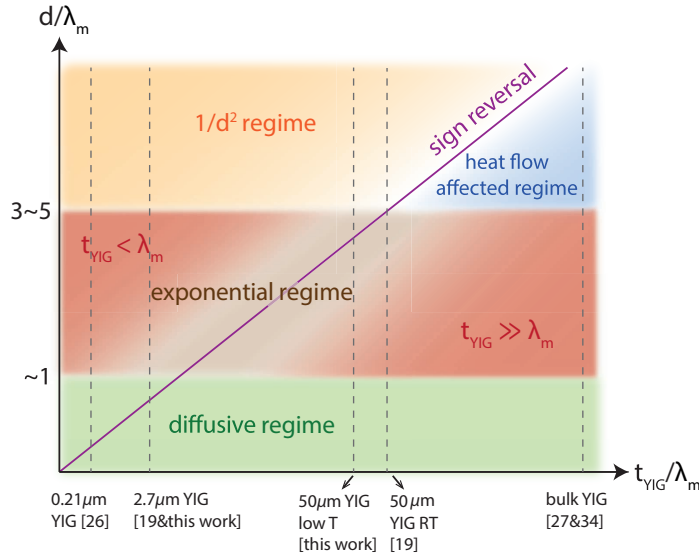


Figure 5.7: Schematic diagram showing different regimes for nonlocal SSE signals and the general rule for extracting λ_m using the thermal method. The purple line indicates the sign reversal, with the location d_{rev} linearly depending on t_{YIG} . Determination of λ_m should be performed only in the exponential regime and far away from the sign reversal, as indicated by the red-shaded areas. Blue-shaded area denotes the deviation from exponential regime caused by heat flowing into the detector.

One should hence be very careful in extracting λ_m from the lateral decay of the nonlocal SSE signal. Here we put forward a general rule of thumb to determine λ_m : One should only fit the datapoints in the exponential regime. t_{YIG} should be chosen such that the sign reversal takes place outside the exponential regime. Hence, t_{YIG} should be either very thin, such that the $d_{\text{rev}} < \lambda_m$ with the exponential decay reflecting the relaxation of μ_m^+ [26], or it should be so thick that $d_{\text{rev}} \gg \lambda_m$, and the exponential decay reflects the relaxation of μ_m^- [27, 34].

If the datapoints from the ultra-far distances are mistakenly evaluated and fitted to an exponential decay, the fitting procedure will result in an overestimation of λ_m . For YIG films where the $1/d^2$ decay dominates the ultra-far distances, the overestimated λ_m will converge to $d_{\text{long}}/2$, where d_{long} is the longest distance included in the fit. It is therefore crucial to look only at the proper regime when determining λ_m .

5.4 Conclusions

We studied the nonlocal SSE signals in a wide distance and temperature range. We find that for thin YIG films such as 2.7 μm in thickness, the signals exhibit first an exponential decay after the sign reversal, from which the magnon relaxation length can be estimated. Then they show a $1/d^2$ decay, due to the nonlocal generation of magnon accumulation by temperature gradient at the YIG/GGG interface near the detector. This observation further confirms the bulk generation mechanism of the SSE, and highlights the ultra-far distance detection of the nonlocal SSE signals assisted by thermal transport. We emphasize the delicate procedure to accurately obtain the magnon relaxation length from the thermally generated nonlocal signals, i.e., only the exponential regime should be investigated, with the sign reversal being far from it.

Combining our previous results on 0.21- μm -thick YIG films [26, 31] and the study of this paper, we found that at room temperature, λ_m 's are comparable between 0.21- μm -thick and 2.7- μm -thick YIG films, being around 9 μm and 15 μm , respectively, and in both cases they almost do not vary as a function of T above 20 K. However, at very low temperatures ($T < 20$ K), the λ_m extracted from the 0.21- μm -thick YIG film does not exhibit a sharp upturn as the 2.7- μm -thick YIG film, which grows to 40 μm at $T = 3.5$ K. Explanation for this different behavior on these two samples requires further investigation.

References

- [1] K. Uchida, S. Takahashi, K. Harii, J. Ieda, W. Koshibae, K. Ando, S. Maekawa, and E. Saitoh, "Observation of the spin Seebeck effect," *Nature* **455**, p. 778, Oct. 2008.
- [2] K. Uchida, J. Xiao, H. Adachi, J. Ohe, S. Takahashi, J. Ieda, T. Ota, Y. Kajiwara, H. Umezawa, H. Kawai, G. E. W. Bauer, S. Maekawa, and E. Saitoh, "Spin Seebeck insulator," *Nature Materials* **9**, pp. 894–897, Nov. 2010.
- [3] G. E. W. Bauer, A. H. MacDonald, and S. Maekawa, "'Spin Caloritronics'," *Solid State Communications* **150**, pp. 459–460, Mar. 2010.
- [4] G. E. W. Bauer, E. Saitoh, and B. J. van Wees, "Spin caloritronics," *Nature Materials* **11**, pp. 391–399, May 2012.
- [5] S. R. Boona, R. C. Myers, and J. P. Heremans, "Spin caloritronics," *Energy & Environmental Science* **7**, pp. 885–910, Feb. 2014.
- [6] A. Kirihara, K.-i. Uchida, Y. Kajiwara, M. Ishida, Y. Nakamura, T. Manako, E. Saitoh, and S. Yorozu, "Spin-current-driven thermoelectric coating," *Nature Materials* **11**, pp. 686–689, Aug. 2012.
- [7] C. M. Jaworski, J. Yang, S. Mack, D. D. Awschalom, R. C. Myers, and J. P. Heremans, "Spin-Seebeck Effect: A Phonon Driven Spin Distribution," *Physical Review Letters* **106**, p. 186601, May 2011.
- [8] K.-i. Uchida, T. Kikkawa, A. Miura, J. Shiomi, and E. Saitoh, "Quantitative Temperature Dependence of Longitudinal Spin Seebeck Effect at High Temperatures," *Physical Review X* **4**, p. 041023, Nov. 2014.
- [9] T. Kikkawa, K.-i. Uchida, S. Daimon, Z. Qiu, Y. Shiomi, and E. Saitoh, "Critical suppression of spin Seebeck effect by magnetic fields," *Physical Review B* **92**, p. 064413, Aug. 2015.
- [10] H. Jin, S. R. Boona, Z. Yang, R. C. Myers, and J. P. Heremans, "Effect of the magnon dispersion on the longitudinal spin Seebeck effect in yttrium iron garnets," *Physical Review B* **92**, p. 054436, Aug. 2015.
- [11] N. Vlietstra, J. Shan, B. J. van Wees, M. Isasa, F. Casanova, and J. Ben Youssef, "Simultaneous detection of the spin-Hall magnetoresistance and the spin-Seebeck effect in platinum and tantalum on yttrium iron garnet," *Physical Review B* **90**, p. 174436, Nov. 2014.
- [12] A. Kehlberger, U. Ritzmann, D. Hinzke, E.-J. Guo, J. Cramer, G. Jakob, M. C. Onbasli, D. H. Kim, C. A. Ross, M. B. Jungfleisch, B. Hillebrands, U. Nowak, and M. Kläui, "Length Scale of the Spin Seebeck Effect," *Physical Review Letters* **115**, p. 096602, Aug. 2015.
- [13] E.-J. Guo, J. Cramer, A. Kehlberger, C. A. Ferguson, D. A. MacLaren, G. Jakob, and M. Kläui, "Influence of Thickness and Interface on the Low-Temperature Enhancement of the Spin Seebeck Effect in YIG Films," *Physical Review X* **6**, p. 031012, July 2016.
- [14] T. Kikkawa, K. Shen, B. Flebus, R. A. Duine, K.-i. Uchida, Z. Qiu, G. E. W. Bauer, and E. Saitoh, "Magnon Polarons in the Spin Seebeck Effect," *Physical Review Letters* **117**, p. 207203, Nov. 2016.
- [15] L. J. Cornelissen, K. Oyanagi, T. Kikkawa, Z. Qiu, T. Kuschel, G. E. W. Bauer, B. J. van Wees, and E. Saitoh, "Nonlocal magnon-polaron transport in yttrium iron garnet," *Physical Review B* **96**, p. 104441, Sept. 2017.
- [16] D. Meier, D. Reinhardt, M. van Straaten, C. Klewe, M. Althammer, M. Schreier, S. T. B. Goennenwein, A. Gupta, M. Schmid, C. H. Back, J.-M. Schmalhorst, T. Kuschel, and G. Reiss, "Longitudinal spin Seebeck effect contribution in transverse spin Seebeck effect experiments in Pt/YIG and Pt/NFO," *Nature Communications* **6**, p. 8211, Sept. 2015.
- [17] R. A. Duine, A. Brataas, S. A. Bender, and Y. Tserkovnyak, *Universal themes of Bose-Einstein condensation, chapter 26*, Cambridge University Press, Cambridge, United Kingdom, Apr. 2017. Edited by David Snoke, Nikolaos Proukakis and Peter Littlewood.

- [18] L. J. Cornelissen, K. J. H. Peters, G. E. W. Bauer, R. A. Duine, and B. J. van Wees, "Magnon spin transport driven by the magnon chemical potential in a magnetic insulator," *Physical Review B* **94**, p. 014412, July 2016.
- [19] J. Shan, L. J. Cornelissen, N. Vlietstra, J. Ben Youssef, T. Kuschel, R. A. Duine, and B. J. van Wees, "Influence of yttrium iron garnet thickness and heater opacity on the nonlocal transport of electrically and thermally excited magnons," *Physical Review B* **94**, p. 174437, Nov. 2016.
- [20] A. Brataas, Y. V. Nazarov, and G. E. W. Bauer, "Finite-Element Theory of Transport in Ferromagnet-Normal Metal Systems," *Physical Review Letters* **84**, pp. 2481–2484, Mar. 2000.
- [21] M. Weiler, M. Althammer, M. Schreier, J. Lotze, M. Pernpeintner, S. Meyer, H. Huebl, R. Gross, A. Kamra, J. Xiao, Y.-T. Chen, H. Jiao, G. E. W. Bauer, and S. T. B. Goennenwein, "Experimental Test of the Spin Mixing Interface Conductivity Concept," *Physical Review Letters* **111**, p. 176601, Oct. 2013.
- [22] J. Xiao and G. E. W. Bauer, "Transport between metals and magnetic insulators," *arXiv:1508.02486 [cond-mat]*, Aug. 2015. arXiv: 1508.02486.
- [23] E. Saitoh, M. Ueda, H. Miyajima, and G. Tatara, "Conversion of spin current into charge current at room temperature: Inverse spin-Hall effect," *Applied Physics Letters* **88**, p. 182509, May 2006.
- [24] M. Agrawal, V. I. Vasyuchka, A. A. Serga, A. Kirihara, P. Pirro, T. Langner, M. B. Jungfleisch, A. V. Chumak, E. T. Papaioannou, and B. Hillebrands, "Role of bulk-magnon transport in the temporal evolution of the longitudinal spin-Seebeck effect," *Physical Review B* **89**, p. 224414, June 2014.
- [25] T. Hioki, R. Iguchi, Z. Qiu, D. Hou, K.-i. Uchida, and E. Saitoh, "Time-resolved study of field-induced suppression of longitudinal spin Seebeck effect," *Applied Physics Express* **10**, p. 073002, June 2017.
- [26] L. J. Cornelissen, J. Liu, R. A. Duine, J. B. Youssef, and B. J. van Wees, "Long-distance transport of magnon spin information in a magnetic insulator at room temperature," *Nature Physics* **11**, pp. 1022–1026, Dec. 2015.
- [27] B. L. Giles, Z. Yang, J. S. Jamison, and R. C. Myers, "Long-range pure magnon spin diffusion observed in a nonlocal spin-Seebeck geometry," *Physical Review B* **92**, p. 224415, Dec. 2015.
- [28] X. J. Zhou, G. Y. Shi, J. H. Han, Q. H. Yang, Y. H. Rao, H. W. Zhang, L. L. Lang, S. M. Zhou, F. Pan, and C. Song, "Lateral transport properties of thermally excited magnons in yttrium iron garnet films," *Applied Physics Letters* **110**, p. 062407, Feb. 2017.
- [29] J. Shan, P. Bougiatioti, L. Liang, G. Reiss, T. Kuschel, and B. J. van Wees, "Nonlocal magnon spin transport in NiFe₂O₄ thin films," *Applied Physics Letters* **110**, p. 132406, Mar. 2017.
- [30] K. Ganzhorn, T. Wimmer, J. Cramer, R. Schlitz, S. Geprägs, G. Jakob, R. Gross, H. Huebl, M. Kläui, and S. T. B. Goennenwein, "Temperature dependence of the non-local spin Seebeck effect in YIG/Pt nanostructures," *AIP Advances* **7**, p. 085102, Aug. 2017.
- [31] L. J. Cornelissen, J. Shan, and B. J. van Wees, "Temperature dependence of the magnon spin diffusion length and magnon spin conductivity in the magnetic insulator yttrium iron garnet," *Physical Review B* **94**, p. 180402, Nov. 2016.
- [32] S. T. B. Goennenwein, R. Schlitz, M. Pernpeintner, K. Ganzhorn, M. Althammer, R. Gross, and H. Huebl, "Non-local magnetoresistance in YIG/Pt nanostructures," *Applied Physics Letters* **107**, p. 172405, Oct. 2015.
- [33] S. M. Rezende, R. L. Rodríguez-Suárez, R. O. Cunha, A. R. Rodrigues, F. L. A. Machado, G. A. Fonseca Guerra, J. C. Lopez Ortiz, and A. Azevedo, "Magnon spin-current theory for the longitudinal spin-Seebeck effect," *Physical Review B* **89**, p. 014416, Jan. 2014.
- [34] B. L. Giles, Z. Yang, J. S. Jamison, J. M. Gomez-Perez, S. Vélez, L. E. Hueso, F. Casanova, and R. C. Myers, "Thermally driven long-range magnon spin currents in yttrium iron garnet due to intrinsic

- spin Seebeck effect," *Physical Review B* **96**, p. 180412, Nov. 2017.
- [35] N. Vlietstra, J. Shan, V. Castel, B. J. van Wees, and J. Ben Youssef, "Spin-Hall magnetoresistance in platinum on yttrium iron garnet: Dependence on platinum thickness and in-plane/out-of-plane magnetization," *Physical Review B* **87**, p. 184421, May 2013.
- [36] L. J. Cornelissen and B. J. van Wees, "Magnetic field dependence of the magnon spin diffusion length in the magnetic insulator yttrium iron garnet," *Physical Review B* **93**, p. 020403, Jan. 2016.
- [37] G. A. Slack and D. W. Oliver, "Thermal Conductivity of Garnets and Phonon Scattering by Rare-Earth Ions," *Physical Review B* **4**, pp. 592–609, July 1971.
- [38] Y. Hakuraku, "Thermal Conductivity of the Gadolinium Gallium Garnet, Gd₃Ga₅O₁₂, between 1.4 K and 20 K," *Japanese Journal of Applied Physics* **22**, p. 1465, Sept. 1983.
- [39] R. Iguchi, K.-i. Uchida, S. Daimon, and E. Saitoh, "Concomitant enhancement of the longitudinal spin Seebeck effect and the thermal conductivity in a Pt/YIG/Pt system at low temperatures," *Physical Review B* **95**, p. 174401, May 2017.
- [40] C. Euler, P. Hołuj, T. Langner, A. Kehlberger, V. I. Vasyuchka, M. Kläui, and G. Jakob, "Thermal conductance of thin film YIG determined using Bayesian statistics," *Physical Review B* **92**, p. 094406, Sept. 2015.

Chapter 6

Nonlocal magnon spin transport in NiFe₂O₄ thin films

Abstract

We report magnon spin transport in nickel ferrite (NiFe₂O₄, NFO)/platinum (Pt) bilayer systems at room temperature. A nonlocal geometry is employed, where the magnons are excited by the spin Hall effect or by the Joule heating induced spin Seebeck effect at the Pt injector, and detected at a certain distance away by the inverse spin Hall effect at the Pt detector. The dependence of the nonlocal magnon spin signals as a function of the magnetic field is closely related to the NFO magnetization behavior. In contrast, we observe that the magnetoresistance measured locally at the Pt injector does not show a clear relation with the average NFO magnetization. We obtain a magnon spin relaxation length of 3.1 ± 0.2 μm in the investigated NFO samples.

6.1 Introduction

The transport of spin information is one of the most extensively studied topics in the field of spintronics [1, 2]. Spin current, a flow of angular momentum, is a non-conserved quantity that is mostly transported diffusively in various material systems, regardless of the carrier being conduction electrons or quasiparticles such as magnons [3]. In traditional metallic systems [4] and 2D materials such as graphene [5], a nonlocal spin valve geometry is usually applied to study the spin diffusion phenomena and their relevant length scales.

Very recently, it was shown that thermal magnons with typical frequencies of around $k_B T/h$ can be excited and detected purely electrically in Pt/yttrium iron garnet (YIG) systems, by also employing a nonlocal geometry where the injector and detector are both Pt strips, spaced at a certain distance [3, 6–9]. An electric current through the injector excites non-equilibrium magnons both electrically via the spin Hall effect (SHE) [10, 11] and thermally via the spin Seebeck effect (SSE) [12–14], and they are detected nonlocally via the inverse spin Hall effect (ISHE) [15]. At room temperature and below [16], a magnon relaxation length λ_m of typically around 10 μm is observed, for both electrically and thermally generated magnons independent from the YIG thickness [17].

An open question is whether the nonlocal effects can be also observed in other magnetic materials, such as ferrites, being ferrimagnetic at room temperature with a relatively large bandgap. Two local effects have been studied in Pt/ferrite systems so far: The first is the spin Hall magnetoresistance (SMR) [18–21], which results from the simultaneous action of SHE and ISHE in the Pt layer, while the magnetization in the magnetic substrate modifies the spin accumulation at the interface and hence the Pt resistance. SMR has been reported in Pt/ NiFe_2O_4 (NFO), Pt/ Fe_3O_4 and Pt/ CoFe_2O_4 systems [20, 22–24]. Second is the SSE, one of the central topics in the field of spin caloritronics [25], which is the excitation of magnon currents when exerting a temperature gradient on the magnetic material. Previously, SSE has been observed in ferrites and other magnetic spinels [26–32]. However, the nonlocal transport of magnon spin has not yet been explored in ferrite systems.

6.2 Experimental details

In this study, we focus on the NFO thin film systems which can be prepared by co-sputtering [33], whereby a typical bandgap of 1.49 eV and a resistivity of $40 \Omega\cdot\text{m}$ can be obtained at room temperature. The electrical properties of the NFO films can be further tuned by temperature [26] or oxygen contents [34]. The employed NFO thin films were grown by ultra high vacuum reactive dc magnetron co-sputtering in a pure oxygen atmosphere of 2×10^{-3} mbar, with the deposition rate of $0.12 \text{ \AA}/\text{s}$. The substrate is MgAl_2O_4 (MAO), a nonmagnetic spinel which is known to have a lattice mismatch to NFO as small as 1.3%. It was heated up to 610°C during deposition and kept rotating to ensure a homogeneous growth.

The crystallinity of the NFO/MAO sample was investigated by x-ray diffraction, confirming a (001) orientation for both NFO layer and MAO substrate. The thickness of the NFO layer was determined by x-ray reflectivity to be 44.0 ± 0.5 nm. The sample was characterized by a superconducting quantum interference device (SQUID) to obtain its magnetic behavior. It is known that in an inverse spinel magnetic thin film with (001) orientation, a four-fold magnetic anisotropy is expected in-plane, with two magnetic easy axes aligned perpendicular to each other [26, 27]. Figure 6.1(a) plots the NFO magnetization when an in-plane magnetic field is applied along one of the magnetic hard axes, showing a coercive field of around 0.2 T.

To study the magnon spin transport in the NFO, two Pt strips, parallel to each other and separated by a center-to-center distance d , were patterned by e -beam lithography and grown on the NFO layer by dc sputtering. The Pt strips are all oriented along one of the magnetic hard axes. The lengths of the Pt strips are typically $10 \mu\text{m}$ and the widths range from 100 nm to $1 \mu\text{m}$. Two series of samples were fabricated, with the Pt thickness of 2 nm (series A) and 7 nm (series B). Due to the difference in thickness,

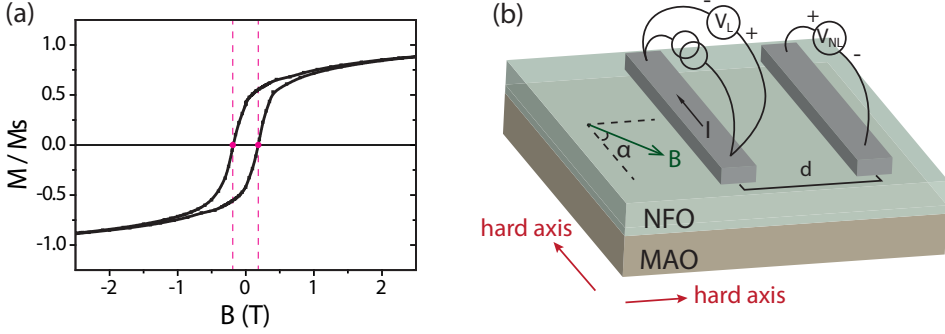


Figure 6.1: (a) In-plane magnetization curve obtained by SQUID measurements. A diamagnetic linear background has been subtracted, where the slope is determined from the high-field regime up to $B = 7$ T. The whole curve is subsequently normalized to the saturation magnetization M_s at $B = 7$ T. The coercive field is around 0.2 T. (b) Schematic representation of the device geometry and measurement configuration. Two Pt strips, one serves as the injector and the other as the detector, were sputtered onto the NFO surface, separated by a center-to-center distance d . The local voltage V_L at the injector and nonlocal voltage V_{NL} at the detector can be measured simultaneously. The magnetic field is applied in the plane by an angle α .

the Pt resistivities of the two series turn out to be quite different, where $\rho_A = (0.9 - 2.4) \times 10^{-6} \Omega \cdot \text{m}$ and $\rho_B = 3.5 \times 10^{-7} \Omega \cdot \text{m}$, respectively, which is within a factor of two in line with literature [20, 35, 36]. As a final step, the Pt strips were connected to Ti (5 nm)/Au (50 nm) contacts.

A lock-in detection technique was employed in the electrical measurements. A low-frequency (~ 13 Hz) ac current, with an rms value I_0 (typically $I_0 = 100 \mu\text{A}$), was sent through the Pt injector as input, while two output voltages can be monitored simultaneously: the local voltage V_L at the same strip, and the nonlocal voltage V_{NL} at the Pt detector, as shown in Fig. 6.1(b). Both V_L and V_{NL} are separated into the first (V^{1f}) and second (V^{2f}) harmonic signals by the lock-in amplifiers, which probes the linear and quadratic effects, respectively. The mathematical expressions are $V^{1f} = I_0 \cdot R^{1f}$ and $V^{2f} = \frac{1}{\sqrt{2}} I_0^2 \cdot R^{2f}$, where R^{1f} (R^{2f}) is the first (second)-order response coefficient [37, 38]. Hence, for the local detection, R_L^{1f} represents the Pt strip resistance, as well as its magnetoresistance, and R_L^{2f} shows the local SSE that was induced by Joule heating [39, 40]. The transport behavior of magnons can be found in the nonlocal detection, where R_{NL}^{1f} denotes the signal due to the magnons that are injected electrically via the SHE, and R_{NL}^{2f} illustrates the nonlocal signals of the thermally generated magnons [3, 16, 17, 41]. All measurements were performed in vacuum at room temperature.

6.3 Results and discussion

Figure 6.2 shows the experimental results obtained by rotating the sample in-plane, under a certain magnetic field strength B . The nonlocal results are shown in the left panel while the local results are plotted in the right panel as a comparison. One typical measurement curve of the nonlocal geometry in its first order response is shown in Fig. 6.2(a), where $d = 1.5 \mu\text{m}$. The applied in-plane magnetic field, $B = 3 \text{ T}$, is large enough to align the NFO magnetization M during the full rotation. The measured data exhibits a sinusoidal behavior with a period of 180° , the same as observed in Pt/YIG systems [3, 16, 17, 41]. In the injector, as a result of the SHE, a spin accumulation μ_s builds up at the Pt/NFO interface, with its orientation always transverse to the electric current. The magnon excitation is activated when the projection of μ_s on the M is nonzero. The excited magnons become maximal when μ_s is collinear with M , and vanish when they are perpendicular to each other. Hence, the injection efficiency is governed by $\sin(\alpha)$, and the same holds for the reciprocal process at the detector, in total yielding a $\sin^2(\alpha)$ dependence.

We further investigate the amplitude of this signal, ΔR_{EI} , as a function of the magnetic field B , as shown in Fig. 6.2(b). Each datapoint that is extracted by fitting the corresponding angular sweep data to a $\sin^2(\alpha)$ curve, represents the amplitude of the oscillation. It can be seen that ΔR_{EI} increases rapidly from 0 to $\pm 1 \text{ T}$, and grows slowly as B becomes larger. Two other devices with $d = 10 \mu\text{m}$ and $12 \mu\text{m}$, show the same dependence despite with different signal amplitudes. This dependence is in accordance with the NFO magnetization curve shown in Fig. 6.1(a). In the non-saturated situation, the local M is not oriented along the external magnetic field B as a result of domain formation. When $\alpha = \pm 90^\circ$, the projection factor of μ_s on M is equal to 1 for the saturated case and becomes smaller than 1 for the non-saturated case. Similarly, when $\alpha = 0^\circ$, the projection factor for the saturated case is 0, but becomes nonzero for the non-saturated case. In this way, the difference between a parallel and perpendicularly applied field decreases when B becomes smaller and M gets more unsaturated.

Simultaneously we recorded the local signals. Figure 6.2(c) shows a typical first-order response under $B = 3 \text{ T}$, exhibiting a magnetoresistance behavior, and Fig. 6.2(d) shows the MR amplitude as a function of the magnetic field. In the SMR scenario, ΔR_{MR} should depend on M instead of on B , as the key ingredient in the SMR theory is the interaction between μ_s and M . Surprisingly, our results show that ΔR_{MR} keeps increasing with a larger B , even when above the saturation field of NFO. This behavior can be alternatively explained by the recently reported Hanle magnetoresistance (HMR), [42] which is an intrinsic property of metallic thin films with large spin-orbit coupling and depends only on B instead of M . The MR ratio we obtained is in the same order of magnitude as reported in Ref. [42]. However, it is not

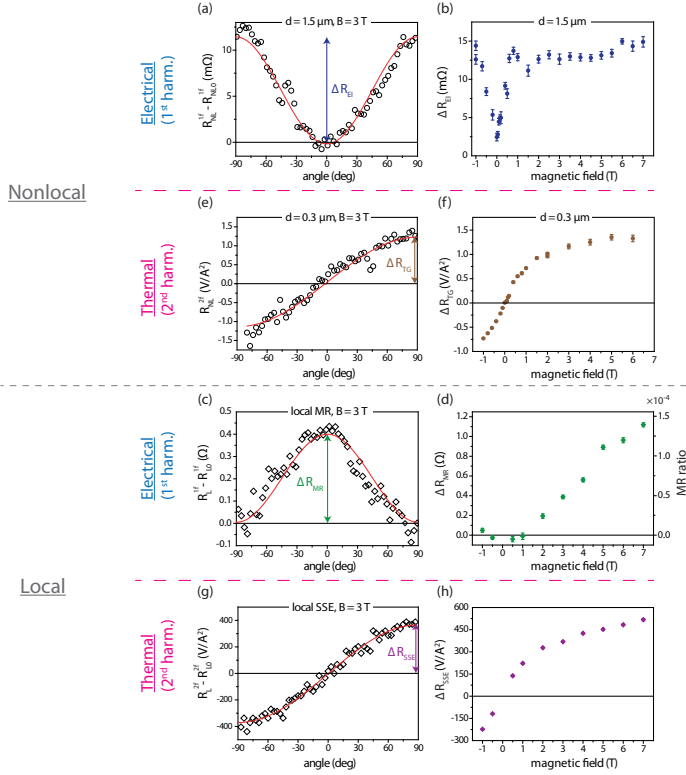


Figure 6.2: Comparison of both the electrical and thermal effects between nonlocal and local geometries under angle sweep, measured with different magnetic fields. (a) The first harmonic nonlocal signal with Pt spacing $d = 1.5 \mu\text{m}$ while sweeping α , measured at $B = 3 \text{ T}$. The background resistance R_{NLO} is -4.733Ω . The red curve shows a $\sin^2(\alpha)$ fit to the data. ΔR_{EI} is defined as the amplitude of the electrically injected, nonlocally detected magnon signal. (b) The dependence of ΔR_{EI} as a function of the magnetic field at $d=1.5 \mu\text{m}$. (c) Local MR measurement at $B = 3 \text{ T}$. The background resistance R_{LO} is 8056Ω . The red curve shows a $\sin^2(\alpha)$ fit to the data. ΔR_{MR} is defined as the amplitude of the local MR signal. (d) The dependence of ΔR_{MR} as a function of the magnetic field. Right axis indicates the MR ratio, which is $\Delta R_{\text{MR}}/8056 \Omega$. (e) The nonlocal detection of the thermally generated magnons with Pt spacing $d = 0.3 \mu\text{m}$, $B = 3 \text{ T}$. The red curve is a $\sin(\alpha)$ fit. Its amplitude, ΔR_{TG} , depends on the magnetic field as shown in (f). (g) The angular dependence of the local SSE measured at $B = 3 \text{ T}$. The subtracted background is -21.4 kV/A^2 . The red curve shows a $\sin(\alpha)$ fit to the data. ΔR_{SSE} is defined as the amplitude of the local SSE signal. (h) The dependence of ΔR_{SSE} as a function of the magnetic field. Data in (e), (f) are from sample series B and the rest are from series A.

yet clear why we do not observe the SMR feature on top of HMR.

The different dependences between the ΔR_{EI} and ΔR_{MR} as a function of B rule out the possibility of any charge current leakage from the injector to the detector, in which case the nonlocal signal would mimic the local magnetoresistance behavior. Moreover, the ratios of the resistance changes compared to the backgrounds differ by two orders of magnitude for the local and nonlocal responses, further eliminating this scenario¹. In addition, the nonlocal signals were also investigated at different lock-in excitation frequencies, and the ΔR_{EI} keeps almost unvaried with no systematic dependence on frequency, implying that the ΔR_{EI} is not affected by any capacitive coupling. Therefore, we can conclude that the ΔR_{EI} we measured is indeed due to magnon spin transport in NFO.

The second-order local responses which are due to thermally generated magnons are shown in the lower right panel of Fig. 6.2, detected in a nonlocal (left) or a local method (right). Both signals show a $\sin(\alpha)$ behavior as a function of α , governed by the ISHE at the detector. Their amplitudes, ΔR_{TC} and ΔR_{SSE} , mainly follow the evolution of M , in accordance with previous studies in the Pt/NFO system [26, 43] and other Pt/ferrite systems [27, 28]. However, the rise of the thermal signals is less sharp than that of M around the coercive field, for reasons that are not yet clear to us. The sign of the local SSE results shows to be the same as in Pt/YIG systems [44].

Experimentally we defined the polarities of the local and nonlocal voltages to be opposite in the measurement scheme (see Fig. 6.1(b)). Hence, the same shape in Figs. 6.2(e) and (g) indicates that the actual signs of the local and nonlocal SSE signals are opposite. This is similar to the observation in Pt/YIG systems, where at closer spacings the sign of the nonlocal SSE signals are the same as the local one, but at further d the sign is reversed [3, 17]. However, to determine the exact sign-reversal distance in this sample and how it evolves on the NFO thickness, requires further study and is beyond the scope of the discussion of this chapter.

Note that Figs. 6.2(e)(f) are obtained from sample series B. Due to the large resistivities of the Pt strips in sample series A and hence a limited electric current that can be sent, the second-harmonic signals in the nonlocal detection, which scale with I_0^2 , are below the noise level. We can, however, detect them in series B. The local behaviors for both series are very similar as a function of α and B , with the amplitude ΔR_{SSE} around 5 times larger in sample series B. However, ΔR_{EI} in series B is observed to be much smaller compared to series A, which can be attributed to the thicker Pt films and lower resistivity. Only for the shortest distance, where $d = 300$ nm, we obtained a ΔR_{EI} response beyond the noise floor, showing the same magnetic field dependence as series A.

¹Except for the devices with $d=1.5$ μm from series A, the first-harmonic background resistances R_{NLO} from devices of both series are all smaller than 100 m Ω in their absolute values.

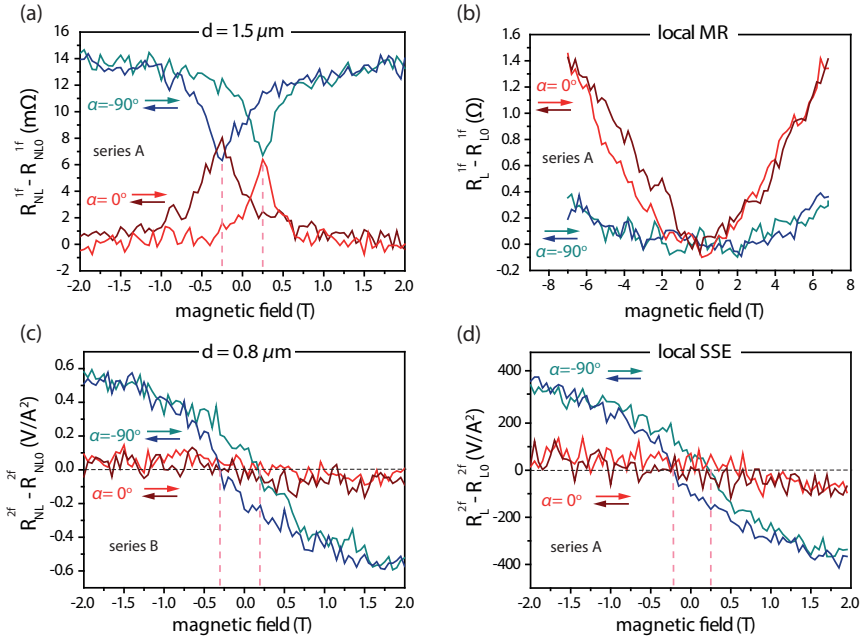


Figure 6.3: Magnetic field sweep results for (a) the nonlocal signal by electrical injection, (b) the local MR, (c) the nonlocal signal by thermal generation and (d) the local SSE at $\alpha = -90^\circ$ and $\alpha = 0^\circ$. The results in (a), (b) and (d) are obtained from sample series A and (c) is from sample series B.

To further study the relation between the observed signals and the NFO magnetization, we also performed magnetic field sweep measurements at two specific angles, $\alpha = -90^\circ$ and $\alpha = 0^\circ$, as shown in Fig. 6.3. In principle, this measurement would yield the same information as obtained from the angular sweep measurements, as the differences between $\alpha = -90^\circ$ and 0° correspond to the signal amplitudes extracted from the sinusoidal curves in Fig. 6.2. However, in the angular sweep experiments, M rotates in the plane, and hence the effects related to the magnetization hysteresis cannot be directly observed. In comparison, field-sweep measurements allow to resolve these features. Note that $\alpha = 0^\circ$ and -90° correspond to the two equivalent in-plane magnetic hard axes. In both cases, the behavior of M can be described by the $M - B$ curve in Fig. 6.1(a).

The field-sweep results are shown in Fig. 6.3. Similar as in Fig. 6.2, the local magnetoresistance do not show any features related to the NFO magnetization curve, which would be produced by the SMR. In contrast, both the local and nonlocal SSE signals show the typical hysteresis behaviors, with the coercive fields being very close

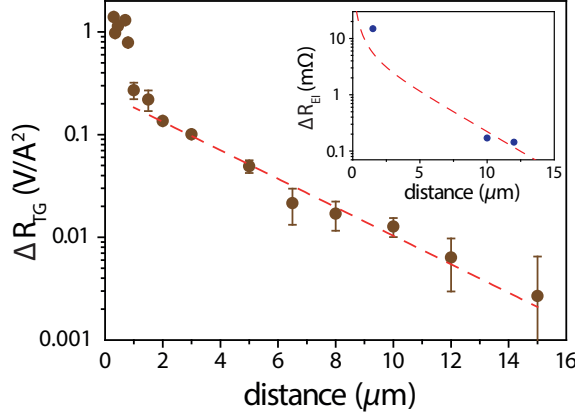


Figure 6.4: The thermally generated nonlocal signal response R_{TG} as a function of d , plotted in logarithmic scale. Red dashed line is an exponential decay fit $A \exp(-d/\lambda_m)$, with A being a d -independent coefficient, yielding a λ_m of $3.1 \pm 0.2 \mu\text{m}$. The results are obtained from series B. Inset shows the dependence of R_{EI} as a function of d from series A, fitted with $C/\lambda_m \cdot \exp(d/\lambda_m)/(1 - \exp(2d/\lambda_m))$ with $\lambda_m = 3.1 \mu\text{m}$. All results are normalized to the typical Pt strip geometry ($0.1 \mu\text{m} \times 10 \mu\text{m}$) as described in Ref. [17].

to the ones extracted from the $M - B$ hysteresis loop.

One interesting observation is the electrically injected magnon transport signal under the field sweep, as shown in Fig. 6.3(a). The peaks and dips for $\alpha = -90^\circ$ and 0° , occurring at the coercive fields, correspond to the situation where the net magnetization in the field direction is zero. In this case, the thermally generated magnon signals vanish to zero, as expected, but interestingly the electrically injected magnon signals show half of its maximum signal amplitude. Considering that multiple domains can form with the magnetizations aligned along both of the magnetic easy axes in this material around the coercive fields, our results hence suggest the transport of magnons in a multi-domain state.

To estimate λ_m in the NFO sample, we performed a distance-dependent study of the nonlocal signals. In Fig. 6.4, we plot the thermally generated nonlocal signals as a function of d when M is saturated by the field. Due to the more complicated behavior for the short- d regime [17], we only fit the data exponentially where $d \geq 1 \mu\text{m}$. This yields a λ_m of $3.1 \pm 0.2 \mu\text{m}$ in the investigated NFO sample. This result is supported by the electrically injected magnon signals from series A obtained at $B = 7 \text{ T}$, which can be fitted satisfactorily with the same λ_m , by applying $\Delta R_{\text{NL}}(d) = C/\lambda_m \cdot \exp(d/\lambda_m)/(1 - \exp(2d/\lambda_m))$ [3] (see inset of Fig. 6.4). Given that the Gilbert damping coefficient α of an NFO thin film is 3.5×10^{-3} [45], around one order of magnitude higher than a typical α of YIG thin films, a reduction of λ_m of NFO

compared to YIG is expected, as observed in our experiments.

6.4 Conclusions

In conclusion, we have experimentally observed the transport of both electrically and thermally excited magnons in NFO thin films. The nonlocal signals of both exciting methods are directly related to the average NFO in-plane magnetization, while the local MR is not, showing that the nonlocal results are more sensitive to the NFO magnetization or domain texture. Our results also suggest that the study of magnon spin transport can be extended to other materials such as ferrimagnetic spinel ferrites, not only limited to YIG, showing the ubiquitous nature of the exchange magnon spin diffusion.

References

- [1] S. A. Wolf, D. D. Awschalom, R. A. Buhrman, J. M. Daughton, S. v. Molnár, M. L. Roukes, A. Y. Chtchelkanova, and D. M. Treger, "Spintronics: A Spin-Based Electronics Vision for the Future," *Science* **294**, pp. 1488–1495, Nov. 2001.
- [2] I. Žutić, J. Fabian, and S. Das Sarma, "Spintronics: Fundamentals and applications," *Reviews of Modern Physics* **76**, pp. 323–410, Apr. 2004.
- [3] L. J. Cornelissen, J. Liu, R. A. Duine, J. B. Youssef, and B. J. van Wees, "Long-distance transport of magnon spin information in a magnetic insulator at room temperature," *Nature Physics* **11**, pp. 1022–1026, Dec. 2015.
- [4] F. J. Jedema, A. T. Filip, and B. J. van Wees, "Electrical spin injection and accumulation at room temperature in an all-metal mesoscopic spin valve," *Nature* **410**, pp. 345–348, Mar. 2001.
- [5] N. Tombros, C. Jozsa, M. Popinciuc, H. T. Jonkman, and B. J. van Wees, "Electronic spin transport and spin precession in single graphene layers at room temperature," *Nature* **448**, pp. 571–574, Aug. 2007.
- [6] S. T. B. Goennenwein, R. Schlitz, M. Pernpeintner, K. Ganzhorn, M. Althammer, R. Gross, and H. Huebl, "Non-local magnetoresistance in YIG/Pt nanostructures," *Applied Physics Letters* **107**, p. 172405, Oct. 2015.
- [7] J. Li, Y. Xu, M. Aldosary, C. Tang, Z. Lin, S. Zhang, R. Lake, and J. Shi, "Observation of magnon-mediated current drag in Pt/yttrium iron garnet/Pt(Ta) trilayers," *Nature Communications* **7**, p. 10858, Mar. 2016.
- [8] H. Wu, C. H. Wan, X. Zhang, Z. H. Yuan, Q. T. Zhang, J. Y. Qin, H. X. Wei, X. F. Han, and S. Zhang, "Observation of magnon-mediated electric current drag at room temperature," *Physical Review B* **93**, p. 060403, Feb. 2016.
- [9] S. Vélez, A. Bedoya-Pinto, W. Yan, L. E. Hueso, and F. Casanova, "Competing effects at Pt/YIG interfaces: Spin Hall magnetoresistance, magnon excitations, and magnetic frustration," *Physical Review B* **94**, p. 174405, Nov. 2016.
- [10] J. E. Hirsch, "Spin Hall Effect," *Physical Review Letters* **83**, pp. 1834–1837, Aug. 1999.
- [11] J. Sinova, S. O. Valenzuela, J. Wunderlich, C. H. Back, and T. Jungwirth, "Spin Hall effects," *Reviews of Modern Physics* **87**, pp. 1213–1260, Oct. 2015.
- [12] K. Uchida, S. Takahashi, K. Harii, J. Ieda, W. Koshibae, K. Ando, S. Maekawa, and E. Saitoh, "Observation of the spin Seebeck effect," *Nature* **455**, p. 778, Oct. 2008.
- [13] K. Uchida, J. Xiao, H. Adachi, J. Ohe, S. Takahashi, J. Ieda, T. Ota, Y. Kajiwara, H. Umezawa, H. Kawai, G. E. W. Bauer, S. Maekawa, and E. Saitoh, "Spin Seebeck insulator," *Nature Materials* **9**, pp. 894–897, Nov. 2010.
- [14] J. Xiao, G. E. W. Bauer, K.-c. Uchida, E. Saitoh, and S. Maekawa, "Theory of magnon-driven spin Seebeck effect," *Physical Review B* **81**, p. 214418, June 2010.
- [15] E. Saitoh, M. Ueda, H. Miyajima, and G. Tatara, "Conversion of spin current into charge current at room temperature: Inverse spin-Hall effect," *Applied Physics Letters* **88**, p. 182509, May 2006.
- [16] L. J. Cornelissen, J. Shan, and B. J. van Wees, "Temperature dependence of the magnon spin diffusion length and magnon spin conductivity in the magnetic insulator yttrium iron garnet," *Physical Review B* **94**, p. 180402, Nov. 2016.
- [17] J. Shan, L. J. Cornelissen, N. Vlietstra, J. Ben Youssef, T. Kuschel, R. A. Duine, and B. J. van Wees, "Influence of yttrium iron garnet thickness and heater opacity on the nonlocal transport of electrically and thermally excited magnons," *Physical Review B* **94**, p. 174437, Nov. 2016.

- [18] H. Nakayama, M. Althammer, Y.-T. Chen, K. Uchida, Y. Kajiwara, D. Kikuchi, T. Ohtani, S. Geprägs, M. Opel, S. Takahashi, R. Gross, G. E. W. Bauer, S. T. B. Goennenwein, and E. Saitoh, "Spin Hall Magnetoresistance Induced by a Nonequilibrium Proximity Effect," *Physical Review Letters* **110**, p. 206601, May 2013.
- [19] N. Vlietstra, J. Shan, V. Castel, B. J. van Wees, and J. Ben Youssef, "Spin-Hall magnetoresistance in platinum on yttrium iron garnet: Dependence on platinum thickness and in-plane/out-of-plane magnetization," *Physical Review B* **87**, p. 184421, May 2013.
- [20] M. Althammer, S. Meyer, H. Nakayama, M. Schreier, S. Altmannshofer, M. Weiler, H. Huebl, S. Geprägs, M. Opel, R. Gross, D. Meier, C. Klewe, T. Kuschel, J.-M. Schmalhorst, G. Reiss, L. Shen, A. Gupta, Y.-T. Chen, G. E. W. Bauer, E. Saitoh, and S. T. B. Goennenwein, "Quantitative study of the spin Hall magnetoresistance in ferromagnetic insulator/normal metal hybrids," *Physical Review B* **87**, p. 224401, June 2013.
- [21] Y.-T. Chen, S. Takahashi, H. Nakayama, M. Althammer, S. T. B. Goennenwein, E. Saitoh, and G. E. W. Bauer, "Theory of spin Hall magnetoresistance," *Physical Review B* **87**, p. 144411, Apr. 2013.
- [22] M. Isasa, A. Bedoya-Pinto, S. Vélez, F. Golmar, F. Sánchez, L. E. Hueso, J. Fontcuberta, and F. Casanova, "Spin Hall magnetoresistance at Pt/CoFe₂O₄ interfaces and texture effects," *Applied Physics Letters* **105**, p. 142402, Oct. 2014.
- [23] M. Isasa, S. Vélez, E. Sagasta, A. Bedoya-Pinto, N. Dix, F. Sánchez, L. E. Hueso, J. Fontcuberta, and F. Casanova, "Spin Hall Magnetoresistance as a Probe for Surface Magnetization in Pt/CoFe₂O₄ Bilayers," *Physical Review Applied* **6**, p. 034007, Sept. 2016.
- [24] Z. Ding, B. L. Chen, J. H. Liang, J. Zhu, J. X. Li, and Y. Z. Wu, "Spin Hall magnetoresistance in Pt/Fe₃O₄ thin films at room temperature," *Physical Review B* **90**, p. 134424, Oct. 2014.
- [25] G. E. W. Bauer, E. Saitoh, and B. J. van Wees, "Spin caloritronics," *Nature Materials* **11**, pp. 391–399, May 2012.
- [26] D. Meier, T. Kuschel, L. Shen, A. Gupta, T. Kikkawa, K. Uchida, E. Saitoh, J.-M. Schmalhorst, and G. Reiss, "Thermally driven spin and charge currents in thin NiFe₂O₄/Pt films," *Physical Review B* **87**, p. 054421, Feb. 2013.
- [27] E.-J. Guo, A. Herklotz, A. Kehlberger, J. Cramer, G. Jakob, and M. Kläui, "Thermal generation of spin current in epitaxial CoFe₂O₄ thin films," *Applied Physics Letters* **108**, p. 022403, Jan. 2016.
- [28] T. Niizeki, T. Kikkawa, K.-i. Uchida, M. Oka, K. Z. Suzuki, H. Yanagihara, E. Kita, and E. Saitoh, "Observation of longitudinal spin-Seebeck effect in cobalt-ferrite epitaxial thin films," *AIP Advances* **5**, p. 053603, May 2015.
- [29] R. Ramos, T. Kikkawa, K. Uchida, H. Adachi, I. Lucas, M. H. Aguirre, P. Algarabel, L. Morellón, S. Maekawa, E. Saitoh, and M. R. Ibarra, "Observation of the spin Seebeck effect in epitaxial Fe₃O₄ thin films," *Applied Physics Letters* **102**, p. 072413, Feb. 2013.
- [30] T. Kuschel, C. Klewe, P. Bougiatioti, O. Kuschel, J. Wollschläger, L. Bouchenoire, S. D. Brown, J. M. Schmalhorst, D. Meier, and G. Reiss, "Static Magnetic Proximity Effect in Pt Layers on Sputter-Deposited NiFe₂O₄ and on Fe of Various Thicknesses Investigated by XRMR," *IEEE Transactions on Magnetics* **52**, pp. 1–4, July 2016.
- [31] K.-i. Uchida, T. Nonaka, T. Ota, and E. Saitoh, "Longitudinal spin-Seebeck effect in sintered polycrystalline (Mn,Zn)Fe₂O₄," *Applied Physics Letters* **97**, p. 262504, Dec. 2010.
- [32] A. Aqeel, N. Vlietstra, J. A. Heuver, G. E. W. Bauer, B. Noheda, B. J. van Wees, and T. T. M. Palstra, "Spin-Hall magnetoresistance and spin Seebeck effect in spin-spiral and paramagnetic phases of multiferroic CoCr₂O₄ films," *Physical Review B* **92**, p. 224410, Dec. 2015.

- [33] C. Klewe, M. Meinert, A. Boehnke, K. Kuepper, E. Arenholz, A. Gupta, J.-M. Schmalhorst, T. Kuschel, and G. Reiss, "Physical characteristics and cation distribution of NiFe₂O₄ thin films with high resistivity prepared by reactive co-sputtering," *Journal of Applied Physics* **115**, p. 123903, Mar. 2014.
- [34] P. Bougiatioti, C. Klewe, D. Meier, O. Manos, O. Kuschel, J. Wollschläger, L. Bouchenoire, S. D. Brown, J.-M. Schmalhorst, G. Reiss, and T. Kuschel, "Quantitative Disentanglement of the Spin Seebeck, Proximity-Induced, and Ferromagnetic-Induced Anomalous Nernst Effect in Normal-Metal/Ferromagnet Bilayers," *Physical Review Letters* **119**, p. 227205, Nov. 2017.
- [35] V. Castel, N. Vlietstra, J. Ben Youssef, and B. J. van Wees, "Platinum thickness dependence of the inverse spin-Hall voltage from spin pumping in a hybrid yttrium iron garnet/platinum system," *Applied Physics Letters* **101**(13), pp. 132414–132414, 2012.
- [36] M.-H. Nguyen, D. C. Ralph, and R. A. Buhrman, "Spin Torque Study of the Spin Hall Conductivity and Spin Diffusion Length in Platinum Thin Films with Varying Resistivity," *Physical Review Letters* **116**, p. 126601, Mar. 2016.
- [37] F. L. Bakker, A. Slachter, J.-P. Adam, and B. J. van Wees, "Interplay of Peltier and Seebeck Effects in Nanoscale Nonlocal Spin Valves," *Phys. Rev. Lett.* **105**, p. 136601, Sept. 2010.
- [38] J. Flipse, F. L. Bakker, A. Slachter, F. K. Dejene, and B. J. v. Wees, "Direct observation of the spin-dependent Peltier effect," *Nature Nanotechnology* **7**, pp. 166–168, Mar. 2012.
- [39] M. Schreier, N. Roschewsky, E. Dobler, S. Meyer, H. Huebl, R. Gross, and S. T. B. Goennenwein, "Current heating induced spin Seebeck effect," *Applied Physics Letters* **103**, p. 242404, Dec. 2013.
- [40] N. Vlietstra, J. Shan, B. J. van Wees, M. Isasa, F. Casanova, and J. Ben Youssef, "Simultaneous detection of the spin-Hall magnetoresistance and the spin-Seebeck effect in platinum and tantalum on yttrium iron garnet," *Physical Review B* **90**, p. 174436, Nov. 2014.
- [41] L. J. Cornelissen and B. J. van Wees, "Magnetic field dependence of the magnon spin diffusion length in the magnetic insulator yttrium iron garnet," *Physical Review B* **93**, p. 020403, Jan. 2016.
- [42] S. Vélez, V. N. Golovach, A. Bedoya-Pinto, M. Isasa, E. Sagasta, M. Abadia, C. Rogero, L. E. Hueso, F. S. Bergeret, and F. Casanova, "Hanle Magnetoresistance in Thin Metal Films with Strong Spin-Orbit Coupling," *Physical Review Letters* **116**, p. 016603, Jan. 2016.
- [43] T. Kuschel, C. Klewe, J.-M. Schmalhorst, F. Bertram, O. Kuschel, T. Schemme, J. Wollschläger, S. Francoual, J. Stremper, A. Gupta, M. Meinert, G. Götz, D. Meier, and G. Reiss, "Static Magnetic Proximity Effect in Pt/NiFe₂O₄ and Pt/Fe Bilayers Investigated by X-Ray Resonant Magnetic Reflectivity," *Physical Review Letters* **115**, p. 097401, Aug. 2015.
- [44] M. Schreier, G. E. W. Bauer, V. I. Vasyuchka, J. Flipse, K.-i. Uchida, J. Lotze, V. Lauer, A. V. Chumak, A. A. Serga, S. Daimon, T. Kikkawa, E. Saitoh, B. J. v. Wees, B. Hillebrands, R. Gross, and S. T. B. Goennenwein, "Sign of inverse spin Hall voltages generated by ferromagnetic resonance and temperature gradients in yttrium iron garnet platinum bilayers," *Journal of Physics D: Applied Physics* **48**, p. 025001, Jan. 2015.
- [45] C. Vittoria, S. D. Yoon, and A. Widom, "Relaxation mechanism for ordered magnetic materials," *Physical Review B* **81**, p. 014412, Jan. 2010.

Appendix A

Fabrication techniques

This appendix describes the typical procedures and techniques for fabricating the devices studied in this thesis. First of all, an introduction is given on the general steps for device fabrication. Then the core techniques—lithography and deposition methods, are explained separately afterwards.

A.1 Overall procedure

The material structures contained in the devices are of micro- or nanoscale in size, and they often need to be layered in accurate positions to contact with, or avoid contacting, the existing material structures on the sample. These processes demand nanofabrication techniques to define their geometries and positions precisely, such as electron-beam lithography (e-beam lithography, or EBL) used in our experiments. The thicknesses of the materials deposited are typical in nanometer scale, and therefore require thin-film deposition technologies. All the fabrication steps are carried out in cleanroom laboratory environments.

The general steps for one round of fabrication are (Fig. A.1):

1. **Substrate cleaning:** Prior to all fabrication steps, the substrate is immersed in warm acetone (around 45°C) for around 10 minutes. Subsequently, it is rinsed with isopropyl alcohol (IPA) and dried with a nitrogen spray gun. This step helps to remove dirt or impurities on the surface of the sample.
2. **Resist spinning:** In our experiments, we have used the positive PMMA (poly-methyl methacrylate) e-beam resists with a molecular mass of 950K dissolved in ethyl lactate, purchased from Allresist GmbH, Germany. PMMA is polymer that is very sensitive to highly focused electron beams or deep UV light. With correct exposure parameters, the exposed part becomes solvable in the developer due to the change of chemical structure.

The PMMA resist is spun on the substrate at 4000 revolutions per minute (rpm) for 1 minute with a spin coater. The resulting PMMA film thickness depends on the concentration of the PMMA solution. In our experiment, 3% and 4% PMMA yield about 160 and 270 nm of the film thickness, respectively. The sample is

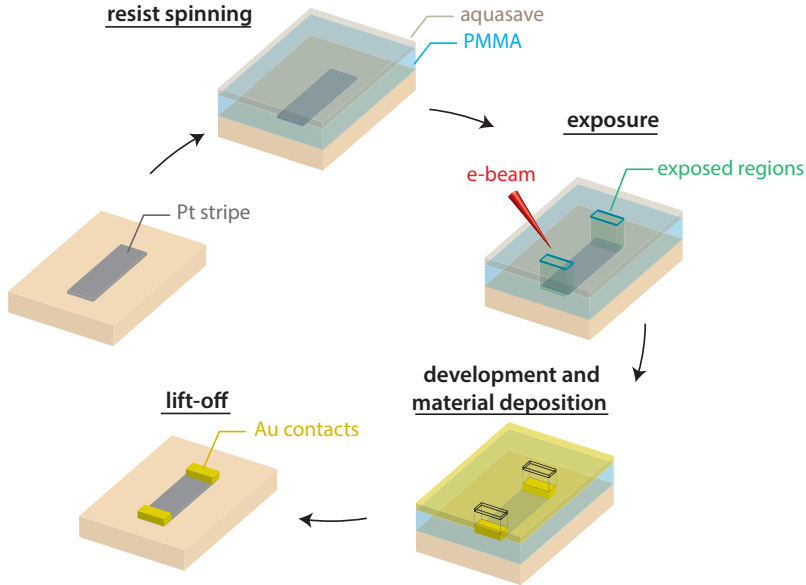


Figure A.1: Flow chart of one round of fabrication steps.

baked at 180°C for 90 seconds on a hotplate immediately afterwards to remove the solvent.

For insulating substrates such as YIG/GGG or NFO/MAO, an additional conductive thin layer is needed on top of the PMMA layer to prevent electrons from accumulating on the resist surface in the EBL step. In our experiments we have spun an conductive polymer aqueous solution “aquasave”, purchased from Mitsubishi Chemical Corporation, at 4000 rpm for 1 minute with a spin coater.

- 3. Exposure:** In our experiments, all samples are patterned by EBL with predefined structures. More details are given in the next section.
- 4. Development:** Before development, first the aquasave layer is removed with the sample rinsed in deionized water for 20 seconds. After being dried, the sample is dipped in the developer, a mixture solution of methyl isobutyl ketone (MIBK):IPA (1:3 of volume ratio) for 30 seconds. This step removes the exposed part of the PMMA layer from the sample. Immediately thereafter, the sample is rinsed thoroughly in IPA to stop the development and dried with a nitrogen spray gun.

5. **Material deposition:** The sample is loaded into a thin-film deposition system to grow the intended material onto the sample. In our experiments, we use two deposition techniques, e-beam evaporation and dc sputtering, which are described in the following sections. In this step, the material is grown directly on the sample in the previously exposed part, and onto the PMMA layer in other areas.
6. **Lift-off:** After deposition, the sample is immersed in warm acetone for at least 15 minutes. This step dissolves all PMMA and removes the material on top of it. After being dried, the resulting sample now has the desired material only at the expose area.

A complete device for measurements usually consists of several materials with different structures. In that case, more rounds are needed with steps 2–6 repeated for each material deposition. Finally, the sample is glued to a chip carrier and bonded for electrical measurements.

A.2 Electron beam lithography

EBL is a powerful lithography technique which can pattern custom structures with an accelerated beam of electrons, allowing for a resolution typically in the order of 10 nm. The EBL system we used is a Raith e-line lithography system.

After a sample is coated with EBL resist, it is loaded into the EBL chamber and pumped to a pressure lower than 2×10^{-5} mbar. After setting the acceleration voltage (30 kV in our experiments) and aperture size (10, 30, 60 or 120 μm , depending on the structure size), a quick current test needs to be performed at the “Faraday cup” location. This allows the system to calculate the beam dwell time during exposure for a certain given dose, which is typically $450 \mu\text{C}/\text{cm}^2$ for the EBL resists and acceleration voltage we use.

For an unprocessed sample without any existing structures, the first step is to define markers (see Fig. A.2), to which all the other structures written in the following steps will be aligned. Depending on the size of the designed structures, a proper write field needs to be chosen, followed by the write-field alignment procedure which adjusts the beam deflection on the sample to the stage movement. The marker structures are usually deposited with gold (Au), and should be preferably thicker than 60 nm for optimal visibility in subsequent EBL steps. In our experiments, the Au material for markers are e-beam evaporated for easier lift-off process.

In the following rounds, an additional step, 3-point adjustment, needs to be carried out after the write-field alignment. This step associates the coordinate of the stage (X,Y,Z) to that of the wafer (U,V,W) with the help of the markers. For multiple devices

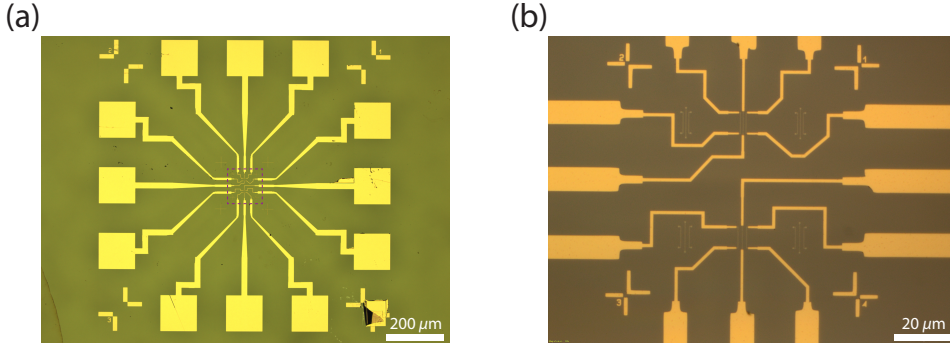


Figure A.2: (a) Optical microscope image of a typical finished device in our experiments. Large Au squares are patterned at the outer part of the sample, which will be connected to the bonding pads of a chip carrier for electrical measurements. They are designed to contact the fine structures in the middle. A write field of $1 \times 1 \text{ mm}^2$ is chosen for writing them, with an aperture of $120 \text{ }\mu\text{m}$. Four markers are patterned at the corner of the write field for coordinate alignment. (b) The zoom-in view of the central region of (a) indicated by the dashed square. To pattern these fine structures, a write field of $100 \times 100 \text{ }\mu\text{m}^2$ is used with an aperture of $10 \text{ }\mu\text{m}$. A set of smaller markers (manual markers) are patterned for finer coordinate adjustment.

arranged in an array, it needs to be performed both globally and locally for accurate alignment with more than one set of markers (Fig. A.2).

A

A.3 Electron beam evaporation

E-beam evaporation is a kind of physical vapor deposition (PVD) technique. In this method, a target material is heated by an accelerated electron beam in a vacuum environment. With the energy of the surface atoms increased by the electron beam, these atoms gradually start to leave the target material and traverse in the vacuum chamber. When they reach the substrate positioned above the evaporating material, a thin film can be formed on the substrate.

The system we used is a Temescal FC-2000 e-beam evaporator. The base pressure for material growth is typically around 1×10^{-6} Torr. The deposition rate is set to be typically $1 \text{ \AA}/\text{s}$ for the initial growth, and can be increased to $3 \text{ \AA}/\text{s}$ after a certain thickness (e.g., 20 nm). In the works described in this thesis, we have used e-beam evaporation to grow materials such as Au, Ti, Al_2O_3 , etc.

A.4 Sputter deposition

Sputter deposition is another PVD method. Different from e-beam evaporation, the target material is bombarded instead of heated by energetic particles. The bombardment results in the ejection of atoms from target materials, which can deposit onto a substrate and form a thin film. A common way to create energetic particles is to accelerate ions in a plasma near the target using strong electric and magnetic fields. The plasma is often generated from an inert gas, such as argon used in our system.

Compared with evaporation, one advantage of sputtering is that the materials with very high melting points can be easily sputtered. Also, the composition of alloys can be largely maintained during deposition, while for evaporation this can be difficult due to the different evaporation rates of materials in the alloy. However, the lift-off process after sputtering is in general more difficult than for evaporation, as the material is coated onto the “side-walls” of the resists during sputtering, so that during lift-off the resist is less exposed to acetone. This is because of the fact that the sputtering process is much less directional than evaporation.

The system we used is a Kurt J. Lesker sputtering system. The base pressure before deposition is around 6×10^{-7} mbar, and the pressure during deposition with a constant Ar flow is typically 3×10^{-3} mbar. We have sputtered Pt and constantan alloy (NiCu) in different studies, with typical deposition rates of 0.7 and 0.6 nm/s, respectively.

Appendix B

Measurement techniques

After a device is fabricated and bonded to a chip carrier, it can be loaded into measurement setups for electrical characterization. An electrical measurement setup in our laboratory typically consists of: 1) One or more lock-in amplifiers (Stanford Research SR 830), which can source an ac voltage and detect the output based on the lock-in technique, as explained in the following section; 2) A homebuilt IV measurement box that functions both as a current source and a preamplifier; 3) A homebuilt switch box that directly connects to the sample holder, and is used to switch each bonded contact on the sample among three statuses: connected, grounded and floated.

A magnetic field is often necessary to be applied on the sample during measurement. In our study, two measurement setups with different types of magnets are employed. In the studies of Chapt. 3 and 4, the used measurement setup includes an electromagnet (GMW 5403), which can generate magnetic fields up to 1 T with a pole distance typically around 5 cm. The sample is placed in the middle of the two poles of the magnet and measured in air at room temperature. In the studies of Chapt. 5 and 6, measurements are performed in a cryostat with a superconducting magnet that can provide magnetic fields up to 7 T. The sample is positioned in the sample space of a variable temperature insert (VTI), which allows measurements to be carried out typically between 2 K and 310 K. This is realized by controlling the helium flow from the helium bath to the sample space with a needle valve, as well as a proportional-integral-derivative (PID) control of the current applied to the heater on the heat exchanger, which adjusts the temperature of the exchange helium gas entering the sample space.

B

B.1 Lock-in technique

The primary electrical measurement method used in our studies is the lock-in technique, which is able to resolve small signals down to nanovolts in a noisy background. Here we present a brief introduction to this technique.

As plotted in Fig. B.1, a lock-in amplifier provides an ac signal with a frequency f to the measured sample as the input, and it can single out the voltage component

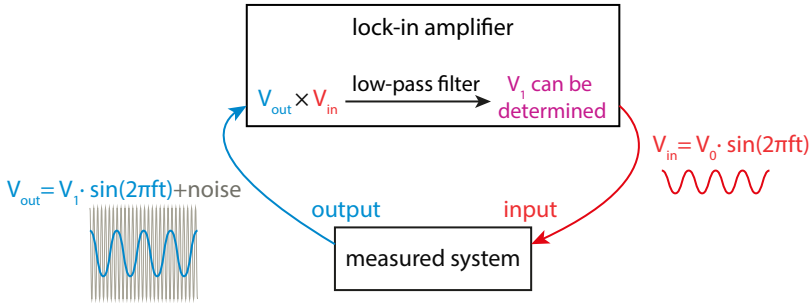


Figure B.1: A schematic illustration of the lock-in detection technique. A lock-in amplifier generates an ac signal V_{in} as an input to the measured system. The output signal V_{out} is sent back to the lock-in amplifier and multiplied by the reference signal (here the reference signal is equal to V_{in} to detect first-order response). After low-pass filtering, a dc signal is obtained which is proportional to V_1 and V_0 , whereby V_1 can be extracted. Ideally, all noise components at other frequencies are eliminated.

at f (or a multiple of f) from the output signal. The multiplication of the output signal with a reference ac signal (with a reference frequency at f or a multiple of f) results in a dc voltage and an extra ac voltage. This dc voltage is of main interest, as it is proportional to the amplitude of the output signal component at that reference frequency. The dc voltage can be extracted by time averaging or low-pass filtering of the product signal. In this way, noise signals at frequencies other than the detection frequency are filtered out. A mathematic description of this technique is given in Sec. 3.6.2 (Eq. 3.5).

Other than reducing noise, another important advantage of the lock-in detection technique is that it can separate different order responses of the output voltage. For instance, in a relatively simple system that includes only linear and quadratic responses, i.e., $V(I) = R_1 I + R_2 I^2$, where R_1 and R_2 are the first and second order coefficients, respectively, the voltage detected at the first ($1f$) and second harmonic ($2f$) are

$$V^{1f} = I_0 R_1 \quad (\phi = 0^\circ) \quad (\text{B.1a})$$

$$\text{and} \quad V^{2f} = I_0^2 \frac{1}{\sqrt{2}} R_2 \quad (\phi = -90^\circ), \quad (\text{B.1b})$$

respectively, where I_0 is the root mean square (rms) value of the input current, and ϕ is the phase of the reference detection signal. Hence with two lock-in amplifiers set with different detection frequencies and phases, the first and second order responses can be separately determined.

However, if higher-order responses are present, V^{1f} will have additional contributions from the higher, odd-order responses and V^{2f} will include part of the higher,

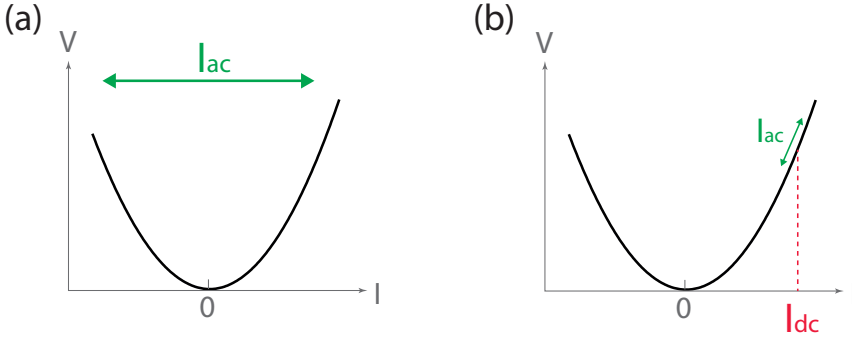


Figure B.2: The concept of lock-in measurements with a dc bias. The black curves represent a possible response relation. (a) The standard lock-in measurement where no dc bias is applied. The excitation ac current needs to be large enough to probe the desired signal, and higher-order responses can thus mix into lower harmonic signals. (b) The lock-in measurement performed with a dc current I_{dc} . The ac modulation from lock-in is small so that the differential signal at I_{dc} is probed.

even-order responses. In this case, the lower-order responses need to be calculated from a linear combination of different harmonic signals. This is explained in detail in Sec. 3.6.2 with expressions of V^{nf} , considering up to 5th-order response in the system (Eq. 3.6).

Obviously, when the measured signal contains non-negligible higher-order responses, it is complicated to separate and determine all different order responses from the standard lock-in measurements. In this situation, another method can be useful which combines the lock-in modulation with a dc bias, as shown in Fig. B.2. This method is employed in Chapt. 3 to measure the I - V characteristics of an MTJ (Fig. 3.7(a)).

For simplicity, we first assume that the response relation of a certain system includes only first and second harmonic responses, i.e., $V(I) = R_1I + R_2I^2$. The input of the system is $I = \sqrt{2}I_0 \sin(2\pi ft) + I_{dc}$, where I_0 is the rms value of the ac modulation and I_{dc} is the applied bias. Based on Eq. 3.5, one can obtain

$$V^{1f} = I_0 \cdot (R_1 + 2R_2I_{dc}) \quad (\phi = 0^\circ) \quad (\text{B.2a})$$

$$\text{and} \quad V^{2f} = I_0^2 \cdot \frac{1}{\sqrt{2}}R_2 \quad (\phi = -90^\circ) \quad (\text{B.2b})$$

as first and second harmonic signals, respectively. Compared with Eq. B.1, the expression of V^{2f} is the same, but the second order coefficient R_2 enters V^{1f} and contributes to a signal that is proportional to both I_0 and I_{dc} . In fact, V^{1f}/I_0 is the differential resistance dV/dI at I_{dc} . Sweeping I_{dc} and integrating V^{1f}/I_0 with respect to I_{dc} can thus recover the full response relation.

Naturally, this method works also for systems with higher-order responses. Considering up to third-order response with $V(I) = R_1 I + R_2 I^2 + R_3 I^3$, it can be calculated that

$$V^{1f} = I_0 \cdot (R_1 + 2R_2 I_{dc} + 3R_3 I_{dc}^2 + \frac{3}{2} R_3 I_0^2) \quad (\phi = 0^\circ), \quad (\text{B.3a})$$

$$V^{2f} = I_0^2 \cdot \frac{1}{\sqrt{2}} (R_2 + 3R_3 I_{dc}) \quad (\phi = -90^\circ), \quad (\text{B.3b})$$

$$V^{3f} = I_0^3 \cdot -\frac{1}{2} R_3 \quad (\phi = 0^\circ). \quad (\text{B.3c})$$

The last term of V^{1f}/I_0 is due to the presence of R_3 . It can be however disregarded if I_0 is substantially small, which is usually preferable for this kind of measurements. The signal amplitude is not sacrificed with a small I_0 provided a relatively large I_{dc} .

Appendix C

Finite element modeling method

Quantitative study is essential in physics research, and especially, plays an important role in this thesis for studying material transport properties. Often, in a complex system that consists of different materials with particular geometries, the analytical calculation can be very hard, or even impossible to perform. The finite element modeling (FEM) method, employed in three studies of this thesis (Chapt. 3, 4 and 5), is a powerful tool for the numerical solution of partial differential equations (PDEs) that embody the physical processes involved in the system. The general idea of FEM is to divide the entire system into many fine parts (finite elements) and solve the equations individually with proper boundary conditions. The function variables (i.e., electric voltage V , spin voltage V_s or temperature T , etc.) can then be evaluated everywhere in the system. The FEM software used in our studies is COMSOL Multiphysics.

The purposes to perform FEM in our studies mainly include:

- * To examine whether the physical processes considered are accurate or complete by comparing the modeling results to the experimental observations;
- * To study the influence of certain (geometrical) parameters on the experimental results, which can be used as a guidance for experimental design;
- * To estimate and report interesting physical parameters of the studied materials, which are not (well-)known from literature.

In this appendix, we describe the FEM method used in our study in detail. First we introduce the basic principles for implementing the physics into the model. Then we illustrate the processes and results with two concrete examples.

C.1 Basic concepts

The models we build for our studies are all stationary, i.e., time-independent. After a device geometry that simulates the actual device structure is created, the model solves the diffusion equations of electron charge, spin and heat transport, along the

same line as described in Ref. [1]. The core equation is the continuity equation, in the form of

$$\vec{\nabla} \cdot (-c\vec{\nabla}u) = f(u), \quad (\text{C.1})$$

where u is the field variable such as V , V_s or T , c is the conductivity, and f is the source term. The expression $-c\vec{\nabla}u$ thus stands for the flux \vec{J} . For different physics processes, different parameters are used for c and f , for instance:

- ★ For charge transport where u is the electric voltage, c is the electrical conductivity and $f = 0$ due to the charge conservation law (Eq. 2.3).
- ★ For magnon spin transport where u is the magnon chemical potential, c is the magnon spin conductivity and f represents the spin relaxation ($f = -\sigma_m\mu_m/\lambda^2$, Eq. 4.6). It means that spin currents are absorbed with the strength parameterized by λ , the spin relaxation length, of that particular material.
- ★ For heat transport where u is the temperature, c is the heat conductivity and f represents the Joule heating ($f = J_c^2/\sigma_e$, Eq. 4.10). It means that heat is produced at the regions where charge currents flow through. The generated Joule heat depends also on the electrical conductivity of that particular material.

In our study we often consider multiple processes altogether, say, n processes. This makes u an $1 \times n$ vector ($\vec{u} = (u_1, u_2, \dots, u_n)$) that contains different field variables and c an $n \times n$ matrix. The coupling between two processes can be then implemented into the off-diagonal terms of c , meaning the driving force of one physical flux can induce also another one, and vice versa (by reciprocity).

By default, no fluxes can leak out from the boundaries, unless indicated otherwise. Two types of boundary conditions can be set for a certain boundary, i.e., a Dirichlet or a Neumann condition, where either u or \vec{J} is specified.

C.2 Nonlocal magnon spin transport

In this section we include more details on the modeling of magnon spin transport in a magnetic insulator, which is employed in both Chapters 4 and 5. The studied device geometry is illustrated in Fig. 2.10(b), and the main procedures are discussed in Sec. 4.4.

Although the sample to simulate is three-dimensional (3D) in reality, in the studies presented in Chapters 4 and 5, we only model its cross-section to reduce the calculation time. This two-dimensional (2D) model is a very good approximation to real device because experimentally, the length of the injector and detector strips is typically much longer than their spacing, making the system almost invariant along the strip direction. The created geometry is partly shown in Fig. C.1(a) and is subsequently meshed as Fig. C.1(b).

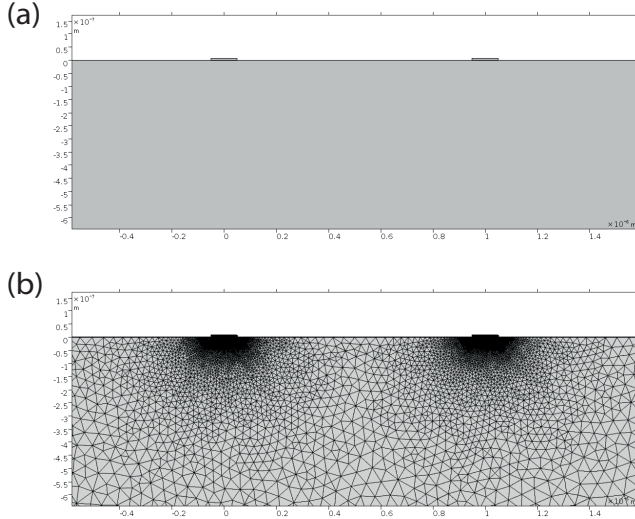


Figure C.1: (a) The zoom-in view of the 2D geometry created in the Comsol software. Only two Pt contacts and part of the YIG layer are shown. The thickness of the YIG layer is $2.7 \mu\text{m}$. (b) The mesh generated by the software with free triangles. The triangles are very fine in small regions to ensure adequate resolution, and gradually grow larger in big regions to boost the calculation efficiency. In total, the number of the finite elements created is in the order of 10^5 .

Next, we indicate in the software what materials different regions stand for. In the studied model, the injector and detector are made of platinum (Pt), while the transport channel is yttrium iron garnet (YIG), on top the substrate gadolinium gallium garnet (GGG). Their material properties, such as electrical/magnon spin conductivities, spin relaxation lengths are inserted into the model following Table 4.2.

The most important step is to implement the physics equations into the model. Experimentally, two physical processes take place in the device simultaneously during the measurement: 1) the creation and transport of electrically injected magnons, and 2) the creation and transport of thermally excited magnons. In our study, we consider these two processes individually by having two models with the same geometry and mesh but different physical equations to solve. The boundary conditions are also given separately.

For electrical injected magnons, the field variable u is the spin/magnon chemical potential (μ_s or μ_m). The input equations and boundary conditions have been described in Sec. 4.4.1. The calculation results determine the μ_s or μ_m for every element, and we can evaluate this variable at the areas of interest. Here we show a visualized solution obtained from the software in Fig. C.2. The μ_m can be evaluated at the bottom

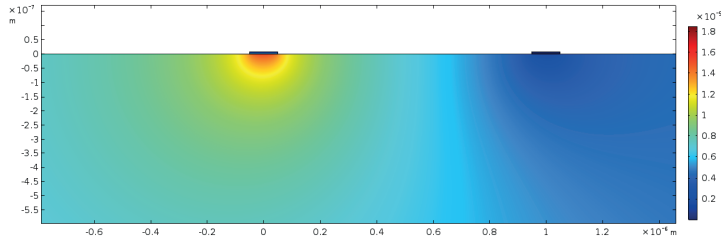


Figure C.2: The magnon chemical potential profile calculated for electrical injection of magnons from the injector (left contact). In this plot, the center-to-center spacing between the injector and detector is $1 \mu\text{m}$.

of the detector, and the inverse spin Hall voltage can be calculated following Eq. 4.8. This is the result which can be directly compared with the experimental signal.

For thermally excited magnons, the field variable u includes both μ_m and temperature T . The profiles of both variables are shown in Fig. C.3, following the procedure described in Sec. 4.4.2. Figure C.3(b) show that the sign of μ_m reverses at a certain distance from the heater, in consistent with our physics picture described in Sec. 2.5.1 and 4.3.2.

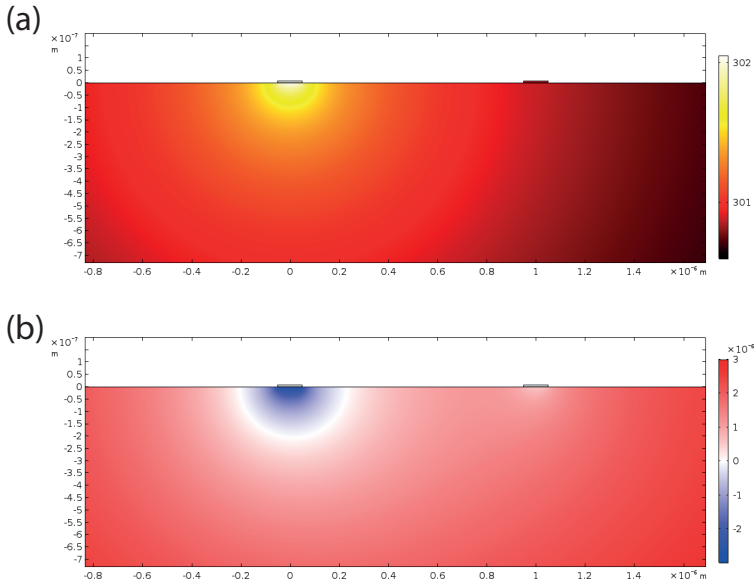


Figure C.3: The profiles of (a) temperature and (b) magnon chemical potential calculated for thermally excitation of magnons as a result of Joule heating in the injector.

C.3 Anisotropic charge transport in a Hall bar geometry

It is standard to pattern a device into a Hall bar geometry (Fig. C.4) for studying its anisotropic transport behavior. With a charge current I sent through the main channel from left and right, longitudinal and transverse voltages, V_L and V_T , can be measured as shown in Fig. C.4. The longitudinal and transverse resistances can be obtained as $R_L = V_L/I$ and $R_T = V_T/I$, respectively.

In anisotropic magnetoresistance (AMR) [2] and spin Hall magnetoresistance (SMR) measurements [3, 4], an in-plane magnetic field is applied to the sample for signal modulation. V_L and V_T are usually recorded with sweeping the angle θ between I and the magnetic field. ΔV_L and ΔV_T are the maximal changes of V_L and V_T induced by the rotation of the magnetic field direction, respectively, from which the longitudinal and transverse magnetoresistances ΔR_L and ΔR_T can be also determined.

Ideally, the ratio between ΔR_L and ΔR_T corresponds to the ratio between the separation of two Hall bar electrodes (l) and the width of the channel (w), assuming that the width of the Hall bar leads (w_{bar}) are negligible. Experimentally, however, the Hall leads are often of certain finite widths. In this case, the exact ratio $\Delta R_L/\Delta R_T$ deviates from l/w and is not straightforward to determine, but needs to be calculated based on the specific Hall bar geometry.

Here we show that the ratio $\Delta R_L/\Delta R_T$ can be evaluated with a 2D-FEM. This is part of the work in Ref. [5], where the spin Hall magnetoresistance (SMR) effect was claimed to emerge in Pt at low temperatures by a ionic liquid gating technique. The exact device geometrical parameters are illustrated in Fig. C.5(a).

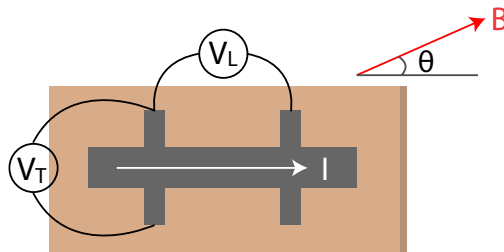


Figure C.4: A Hall bar geometry that is commonly used in transport measurements. A charge current I runs through the main channel of the device, and the longitudinal and transverse voltages, V_L and V_T , are measured using the leads. This figure shows the situation where an in-plane magnetic field is applied with an angle θ respective to I .

We further define longitudinal and transverse resistivities as:

$$\rho_{xx} = R_L \cdot wt/l \quad (\text{C.2a})$$

$$\text{and} \quad \rho_{xy} = R_T \cdot t, \quad (\text{C.2b})$$

where t is the thickness of the Pt Hall bar.

The electrical transport is anisotropic, where ρ_{xx} and ρ_{xy} depend on θ and can be written as [2, 6]:

$$\rho_{xx}(\theta) = \rho_0 + \Delta\rho \cdot \cos^2 \theta \quad (\text{C.3a})$$

$$\text{and} \quad \rho_{xy}(\theta) = \Delta\rho \cdot \sin \theta \cos \theta, \quad (\text{C.3b})$$

where ρ_0 is the baseline of the longitudinal resistivity (it is defined that $\rho_0 = \rho_{xx}(\theta = 90^\circ)$ in this study), and $\Delta\rho$ is the change of resistivity due to anisotropy.

The model solves the electrical transport equation

$$\begin{pmatrix} \vec{J}_x \\ \vec{J}_y \end{pmatrix} = - \begin{pmatrix} \sigma_{xx} & \sigma_{xy} \\ \sigma_{xy} & \sigma_{xx} \end{pmatrix} \begin{pmatrix} \vec{\nabla} V_x \\ \vec{\nabla} V_y \end{pmatrix} \quad (\text{C.4})$$

in the Hall bar, where J_x and J_y are electrical current densities along the x and y directions, respectively. In the transport matrix, σ_{xx} and σ_{xy} are longitudinal and transverse conductivities, and they are related to ρ_{xx} and ρ_{xy} by [7]

$$\sigma_{xx} = \frac{\rho_{xx}}{\rho_{xx}^2 + \rho_{xy}^2} \quad (\text{C.5a})$$

$$\text{and} \quad \sigma_{xy} = \frac{\rho_{xy}}{\rho_{xx}^2 + \rho_{xy}^2}. \quad (\text{C.5b})$$

The nonzero off-diagonal elements in the conductance matrix in Eq. C.4 essentially reflect the anisotropic transport properties.

In the model, a constant current is applied to the main channel by implementing the boundary condition. The model solves for different values of θ and a typical graphic solution of the voltage profile looks like Fig. C.5(a). The voltage drops in longitudinal ($V_L = V1 - V2$) and transverse ($V_T = V1 - V3$) configurations are thereafter evaluated for different θ . The longitudinal and transverse magnetoresistance, ΔR_L and ΔR_T , can be subsequently calculated as

$$\Delta R_L = [V_L(\theta = 0^\circ) - V_L(\theta = 90^\circ)]/I \quad (\text{C.6a})$$

$$\text{and} \quad \Delta R_T = [V_T(\theta = 45^\circ) - V_T(\theta = 135^\circ)]/I, \quad (\text{C.6b})$$

respectively, from which $\Delta R_L/\Delta R_T$ can be obtained.

The calculated results from the 2D-FEM are shown in Fig. C.5(b). As shown in the figure, the ratio $\Delta R_L/\Delta R_T$ decreases almost linearly with the increase of $wbar$. This

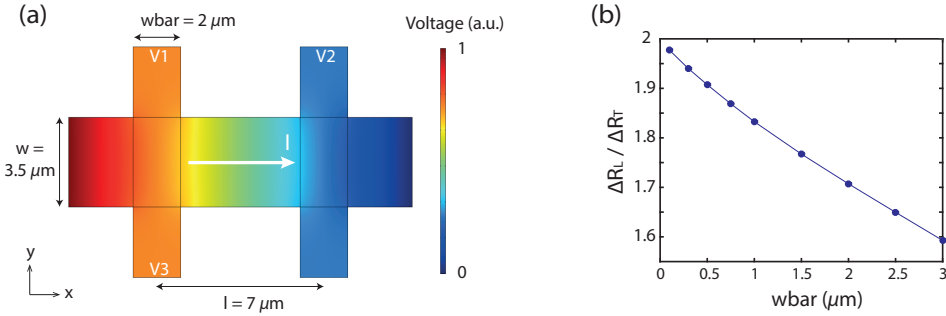


Figure C.5: FEM results of anisotropic electrical transport in a Hall bar geometry. (a) The electrical voltage profile when sourcing a charge current through the Hall bar. Voltages are probed via V1, V2 and V3 terminals. (b) The ratio $\Delta R_L / \Delta R_T$ calculated as a function of the width of the Hall bar leads (w_{bar}).

is a direct result of the fact that more sourced current passes through the side leads when w_{bar} increases. One can extrapolate the linear dependence to $w_{bar} \rightarrow 0$ and obtained a ratio $\Delta R_L / \Delta R_T$ to be 2. This corresponds to the situation where the Pt leads are infinitely narrow, and $\Delta R_L / \Delta R_T$ is equal to the geometric ratio between l ($=7 \mu\text{m}$) and w ($=3.5 \mu\text{m}$). In the experiment described in Ref. [5], for the concern of the device robustness, w_{bar} is designed to be $2 \mu\text{m}$. From Fig. C.5(b) we expect a ratio of 1.7, which is close to the experimental values. The effect of contacts, or the unavoidable inhomogeneous flow of current due to the slight deviation from a perfectly symmetric geometry, may account for small discrepancies.

References

- [1] A. Slachter, F. L. Bakker, and B. J. van Wees, "Modeling of thermal spin transport and spin-orbit effects in ferromagnetic/nonmagnetic mesoscopic devices," *Physical Review B* **84**, p. 174408, Nov. 2011.
- [2] T. McGuire and R. Potter, "Anisotropic magnetoresistance in ferromagnetic 3d alloys," *IEEE Transactions on Magnetics* **11**, pp. 1018–1038, July 1975.
- [3] H. Nakayama, M. Althammer, Y.-T. Chen, K. Uchida, Y. Kajiwara, D. Kikuchi, T. Ohtani, S. Geprägs, M. Opel, S. Takahashi, R. Gross, G. E. W. Bauer, S. T. B. Goennenwein, and E. Saitoh, "Spin Hall Magnetoresistance Induced by a Nonequilibrium Proximity Effect," *Physical Review Letters* **110**, p. 206601, May 2013.
- [4] N. Vlietstra, J. Shan, V. Castel, B. J. van Wees, and J. Ben Youssef, "Spin-Hall magnetoresistance in platinum on yttrium iron garnet: Dependence on platinum thickness and in-plane/out-of-plane magnetization," *Physical Review B* **87**, p. 184421, May 2013.
- [5] L. Liang, J. Shan, Q. Chen, J. Lu, G. R. Blake, T. T. M. Palstra, G. E. W. Bauer, B. J. Van Wees, and J. Ye, "Gate-controlled spin-dependent magnetoresistance of a platinum/paramagnetic insulator interface," *submitted*.
- [6] V. D. Ky, "Planar Hall and Nernst effect in ferromagnetic metals," *physica status solidi (b)* **22(2)**, p. 729, 1967.
- [7] J. Singleton, *Band Theory and Electronic Properties of Solids*, Oxford University Press, Oxford, 2001.

Summary

The study of the behavior of electrons lies at the heart of solid state physics. The best-known property of an electron is its charge, which plays the central role in many fascinating physical phenomena. In this Information Age where we live, the deepest impact people feel from the electron charge is perhaps through *electronics*, based on the electron transport in metals and especially in semiconductors. In digital circuits, several transistors can be arranged to create different logic gates, which are able to perform binary operations. With the invention of integrated circuits (ICs), billions of tiny transistors are fabricated on a small chip to fulfill more complicated functions, like the central processing unit (CPU) of a computer or a mobile phone.

It is impressive to see how fast the technology evolves with utilizing the electron charge. On the other hand, the exploration of another fundamental property of electrons—spin, has unveiled important properties and functions of materials, such as magnetism. Due to the spin angular momentum it possesses, an electron has an intrinsic magnetic moment that can interact with a magnetic field. The research field of *spintronics* mainly concerns the excitation, transport and detection of spin angular momentum in various material systems. In metallic materials, the spin transport is often intertwined with charge transport, with each individual electron being a spin carrier. In magnetic insulators however, the spin information is transported by collective excitations of spin (magnons) and does not involve charge transport. The utilization of electron spin for the transfer and storage of information brings in new possibilities and functionalities in addition to the charge-only electronics, such as modern memory devices.

Applying a temperature gradient onto a material leads to a heat current according to Fourier's law. It has long been known that the heat transport is coupled to the charge transport in a conductive material, and many thermoelectric effects were established, such as the Seebeck effect and the Peltier effect—a heat current can induce a charge current, and vice versa. It is therefore natural to consider that the heat

transport and spin transport is also interconnected in conductive systems, since both are coupled to the charge transport. Following this line, novel spin caloritronic effects, such as the spin-dependent Seebeck effect and the spin-dependent Peltier effect, were discovered in delicate metallic structures.

Intriguingly, the recent discovery of the spin Seebeck effect (SSE) shows that a heat current can create a magnonic spin current in a magnetic insulator, even in the absence of a charge current. This result brought much attention to the insulator-based spintronics. The addition of the heat transport in the field of spintronics leads to the germination of the subfield *spin caloritronics*, where this thesis falls in.

This thesis presents experimental studies on charge, spin and heat transport, and especially the interplay among them in both conductive and non-conductive systems. In the work described in chapter 3, a spin-dependent thermoelectric effect—magneto-Peltier effect, was investigated for the first time in magnetic tunnel junctions (MTJs). MTJs are the key components in magnetoresistive random-access memory technology, and consist of two magnetic layers spaced by a thin oxide layer as a tunnel barrier. MTJs are best known for their large contrast of electrical resistances between the parallel (P) and antiparallel (AP) magnetic configurations. Later, it was found that the Seebeck coefficient of an MTJ depends also on its magnetic configuration. Reciprocally, one can expect that the Peltier coefficient of an MTJ alters between P and AP cases as well, the effect that our experiment aims to demonstrate. We fabricated a micro-scale thermocouple which was electrically detached but thermally coupled to the MTJ, which can convert the temperature information on the top side of the MTJ into an electrical signal. This signal was found to vary between P and AP configurations when a charge current was passed through the MTJ. By careful harmonic analysis we separated the linear response, which reflects the magneto-Peltier effect from higher-order responses, which originate from asymmetric I - V characteristics of the MTJ. Our results show that the Peltier heat current can be modified with a magnetic field in MTJs, opening up a magnetically controllable cooling mechanism in this system.

The next part of this thesis focuses on magnetic insulators, where the spin angular momentum is carried by collective excitations, or magnons. We study the transport properties of magnons excited in the following two ways: by spin transfer from a metal with a spin imbalance adjacent to the magnetic insulator, and by a temperature gradient in the magnetic insulator, i.e., by the spin Seebeck mechanism. Interestingly, the two excitation mechanisms can be studied simultaneously within the same device. Typically, we employ a “nonlocal geometry” in these studies—the magnetic insulator is the spin transport channel in study, and the two metallic strips deposited on top of it, usually made of spin-Hall metals, serve as contacts. An electric charge current through one metallic strip (the injector) not only creates a spin accumulation at the metal/magnetic insulator interface by the spin Hall effect (electrical excitation), but also generates a heat current due to Joule heating (thermal excitation). The magnons

excited by both mechanisms reach the other strip (the detector), and can convert into a measurable electric signal through the inverse spin Hall effect. With our measurement technique, the contributions of the two mechanisms to the output signal can be separated.

In the study described by chapter 4, the nonlocal signals from both the electrical and thermal excitations were studied as a function of yttrium iron garnet (YIG) film thickness. YIG, being ferrimagnetic at room temperature with a low Gilbert damping effect, is the prototypical material for studying magnon dynamics. For the nonlocal signals that arise from electrical injection, surprisingly, we found the dependence with respect to YIG thickness cannot be quantitatively explained with the magnon diffusion-relaxation model. This suggests that perhaps other physical processes need to be taken into account for the description of magnon transport.

While the SSE has already been known and even applied for heat-electricity conversion, a consensus has not yet been reached regarding the underlying mechanism of the SSE. By studying the influences of both the YIG thickness and the heater spin transparency on the thermally excited nonlocal magnon signals, our results point to the contribution of a bulk spin Seebeck current to the SSE signals. With the help of a 2D finite element model, we reported a bulk spin Seebeck coefficient for YIG at room temperature.

The next chapter extends the study of the nonlocal spin Seebeck measurements to low temperatures and ultra-far distances. We found out that the nonlocal SSE signals only decayed exponentially at the intermediate distance regime following their magnon relaxation length. Further than this range, the signals are dominated by the magnon spin current generated by the temperature gradient around the detector, and decay geometrically. This experimental observation is in accordance with the finite element model results. Based on this principle, we investigated the nonlocal SSE signals for a 2.7- μm -thick YIG film at various temperatures, and reported its magnon relaxation lengths between 3.5 K and room temperature.

Finally, we move on to study the magnon spin transport in nickel ferrite (NFO), a non-conductive ferrimagnet with an inverse spinel crystal structure. While most of the study on magnon spin transport is based on YIG, it is of great interest to extend and study this effect in a different material system. We successfully observed both electrically and thermally excited nonlocal magnon signals in NFO thin films, showing the ubiquitous nature of magnon spin transport. Via distance-dependent measurements we extracted its magnon relaxation length at room temperature, which is around 3 μm .

In summary, the research into spin caloritronics advances the fundamental understanding of how charge, spin and heat currents interact with each other in different material systems, and is promising for future applications such as the conversion and utilization of thermal energy. We believe the work described in this thesis helps

increase the current knowledge of this field and paves the way for novel spintronic and spin-caloritronic devices.

Samenvatting

De studie van elektronen ligt in het hart van de vaste stof fysica. De bekendste eigenschap van een elektron is zijn lading, die de centrale rol speelt in vele fascinerende fysische verschijnselen. In het informatietijdperk waar we leven, heeft *elektronica* mogelijk de grootste impact die mensen voelen van elektronenlading en dat is gebaseerd op de elektronentransport in metalen en vooral in halfgeleiders. In digitale circuits worden verschillende transistoren gerangschikt om verschillende logische poorten te creëren, die binaire bewerkingen uit kunnen voeren. Met de uitvinding van geïntegreerde schakelingen worden miljarden kleine transistors gefabriceerd op een kleine chip om meer gecompliceerde functies te vervullen, zoals de centrale verwerkingseenheid (CPU) van een computer of een mobiele telefoon.

Het is indrukwekkend om te zien hoe snel de technologie evolueert door het gebruik van de elektronlading. Aan de andere kant heeft de verkenning van een andere fundamentele eigenschap van elektronen, spin, belangrijke eigenschappen en functies van materialen ontmaskerd, zoals magnetisme. Vanwege het spin-impulsmoment dat het bezit, heeft een elektron een intrinsiek magnetisch moment dat een wisselwerking heeft met een magnetisch veld. Het onderzoeksgebied van *spintronica* heeft voornamelijk betrekking op de excitatie, het transport en de detectie van spin-impulsmoment in verschillende materiële systemen. In metalen is het spintransport vaak gekoppeld met ladingstransport, met het elektron als drager van spin. In magnetische isolatoren wordt de spininformatie echter getransporteerd door collectieve excitaties van spin (magnonen) en niet door ladingstransport. Het gebruik van elektron-spin voor de overdracht en opslag van informatie brengt nieuwe mogelijkheden en functionaliteiten naast de ladingsgerichte elektronica, zoals moderne geheugenapparaten.

Het toepassen van een temperatuurgradiënt op een materiaal leidt tot een warmtestroom volgens de wet van Fourier. Het is al lang bekend dat het warmtetransport gekoppeld is aan de ladingstransport in een geleidend materiaal, en veel thermo-

elektrische effecten waren vastgesteld, zoals het Seebeck-effect en het Peltier-effect - een warmtestroom dat een ladingsstroom kan induceren en vice versa. Het is daarom logisch om te overwegen of warmtetransport en spintransport ook onderling verbonden zijn in geleidende systemen, omdat beide zijn gekoppeld aan het ladingstransport. Deze overweging volgend zijn nieuwe spin caloritronische effecten, zoals het spinafhankelijke Seebeck-effect en het spinafhankelijke Peltier-effect, ontdekt in delicate metaalstructuren.

Intrigerend genoeg laat de recente ontdekking van het spin Seebeck-effect (SSE) zien dat een warmtestroom een magnonische spinstroom kan creëren in een magnetische isolator, zelfs in de afwezigheid van ladingsstroom. Dit resultaat bracht veel aandacht naar de op isolatoren gebaseerde spintronica. De toevoeging van het warmtetransport op het gebied van spintronica was de kiem van de subveld *spin caloritronics*, waar dit proefschrift in valt.

Dit proefschrift presenteert experimentele studies over lading, spin en warmtetransport, en vooral het samenspel tussen hen in zowel geleidende als niet-geleidende systemen. In het werk beschreven in hoofdstuk 3 betreffende het spin-afhankelijk thermo-elektrisch effect genaamd het magneto-Peltier-effect dat voor het eerst werd onderzocht in magnetische tunnelcontacten (MTJ's). Een MTJ is de belangrijkste component in MRAM geheugentechnologie, en bestaat uit twee magnetische lagen op een afstand van elkaar door een dunne oxidelaag als een tunnelbarrière. MTJs zijn vooral bekend om het groot verschil van elektrische weerstanden tussen de parallelle (P) en anti-parallelle (AP) magnetische configuraties. Later bleek dat de Seebeck-coëfficiënt van een MTJ ook afhangt van de magnetische configuratie. Wederom kan men verwachten dat de Peltier-coëfficiënt van een MTJ ook verandert tussen P- en AP-gevallen, het effect dat ons experiment wil demonstreren. We fabriceerden op microschaal een thermokoppel dat elektrisch ontkoppeld maar thermisch gekoppeld was aan de MTJ, die de temperatuurinformatie aan de bovenkant van een MTJ kan omzetten in een elektrisch signaal. Dit signaal bleek te variëren tussen P- en AP-configuraties wanneer een ladingsstroom door de MTJ werd geleid. Door zorgvuldige harmonische analyse hebben we de lineaire respons gescheiden, die het magneto-Peltier-effect weergeeft van reacties van hogere orde, die afkomstig zijn van asymmetrische I-V-kenmerken van de MTJ. Onze resultaten laten zien dat de Peltier-warmtestroom kan worden aangepast met een magnetisch veld in MTJ's, en hebben zo een magnetisch controleerbaar koelmechanisme gecreëerd in dit systeem.

Het resterende deel van dit proefschrift richt zich op magnetische isolatoren, waarbij het spin-impulsmoment wordt gedragen door collectieve excitaties, magnonen. We bestuderen de transporteigenschappen van magnonen die op de volgende twee manieren worden geëxciteerd: door spinoverdracht van een metaal met een spin-onbalans aangrenzend aan de magnetische isolator, en door een temperatuurgradiënt in de magnetische isolator, d.w.z. door het spin-Seebeck-mechanisme. Interessant is

dat de twee excitatiemechanismen tegelijkertijd binnen hetzelfde apparaat kunnen worden bestudeerd. Normaal gesproken gebruiken we in deze studies een “niet-lokale geometrie” - de magnetische isolator is het spintransportkanaal in studie en de twee metalen stroken die erop zijn aangebracht, meestal gemaakt van spin-Hall-metalen, dienen als contacten. Een elektrische ladingsstroom door een metalen strip (de injector) creëert niet alleen een spinaccumulatie op het aanrakingspunt van metaal en de magnetische isolator door het spin Hall-effect (elektrische excitatie), maar genereert ook een warmtestroom als gevolg van Joule-verwarming (thermische excitatie). De magnonen die door beide mechanismen worden aangeslagen, bereiken de andere strip (de detector) en kunnen via het inverse spin Hall-effect worden omgezet in een meetbaar elektrisch signaal. Met onze meettechniek kunnen de bijdragen van de twee mechanismen aan het uitgangssignaal worden gescheiden.

In de studie beschreven in hoofdstuk 4 werden de niet-lokale signalen van zowel de elektrische als de thermische excitaties bestudeerd als een functie van de filmdikte van yttriumijzer-granaat (YIG). YIG, dat ferrimagnetisch is bij kamertemperatuur met een lage Gilbert demping, is het prototypische materiaal voor het bestuderen van magnon-dynamica. Voor de niet-lokale signalen die voortkomen uit elektrische injectie, vonden we verrassend genoeg dat de afhankelijkheid met betrekking tot YIG-dikte niet kwantitatief kan worden verklaard met het magnon-diffusie-relaxatiemodel. Dit suggereert dat misschien andere fysische processen in aanmerking moeten worden genomen voor de beschrijving van magnontransport.

Hoewel het SSE al bekend is en zelfs is toegepast voor energieconversie, is er nog geen consensus bereikt over het onderliggende mechanisme van het SSE. Door de invloeden van zowel de YIG-dikte als de spintransparantie met de verwarmers op de thermisch geëxciteerde niet-lokale magnonsignalen te bestuderen, wijzen onze resultaten naar de bijdrage van een collectieve spin Seebeck-stroom aan de SSE-signalen. Met behulp van een 2D eindige-elementen-model hebben we een collectief spin Seebeck-coëfficiënt voor YIG bij kamertemperatuur gerapporteerd.

Het volgende hoofdstuk breidt de studie van de niet-lokale spin-Seebeck-metingen uit naar lage temperaturen en lange afstanden. We ontdekten dat de niet-lokale SSE-signalen alleen exponentieel vervielen in het middellange afstand regime, hun magnon-relaxatielengte volgend. Op grotere afstanden worden de signalen gedomineerd door de magnon-spinstroom die wordt gegenereerd door de temperatuurgradiënt rond de detector en geometrisch verval. Deze experimentele waarneming is in overeenstemming met de resultaten van het eindige elementenmodel. Op basis van dit principe onderzochten we de niet-lokale SSE-signalen voor een 2,7- μm dikke YIG-film bij verschillende temperaturen en rapporteren de magnon-relaxatie van de film tussen 5 K en kamertemperatuur.

Ten slotte gaan we verder met het bestuderen van het spintransport van de magnonen in nikkelferriet (NFO), een niet-geleidende ferrimagneet met een inverse

spinel-kristalstructuur. Hoewel het grootste deel van het onderzoek naar het spintransport van magnonen gebaseerd is op YIG, zou het van groot belang zijn om dit effect in een ander materiaalsysteem uit te breiden en te bestuderen. We hebben met succes zowel elektrisch als thermisch geëxciteerde niet-lokale magnonsignalen waargenomen in dunne films van NFO, wat de universele aard van het spintransport van magnonen aantoont. Via afstandafhankelijke metingen hebben we de magnon-relaxatielengte verkregen van ongeveer $3 \mu\text{m}$ bij kamertemperatuur.

Samenvattend, het onderzoek naar spincaloritronica bevordert het fundamentele begrip van wisselwerking tussen ladings-, spin- en warmtestromen in verschillende materiaalsystemen, en is veelbelovend voor toekomstige toepassingen zoals de conversie en het gebruik van thermische energie. We geloven dat het werk dat in dit proefschrift wordt beschreven helpt de huidige kennis van dit veld te vergroten en de weg vrijmaakt voor nieuwe spintronische en spin-caloritronische apparaten.

Acknowledgements

When I started my PhD voyage more than four years ago, part of me was actually doubting whether I could eventually acquire the degree. And now, standing at the end of this journey, I am more than grateful for all the help that I have received from many amazing people, without which I could not have come so far.

First of all, I would like to thank my daily supervisor and promoter, professor Bart van Wees. Bart, honestly I cannot thank you enough for all the guidance and support that you have generously provided to me, which have reshaped me from a research rookie to who I am now. I got to know you when I was still a master student in 2011, through the courses you taught to us—semiconductor physics and mesoscopic physics. Your thorough knowledge, profound passion and of course, funny jokes regarding physics has inspired me to perform the master research along your scientific direction. Thanks so much for giving me the chance and bringing me in your excellent group—Physics of Nanodevices (FND), where I could learn from and work with many talented colleagues. Later, you kindly offered me a PhD position even when I myself was not so sure that I would survive. Being a very renowned scientist, you were in fact very available for discussions. Gradually, with all the suggestions and feedback from you, I could start to grasp the gist of scientific research. I truly appreciated all your amazing comments and insights on my results and data, which have enlightened me in many instances and were crucial for publications. I am also thankful for all the detailed revisions you have made to my manuscripts, abstracts for conferences, and of course also to this thesis (and the patience to let me write it rather slowly). In addition, I wish to thank you for giving me many opportunities to attend international conferences and present our works. It was also a great honor for me to see you win the Spinoza Prize in 2016, and I am really happy for and proud of you. Besides work, I appreciate that you invited us to the badminton practice at your club where we had a fun evening, and shared your enthusiasm for trains at many dinner tables. In short, I have learned and benefited very much from

working with you, for which I will be forever grateful.

Next I would like to thank professor Caspar van der Wal, my second supervisor. Caspar, you are literally the first professor I know in this university as you were an admission committee member of the Topmaster Nanoscience program and interviewed me in the spring of 2011. Thanks to you I could enter this excellent master program and become affiliated to the Zernike institute for advanced materials. During my master and PhD time, I often found your words and sayings of great wisdom, and I learned quite a lot from your general attitudes towards research and life.

I want to also thank professor Tamalika Banerjee, who has encouraged me every now and then and soothed my heart with many friendly gestures. Being diligent and passionate about research, you are definitely a role model for many young female scientists, including me.

Dear professors Joseph Heremans, Mathias Kläui and Ryan Chiechi, thank you very much for being part of the reading committee and all your precious time and efforts spent on reading my thesis. I really appreciate all your helpful comments, which have both extended and deepened my understanding about my own works, as well as helped improve the quality of this thesis. I hope to see you at my defense or near future so that I could thank you in person.

I would also like to thank several other professors in the field of spintronics, with whom I had the privilege to collaborate with: Gerrit Bauer, Günter Reiss, Markus Münzenberg and Rembert Duine. Gerrit, I am always so delighted by your visits to Groningen so that we could gain theoretical perspectives on our experimental results. You are always so friendly and polite, patient to understand our knotty data, and especially I appreciate your hearty laughs that can lighten up the mood of everyone around you (and people in neighboring offices as well :P). I am also amazed by your time management as you always manage to reply e-mails so fast. Furthermore, I want to mention the spintronics lecture series you gave at this institute in 2016, from which I learned a lot. Rembert, your theoretical contributions to our works are invaluable. Thanks to you we were able to understand the magnon system better. I appreciate your long e-mails that have clarified my confusions when I was preparing the manuscript. Besides, I wish to thank you for being so friendly, and kindly helped me in French Polynesia during the spin superfluidity conference, when I had trouble getting cash out of my credit card. I am very happy that you agreed to be part of the defense committee and looking forward to your questions at the defense. Günter and Markus, thanks so much for your constructive input in my papers, where I also communicated several times with you through e-mails. Your comments and suggestions have absolutely improved the quality of our publications.

During workshops and conferences, I have also benefited from the inspiring discussions with many friendly and knowledgeable professors in this field, including Felix Casanova, Jiang Xiao, Joseph Heremans, Mathias Kläui, Olivier Klein, Xia Ke,

Yaroslav Tserkovnyak, etc. Within the Zernike institute, I also had plenty of chances to communicate with many nice professors during my PhD time, such as Bart Kooi, Justin Ye, Maxim Mostovoy, Thom Palstra, etc. I am thankful for you all, and many other researchers, for openly sharing your knowledge and opinions with me.

I would like to also acknowledge Jamal Ben Youssef and Polina Bougiatioti for providing YIG and NFO films with nice quality, which are indispensable for the works in this thesis.

Let me now move to thank the group members of FND. I would like to first express my gratitude to our technical staff, Anna, Andrea, Herman, Johan, Martijn and Tom. Thanks to all your efforts can this group run smoothly, and we have the luxury to focus on research, unlike PhD students in some other countries who have to solve technical problems themselves. Martijn, I remember calling or walking to your office many times when I had troubles with TFC, sputtering and bonding machine, cryostat, stepper motor, etc. You always kindly offered help and fixed the equipment in no time. Thanks so much for that! Johan, thanks for fixing the wires in the Tesla sample holder after I accidentally screwed it up. You were gentle enough to not blame me but instead fixed them patiently. I also appreciate the casual talks with you in the corridor which have many times brightened my mood. Tom, I am really impressed by your professionalism. You never once rejected or postponed solving our problems. Thanks a lot for that. Herman, I hope your healthy condition will improve soon and thanks for fixing wires and making switchbox in the measurement setups.

Nynke, you are a really nice supervisor and colleague, and I learned a great deal from you during working with you, especially in my master period. Thanks so much for introducing every step of research to me patiently, and answering numbers of my questions. Also, thanks for being very tolerant of my mistakes (so sorry about the sign...). Your friendly character makes it very pleasant to collaborate with you. After entering the PhD phase, I still often walked into your office and had plenty of discussions with you. I also really admire your attitude towards work, that you are always optimistic and very well-organized. And of course thanks for sharing the thesis template with me! The trips together with you to Dresden and Munich have also left me nice memories. I sincerely hope the best for your future and hopefully see you somewhere someday!

Fasil and Joost, you guys are probably the most efficient working dual I have ever known. When I started my PhD research you were already in your final year of PhD, but I am so glad that I could have the chance to collaborate with both of you. Fasil, thanks for generously sharing your knowledge and skills with me when we worked together on the magneto-Peltier project. From you I got to know how to perform finite element modeling with Comsol and many other sides of research. Thanks also for the thesis latex template you shared with me. I feel blessed to have a friendly and talented colleague like you and best wishes for your career move to UK.

Joost, your high efficiency and in-depth analysis on your research projects have set a great example for me. I really appreciate your trust in me when you handed over the magneto-Peltier project to me, and the nice suggestions you have given. I would also like to thank Frank (Bakker) and Bram (Slachter) for building the foundation of the spin caloritronics research in our group, and the high-quality PhD theses you wrote, from which I have acquired much knowledge.

Timo, your decision to come to Groningen has proved to be beneficial not only for yourself but also for many of us in FND. You were always friendly and patient to discuss with us and able to provide useful comments. I appreciate very much your critical reading on my manuscripts and all the detailed but necessary modifications you suggested. Because of you, I could study the magnon spin transport in NFO materials, which have resulted in a publication, and hopefully another one soon. Thanks also for your company and the nice memories in San Diego. I enjoyed working with you and I wish you a very successful scientific career.

Ludo, the whole metallic/YIG subgroup would not be the same without you. Not only are you exceptionally talented and efficient at work, but also you are very willing to help others. You have helped me in many aspects of research—experiments, modeling, further understanding of the magnon spin system, etc. The discussions with you are inspiring and helpful. Also, I really appreciate your efforts in upgrading the Tesla setup for more measurement functions and equipping it with the handy qtlab scripts. Thanks for your detailed introduction of the setup to other Tesla users like me. Besides, I am thankful for the data-fitting python program you shared with me, which has freed me from many hours of repetitive work! It is very lucky to have you as a colleague and I wish you a sweet life with Maartje and kids.

Geert, I am very grateful that you agreed to be my paranymph and especially your efforts in translating the “summary” into “samenvatting” in this thesis. I am very glad that we became officemates after you were a full member of FND, which gives me the chance to know you more as a nice and interesting person. I really enjoy all the casual chats with you, both in office and at lunch tables. I wish you the best of luck with your studies in antiferromagnets and a bright future after PhD!

Jing, it is very nice to have you as a colleague. Although we are both from China and similar in age, we seem to have quite different characters. In this way I could learn a lot from you, such as your cheerfulness, perspectives towards work and many other aspects. Thanks for all the discussions and your help in my experiments, and I wish you enjoy the rest of your PhD time, and a happy life afterwards!

I would like to thank other metallic subgroup members for many fruitful discussions and meetings together: Kumar, it is nice to have many random chats at lunch with you, good luck finishing PhD with your nice papers; Aisha, the trips together with you to Grenoble and other places for conference were enjoyable experiences for me, best wishes for your scientific career and marriage; Vincent, thanks for all

your help during my master phase; Miren, although your visit in our group was very short, you shared many thoughts with me and motivated me a lot, which I really appreciate; Bart (Hake), as a master student you are surprisingly independent in research, which has saved me a lot of time as your supervisor. The results you got were quite publishable which proved the quality of your work. It was nice working with you and I wish you a great future.

I would of course like to thank other members in our FND group. Christian, I am happy to have co-authored with you because of the sophisticated tunnel junctions that you made, without which the study of the magneto-Peltier effect would be impossible. Also thanks a lot for helping me with the FMR experiments on YIG samples. I am pretty sure your projects will work out nicely after numerous samples you have fabricated, as hard work does pay off!

Sid, Mallik and Eric, my topmaster classmates, we entered this group together for the master research and became colleagues as we all chose to continue our research in FND. During the past five years, I did not feel a tiny sense of competition from you, but rather gained much help from you guys when I was in need. Thanks for being so friendly and I am very glad to see that we all have obtained nice results during the PhD research. Somehow you all managed to become doctors before me, I hope to join you soon and wish you the best for your future careers.

Crystal and Ping, with the same native language and similar cultural backgrounds, we seem could have endless girl talks (together with Jing also). I am very happy that you have joined FND and quickly proceeded along the right track of research. In fact both of you work so hard, always coming to office earlier and leaving later than me. Thanks also for your hospitality and the good times together when I was invited at your places. I wish you both very successful PhD and the careers beyond, as well as sweet lives with your better-halves (Wytse and Gang, to be exact)!

Tian and Xu, it is also very nice to meet you here in FND while we all came from the far East. You guys are both smart and friendly, and thanks so much for inviting Lei and me for dinners at your places, which are really nice memories to me. Xu, thanks for organizing many fun group outings and dinners, and also took maybe a bit risk to bring the exotic coca candies to us all the way from Peru. Good luck with both of your PhD as well!

Alexey, you entered the group almost the same time as I started my PhD. Although we did not have a chance to work closely together, I find you a very nice and warmhearted person. I appreciate all the tips and help from you, especially when you are not really obligated to, such as walking me together to return the helium vessels lately, as it was very difficult for me to do it on my own.

Pep, we also started our PhD at similar time and I really like the fact that you are a just few days older than me! You are both clever and hardworking, and there was a time when I could always meet you when I occasionally went to office during

weekends. I still remember discussing with you about one detail of the meetkast in the measurement room in a cold weekend. I feel like that I could always learn something from talking to you, and you are nice enough to never let me feel stupid (a pep talk indeed).

I also benefited a lot from many tuesday and wednesday meetings, and had so much nice time together with all members in FND, including former group members: Alina, Alok, Eek, Gaurav, Ivan, Jakko, Jasper, Juliana, Magda, Marcos, Olger, Paul, Sander O, Sander K, Saurabh, Subir, Roald, Thomas; and present group members: Arijit, Arjan, Carmem, Gertjan, Jorge, Julian, Madhu, Talieh, Tom (Bosma), and many master and bachelor students, including: Anouk, Dirk, Frank (Feringa), Freddie, Frits, Jantje, Nilesh, Rick, Saurabh (Soni), Sebastian, Xiangyang and many others. I wish you all have (or had) a nice time at FND and loads of successes in research!

I would also like to thank other friends that I have made in Groningen. Wlada and Perry, you are among the first people I knew in this town and you guys are amazingly nice! In the past 7 years we have shared many “gezellig” moments together, exploring all sort of cuisines and talking about everything in life. Our friendship means a lot to me, and I feel so happy to know that you are going to marry soon. Best wishes to you! Jin and Zhen, Qihong, Jie and Honghua, thanks a lot for inviting us multiple times to your place for great food and board games. I am happy to see that our careers have all moved forward recently, and I am sure that the future will become even better. Astone and Jiapan, you guys are like old friends to us and the double dating with you on 2015 Valentine’s day was really an unforgettable moment to me! Zhaoli, how tiny is the chance that I could meet my high-school classmate here in Groningen, where you also pursued your PhD degree in mathematics. I wish you a smooth graduation and bright future. Yingfen Wei and Min Wang, thanks so much for taking care of our cat while we were away. It must be a lot of efforts and I hope we could return the favor someday. Further I would like to thank Lijuan and Peiliang, Bin Chen, Puhua Wan, Minpeng Liang, Jianming and Chunrui, Fangfang and Quan, Ya’nan, Guowei, Jiquan and Zhonghong, Qiuyan, Huatang, Liqiang and Yuanyuan, Jing Wu, Xianming Gu, Chengtao Ji, Jinfeng Shao, Sheng He, Qi Liu and Deli, Xuanbo Feng, Hong Lian, as well as Klaas Bernd (KB), Gert (Jan Hoeve), Jan and Wilma, Laaya, Sasha, Ali, etc., for all the good times together! I wish you all the best.

I want to mention friends in other parts of the Netherlands, including: Jianglei Niu and Haifeng, Shengnan Lu, Yuanhao Bi, Liang Li and Zao Ye, etc. Thanks for your hospitality when I visited Eindhoven. All my best to you as well!

My Topmaster buddies, thanks for the precious time together, and I wish you all the best whatever career choice you chose: Artem, Daniel, Diederik, Edmond, Jorge, Piet, Rolf, Sander, Solmaz and Tadesse. Especially I want to thank Solmaz for sharing your experience of “inburgering” to me, which is so helpful!

I wish to also thank many old friends I made before I came to the Netherlands,

with whom I still keep in touch, showing much care about me during my PhD time: my best friends Mengyi Liu, Lili Jiang, Xiaoxiao Yang, Yuting Zhang, Ying Wu, Yu Shuai; my bachelor-time roommates Hui Yi, Meng Xia and Wenqian, Zhenzhen and Jin Zhao, as well as Qian Di, Yang Meng, Changyu Lin, etc. You may not actually read this thesis but I want to say that each one of you is special to me.

In the end, I want to say a few words to my dearest family members. Dear Lei (PiPi), how wonderful it is to get to know you and eventually build a family with you. Born to be an optimist, you can always cheer me up and I cannot remember how many times we laughed like a drain. During the past 8 years, we became closer and closer, not only geographically but also spiritually. In work, we are also able to help each other and to me that is very special. Thanks, for instance, for drawing figures (Figs. 2.11 and 2.12 in this thesis) and performing many SQUID measurements on my samples. I am looking forward to creating a splendid future with you. Dear my parents, I have received infinite love from you ever since I came to this world. Being the only child of you, I was not spoiled but grew up happily under your proper guidance and hearty encouragements. You support me no matter what choice I make and are always there with me for my accomplishments or setbacks. I also want to thank my grandparents and other relatives for constantly caring about me. I love you all!

Juan Shan
Groningen
March 27, 2018

List of publications

Publications described in this thesis

1. Criteria for accurate determination of the magnon relaxation length from the nonlocal spin Seebeck effect
J. Shan, L. J. Cornelissen, J. Liu, J. Ben Youssef, L. Liang & B. J. van Wees.
Phys. Rev. B **96**, 184427 (2017). [Chapter 5]
2. Nonlocal magnon spin transport in NiFe₂O₄ thin films
J. Shan, P. Bougiatioti, L. Liang, G. Reiss, T. Kuschel & B. J. van Wees.
Appl. Phys. Lett. **110**, 132406 (2017). [Chapter 6]
3. Influence of yttrium iron garnet thickness and heater opacity on the nonlocal transport of electrically and thermally excited magnons
J. Shan, L. J. Cornelissen, N. Vlietstra, J. Ben Youssef, T. Kuschel, R. A. Duine & B. J. van Wees.
Phys. Rev. B **94**, 174437 (2016). [Chapter 4]
4. Comparison of the magneto-Peltier and magneto-Seebeck effects in magnetic tunnel junctions
J. Shan, F. K. Dejene, J. C. Leutenantsmeyer, J. Flipse, M. Münzenberg & B. J. van Wees.
Phys. Rev. B **92**, 020414(R) (2015). [Chapter 3]

Other publications

5. Magnon planar Hall effect and anisotropic magnetoresistance in a magnetic insulator
J. Liu, L. J. Cornelissen, J. Shan, T. Kuschel & B. J. van Wees.
Phys. Rev. B **95**, 140402(R) (2017).

6. Temperature dependence of the magnon spin diffusion length and magnon spin conductivity in the magnetic insulator yttrium iron garnet
L. J. Cornelissen, J. Shan & B. J. van Wees.
Phys. Rev. B **94**, 180402(R) (2016).
7. Simultaneous detection of the spin-Hall magnetoresistance and the spin-Seebeck effect in platinum and tantalum on yttrium iron garnet
N. Vlietstra, J. Shan, M. Isasa, J. Ben Youssef, F. Casanova & B. J. van Wees.
Phys. Rev. B **90**, 174436 (2014).
8. Exchange magnetic field torques in YIG/Pt bilayers observed by the spin-Hall magnetoresistance
N. Vlietstra, J. Shan, V. Castel, J. Ben Youssef, G. E. W. Bauer & B. J. van Wees.
Appl. Phys. Lett. **103**, 032401 (2013).
9. Spin-Hall magnetoresistance in platinum on yttrium iron garnet: Dependence on platinum thickness and in-plane/out-of-plane magnetization
N. Vlietstra, J. Shan, V. Castel, J. Ben Youssef & B. J. van Wees.
Phys. Rev. B **87**, 184421 (2013).
10. Inducing ferromagnetism and Kondo effect in platinum by paramagnetic ionic gating
L. Liang, Q. Chen, J. Lu, W. Talsma, J. Shan, G. R. Blake, T. T. M. Palstra & J. Ye.
accepted in *Science Advances*.
11. Gate-controlled spin-dependent magnetoresistance of a platinum/paramagnetic insulator interface
L. Liang, J. Shan, Q. Chen, J. Lu, G. R. Blake, T. T. M. Palstra, G. E. W. Bauer, B. J. van Wees & J. Ye.
submitted to *Physical Review Letters*.
12. Nonlocal magnon spin transport in yttrium iron garnet with tantalum and platinum spin injection/detection electrodes
J. Liu, L. J. Cornelissen, J. Shan, B. J. van Wees & T. Kuschel.
submitted to *Journal of Physics D: Applied Physics*.
13. Giant anisotropic magnetotransport in two-dimensional $\text{Mn}_{1/4}\text{TaS}_2$ thin films
L. Liang, Q. Chen, A. A. El Yumin, J. Shan, J. Lu, G. R. Blake, T. T. M. Palstra, B. J. van Wees & J. Ye.
in preparation.

Curriculum Vitae

Juan Shan

2 July 1990 Born in Leshan, Sichuan, China

Education

- 09/2013 - 09/2017 University of Groningen, The Netherlands
Ph.D. research in the group of Physics of Nanodevices
under the supervision of prof. dr. ir. B. J. van Wees
- 09/2011 - 08/2013 University of Groningen, The Netherlands
Topmaster program in Nanoscience
Research project: *"Spin Hall magnetoresistance in YIG/Pt systems"*.
- 09/2007 - 07/2011 University of Electronic Science and Technology of China,
China
Bachelor Electronic Science and Technology
Research project: *"Two-channel organic thin-film transistor based on Pentacene"*.
- 09/2004 - 07/2007 Chengdu Shishi High School, China

